Numerical Modelling of Tidal Energy Devices and Structures as part of Net Zero

This thesis is submitted in candidature for the degree of
Doctor of Philosophy (Ph.D.)

by

Nicolas Hanousek

Hydro-environmental Research Centre
School of Engineering
Cardiff University

August 2023

“There is no perfection, only life”

― Milan Kundera

Abstract

The world is in search of ways in which to counter the growing energy demands arising from the growing global population and electrification to reach net zero greenhouse gas emissions. A key component of this is the electrical network, which must be supplied in a manner that is both low-carbon, secure, and affordable. Major investment has been placed into wind and solar generation; however, these technologies lack the relative dispatchability and predictability that ensures security and affordability of the future energy network. Tidal energy, with tidal range using the gravitational potential from the elevation changes, tidal stream utilising tidal flows, and riverine energy, are highly predictable. These methods have dispatchable forms that could have a transformative potential on a global scale. However, challenges around cost effectiveness and environmental impact have stymied uptake and development.

To model a numerically challenging turbine, a new method of representation of vertical axis devices was developed and applied to a prototype concept. A 2D Smoothed Particle Hydrodynamics method using the open-source software DualSPHysics, was applied to the Cardiff University CarBine and found to effectively reproduce device behaviour, without the need for prescribed motion. Though the method still lacks the ability to extract power from the device and thus develop power performance metrics, self-start behaviour using only hydrodynamic forces was modelled.

To improve operational characteristics of tidal range energy, a 0D analysis was carried out on existing schemes, validated by 2D hydro-environmental modelling using a bespoke modification to the open-source TELEMAC system. Finding that operational changes can yield improvements without incurring extra capital costs – without majorly affecting environmental impact. Retrofitting disused docks as small tidal range energy generators was evaluated. For tidal docks, the spatial distribution and physical characteristics may reach an improved cost balance on the traditional concept. This was done using a widely applicable and accessible method to aid expansion of tidal range resource assessment to regions and concepts hitherto unexplored.

The technologies assessed in this work have the potential to contribute significantly to the global net zero ambitions, and the methods developed seek to accelerate their development and widen uptake.

Acknowledgements

First, I would like to thank Prof. Reza Ahmadian for his unending support throughout my PhD, from encouraging me to apply in the first place, to the guidance and advice given throughout the process. Without this, and a shared love of extended metaphors, I would not be where I am today. I would also like to thank Prof. Roger Falconer for his support, and the inspiration that underpins much of what I have done. Thank you to Prof. Simon Neill and Dr Allan Mason-Jones, whose suggestions, and insights from examining this work have improved it greatly.

I am grateful to the Engineering and Physical Sciences Research Council (EPSRC) who generously funded this work through grant number EP/L016214/1, the Water Informatics Science and Engineering (WISE) Centre for Doctoral Training.

Thank you to my collaborators. Shaun, Meysam, Aaron, Bikash, and Tong, your hard work in our joint projects is much appreciated. It was a pleasure to work with you all. Bin and Catherine, your guidance, advice, and thesis feedback are greatly appreciated. Thank you to all my ‘office’ friends along the way, notably Sam, Fawaz, Ceri, Laura, Steph, and Richard, for the discussions, assistance, lunches, and drinks over the years.

To my family, Dad, Kate (sister) and Kate (aunt), thank you for your unending belief in me, I look forward to continued holidays to snow or sea. Jake, our surfs have brought life to me in the lulls along the way. Ryan, and the Foodie group at Whitchurch, from rainy trainings in the wintertime to sun-soaked cup finals; the running around on the pitch, talking about hockey too much, and many shared meals have been highly appreciated.

Finally, my deepest gratitude goes to Hannah. Your patience, loving support, and encouragement of my work, along with your willingness to play along with my silly plans has been invaluable in keeping me motivated. I look forward to everything the future has in store for us.

Related Publications

Journal Papers

Zhang T, **Hanousek N**, Qadrdan M, Ahmadian R (2022) *A day-ahead scheduling model of power systems incorporating multiple tidal range power stations.* iEEE Transactions on Sustainainable Energy - 14, pp 826-836, doi: 10.1109/TSTE.2022.3224231

Hanousek N, Ahmadian R, Lesurf E (2023) *Providing distributed electrical generation through retrofitting disused docks as tidal range energy schemes*, Renewable Energy - 217, doi: 10.1016/j.renene.2023.119149

Hanousek N, Ranabhat B, English A, Ahmadian R (**Accepted Pending Revisions:** 14/02/2024) *A Smoothed Particle Hydrodynamics method for Vertical Axis Turbine design and assessment*, Journal of Hydrodynamics (https://www.springer.com/journal/42241)

Hanousek N, Ahmadian R, Qadrdan M, Harrison J (**UNDER REVIEW:** Submitted 15/10/2023) *Enhancing financial viability of tidal range schemes through revenue optimisation.*

Conference Proceedings

Hanousek N, Ranabhat B, Ahmadian R (2021) *Using SPH modelling to complement flume study in the development of a novel turbine design.* In: Altomare C, Gironella i Cobos X, Sanchez-Arcilla A, et al (eds) Virtual 5th DualSPHysics Users Workshop. Barcelona, p 7 **(Oral presentation online)**

Hanousek N, Ranabhat B, Ahmadian R (2021) *Using Smoothed Particle Hydrodynamics in the development of a novel vertical axis stream turbine design*. In: Kalinowska M, Rowiński

P, Okruszko T, Nones M (eds) 6th IAHR Europe Congress. Warsaw, pp 625–626 **(Poster presentation online)**

Hanousek N, Ahmadian R (2022) *Assessing the sensitivity of tidal range energy models to water level accuracy*. In: Ortega-Sanchez M (ed) Proceedings of the 49th IAHR World Congress: From Snow to Sea. IAHR, Granada, pp 4688–4697 **(Oral presentation)**

Awarded 3rd place John F Kennedy student paper competition:

https://www.iahr.org/index/dawards/5

Magazine Articles

Ahmadian R, **Hanousek N** (2021) *Exploring broader benefits of tidal range schemes*. IAHR Hydrolink 2021-3 https://www.iahr.org/library/hydrolink?hid=409

Ahmadian R, **Hanousek N** (2020) *New Development in Design of Tidal Range Schemes*. BHA Spotlight V:21 https://www.british-hydro.org/bha-spotlight-magazine/

Paper Reviewer

Renewable Energy, Elsevier, https://www.sciencedirect.com/journal/renewable-energy

Table of Contents

Nomenclature

Abbreviations

0D	Zero Dimensional
2D	Two Dimensional
3D	Three Dimensional
BEIS	Department for Business Energy and Industrial Strategy
BODC	British Oceanographic Data Centre
BP	Boundary Particle
CAPEX	Capital Expenditure
CCGT	Closed Cycle Gas Turbine
CCUS	Carbon Capture Utilisation and Storage
CD	Chart Datum
CFD	Computational Fluid Dynamics
CFL	Courant-Freidrichs-Lewy
CM	Capacity Market
CO_2	Carbon Dioxide
CPU	Computational Processing Unit
DBC	Dynamic Boundary Condition
DDT	Density Diffusion Term
EHN	Every Half Next
EMEC	European Marine Energy Centre
EPSRC	Engineering & Physical Sciences Research Council
ETN	Every Tide Next
FEM	Finite Element Method
FVM	Finite Volume Method
GB	Great Britain
GIS	Geographic Information Systems
GPU	Graphical Processing Unit
HAT	Highest Astronomical Tide
HPC	High Powered Computer
IEA	International Energy Agency
IPCC	International Panel on Climate Change
LAT	Lowest Astronomical Tide
LCoE	Levelized Cost of Energy
MNR	Mean Neap Range
MRF	Moving Reference Frame
MSR	Mean Spring Range
MTR	Mean Tidal Range
NERC	Natural Environment Research Council
NOAA	National Oceanic and Atmospheric Administration
NTSLF	National Tidal and Sea Level Facility
NWL	North Wales Lagoon

OD	Ordnance Datum
OPEX	Operating Expenditure
RANS	Reynolds Averaged Navier Stokes
RMSE	Root Mean Square Error
SDG	Sustainable Development Goal
SEBC	Severn Estuary Bristol Channel
SPH	Smoothed Particle Hydrodynamics
SPS	Sub Particle Scale
SSP	System Sell Price
STPG	Severn Tidal Power Group
T2D	TELEMAC Two Dimensional
TRS	Tidal Range Scheme
TSR	Tip Speed Ratio
UK	United Kingdom
UN	United Nations
UTM	Universal Transverse Mercator coordinate system
VAT	Vertical Axis Turbine
VLH	Very Low Head
WM	Wholesale-energy Market
WSL	West Somerset Lagoon

Symbols

Greek Letters

$\boldsymbol{\alpha}$	-	Artificial viscosity factor
$\boldsymbol{\delta_{dir}}$	-	Directional indicator
$\boldsymbol{\eta}$	m	Free surface elevation
$\boldsymbol{\theta}$	°	Angle
$\boldsymbol{\mu}$	-	Mean
$\boldsymbol{\sigma}$	-	Standard deviation
$\boldsymbol{\lambda}$	-	Tip speed ratio
$\boldsymbol{\nu_e}$	m^2/s	Diffusion coefficient
$\boldsymbol{\xi}$	m	Intertidal range
$\boldsymbol{\rho}$	kg/m^3	Density
$\boldsymbol{\phi}$	rad	Angular displacement of body
$\boldsymbol{\phi_i}$	°	Phase of i^{th} tidal constituent
$\boldsymbol{\Omega}$	rad/s	Body rotational velocity
$\boldsymbol{\omega}$	rad/s	Angular velocity of device
$\boldsymbol{\omega_i}$	°/hr	Frequency of i^{th} tidal constituent

Latin Letters

$\boldsymbol{A}$	m^2	Area
$\boldsymbol{a_i}$	m	Amplitude of ith tidal constituent
$\boldsymbol{A_{SL}}$	m^2	Area of sluice gates
$\boldsymbol{c}$	m/s	Celerity
$\boldsymbol{C_D}$	-	Coefficient of discharge
$\boldsymbol{C_f}$	-	Friction coefficient
$\boldsymbol{d}$	m	Water depth
$\boldsymbol{\Delta H}$	m	Head difference
$\boldsymbol{\Delta t}$	sec	Time step
$\boldsymbol{dp}$	m	Initial particle spacing
$\boldsymbol{D_{TB}}$	m	Diameter of turbine
$\boldsymbol{E}$	MWh	Energy
$\boldsymbol{f_k}$	N	Sum of forces on the particle set k
$\boldsymbol{F^q}$	m/s^2	Momentum source or sink from culvert
$\boldsymbol{g}$	m/s^2	Gravitational acceleration
$\boldsymbol{h}$	m	Kernel smoothing length
$\boldsymbol{h}$	m	Water depth
$\mathbf{I}$	g	Body inertia
$\boldsymbol{L2}$	-	L2 error norm
$\boldsymbol{M}$	g	Body mass
$\boldsymbol{m}$	kg	Mass
$\boldsymbol{n_{TB}}$	-	Number of turbines
$\boldsymbol{np}$	-	Number of particles
$\boldsymbol{P}$	N	Pressure
$\boldsymbol{P_{HK}}$	MW	Power from hydrokinetic device
$\boldsymbol{P_{TB}}$	MW	Power from turbine
$\boldsymbol{Q}$	m^3/s	Discharge rate
$\boldsymbol{q}$	-	Normalised relative position vector
$\mathbf{r}$	-	Position vector of particle
$\mathbf{R_0}$	-	Body centre of mass
$\boldsymbol{R^2}$	-	R^2 error
$\boldsymbol{S_h}$	m/s	Momentum source or sink term
$\boldsymbol{t}$	sec	Instantaneous time
$\boldsymbol{T}$	sec	Total time
$\boldsymbol{u}$	m/s	Velocity in x direction
$\boldsymbol{u'}$	m/s	Velocity fluctuation
$\boldsymbol{U_\infty}$	m/s	Flume inlet velocity
$\mathbf{v}$	-	Velocity vector of particle
$\boldsymbol{V}$	m^3	Volume
$\boldsymbol{v}$	m/s	Velocity
$\boldsymbol{V}$	-	Body velocity vector
$\boldsymbol{v_t}$	m^2/s	Eddy viscosity
$\boldsymbol{W}$	-	Kernel function
$\boldsymbol{W}$		Width of basin entrance
$\boldsymbol{z}$	m	Elevation

List of Figures

List of Tables

1 Introduction

1.1 Background

Since the industrial revolution, humanity has relied on fossil fuels to generate electricity, and by doing so has released carbon dioxide into the atmosphere to a degree that has changed the global climate. This has led to an increase in both the intensity and frequency of extreme events, changes in atmospheric patterns, and rising sea levels, all of which are hazardous to life on earth. To combat this, 192 countries signed the Paris Agreement in 2015. Many parties have since reaffirmed or tightened imposed limits since [1], and over 70 countries including the largest polluters have set net zero goals. The goals set out by the agreement include keeping global temperatures within 1.5ºC of pre-industrial levels, limiting greenhouse gas emissions, and for economically prosperous states to provide "climate finance" to aid the global progression [2]. The Paris Agreement also encourages member states to set and review individual goals at regular intervals, to ensure the pathway was being followed. The Paris Agreement was updated by further Conference of Parties (COP) meetings; in Katowice in 2018 a rulebook for implementing adaption was laid out, a meeting in Glasgow in 2019 established the Glasgow Climate Pact to reduce the gap between existing plans and required levels; and the United Arab Emirates in 2023, a global stocktake hailed as signalling the end of the fossil fuel era. Furthermore various regional and national targets have been set since The Paris Agreement, including the European Green Deal in 2019 [3] which aims to make Europe the first continent with no net emissions of greenhouse gases in 2050 and where economic growth is decoupled from resource use, and China's Pledge in 2020 to reach carbon neutrality by 2060 [4]. The International Energy Agency (IEA) discuss how the Russian invasion of Ukraine interrupted the post-pandemic recovery of the global energy market, and how global energy policies are being used to accelerate the transition to low-carbon [5]. The report also describes how newer governmental policies are bringing a global temporal peak for fossil fuel usage and the subsequent decline into view, though still not in line with the 1.5°C target laid out in the Paris Agreement.

Access to electricity has been linked to a number of the United Nations Sustainable Development Goals (UN SDGs) [6], by improving the quality of life, education rates, and equality measures [7]. Compounded with a globally increasing population [8], and usage of electrical technologies the need for energy is likely to continue to grow for many years to come.

In parallel to this growth, there is an ever-present expectation for the electricity supply to be formed of low-carbon sources, in line with social and political pressure to mitigate the effects of anthropogenic climate change [9]. This rising demand for electricity must be met through low-carbon sources so as not to make this consumer change redundant by simply moving emissions from the individual to the generators. Global electricity demand has been and (except for a pause due to the Covid-19 pandemic) is still rising [10]. The technology used to meet this rise is not constant globally, with Asia in particular undergoing an increase in coal generation. With the changing global climate, the demand for space heating and cooling as intermediate climates become more extreme will, in turn, incur an increasing electricity demand globally [5].

With the global population forecast to grow, the demand for increased technological power in the developing world, and a drive towards electrified transport in the developed world, the need for clean electricity to underpin the net zero transition is paramount [5]. Growth in the low-carbon energy sector has been focussed on nuclear, wind, and solar technologies; however, an effective national or multinational electrical grid requires careful balancing and a diverse energy mix to ensure safe and effective operation. As the demands on the system fluctuate on a daily, weekly, and seasonal basis, the suppliers must be able to match that demand or call upon storage systems to absorb the differences.

In the UK, the Low Carbon Transition Plan [11] from 2009 set out a national strategy for climate and energy, aiming to produce 40% of the nation's electricity from low-carbon sources and 30% from renewables, and help make the UK a centre of green industry through supportive policy and funding decisions. The 2020 white paper – 'Powering our Net Zero Future' [12] further develops this roadmap, published during the Covid-19 pandemic, the Department for Business Environment and Industrial Strategy cite the compelling case for tackling climate change and how this forms the domestic agenda. An increase in renewable energy capacity of 500 % and a 72 % reduction in CO_2 reductions from electricity generation since 2009 show that progress is being made towards decarbonisation of the energy sector. The report also states that there will be a push to reduce fossil fuel usage on a number of societal levels, with 2030 bringing the end of new diesel and petrol vehicles for example [12]. Powering Up Britain is a blueprint for the future of energy7 in the UK, formed of two parts - the Net Zero Growth Plan [13], and the Energy Security Plan [14]. These documents along with the creation of a new government Department for Energy Security and Net Zero highlight the state desire to balance net zero goals and do so in a secure manner.

To reach net zero goals, increased usage of low-carbon or renewable energy methods is fundamental. There are a number of these, and their strengths and weaknesses must be balanced in order to maintain energy security to prevent a fallback to foreign fossil fuel imports or reliance on UK fossil fuels. The key technologies outlined by the government to fill this need are wind (offshore and onshore) and solar power. Both of these are classified as intermittent renewables, only generating at given times, when the wind speed is between the cut-in and cut-off velocities or solar irradiance is above the threshold level respectively, without the ability to be dispatched at times of need. Though offshore wind has a typically less variable energy profile than onshore wind, the fluctuating nature of the national grid needs cannot be answered by wind and solar alone [15]. The consistent daily pattern of variation in demand (defined by energy price) over the course of a day is shown in Figure 1.1, where the average price at each time of day is normalised to the average price for the year – for the decade 2012-22. Note the peaks around the start of the traditional workday and the times when workers are returning home and preparing an evening meal. To provide a balancing mechanism between the varying demand and supply levels, an expansion of the storage systems will be required, these take a variety of forms including physical forms such as pumped hydro schemes, and other developing forms. The major source of storage is likely to be chemical batteries, which themselves can be costly and require rare-earth minerals in their manufacture. Pumped storage and hydropower schemes have been used successfully both in the UK and internationally [16], but require suitable terrain to be effective.

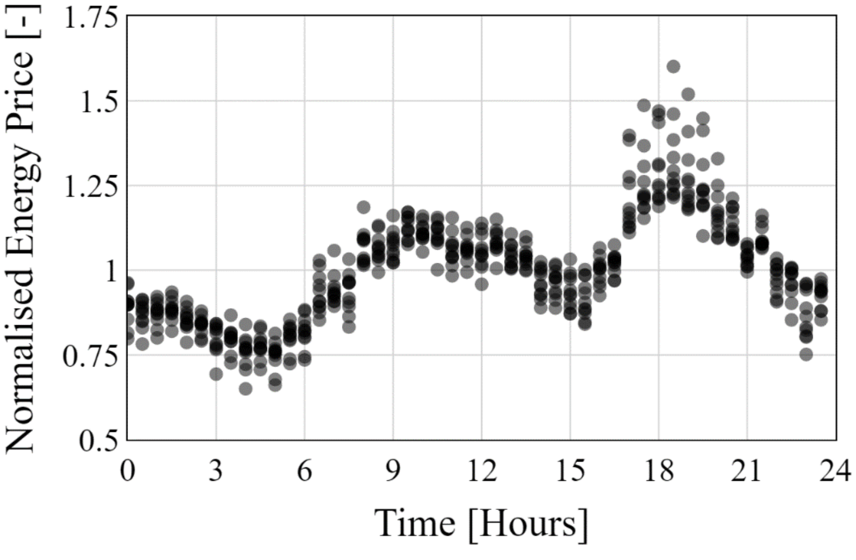

Figure 1.1: Annual average energy price at a given time of day, normalised to the average price of energy for the year, 2012-2022. Energy price from Elexon Knowledge Base [17].

Tidal energy has been long considered a potentially powerful source of energy for the UK, with its long coastline and strong tidal effects. With tidal stream turbines being deployed at a small number of locations to varying degrees of success [18], including the world's largest tidal stream device – the Orbital O2, operating off the Scottish coast [19]. Due to the large tides found around the UK coast, tidal range schemes have been proposed repeatedly by engineers and developers hoping to produce renewable energy from the potential energy developed by the tides [20]. Tidal range energy can ostensibly store energy by operating in a manner akin to a pumped-hydro storage system, creating additional dispatchability and flexibility of operation [21, 22]. These features along with the highly predictable nature of the tides make this an energy generation technology whose strengths complement the weaknesses of other renewables. A tidal range scheme has a degree of dispatchability (the ability to control when the scheme generates electricity) beyond that of the wind and solar powers. However, this is reduced based on the availability windows defined by the tidal conditions as opposed to the full dispatchability of some fossil fuel technologies. Improving the understanding of how tidal range schemes in a developed form would interact with the energy mix that is transitioning towards net zero could accelerate the uptake of tidal range energy, and crucially lead to a more secure energy mix in the future.

Two factors have held tidal range back in the UK since the dissolution of the tidal mills [23], the capital expenditure required to construct a tidal range scheme, and the not-insignificant environmental impact that such schemes have had in other places, and would incur once operational. For more recent examples, the Swansea Bay lagoon proposal was costed at 800-850 million GBP [24], and the Annapolis Generating station was decommissioned on environmental grounds in 2019 [25], described in Section 2.5.2. To counter this, proposals by engineers and developers have focussed on improving the operation of the schemes to either reduce the environmental impact (through lower head turbines and less sensitive positioning of the impoundment) or increase the financial yields achieved by iterative improvements to the designs and operational schedules considered. For a large scheme – one that would generate an electricity output that fundamentally changes the national mix – to be feasible in being deployed, this process is still fundamentally required. Utilising operational tools to best optimise both the engineering design and the operational characteristics can shift the scales enough that the margins become acceptable. This is likely to be improved in the future, as the wholesale energy price for the UK becomes not only greater but more variable [15]. Shown in Figure 1.2 are the distributions of the energy price for three of the past five years, the transition from the consistent pricing of the late 2010s to a highly spread (and on average more expensive energy) price is clear. This is a combined function of not only the energy network becoming increasingly driven by intermittent renewables but also the effects of the Russian invasion of Ukraine destabilising the gas market [26]. Tidal range energy, with its degree of dispatchability, storage, and predictability could flourish in this market and bring an improved level of stability with it.

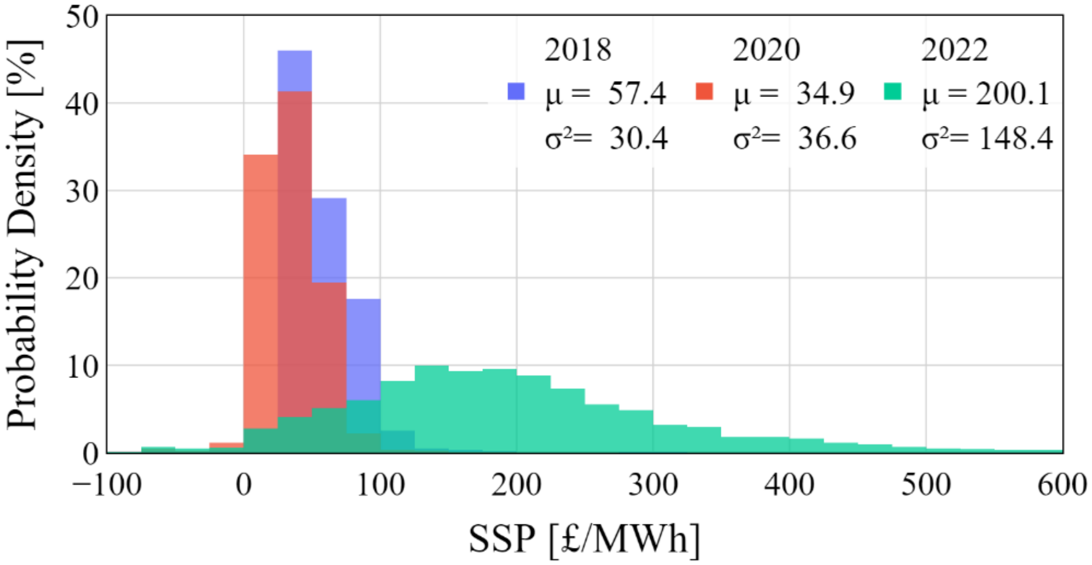

Figure 1.2:UK wholesale energy price distribution, 2018, 2020, and 2022. Data from Elexon knowledge portal [17].

The advantages of a large tidal range scheme have been briefly summarised (and are covered further in the remainder of this thesis), but they come at a cost as mentioned. The Severn Barrage is likely the best-known tidal range scheme to never be built, with huge energy potential – and environmental and financial costs to match. In the 100+ years that it has been discussed, the development has broadly been about finding the best place to build an impoundment from one bank of the estuary to the other and how many turbines and sluice gates to install in said bund wall [27, 28]. The tidal range concept however has been implemented historically in a smaller form, the tidal mills found across Europe in the middle ages [23]. These use the same benefits of a large tidal range scheme, but due to a small size and the economics of the period, these were widely used. This was however overtaken by the industrial revolution raising other forms of power that were more cost effective. Taking this line of reasoning a little further begs the question, could tidal range energy provide the benefits of its concept without the need for vast structures and harmful operations? Whether the risk and return could balance is still key, but using existing structures such as disused dock basins (left behind by the evolution of the maritime industry) could strike a balance point. This could make the concept of tidal range not only more palatable to areas already considering tidal range in some form, but along with a clear method for initial scoping, could expand the interest in tidal range to new regions.

Tidal range schemes use turbines built into the wall or impoundment structure of the scheme. These convert the difference in gravitational potential energy across the structure to kinetic energy when opened. The inlet and outlet structures conditioning the flow over the runners and into the environment [29]. Alternatively, turbines can be designed to be installed in open bodies of water such as rivers or tidal flows, directly extracting power from the water movement itself. Coming from the Greek words for water and movement, these are known as hydrokinetic turbines. Flow conditioning for these turbines can be achieved through the use of ducts built around the device where required [30].

Hydrokinetic turbines have the potential to be deployed in a variety of flow conditions and could be valuable in the global migration to net zero. In developed national grids such as those in Europe, the predictable nature of tidal stream turbines in coastal regions can add a new high-value element to the mix, or form the power behind techniques such as hydrogen production (as is being explored at the European Marine Energy Centre [19]). Riverine hydrokinetic energy on the other hand can be found around the world [30], including in regions where electricity demand is growing and the prevailing tool of electrification is the diesel generator [31]. Empowering off-grid communities with improved electrical supply through renewable energy would improve quality of life not only in terms of electricity but also factors such as air quality, leading to schemes such as the Off-Diesel Challenge led by Natural Resources Canada [32]. A potential future location for hydrokinetic turbines being the downstream of tidal range schemes where velocities are higher, and the extraction of energy from such flows could reduce potential environmental impacts. The vast majority of research however has focussed on the development of large devices for deep and fast-flowing waters, and the tools to assess these turbines are both financially, numerically, and in terms of expertise – expensive [33]. Smaller, more widely applicable devices could have a transformative power in the coming years with the growing drive towards electrification [31]. However, without robust, open, and accessible tools to assess the suitability of turbine designs, this growth will struggle to come to fruition. Alternative modelling techniques must be investigated and honed to better enable the modelling of challenging designs, but in a manner that can be utilised in a wide variety of scenarios.

If the UK, and the world as a whole are to meet net zero targets and ensure a liveable planet for future generations, new technologies and approaches will be critical. With tidal range, stream, and hydrokinetic energy being potential avenues for this change – expanding our understanding of their power outputs, grid interactions, and environmental impacts may expedite and expand deployment. Numerical modelling tools have been used to assess these technologies in the past, but require further development to make their usage in these fields more accessible and effective.

1.2 Research Objectives

This thesis takes a number of modelling approaches and applies them to a selection of case studies with the combined goal of developing an understanding of how marine renewables can contribute to a net zero energy mix, with particular attention to the UK, though with an intent to make the processes used as widely applicable as possible in aid of accessibility and open-science. The thesis has three major themes, the novelties and aims of which are as follows.

Can a new efficient modelling methodology be utilised in designing and developing a new turbine concept?

Chapter 4 provides the details on the modelling process carried out upon a vertical axis turbine, suitable for use in off-grid locations. Due to the technical complexities of the given design (several interconnected elements whose domains of motion interact significantly), traditional mesh-based modelling methods fail to fully represent the motion of the device. As such Smoothed Particle Hydrodynamics, was used to model the turbine in 2D free-spin scenarios, without power take-off, in tests designed to represent conditions in the laboratory. The objectives of this study are to:

- Determine the applicability of Smoothed Particle Hydrodynamics to the development process of vertical axis turbines.
- Model the numerically challenging turbine design concept known as CarBine with SPH, with validation to measured behaviour.
- Examine an initial set of design options for the concept, including cases where the turbine has been damaged.

What steps could make tidal range energy viable, without costing the environment?

Chapter 5 applies two bespoke numerical modelling techniques to the study of large tidal range schemes proposed for the UK. These two schemes were selected based on their perceived state of development, and complimentary characteristics. The model outputs help to both improve behaviour and design, account for environmental impact and demonstrate potential grid interaction. The intentions are to:

- Develop 0D and 2D tools for the modelling of tidal range schemes to aid uptake and improve understanding of the concept.
- Develop the operational control of tidal range schemes to generate electricity in a profitable and grid-beneficial manner.
- Provide an overview of how the design of the schemes would impact performance based on updated operational optimum.
- Validate the operational improvements identified using 0D modelling, using a 2D physically founded model.

Can small tidal range schemes find strength in numbers?

Chapter 6 takes the established tidal range concept, and explores a mechanism to expand it to new applications. Disused docks in the UK are used as a starting point for assessing the benefits of a distributed fleet of small tidal rage schemes. This research aims to:

- Identify a base set of dock basins that could act as tidal range schemes in the UK.
- Assess the generating potential of the docks, when acting as tidal range schemes.
- Establish a clear and accessible method for this analysis.
- Provide a detailed example of the process for one of the docks identified.
- Examine how the fleet of docks may interact with the national grid as a set of distributed generators.

These objectives seek to provide a new level of insight into how the UK energy network could best look to utilise the marine energy resource around its shores as part of the climb towards a net zero energy system.

1.3 Outline

This thesis is composed of 7 chapters as follows:

1. Introduction**,** provides the context within which the research sits, the objectives of the work, and the structure of the thesis.

2. Literature Review**,** offers a summary of the existing state of the knowledge on the subjects to be investigated, introduces some key prior works, and describes some fundamental concepts around which the work is built.

3. Numerical Models**,** describes the numerical modelling tools used throughout, their fundamentals, availability and access links, and an overview of their prior usage.

4. Using Smoothed Particle Hydrodynamics to model a Vertical Axis Turbine**,** presents the process used to assess a hydrokinetic energy device using an unconventional modelling technique.

5. Tidal Range Schemes and Net Zero**,** uses modern knowledge of how a tidal range scheme can be operated and updated modelling techniques to ascertain an improved energy potential of classical tidal range schemes and pins their operation within the context of the energy mix.

6. Disused Docks as Tidal Range Schemes**,** develops the concept of using a disused dock as a small tidal range scheme from first principals including sensitivity analyses and potential interactions of a fleet of lagoons with the national grid.

7. Conclusions and Recommendations**,** compounds the key findings of the research, weighs their strengths and weaknesses, and finally provides avenues for future research based on this work.

The references used are then presented, followed by additional information in the form of appendices.

2 Literature Review

2.1 Introduction

This chapter provides an overview of the literature regarding the study of tidal range energy and of small-scale hydrokinetic devices, and the background to the energy markets and mix of the UK – in the march towards net zero. To reach this point the fundamental principles behind the formation of tides, the various existing tidal range schemes, key proposals, and the tools used in their study are developed. The common methods for the assessment of vertical axis turbines, and an overview of the net zero goal of the GB electrical network is also provided.

2.2 Net zero in the UK

The power market of the United Kingdom is formed of multiple components, including the Wholesale-energy Market (WM) – wherein energy generation contracts are agreed upon on a scale of years to days in advance, with operators dispatching energy to the grid at the appropriate time [34]. The Capacity Market (CM), introduced in 2014 to mitigate the potential of blackouts, rewards generators for their ability to generate during a forecast period, providing power to the system if the wholesale market falls short [35]. The Balancing Market (BM) (or Ancillary Services market) ensures security and quality of electricity through near real-time procurement of power and frequency response. The latter two markets deal with potential and actual deviations from the predicted supply or demand to the system, driven significantly by natural effects. As the severity and likelihood of extreme events increases, the demand for energy to charge electric vehicles, to heat and cool homes etc. becomes more challenging to anticipate, whilst the potential availability of wind and solar energies cannot inherently be relied upon [15]. As such, storage, and balancing mechanisms, along with reliable sources of renewable energy are critical to ‘keeping the lights on’ around the UK [36].

A ten point plan was drawn up to accelerate the transition to net zero for the UK in 2020 by the Department for Business Energy and Industrial Strategy (BEIS) [37], breaking the shift to net zero down into buildings, vehicles, energy, and Carbon Capture Usage and Storage (CCUS) – with notes on protecting the natural environment and changes to green financing to aid this process. This was followed and expanded upon by the energy white paper “Powering our Net Zero Future” [12], which covered a range of themes across industry and technology, with a view to ensuring that energy security and affordability are maintained with the net zero transition, in light of the Covid-19 pandemic. This white paper also raises how the capital costs and long timescales will be a challenge, and highlights the role of offshore wind to be a leading contributor to the future energy network, with a proposed total capacity of 40 GW by 2030. The BEIS Net Zero Strategy Build Back Greener [38] published in 2021 built on the ten point plan with a focus on what the different sectors should be working towards and the progress made so far. The British Energy Security Strategy [39] continues to place offshore wind as a key element of the 2030 energy mix, but has more of a focus on the energy network than the prior pieces mentioned, this includes expansion of storage and flexibility features, and the transition to minimise dependence on Russian oil as a response to the invasion of Ukraine in 2022. The primary renewables focus is on wind, with an expected five-fold increase in solar generation by 2035, however the document does state that as an island nation there is an opportunity for aggressive exploration of alternative renewable opportunities including tidal and geothermal generation.

In the 2018 energy mix for the UK, the base-load requirement was carried by nuclear energy (at 19.5 % of total energy generated), with renewables making up 33.3 % (of which 51.4 % was wind), coal saw a significant drop from the previous year to 5.0 %, and the largest source was gas (39.4 %) [40], due in part to an ability to modulate output on demand. Note the increasing proportion of wind energy in the national electricity mix and the decline in coal usage from the first quarters of 2018 to 2022 in Figure 2.1. Note that the contributions are shown as components of the net demand, which in itself changes on a consistent basis as shown in Figure 1.1 and Figure 2.2, and thus the variation of the nuclear contribution for example is a steady output in a varying total mix.

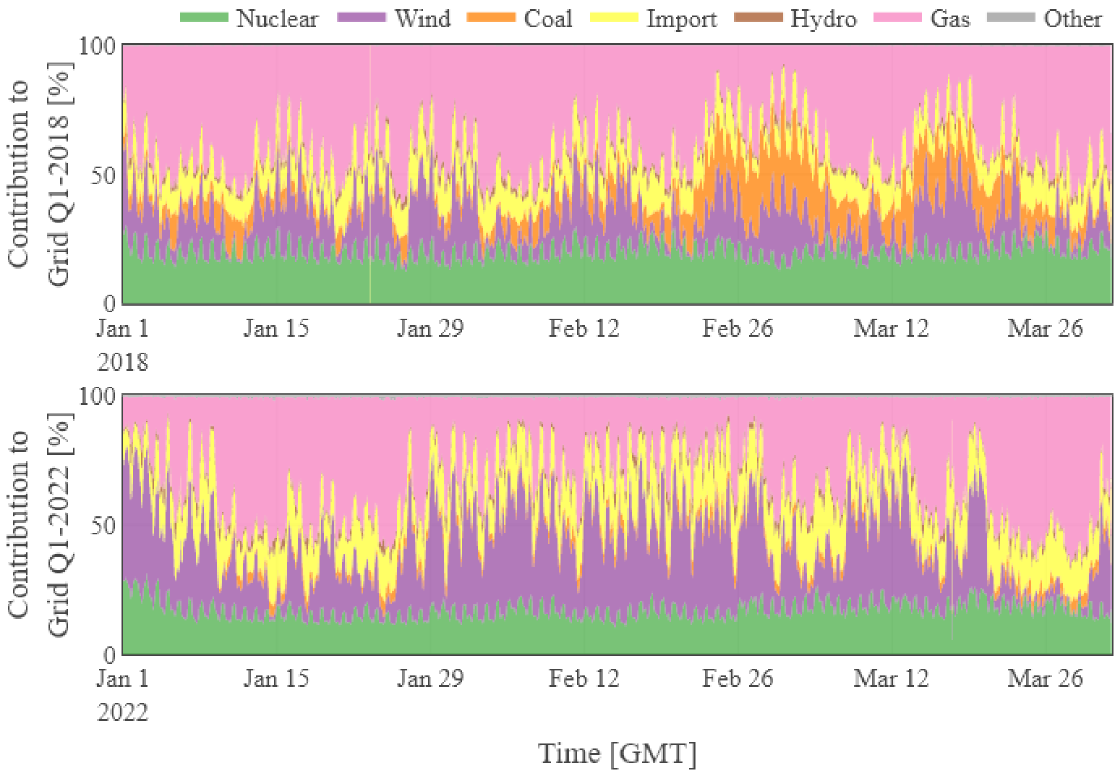

Figure 2.1: GB energy mix, first quarters of 2018 and 2022, data from Elexon knowledge base [17].

The operational patterns of power generation sources in the UK are depicted in Figure 2.2. Nuclear power maintains a consistent output of 6.9 GW throughout the day, while wind power and imports contribute between 4 and 5 GW. Fossil fuels and hydropower exhibit a similar pattern that aligns with periods of higher demand. These sources possess greater flexibility and are responsible for meeting network demands, with gas being the most prevalent. Although nuclear reactors excel at providing sustained electricity, they lack the capability to adjust output according to demand fluctuations. Conversely, traditional renewables are highly variable and dependent on weather conditions, making it challenging to match operation to rising and falling demand. Gas power closely follows the grid's demand, with coal, hydro power, and imported energy exhibiting a similar pattern at lower levels. Wind power demonstrates relative consistency throughout the year, with the lowest output around 06:00, increasing during daylight hours, and then declining after 18:00 [17].

As the rising usage of wind and solar energy continues, the impact of how they generate electricity becomes more significant. Figure 1.2 shows the increasing volatility (spread) in the energy price over time from 2018 to 2022, this can be attributed to geo-political factors, but also to the growing role of intermittent renewables in the mix [15, 41]. This can be absorbed by increasing the storage capacity of systems about the grid, with distributed batteries acting in energy arbitrage (buying at low prices and selling at high prices) [42].

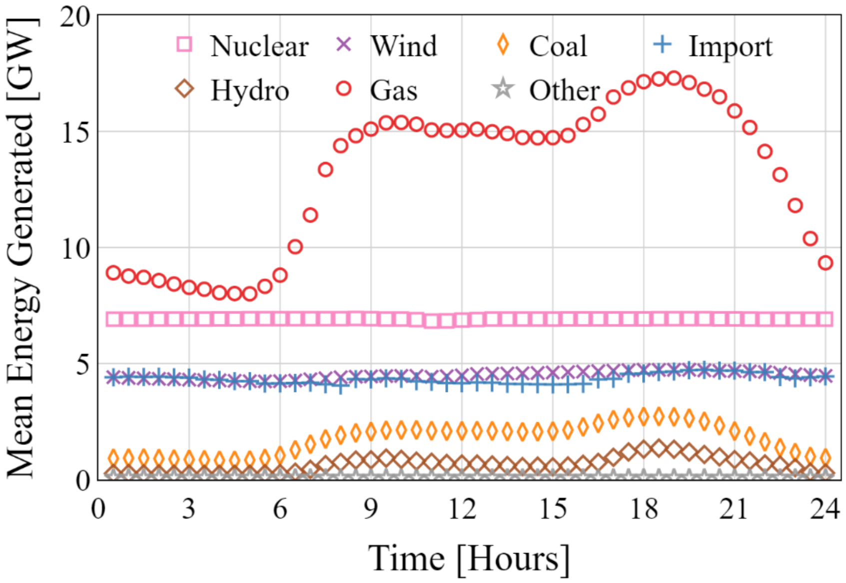

Figure 2.2: Mean power output at half hour intervals of the day, for each generation method in the UK for 2018.

2.3 Tides: Generation, Analysis and Prediction

The tides, being driven predominantly by the gravitational pulls of the sun and moon on the earths oceans – are highly predictable [43]. This predictability offers a degree of planning to the energy sector that has been a challenge to overcome with the uptake of more variable renewable energy technologies [15]. This section summarises how the tides are generated, how this is used in prediction and forecasting, and the UK tidal environment.

2.3.1 Fundamentals of Tides

The Newtonian principle of gravitation posits that the attractive force between two bodies is proportional to the product of their masses over the square of the distance between them. In the context of the earths oceans, the most gravitationally impacting bodies are the earth itself – keeping the water upon its surface, the moon, and sun. The orbit of the moon around the earth, the orbit of the earth about the sun, and the axial spin of the earth all contribute to the rise and fall of the oceans surface – the tides.

In the simplest view, the sun and moon can be thought of as pulling the water towards them. When the sun and moon are in alignment about the earth, when the moon is ‘full’ or ‘new’ – the gravitational forces are additive and so the tides are at their largest, known colloquially as Spring tides. When the bodies are oriented at right angles to each other – the gravitational forces are in opposition to each other, leading to smaller variations – known as neap tides [44, 45]. This system, known as the equilibrium tidal model, is shown schematically in Figure 2.3.

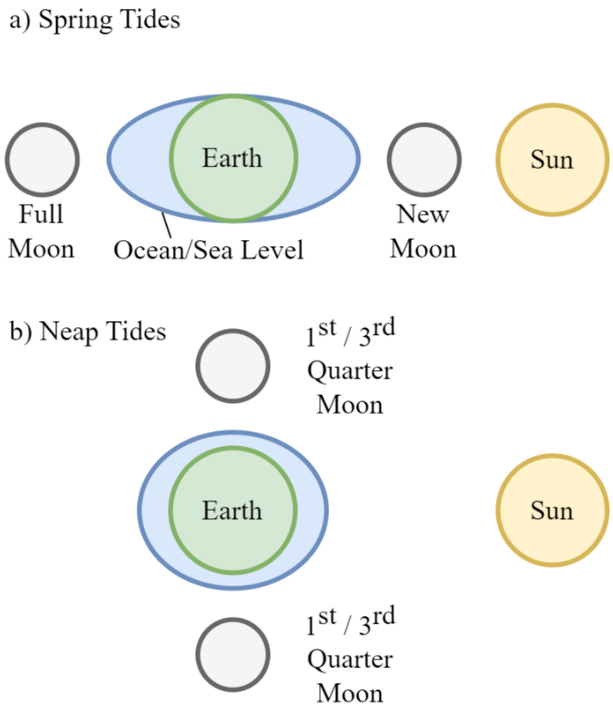

Figure 2.3: Simplified equilibrium tidal model schematic.

The model does however not account for a number of effects that influence tidal characteristics around the world. Frictional effects from landmasses and the seabed dampen the tides, the model assumes a homogenous and featureless ocean, whereas in reality the impact of the ocean floor, and landmasses themselves influences tidal patterns. The Coriolis effect (the curving of a path of motion due to the rotation of the earth) deflects the movement of the tidal propagation. Finally, the model assumes that the oceans achieve equilibrium instantaneously – however, due to the speed at which a tidal wave propagates, this is inherently impossible. The tidal wave, upon reaching shallow water, where the frictional effects from the sea bottom impacts the wave, moves with a speed (or celerity) equal to c (m/s) calculated per Equation 2.1:

$$c = \sqrt{gh} \tag{2.1}$$

where g (m/s^2) is gravity and h (m) is the water depth. Since tidal waves are by their nature very long they are always considered as shallow water waves. Thus, a progressive wave moving from deep to shallower waters will decelerate and the amplitude of the wave increases [45]. The speed of the wave moving through a region can be exemplified by identifying locations where the same tidal event is seen concurrently. Connecting locations of concurrent tidal elevations leads to the development of cotidal lines. The progression of a mean spring tide from the ocean is shown in Figure 2.4, where a cotidal line reaches from Brittany in France, up past the southern UK, passing up from the Celtic Sea, north into the Irish Sea and east into the English Channel [46].

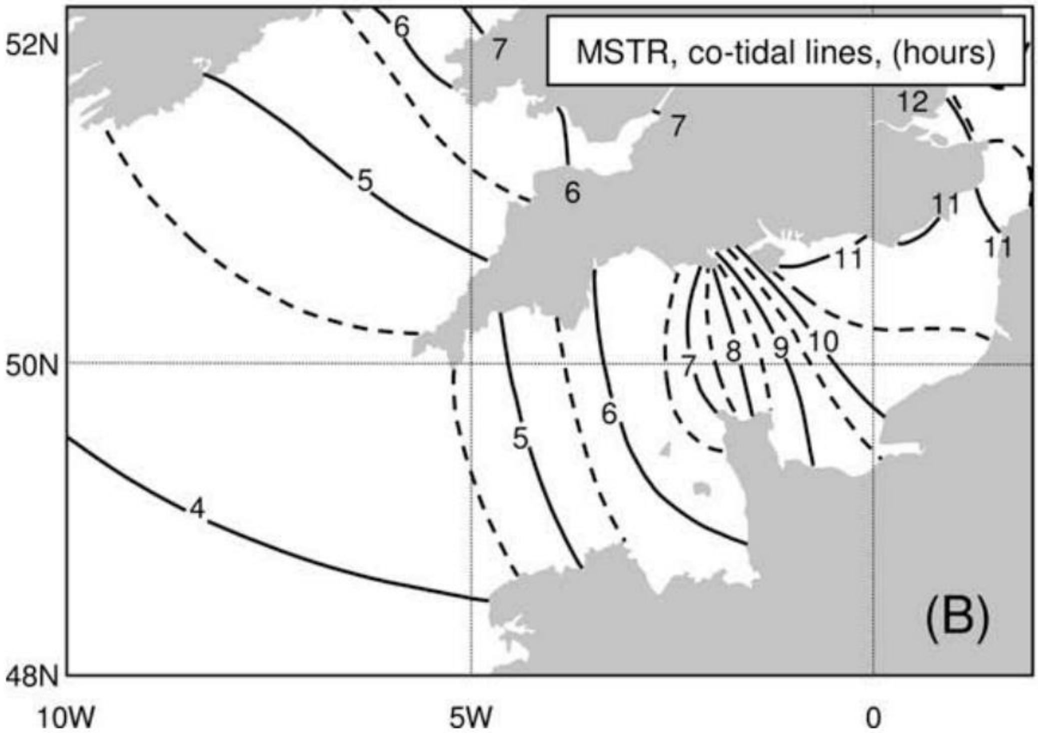

Figure 2.4: Mean Spring Tidal Range co-tidal chart of southern Britain and English Channel, reproduced from Fig 1 in Uncles [46].

The individual rise and fall of the tide at a given location is broken down into a number of key phases, due to their inherent usage throughout this work they are summarised herein. The highest and lowest points of a given tide are referred to as High and Low tide respectively, with there being a number of key parameters around these (the highest and lowest astronomical tides for example are the levels reached by astronomical effects over a given time period – not accounting for local weather effects). The elevation distance between the high and low tide levels is the tidal range, with the tidal amplitude being the distance from the mean sea level to the high or low tide level. The transitional phases between high and low are the ebb – moving from high to low, and the flood – the rising tide [44]. Figure 2.5 shows these variables for a simplified semi-diurnal style tide (two tides per day). Many locations experience diurnal (one tide per day) or mixed tides – where there are alternating sizes of high and low tides, however the areas of study considered here are heavily semi-diurnal.

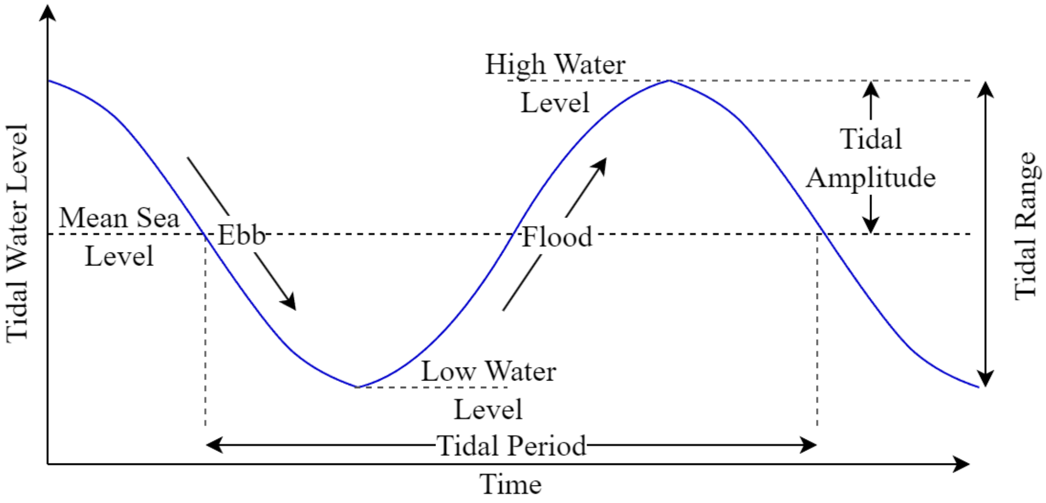

Figure 2.5: Key components of semi-diurnal tides.

2.3.2 Tidal Prediction

The prediction of tides has been an important challenge for human civilization for thousands of years, as the tides have had a significant impact on navigation, fishing, and coastal economies. Early tidal observations were made by applying the Newtonian principles to a spherical body by Laplace among others in the 18th century, though these were challenging to solve analytically prior to the advent of digital computing. At a given site, the component effects forcing the tide could be extracted from a measured dataset and thus mechanical prediction machines used. From these point locations, further observations were combined to map co-tidal lines and amphidromic points, developing the understanding of the motion of the global ocean [47].

Satellite observations constituted one of the largest developments in the field of tidal analysis and prediction – allowing accurate monitoring of the surface of the earths oceans.

Notable among these is the TOPEX/POSEIDON satellite, a collaborative venture between NASA (USA) and CNES (France), launched in 1992. This orbits on a 9.916 day cycle with a grid spacing of 2.835°, positioning it between the earlier 3-day SeaSat and 17-day GeoSat systems. The data from this and other satellite datasets has been used to develop much more detailed tidal estimates such as the TPXO database [43, 48].

2.3.3 Tidal Constituents

By considering the tidal water surface elevation $\eta(t)$ at a location to be the time varying sum of a number of constituent waves, driven by the solar and lunar gravities – a tide can be described as in Equation 2.2, where a_i is the amplitude of the constituent, ω_i the temporal frequency, and ϕ_i the phase of the constituent (typically taken relative to the Greenwich meridian).

$$\eta(t) = \sum_{i=1}^{N} a_i \cdot \cos\left(\omega_i t - \phi_i\right) \tag{2.2}$$

The first 8 tidal components (based on the NOAA ordering [44]) for the mouth of the Severn are combined for a sample 24 hour period in Figure 2.6. The size of the M2 – principal lunar semidiurnal and S2 – principal solar semidiurnal, and N2 – larger lunar elliptic semidiurnal tides, relative to the other constituents can be seen here. This distribution is largely true within the Severn area (a region of particular interest to tidal energy developers in the UK for over a century), with Vazquez and Iglesias [49] reporting the constituents at the mouth of the Severn shown in Table 2.1. These are identified by pre-supposing the constituents in effect, whose frequencies are known – and using a statistical fitness or Fourier analysis to determine the phasing and amplitudes. Various packages are available to do this analysis based on a timeseries of water level data – such as the T_TIDE Matlab toolkit developed by Pawlowicz et al. [50].

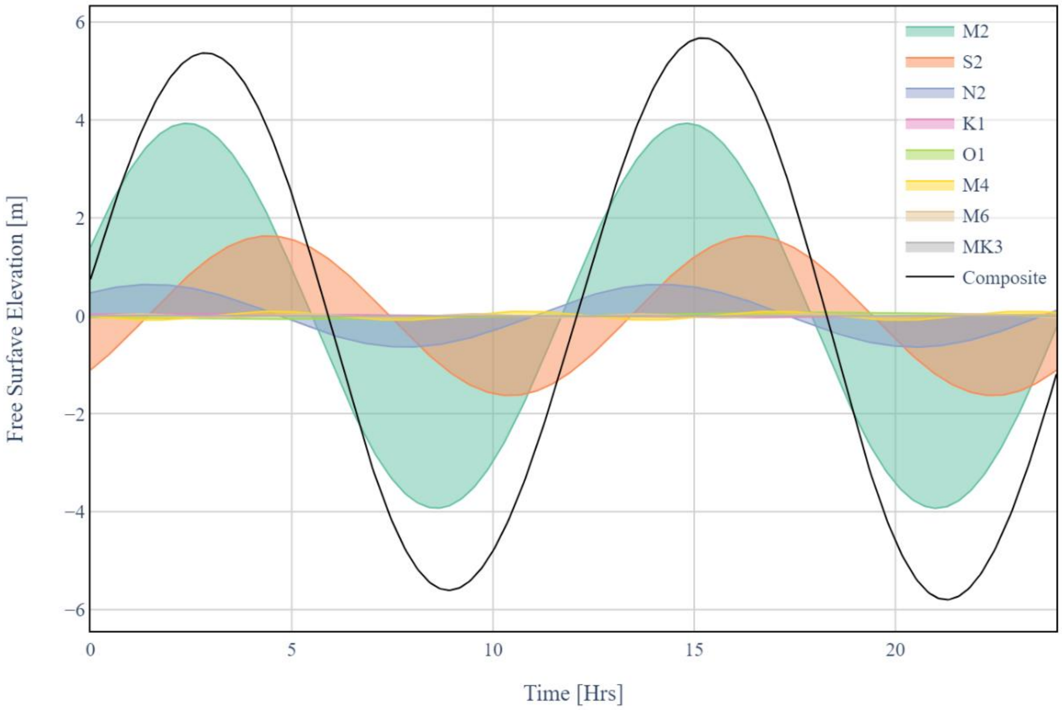

Figure 2.6: Composite tidal elevation trace for the Severn Estuary extracted at Hinkley Point measuring station.

Table 2.1: Tidal constituents at mouth of the Severn per Vazquez and Iglesias [49].

Constituent	**Amplitude [cm]**	**Phase [°]**
M2	235.24	156.87
S2	84.17	201.21
N2	44.79	138.48
K2	24.45	195.8
K1	6.77	127.34
O1	6.7	351.17
P1	2.23	121.81
Q1	1.95	305.66
M4	3.69	290.99

2.3.4 UK Tidal Conditions

The United Kingdoms of Great Britain and Northern Ireland have a long maritime history, and intertwined with this history is the nature of the tides about the isles. From King Canute attempting to stop the tide, to the observations of the Venerable Bede and Gerald of Wales in the middle ages, through to the works of Lord Kelvin in the 19th century – the UK tides have always been of interest [47]. This is undoubtedly a function of the scale of tides experienced in the UK, with tidal ranges in the Severn Estuary being the second largest in the world [20].

Tidal currents around the UK can reach speeds in excess of 4 m/s, although on the whole this is rare – and confined primarily to remote areas such as the Pentland Firth at the North-East tip of Scotland. The peak spring tidal velocities around the country are shown in Figure 2.7, this gives an indicator of the highest velocities that can be expected. Generally, this peak is less than 1 m/s for UK waters – with a mean peak velocity of ~0.5 m/s. The areas of high flow velocity have been of interest for renewable energy with the European Marine Energy Centre (EMEC) being based in the Orkney Isles [51], home of the Orbital O2 – a prototype of the world's most powerful tidal stream turbine with a capacity of 250 kW [19].

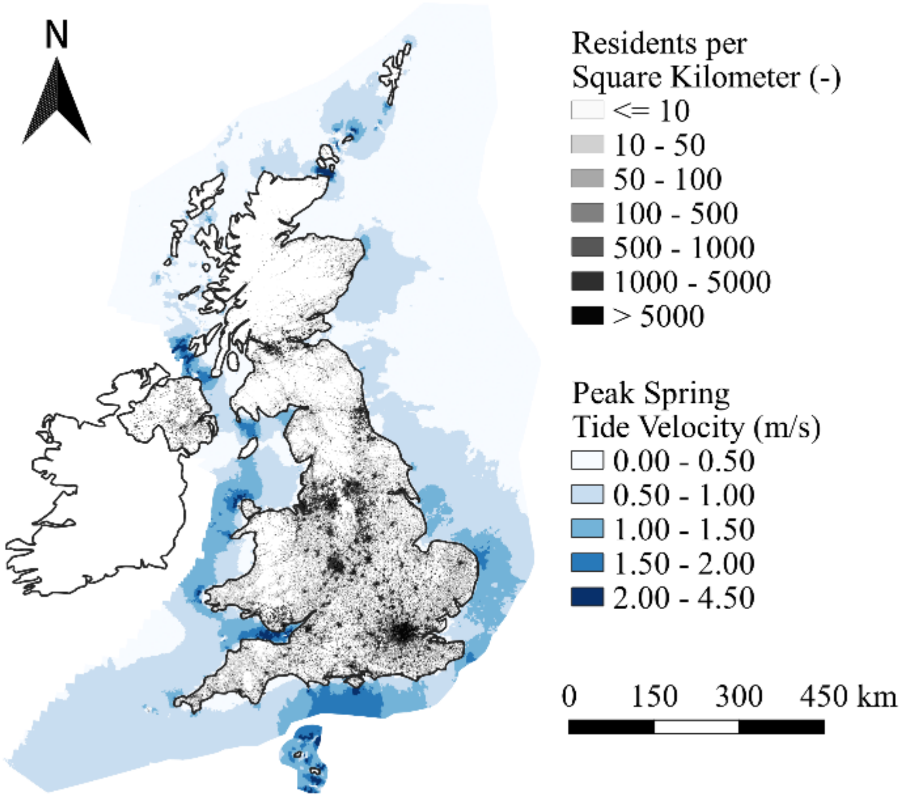

Figure 2.7: Map of UK tidal velocities and population density, tidal data from DTI Renewables Atlas [52], population data from the Office for National Statistics [53].

When a tidal wave (or any progressive wave) enters a closed space, in this case an estuary or inlet, it is attenuated and reflected against the end of the inlet to form a standing wave, the incoming and outgoing (reflected) waves interact based upon the length and depth of the inlet. When the natural frequency of the space and the frequency wave are coincident (or multiples of each other), the two waves combine to amplify the tidal range, an effect known as estuarine resonance [44, 54]. This can be seen in the Severn Estuary/Bristol Channel, where the tidal range (exceeding 14 m at Avonmouth) is a combination of incident tide and resonance of the estuary accentuating the incident tide Figure 2.8. This leads to the formation of one of the worlds best known tidal bore waves, popular among surfers. Also visible in Figure 2.8, the second region of significant tidal range is in the Irish sea – between North Wales, the North-West coast of England and the Isle of Man. Thirdly, The Wash (on the East coast of England) has a spring tidal range of 5-7.5 m.

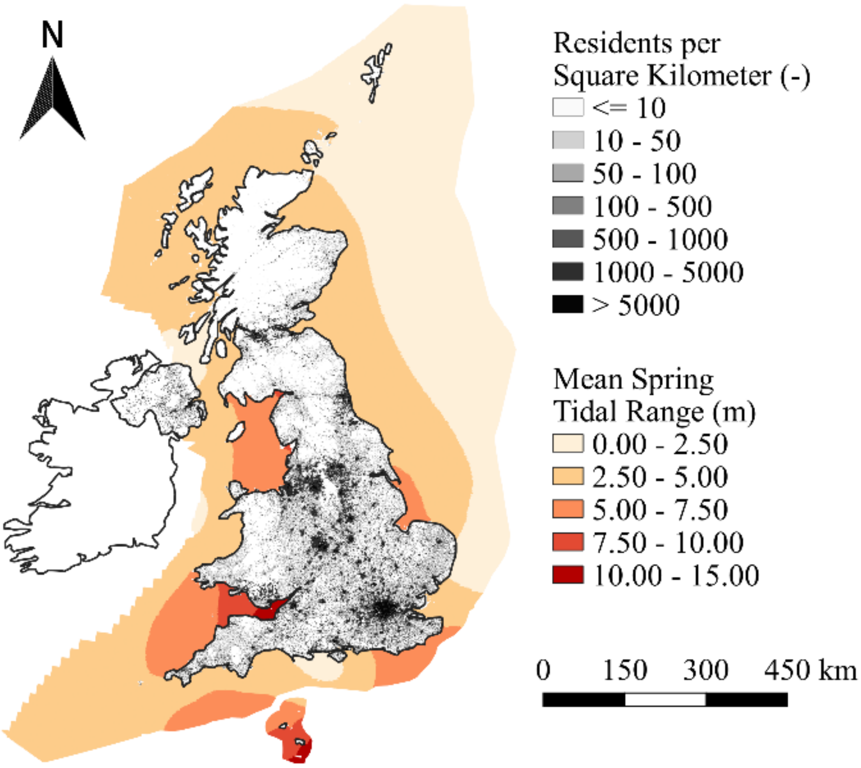

Figure 2.8: Map of UK tidal range and population density, tidal data from DTI Renewables Atlas [52], population data from the Office for National Statistics [53].

2.4 Hydrokinetic Energy

Bernoulli’s principle, derived from the conservation of energy states that water flowing along a streamline has a constant amount of energy, this energy is wrought from three major constituents, a velocity term v, a pressure term P and an elevation term z. For an incompressible flow at a low Mach number, this takes the form given in Equation 2.3 where g is the local acceleration due to gravity (and viscous forces are assumed to be negligible) [55].

$$\frac{v^2}{2g} + \frac{P}{\rho g} + z = const \tag{2.3}$$

For example, when atmospheric water is deposited (via precipitation) upon areas of high ground it will flow to areas of low ground, converting energy from the gravitational potential to kinetic energy. As creeks and streams merge into rivers, on their way to the sea; the flow conditions become increasingly suited to the abstraction of the energy entrained within them, referred to as hydrokinetic energy. This principle can be applied to rivers, streams, and tidal flows.

Ridgill et al. [30] carried out a multi-faceted approach to determining the global potential resource of riverine hydrokinetic energy, finding that of the 58400±109 TWh of potential energy annually, only 1.3 TW of power are currently in use, with hydropower accounting for ~16 % of the global energy production. This resource is distributed both spatially across the globe, as shown in Figure 2.9, with the highest potential found in Asia, South America, and Africa. As society has clung to rivers and coasts throughout human history, the proximity of this resource to end-users is inherent – and could prove beneficial in leveraging this form of energy in the development of smaller communities and economies where the desire for electrification is impeded by the cost of both generation and transport. Connecting end-users more directly to the locally available sources of energy could allow for skipping the stage of using fossil fuel-based systems and provide a more effective track towards a globally connected society operating in a low-carbon manner.

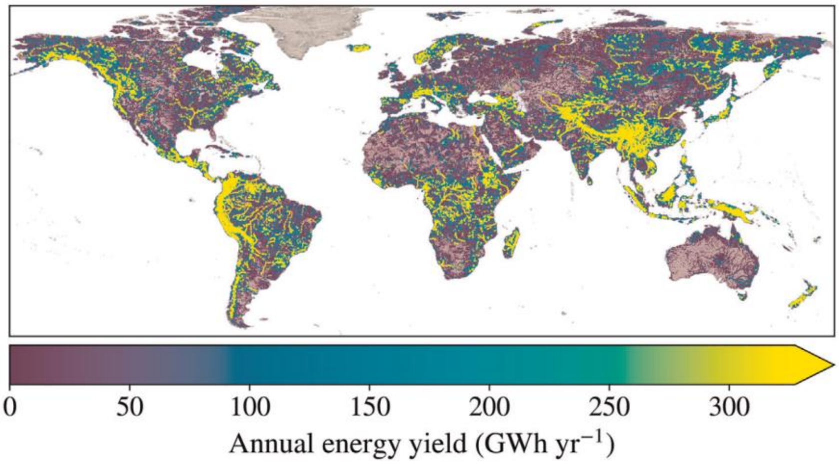

Figure 2.9: Global hydrokinetic resource estimate, from Ridgill et al. [30].

In developed energy systems, the role of riverine hydrokinetic energy could be seen as a mechanism by which to decentralise the energy mix, allowing smaller scale contributors to the system to operate feed-in plants as has been seen in various forms with rooftop solar. A larger scale option would be to capitalise on the flows induced by the tidal motion around a country such as the UK, whose riverine hydrokinetic resource is relatively small. Energy abstraction from the tides around the coast have the potential to provide up to 95 TWh/yr of energy [56], though a 'practical' estimate of 34 TWh/yr of tidal stream energy or (11 % of the national energy demand) is provided by Coles et al. [57].

The theoretical energy from hydrokinetic turbines has been calculated in a number of ways, the simplest form of this is the power P_{HK} available from a device with a cross-sectional area A in a flow with velocity v, Equation 2.4. Thus, the drive toward designing devices with the capability to operate in higher velocity flows is clear due to the higher energy potential, with deeper flows typically containing both higher velocities and the space required for large swept areas [31, 58].

$$P_{HK} \propto Av^3 \qquad 2.4$$

Kirke [31, 58] however, found that turbine designers have a tendency to design devices for flow velocities far in excess of those typically found in real rivers, and that river water depths make turbines with diameters over 1 m challenging to deploy. The global resource from tidal and riverine flows has been assessed on a number of occasions, Kirby et al. [59] reviewed a number of riverine hydrokinetic energy assessments, noting that the methods used for local assessments vary significantly, but that the general trend is moving from physics based models toward data and statistical techniques. Ridgill et al. [30] utilised a global dataset of river flow data – Global Reach-level A priori Discharge Estimates for Surface Water and Ocean Topography (GRADES) [60], combined with data describing the river reach characteristics to ascertain the riverine hydro-kinetic resource.

2.4.1 Hydrokinetic Turbines

The kinetic energy of a flow can be converted to mechanical energy by a turbine – with the blades translating the pressure from the flow into torque, a generator connected to the turbine then converts this rotation into electrical energy. The turbine itself can be categorised into two primary forms, axial-flow and cross-flow turbines, simple versions of which are shown in Figure 2.10, where the rotational axis of the turbine relative to the flow direction is the determining factor. In the design of an axial-flow turbine the rotational axis and the flow direction are parallel, with the turbine rotating about a mounting structure (in the case of hydrokinetic devices this is typically a horizontal axis). Cross-flow turbines have the flow direction normal to the axis of rotation, often with this axis being aligned vertically – although some devices have the turbine rotating about a horizontal axis perpendicular to the flow direction.

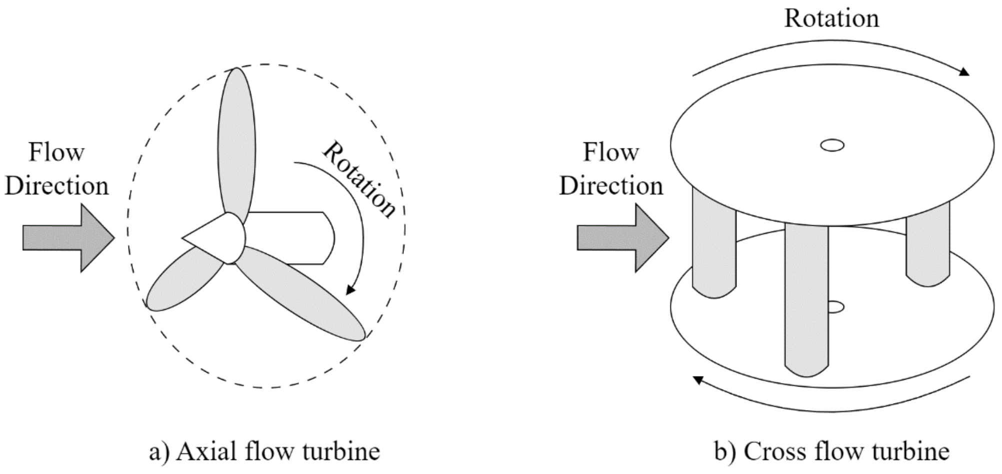

a) Axial flow turbine

b) Cross flow turbine

Figure 2.10: Axial and cross flow turbine, simplified concept diagrams.

Axial flow turbines have received significant attention in terms of development, particularly in the field of wind energy [61], and are the most common form of turbine used in tidal range (though in confined space as built into a housing structure as opposed to being in open flow). Due to having a higher density than air (~820 times), water flows contain vastly more energy than wind, however the challenges of mounting and maintaining hydro-turbines, particularly in marine environments when compared to wind turbines has contributed to the relatively slow development process. The choice of device is dependant on a multitude of factors, from design flow operating depth, velocity – to directionality, mounting or placement options, and grid connection requirements [62].

A comparison of various different wind turbine design options in terms of C_p (power coefficient) and λ (tip speed ratio, normalised rotation) is shown in Figure 2.11. Though this figure is taken from wind turbines, the fundamentals of the operation and relative performance of the different technologies is analogous to that of hydrokinetic turbines. Note that for each option there are lower and upper limits to the operational window, with a peak of power output between the two. A turbine is said to cut-in at the leftward end of the arc as it begins to develop power, and be free spinning (turning in an unrestricted manner and not extracting energy from the flow) at the right hand end. Here it is moving at its maximum rotational speed – but is not able to develop power as extracting power intrinsically reduces the available energy to rotate the turbine itself.

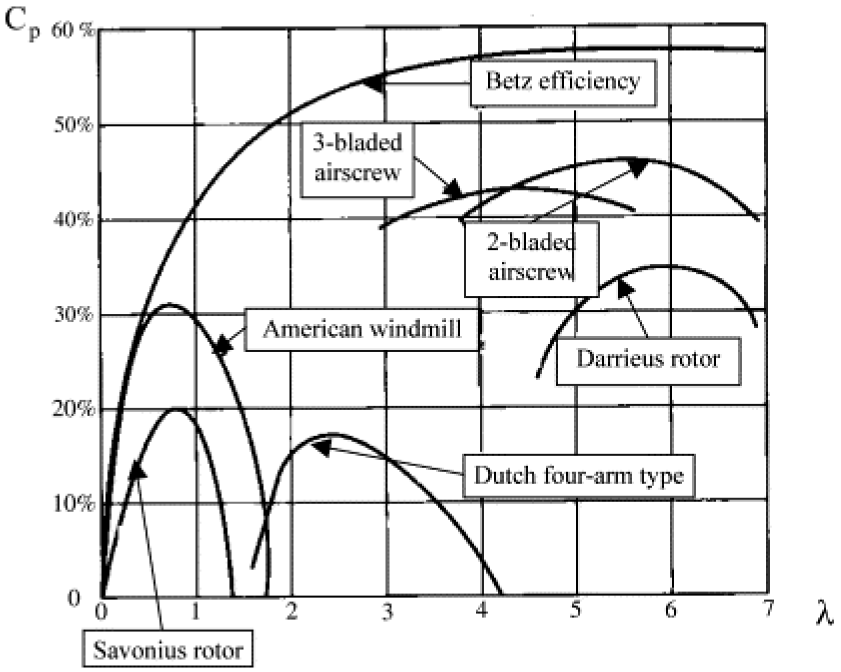

Figure 2.11: Performance of conventional wind turbine designs, both of axial and cross flow type, reproduced from [63].

The ability of tidal stream generators to interact positively with other low-carbon energy components of a net zero grid was considered by Pudjianto et al. [64], with the predictability and consistent nature of tidal stream being key benefits – however the challenge of the high Capital Expenditure (CAPEX) associated with tidal energy was still a key limiter, with the need to consider the whole-grid impacts of tidal range and their value being highlighted [24]. An increased deployment of tidal stream energy devices about the UK was predicted to aid in driving down the levelized cost of energy of tidal stream by Coles et al. [57]. This would make tidal stream much more competitive in the energy market where other energy generation technologies are currently able to operate at a lower cost than tidal stream.

Encarnacion et al. [65] presented a method for the design and assessment of an axial flow turbine aimed at flow velocities below 2 m/s, using steady state modelling and quasi-unsteady Blade element Method (BEM) to optimise the designs for two test locations – Mexico and the Philippines, though not including startup of the devices. Numerical modelling of a horizontal axis tidal turbine was carried out to assess the wake characteristics by Ebdon et al. [66] using ANSYS Fluent – a popular commercially licensed software for fluid simulation. The finite volume solver used a sliding mesh scheme wherein a cylindrical section containing the rotating components of the turbine was rotated at a predefined rate with each timestep, a popular approach that is however highly demanding to implement where different elements are required to pass through the same motion region.

The environmental impact of tidal current devices is discussed by Fraser et al. [67], as tidal turbines are typically considered for dynamic coastal areas. A seabed mounted echosounder was used to track the behaviour of schools of fish in the vicinity of a tidal energy installation at the EMEC Fall of Warness test site in the Orkney Isles [51]. As a whole, the turbine was found to lead to an increased fish population – particularly in the wake region of the turbine compared to the base population and behaviour, with the increase being more prevalent at night. The impact on the regional impact of tidal stream devices are measured using hydro-environmental modelling by Ahmadian et al. [68], where the water levels are found to be generally unaffected – however the velocities are increased around the turbines, whilst being reduced upstream and downstream of the turbines. Dirieh et al. [69] used TELEMAC3D to study tidal stream turbines in the Alderny Race - a highly dynamic flow region. Here the blockage effect from an array of turbines was used to improve the performance beyond the peak of the individual turbines applying a correction to the actuator disk model commonly used to simulate turbines in large-scale models such as this.

2.4.1.1 Axial Flow

The largest deployed tidal stream energy devices, such as the MeyGen project [57], Orbital O2 [19], and SeaGen [33] have all been axial flow turbines. The European Marine Energy Centre (EMEC) [70] lists 97 known tidal energy concepts, of these – 43 are classified as 'Horizontal Axis Turbines'. This form of tidal energy is the market leader in terms of developer interest.

Axial flow devices have some distinct advantages over vertical axis or cross-flow turbines when considering them for design and deployment. The first key being the expanded knowledge-base on these devices [71], with the majority of existing schemes being of this form, whilst also being the predominant form of wind turbine design [72]. The second being the performance that is associated with both this design form but also the degree of knowledge amassed into their design – the use of self-regulating speeds eases generator connection, and manual control over blade angles allows for control to further improve operation and allow shutoff at times of threat [73].

The purpose of a turbine is to extract power from the location in which it is installed, be it a hydrokinetic turbine in a tidal or riverine flow, or a turbine installed in the bounding wall of a tidal range scheme. Therefore, the key output parameter in turbine selection and comparison is the output power, which should be large enough to serve the purpose of the installation, at a suitable cost [31]. For different types of turbine, the power coefficient may not directly translate to the energy extracted by the devices, with aspects such as ducting, blockage effects, and installation method compounding to a multi-faceted design problem which goes beyond comparison of power coefficient.

2.4.1.2 Cross Flow

There are many turbine styles where the flow of the water is normal to the rotational axis, for simplicity these have been delineated here from axial flow turbines under the name cross-flow, but often these are referred to by other features. Many studies of vertical axis wind turbines have been carried out [74–76], these have a number of typical advantages over axial flow devices that translate generally across to fluid devices.

The ability of vertical axis wind turbines to handle multi-directional wind flows, as are often found in urban areas – as well as having a typically compact design. Roberts et al. [77] found that for small scale and shallow water applications the degree of interest had been lower, where the reduced costs of installation and ability to provide energy to coastal communities could compare favourably with larger schemes. Cross-flow turbines were found to compare favourably due to the reduced constraint on water depth and potential power density.

The use of microturbines in the form of vertical axis Gorlov (helical Darrieus turbines) with a cross sectional area of 1 m² sited as part of a distributed smart grid was carried out by Alvarez et al. [78]. This study used the Nalón river in northern Spain using a combination of HEC-RAS and Geographical Information System (GIS) based analysis. The study provides a thorough example of how small turbines could be used in conjunction with an awareness of the local energy needs to meet the needs of an area.

2.5 Tidal Range Energy

2.5.1 Fundamentals

As raised in Section 1.1, the rise and fall of the tides has been tapped to provide power dating as far back as 10th century, in the form of tidal mills [79], and tidal range schemes operate still in a handful of locations (described in Section 2.5.2). The amplitude of the tidal movement at a given location comes from a combination of factors that influence how the solar and lunar constituents, as shown in Figure 2.6, interact with the local geography. The largest tidal ranges in the world, namely the Bay of Fundy in Canada, and the Severn Estuary in the United Kingdom have spring tidal ranges of 16 and 14 metres respectively [80, 81]. Tidal range schemes use the vertical change in elevation of the water surface at a suitable location to produce energy by containing a volume of water in a space connected to the varying external water level by engineering structure, as shown in Figure 2.12.

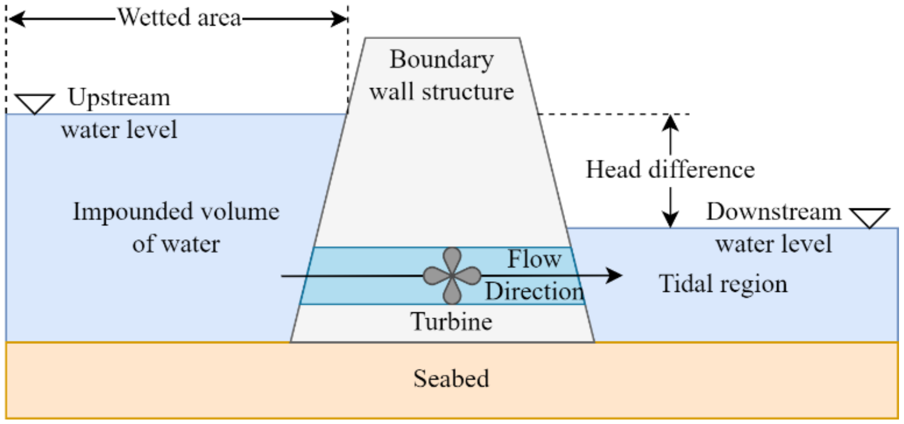

Figure 2.12: Tidal range scheme idealised structural cross section diagram.

By intentionally ‘holding’ a constant water level within the impoundment, allowing the external tide to rise (flood) or fall (ebb) as expected, a head difference can be achieved across the structure that is large enough to extract energy when a flow of water is passed through the turbine(s) [82]. When the head difference has reduced to a point where the turbines are no longer able to produce energy, they are closed off, and depending on the operational schedule of the system, a state of holding (maintaining the internal water level until generation is once again feasible), sluicing (opening the sluice gates, allowing water to flow through bringing the exterior and interior levels together), or pumping (using the turbines or dedicated pumps to force the internal level to a desired target) to improve energy yield or maintain internal hydro-environmental regime [21]. The order of operations can vary from scheme to scheme as is discussed in Section 2.5.3, with two typical examples illustrated in Figure 2.23.

In the study of tidal range energy schemes, there are two primary physical categories of scheme, the barrage (for example the Rance or Sihwa schemes summarised in Section 2.5.2, and the Severn and Mersey proposals covered in Section 2.5.3), and the conceptual only lagoons (such as the Swansea Bay Tidal Lagoon). Both forms use the same fundamental concepts, with the key differentiator being that a barrage is used to close-off a natural area of impoundment such as an estuary or inlet. A lagoon on the other hand, is designed to impound an area of open water, using natural bathymetric patterns as a guide and a much larger length of constructed wall per area. Lagoons can be further classified as either coastal, whereby the lagoon is partially bordered by the coastline, or offshore, with the boundary structure forming the entirety of the bund, shown in Figure 2.13. In terms of design and operational philosophy, tidal barrages and lagoons are largely the same, with the key differentiating factor being the extent to which the impoundment spans across a river [83]. A barrage blocks a river or estuary whereas a lagoon, either offshore or land-connected does not fully block a river or estuary.

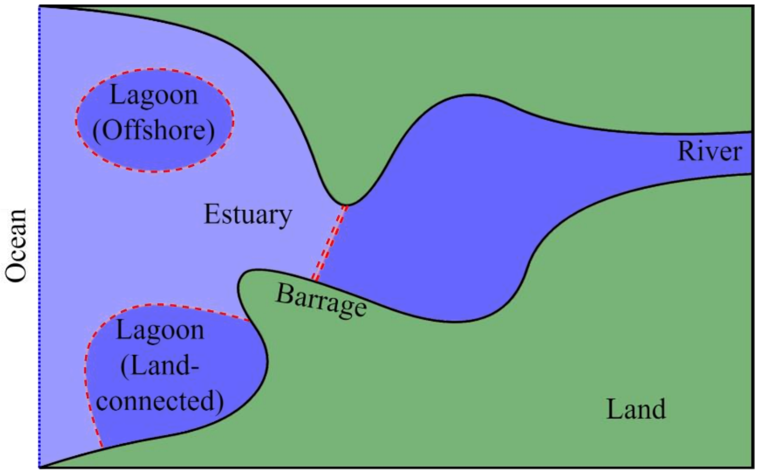

Figure 2.13: Types of tidal range scheme by layout.

The energy available from a tidal range scheme E is proportional to the wetted area A, and the square of the intertidal range at the location ξ (Equation 2.5).

$$E \propto A \cdot \xi^2 \tag{2.5}$$

The cost of the scheme is primarily related to the cost of the turbines and sluices, and the length of the bounding wall, Vandercruyssen et al. [24] developed equations for the approximate cost of new schemes based on the costs of constructing the existing schemes – though the authors note that this should be paired with wider life-cycle assessments. The prevailing style of scheme historically has been the barrage – wherein a small length of bound can be used to entrain a large area in a region with a large tidal range, however this has a tendency to place the scheme in a location of high environmental value (as transitional waters tend to be host to delicate ecosystems). The concept of the lagoon was borne of the advances in offshore construction, and changing views over marine/land usage, making a longer bound for more feasible for the same impoundment. This also afford developers more flexibility in their planning of the scheme, be it offshore or land-connected. Offshore lagoons, though the most expensive layout on a pro-rata basis do afford some interesting characteristics that have been largely unexplored. The ability to pump the scheme to beyond the tidal limits (over or under) to a more significant degree than the other options (as there is no connected land to flood, and the bed level is likely well below the tidal limit) can allow the scheme to operate almost wholly as a pumped storage system akin to that as found on land.

There are a number of common configurations for the turbine and generator for use in hydropower applications, for low head uses three are common. The first is the vertically aligned turbine and generator, here the water flows down through the turbine with the generator mounted in line with the turbine either above or below, item (a) in Figure 2.14 shows this arrangement with an example flow path marked in cyan. The most common turbine form considered for tidal range applications is that of the Bulb Turbine, Figure 2.14 (b), note that this turbine is only able to operate in one direction. Here the generator mechanism is built into a submersible bulb mounted ahead of the turbine itself, both converting the mechanical energy of the turbine to electrical energy but also aiding with flow conditioning. The Straflo turbine, as was utilised at Annapolis Royal for example (Section 0) has the generator typically mounted in a rim around the turbine, which has electromagnets in the rim of the runner to form the rotating component of the generator.

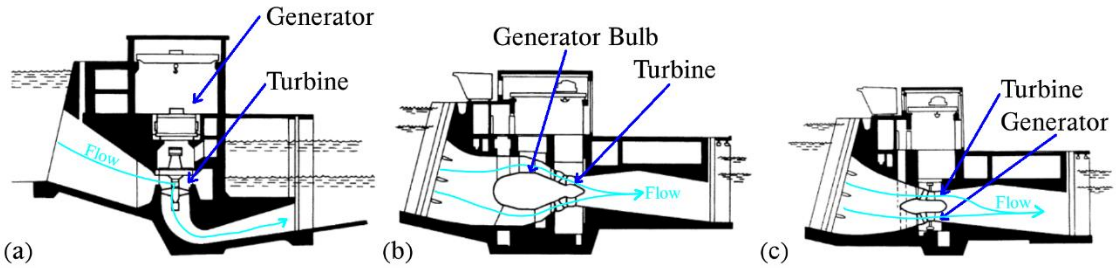

Figure 2.14: Schematics of commonly used turbines for low-head hydropower applications (adapted from Charlier [84]):
(a) vertical turbine-generator, (b) horizontal bulb turbine, (c) Straflo turbine.

Each of these types of turbine also offers varying levels of control. The ability to control elements of the device during operation is termed regulation. The turbines used in hydropower schemes are typically double or triple regulated [29]. This control typically comes from some combination of the inclination of the runner blades, angle of guide vanes, and runner speed itself [85]. Improved control over the torque generated allows an increasingly nuanced development of power from a turbine which in turn improves its performance.

2.5.2 Tidal range schemes past, present and proposed

One of the oldest tidal range schemes considered by engineers is the Severn Barrage – though proposals have never come to fruition, the prospect of barraging the Severn at some location has been considered for over a century [28]. This has been iterated through various forms such as the Brean-Lavernock schemes of Hafren Power [86] and Severn Tidal Power Group (STPG) as shown in Figure 2.15, and Cardiff-Weston barrages that have been laid before the relevant parliamentary committees at various points [87–89]. Typically ~16 km long, impounding an area of over 500 km², with an estimated output of 14000-17000 GWh/year [80], this size and potential underpins the continued interest in a Severn Barrage. These schemes were ultimately shelved due to a combination of high capital expenditure and the environmental impacts predicted by numerical modelling studies [90, 91] – this scheme however has been critical in establishing the concept of tidal range in the public and scientific eye. Research on the Severn Barrage also carries forth to other schemes, developing the concepts and understanding of how a future tidal range scheme would operate [92, 93].

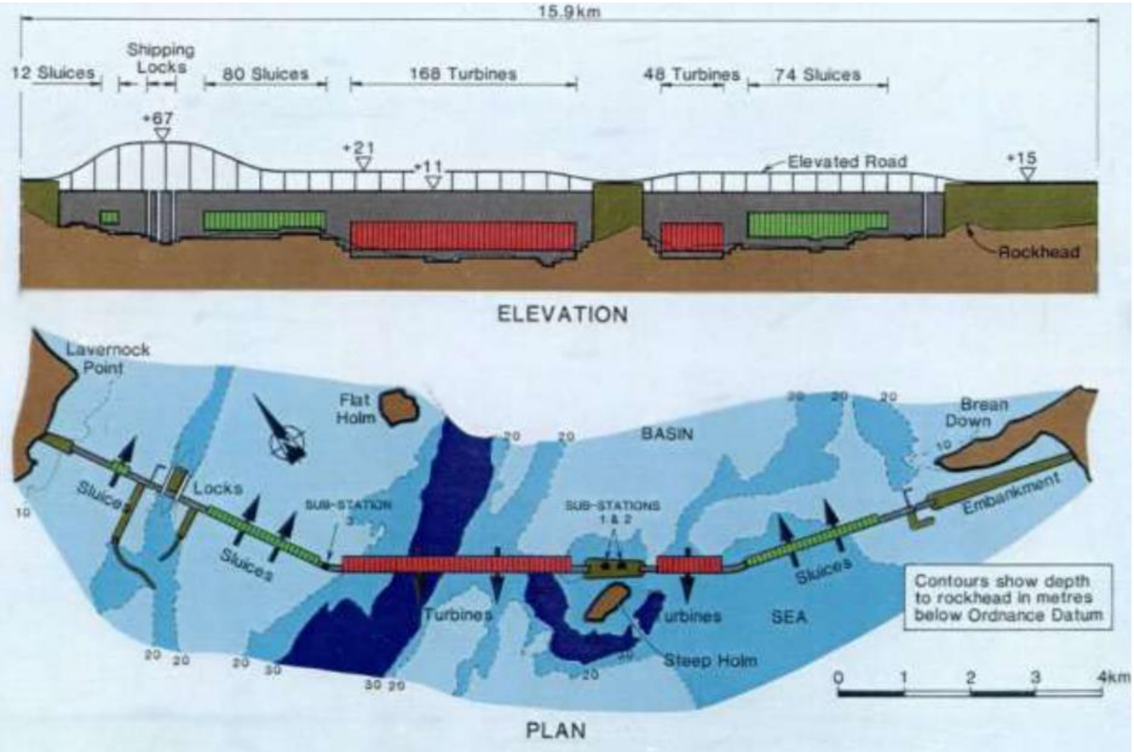

Figure 2.15: Severn Barrage design by STPG, from Department of Energy [94].

One of the most developed examples of this being the Swansea Bay Tidal Lagoon [95], a layout of which is shown in Figure 2.16. This scheme was to be the largest tidal range scheme in the world, with a capacity of 320 MW, generating estimates in the region of 500 GWh of energy per year [96]. The lagoon was identified as having the potential to form a ‘pathfinder’ scheme to provide a foothold and establish industry for further tidal range energy around the UK in the independently conducted government report on tidal range carried out by Charles Hendry [97], this report identified a number of ways in which the Swansea Bay Tidal Lagoon would benefit the community and sustain a British supply chain. Although a large number of the environmental requirements had been met, the proposal was found to be uneconomical by the government and was denied the Contract for Difference upon which the proposal was based [89]. The Swansea Bay lagoon was costed at 800-850 million GBP, with the biggest components of this being the turbines/generators and the bund-wall [24].

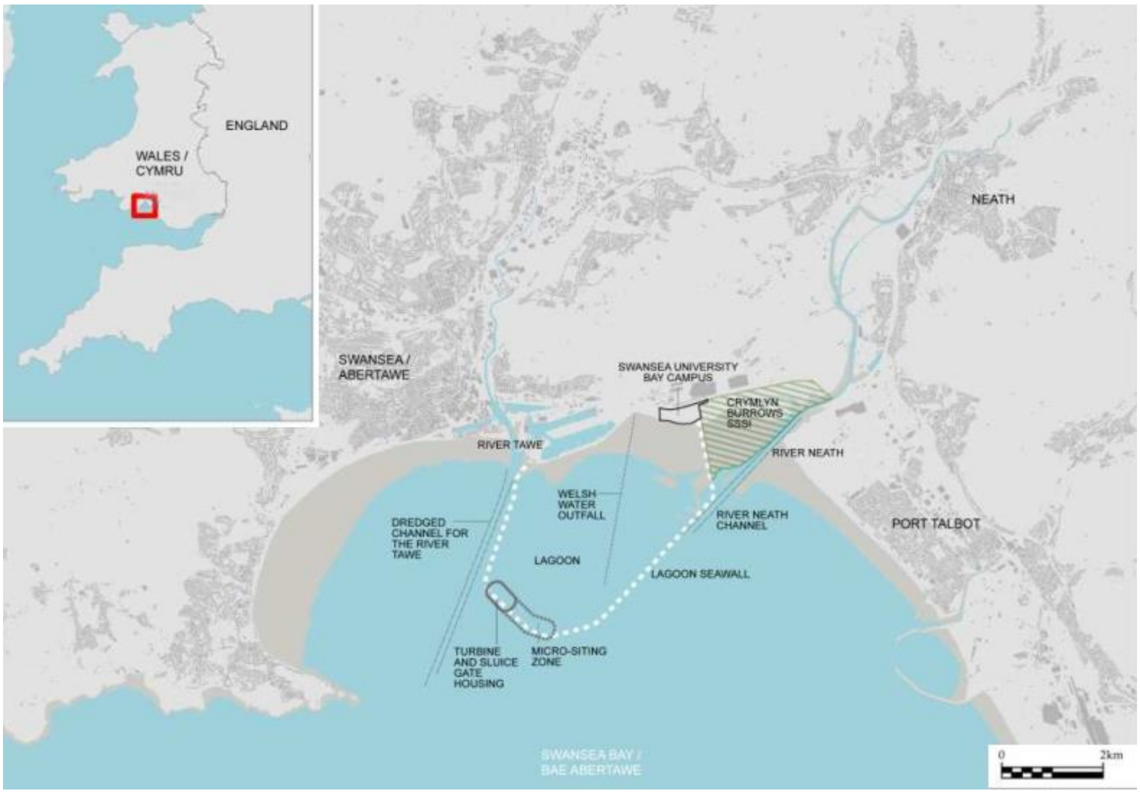

Figure 2.16: Swansea Bay Tidal Lagoon layout, adapted from Tidal Lagoon PLC [98].

The first modern tidal range scheme to be constructed is still in operation and was the largest in terms of power output for almost half a century. The Rance Tidal Barrage near the town of St Malo in northwest France (Figure 2.17 was constructed in the 1960’s and generates approximately 500 GWh of energy per year, with an installed capacity of 240 MW [99]. This scheme has been operating under two-way generation with a high degree of consistency since being brought online, and is held as a key component demonstrating the longevity of tidal range schemes compared to other generating methods [100]. The scheme also provides additional benefits to the region, being a popular location for fishing, providing a road crossing over the Rance river (the next being ~10 km upriver). The visitor centre on site has an estimated 70000 visitors a year, providing education and information about the scheme and its environs [101]. An aspect of the barrage that has grown in general awareness since the 1960s construction is the environmental impact of such a scheme. To build the barrage, the contractors opted to utilise cofferdams to install the components, causing ecosystem damage [84]. After 20 years of operation, a study of the aquatic environment was made by Retiere [102], this paper concluded that the ecosystem in the upstream of the scheme had been fundamentally changed, and was still fragile whilst being highly dependent on the operations of the barrage. The 24 bulb turbines used in the construction of the Rance Tidal Barrage were developed for the purpose, are maintained using a cathodic protection system, and have become a staple component in the design of tidal range schemes (being used at Sihwa Lake and Kislaya Guba) [103]. The sediment dynamics in and around the scheme have been found to have highest levels of suspended sediment during sluicing phases [104], with greater salinity intrusion into the estuary during summer [105].

Figure 2.17: Aerial view of the Rance Tidal Barrage (public domain image).

The most recently built tidal range scheme was originally constructed to act as an irrigation reservoir and flood defence for the city of Incheon, South Korea, but pollution issues meant that it was unsuitable and so a power plant was installed in the bund-wall to convert the impoundment to a tidal range scheme, known as Sihwa Lake, Figure 2.18. Sihwa Lake has 10 bulb turbines rated at 25.4 MW each, supplied by Andritz Hydro for a combined 254 MW capacity [106]. The net energy generated is in the region of 550 GWh per year [107]. This scheme uses flood-only generation, due to the environmental constraints placed on the inner region – flood-only operation maintains a lower average water level within the impoundment than the external tidal regime, and for a location with a history of flooding this was held to be more valuable than the energy gains of two-way operation [108]. Other concepts for tidal power stations in South Korea have been developed but none constructed to date [109].

Figure 2.18: Sihwa Lake Tidal Barrage, Incheon, South Korea, background imagery from Google Satellite.

The Annapolis Royal Generating Station, in the Bay of Fundy, Canada, was built in 1984 [110], an overview is shown in Figure 2.19. The station utilised a large singular Straflo (straight flow) turbine in ebb-generation to produce a capacity of 20 MW and an annual energy generation of approximately 50 GWh [111]. This scheme also features a connecting road bridging the Annapolis River. This barrage was operational for over 30 years, however a governmental review into fish mortality raised questions as to the impact the scheme was having on the environment [25]. This, coupled with various components reaching end-of-life and requiring replacement led to Nova Scotia Power decommissioning the scheme in 2019 [112].

Figure 2.19: Annapolis Royal Barrage, Nova Scotia, Canada. Background imagery from Google Satellite.

With a lengthy coastline and scope to develop renewable energy, there is significant scope for tidal range energy around China, with hundreds of potential locations for barrages. The largest operational scheme being the Jiangxia Tidal Power Plant [113]. This 3.9 MW capacity tidal barrage was constructed between 1974 and 1985, with a staged deployment of variously sized turbines, is shown in Figure 2.20. This scheme generates a significant degree of income from the wider benefits it provides to the region, as a location for aquaculture and land reclamation [114], components of the wider facilities that tidal range can be used to provide [115, 116].

Figure 2.20: Jiangxia Tidal Range Power Plant, Zhejiang Province, China. Background imagery from Google Satellite.

North of the arctic circle in Russia, the Kislaya Guba Tidal Barrage sits across a narrow (40 m wide) inlet in the Barents Sea – Figure 2.21. The power plant, built in 1968, is notable for the engineering challenges faces in its deployment – isolation, deep water, steep slopes, and the harsh climate of Kola peninsula required caissons constructed of specialist concrete, supporting a singular 3.8 m diameter bulb turbine with a capacity of 1.5 MW [117]. This small tidal power plant has been viewed as an exploratory project for the then USSR into developing alternatives to supplies of oil and gas, as opposed to a serious contributor to the energy supply [118]. Perhaps as a function of this, other basins about the Russian federations have been assessed for tidal range due to a combination of tidal characteristics and potentially suitable topography, with some particularly large concepts penned for the Sea of Okhotsk [100].

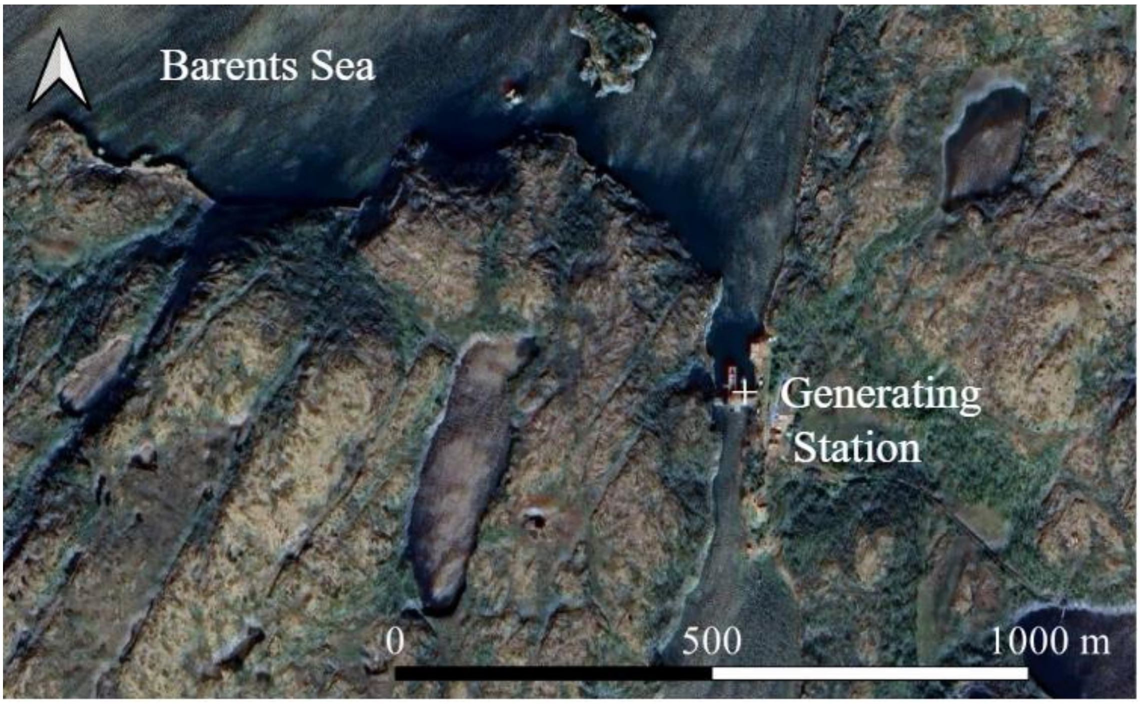

Figure 2.21: Kislaya Guba Tidal Barrage, Murmansk Oblast, Russia. Background imagery from Google Satellite.

Constructing a tidal range scheme in the present forms (barrage or lagoon) has a high capital cost, financially and environmentally. Typically the key environmental costs are the changes in regional water levels, losses in intertidal area (habitat and feeding for a variety of coastal life) [119], and impediment to the navigability of an area to both marine life [25] and vessels [120]. This challenge can also be seen globally, Neill et al. [121] note that the areas in Australia with the largest tidal range potential also suffer from some of the more severe challenges to construction, including distance to significant population centres, and various challenges such as localised hydro-environmental issues. These costs have pushed the scope of proposals towards increasingly large schemes, in the hope that the increased energy production can be leveraged in a societal context and thus earn governmental financial support, however this has proved difficult to acquire [122]. The existing major tidal range schemes around the word are summarised in Table 2.2, each of these represents a point in time at which the balance of expenditure and return was deemed in favour of construction. With rising awareness of the risks posed by anthropogenic climate change paired with growing environmental conscience, the strength of argument on both sides of the fence is ever stronger. New concepts, insights, and methods must be developed if tidal range is to see ground broken on a new project.

Table 2.2: Summary data of existing tidal range schemes.

Name	Country	Operational Period	Capacity [MW]	Basin Area [km²]	Tidal Range [m]	Cost [Million USD]
Rance	France	1966 -	240	22	14	100
Sihwa Lake	South Korea	2011 -	254	30	6	355
Annapolis Royal	Canada	1984 – 2019	20	6	7	36
Jiangxia	China	1985 -	3.9	2	8.4	9.8
Kislaya Guba	Russia	1968 -	1.7	2	9-13	n/a

2.5.3 Scheme Design and Operation

To define a tidal range scheme, two aspects are typically required: the physical, and the operational characteristics. Some key physical descriptors have already been discussed in Section 2.5.1, delineating a barrage from the various forms of lagoon. The true value of a tidal range scheme however is derived from the operational mechanics and schedule, with the power output being not merely a function of time and tide – but of operator decisions. The general physical layout of a tidal range scheme is often a relatively simple component of the design process, with the aims of maximising impounded area whilst minimising wall length and avoiding or including key features within the region of the impoundment.

2.5.3.1 Operation

The initial factor to consider in the operation of a tidal range scheme is how many generation periods are desired per tide, two-way operation denotes that the scheme will generate electricity on both the incoming and outgoing tides (flooding and ebbing), this method is becoming increasingly popular, however was less considered historically due to the assumption that the installed turbines would not be capable of operating in both direction (they would be unidirectional as opposed to bidirectional). Therefore, one-way generation was often applied, this could be configured either to take place on the ebb tide (termed ebb-only), or solely on the flood tide (flood-only) [80]. Each of these has its own empirical advantages, due to the tidal prism effect the typically higher water levels developed by ebb-only schemes yield in increased energy return than flood generation [123], this was used at the Annapolis Royal Generating station. The typically lower internal levels of flood-only generation however have the benefit of reducing the internal risk of flooding (and as such this method is used at the Sihwa Lake Tidal barrage) [108].

A comparison diagram of ebb-only and two-way generation methods is shown in Figure 2.22, here the dashed line is the ebb-only and the solid two-way. Note the way in which the ebb-only scheme maintains a higher water level than the two-way, which has a broadly symmetrical operation about the mean water level. The head difference across the scheme has been used to control the operation of tidal range schemes since the first principles laid out by Prandle [124], who assumed a minimum generating head trigger above which generation would occur. This has been expanded to differentiate the start and end head differences, these are indicated in Figure 2.22 by the vertical lines, with the dashed lines again referring to ebb-only and the solid to two-way. The open-green circles represent the head difference at which to commence generation, and the closed-red the head difference at which to cease generation. Changing these triggers over time is known as flexible operation, and can allow the scheme to operate in a dynamic manner with an optimal level ascertained based on the desired operation for a given period [22, 125].

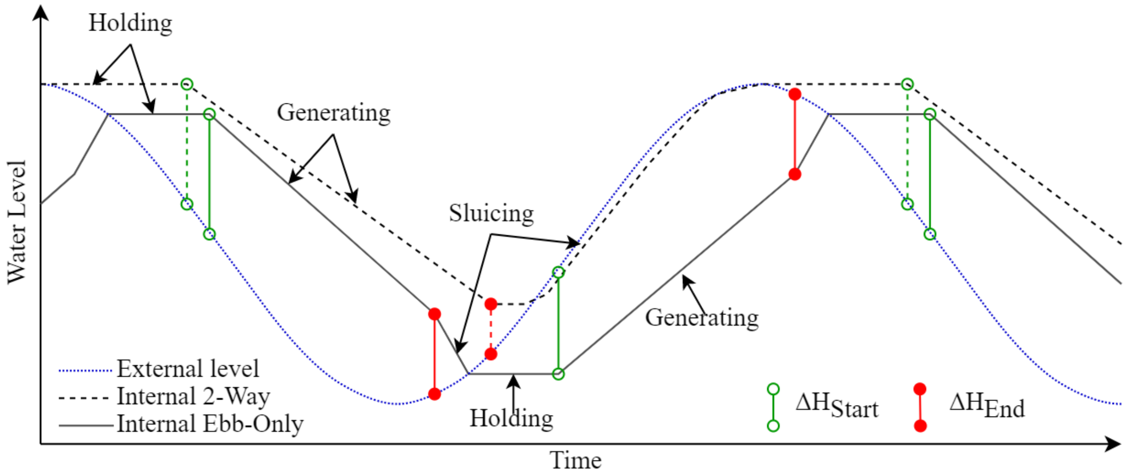

Figure 2.22: Simplified schematic of ebb-only and two-way generation patterns.

The turbines themselves can be used as pumps, accelerating the flow across them to increase the changes to the internal regime (as is done at the Rance Tidal Barrage [126]), or to extend the range of the water level to beyond what is achievable with the turbines and sluices operating under the influence of gravity alone. This expansion to the operation can result in a net energy gain, by pumping at time when the levels are close together (and so the energy requirement is lower) the scheme can increase the head difference later on as the tide moves farther away improving the generation profile over the course of the period [21]. Pumping in this manner is close in principle to that of energy arbitrage (the process of buying at times of low price and selling at times of high price), and this can allow the scheme to be orders more profitable if the price of energy is not constant. Pumping can also be used to govern the internal hydro-environment, with goals such as maintaining the internal tidal range, or a minimum internal water level being possible.

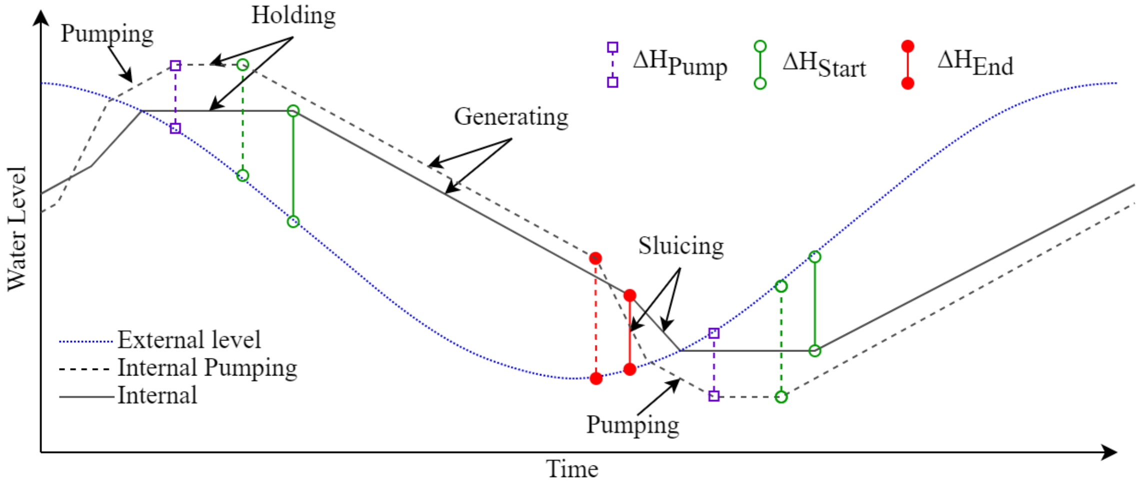

Figure 2.23: Schematic demonstrating the impact of pumping on internal regime.

The progression through the operational modes of the tidal range scheme is driven by the condition of the scheme and the external water level, each operating mode has a different role in the cycle, and the behaviour of the components is specified by the mode. The four key modes are shown in Table 2.3 (with two mechanisms of sluicing). During holding the turbines and sluices are closed, with no water passing into or out of the scheme through them, this is done to allow the external water level to change and develop a suitable head difference for generation, additionally this mode allows the water within the basin to settle out any oscillations. Once a suitable head difference has been reached generation begins, with the turbines being opened and water passing through to generate electricity, maximising the duration and difference is the key underlying principle to maximising energy output, during this phase the water level within the scheme trends towards the external (rising in flood generation and falling during ebb generation). Once the head difference is too small for generation to be efficient the turbines are stopped, and water allowed to pass through them whilst the sluices are opened to allow a greater deal of water to pass into or out of the scheme

– this is the mechanisms known herein as serial sluicing. Parallel sluicing, as discussed by Moreira et al. [127] has the sluices opened relatively sooner, with the turbines kept in generating mode for longer, accelerating the change within the scheme and developing a longer generation window. A comparison of the differences between these two modes is shown in Figure 2.24.

Table 2.3: Modes of operation for tidal range scheme.

Name	Turbine State	Electricity	Sluice State	Internal State
Holding	Closed	None	Closed	Constant water level
Generating	Open	Generating	Closed	Trend towards external
Sluicing (Parallel)	Open (Hill Chart)	Generating	Open	Trend towards external
Sluicing (Serial)	Open (Orifice)	None	Open	Trend towards external
Pumping	Induced	Consuming	Closed	Force away from external

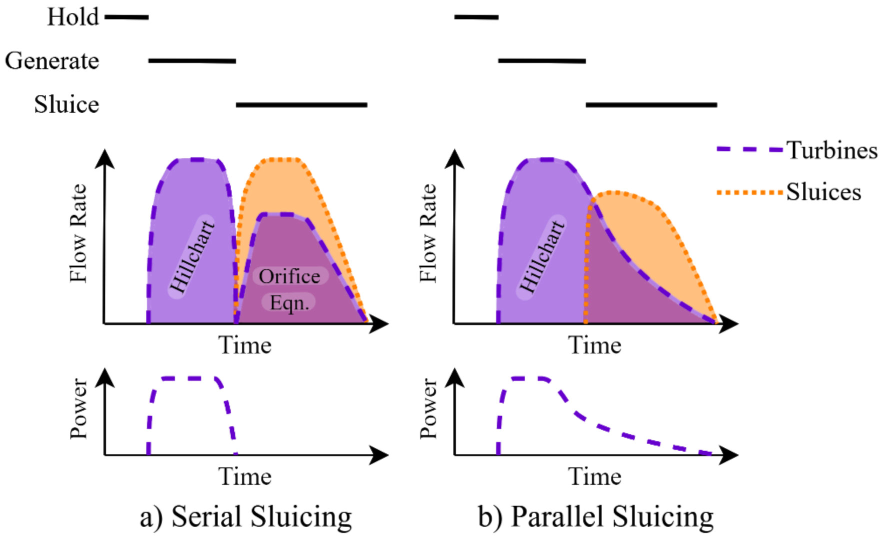

Figure 2.24: Simplified flow through and power from a TRS when operating under serial and parallel sluicing modes.

2.5.3.2 Design and design optimisation

Scheme design in terms of layout, number and size of turbines, and number and size of sluice gates underpin the operational output of a tidal range scheme, but also the cost. The capital expenditure (CAPEX) required for a tidal range scheme has been consolidated to Equation 2.6, from Vandercruyssen et al. [24].

$$CAPEX = N_{t+g}\left(C_{t+g} + C_p\right) + N_S C_S + L_C C_C + L_b C_b \qquad 2.6$$

Here, N_{t+g} is number of turbines and generators (where each turbine has a generator), C_{t+g} cost of turbo-generators including electrical control and instrumentation, C_p is cost of powerhouse section (caisson or otherwise) per turbine unit, N_S number of sluices, C_S cost of sluices, L_C length of cofferdam as total width of powerhouses plus sluices, C_C cost of cofferdam per metre. The remaining impoundment is accounted for by L_b the length of bund, C_b cost of bund per unit length. Typically, the net cost of sluices and turbines and their associated works to be the largest constituent of the cost of the scheme. Vandercruyssen et al. [24] estimate this to be 95 % of the Sihwa Lake costs (though the majority of the bund had been previously constructed), and 66 % of the estimated cost of the Swansea Bay scheme. As such, balancing this cost against the return is likely to be the most impactful.

To normalise the different costs of energy generation proposals against their returns over the expected lifespan of the scheme, the Levelized Cost of Energy (LCoE) is often used. This reduces the lifespan of the scheme down to a cost per energy rate, one form of which is given in Equation 2.7. For a lifespan of N years, the LCoE is sum of the CAPEX and annual costs of Operational Expenditure (OPEX), adjusted for the discount rate r, divided by the sum of the annual energy outputs E_i normalised to the discount rate [80]. As the CAPEX is typically expected to be many orders of magnitude greater than the OPEX, the impact of lifespan N is clear, with the longer the expected lifespan, the lower the cost of energy, a factor that has been advantageous to tidal range proposals and existing schemes (such as the half century of operations at the Rance and Kislaya Guba barrages).

$$LCoE = \frac{CAPEX + \sum_{i=1}^{N} \frac{OPEX_i}{(1+r)^i}}{\sum_{i=1}^{N} \frac{E_i}{(1+r)^i}} \qquad 2.7$$

2.5.4 Proposed UK Tidal Range Schemes

With large tidal ranges at a variety of locations around the UK, there have been a number of key proposals in the past (the Severn Barrage and Swansea Bay Lagoon for example). Much like the tides however, interest in the various proposals rises and falls – often as a function of external pressures. Therefore, three proposed schemes felt at time of writing to be the closest to development are summarised here, as they were used at various stages of the studies herein.

2.5.4.1 West Somerset Lagoon

The West Somerset Lagoon (WSL), shown in Figure 2.25, has been proposed for the Somerset coast in south-west England by Tidal Engineering and Environmental Service Ltd.[1], where the Severn Estuary/Bristol Channel is known to have the second-highest tidal range in the world and has been considered for some form of tidal range energy scheme for over a century [28]. The scheme is laid out in the form of a circle – centred at UTM30(472900, 5672000), with a radius of ~7 km, forming a semi-circular impoundment on the Somerset Coast between Hinkley and Bridgwater. The 80 km² WSL has been predicted to generate up to 7.16 TWh/yr, with 125 turbines (each having 7.2 m diameter, 20 MW capacity) split into five banks, and 20,000 m² of sluice gates, utilising a pumped flexible operation [128, 129]. This particular location within the Bristol Channel (shown in Figure 2.25) benefits from reduced obstruction of the major shipping and migratory fish routes in the area as compared with a traditional Severn Barrage, potential flood mitigation in the area, and proximity to the National Grid connection to the Hinkley Point nuclear power station.

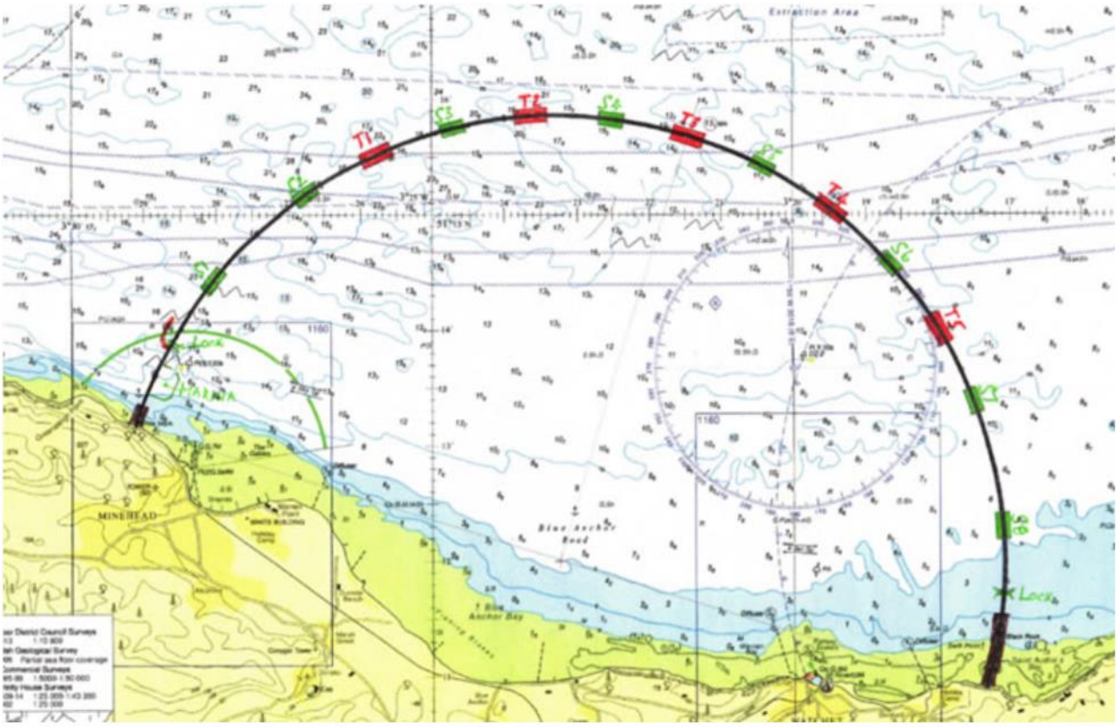

Figure 2.25: West Somerset Lagoon concept drawing from Tidal Engineering & Environmental Services[1].

---

[1] tidalengineering.co.uk

2.5.4.2 North Wales Tidal Lagoon

The northern coast of Wales has been another key focus region for the development of tidal range schemes. A mean spring tidal range of ~7 m and a history of coastal flooding mean a scheme that could both provide power and mitigate the risks from rising sea levels could provide value on a combination of fronts. One of the most promising schemes has a configuration reaching from Llandudno to Prestatyn, with a 31 km boundary wall impounding 157 km² being proposed by North Wales Tidal Energy[2], shown in Figure 2.26. Xue [130] studied the scheme and proposed 150 turbines (7.5 m diameter, 20 MW capacity), and 30,000 m² of sluice gates. The installed capacity of 3 GW when used in a flexible pumped operation was found to be capable of producing an annual output of 5.49 TWh.

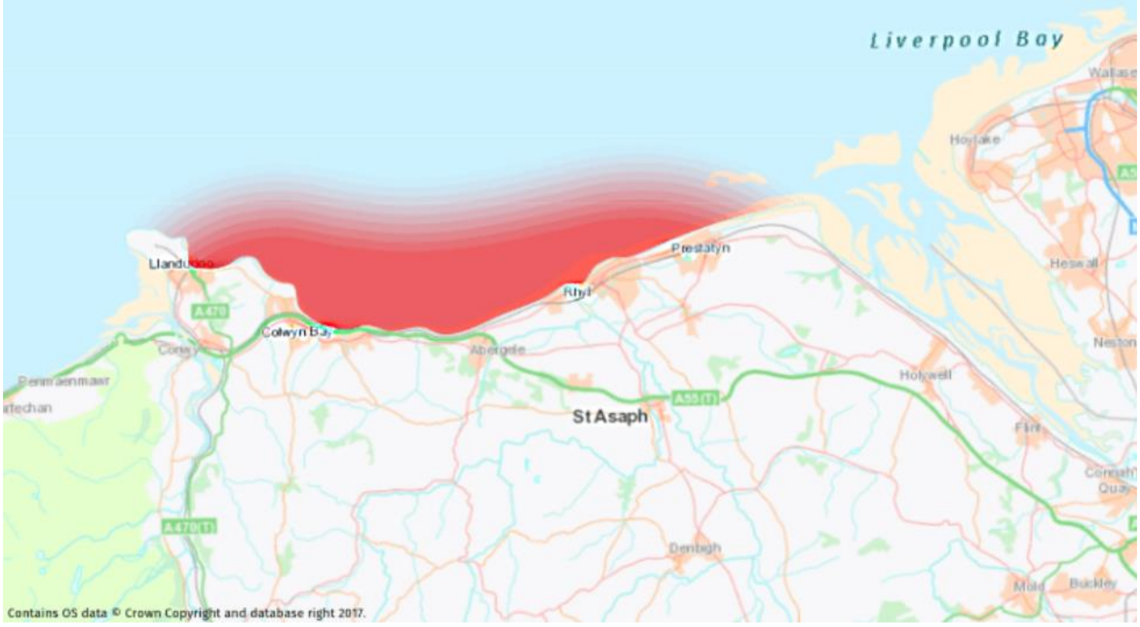

Figure 2.26: North Wales Lagoon general position, from North Wales Tidal Energy[2].

2.5.4.3 Mersey Tidal Barrage

The Liverpool City Region Combined Authority[3] has taken a leading stance in the development of the proposal for a barrage across the Mersey River. This group, being led by the city's mayor, represents a stronger interest from a governmental group than other sites have seen in recent years. Tidal barrages have long been considered for the Mersey [131], where significant tidal range and a history of maritime industry and development [132] place the city well to construct

---

[2] www.northwalestidalenergy.com

[3] www.liverpoolcityregion-ca.gov.uk/its-time-for-tidal

and operate a tidal range scheme. Aggidis and Benzon used 0D models to assess the annual electricity generated by a variety of the previous barrage proposals [133], also providing a summary of the key scheme options at the time. The concept of using a tidal range scheme to provide more to the region than energy alone (as demonstrated at the Jiangxia barrage [114] was expanded around the Mersey Barrage by Petley et al. [116], with an artists concept of the scheme shown in Figure 2.27.

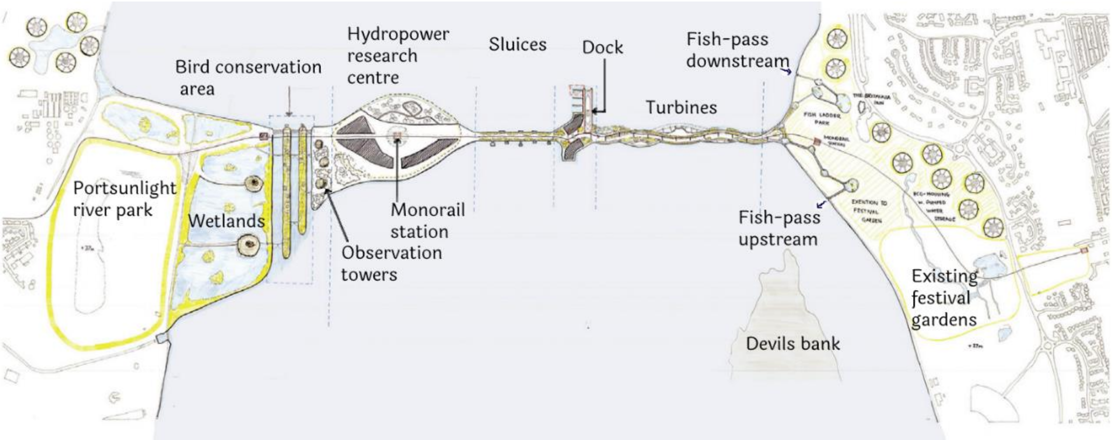

Figure 2.27: Artists impression of Mersey Tidal Barrage with inclusion of features beyond energy generation, adapted from Petley et al. [116].

2.5.5 Numerical Modelling of Tidal Range Schemes

Due to the environmental and capital cost of constructing a tidal range scheme, significant effort has been placed into developing numerical modelling tools that can be used to better understand and optimise proposed and existing schemes. For each question that can be considered about a tidal range scheme, there are multiple modelling tools that can be used in answering that question. A brief summary of these tools is provided here, with details of the tools used provided in Chapter 3.

2.5.5.1 0D Modelling

The most computationally lightweight method commonly used for tidal range scheme modelling is the 0D model. Such models are based on the conservation of volume as established by Prandle [124]. This low-cost simulation method enables simulations of both long duration, and large quantity – making them well suited to initial case assessments and optimisation processes. In one of the earliest 0D studies, Burrows et al. [134] assessed a number of tidal range proposals located about the eastern Irish Sea, complemented by a select number of 2D models for validation and initial environmental impact assessments.

Aggidis and Benzon [133] used a 0D model to calculate the annual energy of the Mersey Tidal Barrage, validating their results against previous methods used in a number of studies describing various modifications to the core barrage proposal. This study helped to explore a number of factors within barrage operation and validate the 0D method against higher fidelity approaches. Petley and Aggidis [96] used 0D modelling to calculate the annual energy that would be produced by the (then under proposal) Swansea Bay tidal lagoon, helping to develop a numeric estimate of potential power produced. This was done under the assumption of two-way fixed-head operation as had been proposed by the developers, along with an assessment of the gains realisable through pumping. The benefit that pumping can bring to a tidal range scheme (through the mechanisms as described in Section 2.5.3.1) was developed by Yates et al. [21] using 0D models. Lewis et al. [135] used 0D modelling to assess the sensitivity of tidal range energy resource to storm surges (changes in local free-surface elevation associated with storm conditions). Finding that the short-term impacts were effectively neutralised by the general balancing of storm surge effects relative to other sources of uncertainty in the process over long periods. Angeloudis et al. [136] used 0D and 2D modelling to optimise the operation of a number of tidal lagoons, highlighting the variation between the two methods in their predictions of power. Finding that though there was some deviation – the low cost of use for the 0D model made it valuable in guiding the more detailed 2D modelling.

A critical study in tidal range was that of Harcourt et al [22]. Utilising the flexible generation potential of tidal range was applied to optimise the revenue obtained from the Swansea Bay lagoon. The ability to expedite or delay operation to maximise power production had long been considered a staple of the tidal range method – expanding this principal to the revenue yield has since become the de-facto in tidal range scheme revenue analysis. Conversely, the potential for tidal range to provide continuous power for the UK was assessed by Mackie et al. [125] using multiple centrally controlled tidal range schemes represented in 0D. The conducive tidal phasing between north and south Wales was utilised by considering the West Somerset and Colwyn Bay lagoons, successfully leveraged to produce a base-energy output of 500 MW on half the days in the period assessed. This work established the potential and limitations of tidal range in providing a base-load supply of energy from only two schemes, for a true tidal base-load more (well spatially distributed) schemes would be required, or significant financial incentivisation. The impact upon the grid was broadly taken as a unidirectional relationship, with the grid merely absorbing and load produced by the tidal range scheme at the base price, Zhang et al. [137] used classical 0D modelling to benchmark a linearised 0D formulation that was included into a whole-grid model of the GB energy network. This work was able to demonstrate that the inclusion of tidal range schemes within the operation of the grid was beneficial to the grid as a whole – reducing the net operating cost of the system.

Xue et al. [138] developed terminology and methods for carrying out the optimisation of the operation of tidal range schemes, with a comparison to corroboratory 2D simulations. These methods were then expanded by evaluating the performance increase yielded through utilisation of a genetic algorithm within the predictor-search process [128]. Moreira et al. [99] utilised deep reinforcement learning to drive a 0D model of the Rance Barrage, deviating from the prior mechanisms of prediction search or fixed operation. This yielded a small performance increase from the scheme using real-time control.

Vandercruyssen et al. [139] used a 0D model in conjunction with a costing model to carry out a cost-benefit comparison of two schemes based around the Irish Sea. This study also highlights the “chicken and egg” nature of early assessments of tidal range schemes, wherein a developer needs to produce a cost and production estimate – in order to obtain funding to calculate said cost and return. Highlighting a need for open and user-friendly tools developed for tidal range study.

2.5.5.2 2D Modelling

Tidal range schemes naturally exist in coastal environments, and so their impact on the regions in which they operate can have a detrimental impact on ecosystems, navigation, flooding and more. 2D tidal range scheme models use depth averaged forms of the Navier-Stokes equations for fluid motion, typically applied to a finite element, volume, or difference method to represent a tidal range scheme and the surrounding environs.

DIVAST, developed at Cardiff University and used as the engine for the commercially licensed Flood Modeller toolkit, is a finite difference scheme using a variety of solvers including Alternating Direction Implicit (ADI) and Total Variation Diminishing (TVD). DIVAST has been used for a variety of tidal range applications. Xia et al. [90] assessed the hydrodynamic impact of two barrage proposals and a Newport based lagoon within the Severn Estuary. They concluded that the largest of the schemes would have the greatest impact on the hydrodynamics of the area, but in-turn generate the most electricity. All three schemes were represented in ebb-only fixed operation. The procedure for representing the scheme within the model, decomposing the domain to two parts, and using a bespoke protocol to define the turbines and sluices to transfer flows between the domains is the underlying method used in the vast majority of 2D tidal range scheme studies. Lin et al. [91] modelled the STPG configuration of the Severn Barrage, with an assessment of the environmental impact through modelling of the sediment transport processes, which would affect light levels in the water column and thus development of bacteria. Along with an expected reduction in maximum water levels, they predicted the barrage to increase benthic biodiversity. To complement and validate 0D modelling, Xue et al. [128] used DIVAST models of West Somerset lagoon, with the focus primarily being on the power gains realisable through improved operational optimisation in the aforementioned 0D model. The effects on the wave conditions within Bristol channel due to a Severn Barrage were assessed by pairing DIVAST with the spectral wave model Swan. The wave climate was reduced within the impoundment, and changes to the waves outside the barrage were within the existing tidal effects, though some regions of increased wave conditions were seen in the region.

The TELEMAC suite of solvers has been used to simulate tidal range schemes using a number of approaches through the TELEMAC2D Saint-Venant equation solver, which applies a finite element forward differencing scheme to unstructured meshes. Two significant approaches have been the overloading of the culvert control process by Guo et al. [129, 140], used for simulations of the North Wales, Swansea, and West Somerset lagoons. For the Rance Barrage, Rtimi et al. [104, 126] applied temporal and custom head-flow relationships to the weir operation mechanisms within the model. Further information on these approaches, and the TELEMAC system is provided in Section 3.4.

The Environmental Fluid Dynamics Code (EFDC) has been used in a number of tidal range scheme studies, Zhou et al. [141] examined the impact of open boundary location on the far-field impacts of a Severn Barrage, finding that for a scheme of this scale a coastal-shelf model can be necessary to account for all the impacts. This was then applied to a modelling process to optimise the operation of a Severn Barrage in a coastal shelf model, with the environmental impacts found to be reduced when using two-way operation – and that very-low-head (VLH) turbines may have significant scope for improved performance [142]. The effects of choices made in the representation of turbines and sluices within far-field hydro-environmental models was investigated by Bray et al. [143], with the study concluding that the net operation was insensitive to the discharge coefficient – with changes tending to

Thetis is a model developed using the Firedrake automatic code generation system [144], has been used in a number of tidal range scheme studies. The gains realised utilising the flexible potential of tidal range schemes was assessed by Harcourt et al. [22] (with 0D complemented by 2D), and the opposing goal of continuous operation from a number of schemes assessed by Mackie et al. (again with 2D supporting 0D) [125]. In design terms, the potential of linked basins to produce improved temporal availability of energy was assessed by Angeloudis et al. [145], with a linked basin system producing energy for 80 % of the time, but at a total net energy of 30 % of the original scheme (prior to splitting). The individual and compounded impacts of multiple tidal lagoons of a consistent design was assessed by Mackie et al. [146], the effects were found to be ostensibly consistent and when multiple lagoons were included the effects of the individuals were summative. Complementarity of marine energy with wind and solar resources was assessed by Pennock et al. [147], with Thetis being used in the calculation of tidal stream and range generation. Impact of tidal range on species communities was assessed by Baker et al. [148], finding that species lower at lower trophic levels would likely suffer with the inclusion of a Severn Barrage, whilst species in higher trophic levels would benefit – suggesting that a large scale barrage would alter food web dynamics within the Estuary.

2.5.5.3 3D Modelling

The Delft suite of models is popular for a variety of applications, with 2D and 3D implementations. Using Delft3D, Čož et al. [149] to investigate the vertical effects in the vicinity of tidal range scheme turbine and sluice structures, comparing the vertical velocity distributions in the wake of these structures using either five or three vertical layers. Rocha [150] used Delft3D to evaluate various impoundments in the Ria de Aviero, Portugal, using the method for an initial assessment purpose.

2.5.6 Physical Modelling of Tidal Range Schemes

Prior to the advent of numerical modelling techniques, physical scaled models were the cornerstone of fluids research, and using physical models is still able to investigate effects that are challenging to define and bound within numerical schemes. Jeffcoate et al. [151] compared physical modelling results from an idealised tidal range scheme to numerical simulations carried out using STAR-CCM. This 3D numerical model was found to agree well to the physical models and showed that depth averaged assumptions are suitable wider field testing of tidal range structures – though 3D effects are evident in the areas adjacent to the turbines and sluices.

Brammer et al. [152] model the Severn Barrage, comparing results from a physical model (with an augmented depth scale) and DIVAST simulations to investigate the environmental impacts of two options for the Severn Barrage, finding good agreement between physical and numerical representations. A physical modelling study using idealised tidal range scheme models under a variety of configurations was carried out by Leech [153]. This study examined how the spacing and arrangement of turbines around a scheme influenced flow regimes, the impact of scheme shape on the external and internal fluid conditions, and how the bed materials and slope affected the operation of the schemes. This was then compared to numerical simulations of the same conditions using Delft3D, with the numerical scheme showing weaknesses in representing some of the behaviours seen in the lab.

2.6 Summary

Globally rising population and growing electrification require an expanded scope and capacity of the electricity networks. This against the backdrop of climate change requires that the energy supplies be secured, reliable, and moving towards low -carbon methods. The importance of this transition has been established both globally by governing bodies such as the International Panel on Climate Change, and in the UK specifically by a series of departmental and ministerial targets being set as part of a longer plan.

The key composition of the UK energy mix was discussed, briefly highlighting the different roles that the various generators carry out within the system, and how the renewables that are seeing the biggest growth have weaknesses particularly related to dispatchability and predictability. Tidal energy has been highlighted by numerous academic studies and a significant government ordered review (Hendry [97]) as being an underutilised source of electricity in this context, with scope to be invaluable to the UK both as an energy source but as an industrial leader. The predictable nature of the tides is therefore examined, with a summary of available datasets, the methods used in tidal assessment, and the tides of the UK.

Hydrokinetic energy devices can be applied to a diverse range of flow situations, though the typical deployments are carried out in deep water – high velocity flows, there is a significant global scope smaller waterways and tidal flow regions. The fundamental turbine forms are described, delimited by the vectors of the flow and rotational axis, and the forcing mechanisms, drag and lift. Much work has focussed on horizontal axis designs, partly due to the correlation to common wind turbines, and the high power output and output control that can be achieved with these axial lift turbines. However, vertical-axis (or crossflow) turbines have a set of advantages including typically lower flow condition requirements, a reduced sensitivity to flow direction, depth and turbulent effects, and conceptually simpler components and connections.

For over a century engineers have theorised plans for tapping the globally high tides that are found in parts of the UK to extract energy via tidal range schemes. Tidal range as a concept is described, with the major components and elements that describe a scheme, and the operational choices that describe the operation are presented. There have been tidal range schemes operating in the world for over half a century, with the Rance Barrage being the longest tenured of the small global fleet. Well placed proposals for new tidal range schemes in the UK, both historic and current, along with the contributions their consideration made to the picture of tidal range in the UK is critical to understanding the future that tidal range could have. Typically focussed about large schemes with high financial and environmental costs in their construction, tidal range study has aimed to improve the outputs both in terms of energy and revenue to better balance the scales, whilst looking to tailor operations to minimise and understand the environmental risks posed by the schemes.

There are two fundamental principles by which tidal range schemes are modelled in a numerical context. Modelling processes based on the physics of fluid flow either in 2D or 3D, or 0D models driven solely by conservation of volume between the internal and external zones. The principals and some common models used for these purposes are given in this chapter, with Delft2D, Thetis, and TELEMAC being the key 2D models used in tidal range, and 0D models usually being bespoke. The advantage of Navier-Stokes driven models is that the full representation of the hydro-environment of the scheme allows for the impacts to be assessed, and reduces the levels of assumption within the modelling framework. Lightweight 0D models on the other hand are able to simulate a large number of runs and configurations in an equivalent time – and so have long been used for various optimisation and scoping studies. Both of these toolkits require significant expertise to use and require updating and expanding to make assessment of tidal range schemes more palatable.

3 Numerical Models

3.1 Introduction

The statistician George Box is often quoted as saying "All models are wrong, some are useful", this can refer to several modelling principles over all fields of study, but the underlying message is always relevant – use the appropriate tool for the task at hand and understand its strengths and weaknesses. This chapter describes the numerical models used (and built) as part of this study. The fundamental equations upon which each is based, the method for applying this equation over a period of time, and the computational tools to do so are discussed here.

Smoothed particle hydrodynamics (SPH), originally developed in the field of astrophysics (simultaneously) by Gingold and Monaghan [154], and Lucy [155], is a Lagrangian meshless method that solves the Navier-Stokes equations over a domain containing particles effectively representing units of fluid. These particles enact forces upon each other based on a kernel function and can be held in fixed relations to represent solid bodies, free to move under the influence of the flows around them, with material parameters such as density being related to the particles themselves. The use of SPH has expanded to a diverse range of engineering applications including fluid-structure interaction [156], wave-structure interaction (both in 2D [157–159] and 3D [160]), multi-phase flow problems[161–163], and floating body analysis [164–166]. The potential of SPH to represent situations with a complexity that is prohibitive to traditional mesh-based numerical modelling could complement mesh-based methods and allow for better insights into an array of engineering situations [167]. SPH was identified as a method that could provide insights into the design and operation of the turbine, having been used by Marongiu, Leboeuf and Parkinson [168] to simulate the complex flows and rotating geometry within a Pelton turbine. The complexities of representing this turbine concept numerically are well mitigated by the SPH method, and with the solid body interaction capability of CHRONO [169] – the DualSPHysics software was found to be an ideal candidate for this work as a near field modelling tool.

When considering a tidal range scheme, the physical effects vary in scale vastly – with small changes to the operation having potentially large impacts on the hydro-environment. The computational cost of running a large number of full physics models can easily outweigh the potential benefits yielded in scheme performance. This is particularly true at the early stages of design, where large uncertainties are present in the potential layout and configuration. To best optimise the design and configuration without high computational cost, 0D or behavioural modelling represents the relationship between the internal and external levels using a simple conservation equation, allowing a wider and more thorough search of the design domain to unearth better design options as early in the process as possible [133]. The 0D model used to develop the operation of existing large tidal range proposals and provide first estimates of production and possible operational philosophies for small schemes is developed and described.

Numerous far-field 2D models have been used in the study of tidal range energy schemes to represent the region in which they operate though not the fine details of designs. These include Delft (2D and 3D) [149], EFDC [143] and Thetis [145, 146] among others. TELEMAC2D [170] was used to assess the degree to which operational choices affect the hydro-environmental impact of a tidal range scheme in a coastal-scale model. TELEMAC was chosen due to being an open-source model, with the ability of the user to modify the source code at execution, key to implementing a tidal range scheme structure within the model of an area. This finite element solver has been used in many tidal range studies in the past, using one of two methods. Either overloading the weir functionality (Rtimi et al. [126]), or by modifying the culvert flow module of Smolders et al. [171] as done by Guo [172]. The culverts approach was taken on here and expanded to include additional functionality as well as adjustments to the user experience – with the intent of making the features more broadly accessible. The TELEMAC method itself, and the tidal range scheme module are presented in this chapter.

3.2 Smoothed Particle Hydrodynamics

Numerical modelling of the Cardiff Turbine (or CarBine) required a modelling method that allowed for the multi-physics effects to adequately interact with the fluid dynamics. Where traditional turbine modelling methods typically rely on prior knowledge of the motion of the device, and meshed methods would require high levels of re-meshing due to the multibody nature of CarBine. To achieve this, Smoothed Particle Hydrodynamics (SPH) was identified as suitable, with the ability to define fixed and free bodies subject to the fluid forces, and the potential for speedup due to hardware acceleration techniques.

3.2.1 SPH Formulation

To represent the behaviour of an incompressible fluid the SPH model uses the Navier-Stokes governing equations for a weakly-compressible fluid in the Lagrangian forms of the continuity (3.1) and momentum (3.2) equations. Where ρ is the fluid density, t time, **v** the velocity (with bold lettering herein indicating vector form), P is the pressure, Γ the dissipative terms and **f** is an external source acceleration vector (typically gravity).

$$\frac{d\rho}{dt} = -\rho\nabla \cdot \mathbf{v} \tag{3.1}$$

$$\frac{d\mathbf{v}}{dt} = -\frac{1}{\rho}\nabla P + \Gamma + \mathbf{f} \tag{3.2}$$

The mathematical principals of SPH are based on the integral approximation of a continuous function at a position $\boldsymbol{r}$ over a domain Ω, here denoted by $\mathrm{F}(\boldsymbol{r})$ (3.3). Where a kernel function W (-) defines the degree of contribution of the neighbouring region to the point being considered, that region being set around the point by the parameter h, with the particles in this zone forming the set B. Multiple kernel functions are available in DualSPHysics, the Quintic Wendland kernel (3.4) was used here (α_D ensures that $\int W(|\boldsymbol{r}-\boldsymbol{r}'|)d\boldsymbol{r}' = 1$, and is equal to $7/\ 4\pi h^2$for 2D implementations).

$$F(\boldsymbol{r}) = \int_{\Omega} F(\boldsymbol{r}')W(\boldsymbol{r}-\boldsymbol{r}', h)d\boldsymbol{r}' \tag{3.3}$$

$$W(q) = \alpha_D\left(1-\frac{q^4}{2}\right)(2q+1), \\ where\ 0 \le q \le 2, and\ q = \frac{|\boldsymbol{r}-\boldsymbol{r}'|}{h} \tag{3.4}$$

Considering a particle a, at a position $\boldsymbol{r}_a$ velocity $\boldsymbol{v}_a$, with volume V_a, mass m_a and density ρ_a, linked by (3.5) and (3.6). Equation (3.3) can be discretised into a summation of the influences of the neighbourhood of particles, denoted b, each having characteristics like those of a, leading to (3.7).

$$\frac{d\boldsymbol{r}_a}{dt} = \boldsymbol{v}_a \tag{3.5}$$

$$V_a = \frac{m_a}{\rho_a} \tag{3.6}$$

$$F(\boldsymbol{r}_a) \approx \sum_{b\in B} F(\boldsymbol{r}_b)W(\boldsymbol{r}_a - \boldsymbol{r}_b, h)\frac{m_b}{\rho_b} \tag{3.7}$$

In Equation (3.2), the momentum source term $\mathbf{f}$ is hence taken as gravity $\boldsymbol{g}$**.** The dissipative term Γ was handled in DualSPHysics by the Artificial Viscosity scheme described by Monaghan [173], and is added to the pressures terms whereby the particle has velocity $\boldsymbol{v_a}$, P_a and P_b are the pressure at a and b respectively, resulting in the momentum term of the Navier-Stokes equations in discrete Lagrangian form (3.8). Π_{ab} is the viscosity term (3.9), formed by the relative positions and velocities of the particles, where $\overline{c_{ab}}$ is the average speed of sound, $\overline{\rho_{ab}}$ the average density, ∇_a is the gradient operator, and finally α is a dimensionless tuning coefficient that needs ascertaining based on the model configuration in order to provide stability and mitigate spurious oscillations [157]. This viscosity term thus produces a repulsive force on two particles approaching, and an attractive force on particles moving apart. Alternatively, DualSPHysics offers a Laminar viscosity with Sub-Particle Scale (Laminar + SPS) scheme, however, this is a 3D method and so was not suitable for this application.

$$\frac{d\boldsymbol{v}_a}{dt} = -\sum_{b\in B} m_b\left(\frac{P_a + P_b}{\rho_a \cdot \rho_b} + \Pi_{ab}\right)\nabla_a W_{ab} + \boldsymbol{g} \tag{3.8}$$

$$\Pi_{ab} = \begin{cases} -\alpha\dfrac{\overline{c_{ab}}\mu_{ab}}{\overline{\rho_{ab}}}, & \boldsymbol{v}_{ab} \cdot \boldsymbol{r}_{ab} < 0 \\ 0, & \boldsymbol{v}_{ab} \cdot \boldsymbol{r}_{ab} > 0 \end{cases} \tag{3.9}$$

$$\boldsymbol{r}_{ab} = \boldsymbol{r}_a - \boldsymbol{r}_b, and\ \boldsymbol{v}_{ab} = \boldsymbol{v}_a - \boldsymbol{v}_b$$

$$\mu_{ab} = h\frac{\boldsymbol{v}_{ab} \cdot \boldsymbol{r}_{ab}}{\boldsymbol{r}_{ab}^2 + 0.01h^2}$$

$$\overline{c_{ab}} = \frac{1}{2}(c_a + c_b)$$

In complement to (3.8), the conservation of mass in SPH form for a weakly compressible fluid is given by (3.10). Here the compressibility of the fluid is governed by the equation of state for the fluid (3.11) based on Monaghan [173] with the relationship between the pressure P, the polytropic constant γ, the reference density ρ_0, and the particle and reference speeds of sound c and c_0 respectively.

$$\frac{d\rho_a}{dt} = -\rho_a \sum_{b\in B} \frac{m_b}{\rho_b} \mathbf{v}_{ab} \cdot \nabla_a W_{ab} \qquad 3.10$$

$$P = b\left[\left(\frac{\rho}{\rho_0}\right)^{\gamma} - 1\right] \qquad 3.11$$

$$\gamma = 7, b = c_0^2 \rho_0/\gamma, \rho_0 = 1000\ kg/m^3, c_0 = c(\rho_0) = \sqrt{\partial P/\partial \rho}\Big|_{\rho_0}$$

To reduce density fluctuations, the density diffusion term (DDT) is added to (3.10) using the DDT term Ψ_{ab} leading to the conservation mass in the form (3.12). Where a tuning coefficient δ_Φ of 0.1 is recommended for most applications by Fourtakas et al. [174].

$$\frac{d\rho_a}{dt} = -\rho_a \sum_{b\in B} \frac{m_b}{\rho_b} \boldsymbol{v}_{ab} \cdot \nabla_a W_{ab} \ + \delta_\Phi h c_0 \sum_{b\in B} \Psi_{ab} \cdot \nabla_a W_{ab} \frac{m_b}{\rho_b} \qquad 3.12$$

This density diffusion term (3.13), initially presented by Molteni and Colagrossi [175] is derived from the difference between the densities of two particles ρ_a and ρ_b, and their relative positions $\boldsymbol{r}_{ab}$.

$$\Psi_{\mathrm{ab}} = 2(\rho_b - \ \rho_a) \frac{\boldsymbol{r}_{ab}}{\|\boldsymbol{r}_{ab}\|^2} \qquad 3.13$$

This was then developed by Fourtakas et al. [174] into (3.14) where the density term is separated into the total and hydrostatic constituents ρ_{ab}^T and ρ_{ab}^H, where the total density is the sum of the dynamic and hydrostatic components. The hydrostatic pressure is calculated using (3.15) where the hydrostatic pressure P_{ab}^H is a product of the vertical difference between the two points z_{ab}. Note that for planar 2D uses, where gravity is excluded in all dimensions the Fourtakas density diffusion term reduces back to the Molteni and Colagrossi term.

$$\Psi_{\mathrm{ab}} = 2\left(\rho_{ab}^T - \ \rho_{ab}^H\right) \frac{\boldsymbol{r}_{ab}}{\|\boldsymbol{r}_{ab}\|^2} \qquad 3.14$$

$$\rho_{ab}^{H} = \rho_0 \left(\sqrt[\gamma]{P_{ab}^{H} + 1 \Big/ \frac{c_0^2 \rho_0}{\gamma}} - 1 \right) \qquad 3.15$$

$$P_{ab}^{H} = \rho_0 g z_{ab} \qquad 3.16$$

To mitigate the excess propagation of voids within the domain, Lind et al. [176] applied Ficks first law of diffusion (3.17) to apply a shifting function, moving the particles from areas of high density to areas of low density, the particle flux $\mathbf{J}$ being proportional to the concentration gradient C by a degree of the Fickian diffusion coefficient $\mathrm{D_F}$.

$$\mathbf{J} = -\mathrm{D_F} \nabla C \qquad 3.17$$

To allow an effective degree of particle shifting without introducing excessive instability the diffusion coefficient D (3.18) is limited by a Von Neumann stability analysis using the kernel limit h and the maximum timestep Δt_{max} permissible under the Courant-Friedrichs-Lewy condition. Developed from the particle spacing and local velocity $\|\boldsymbol{u}\|$ (3.19).

$$\mathrm{D} \leq \frac{h^2}{2\Delta \mathrm{t_{max}}} \qquad 3.18$$

$$\Delta t_{max} \leq \frac{h}{\|\boldsymbol{u}\|_i} \qquad 3.19$$

The gradient of the particle concentration ∇C_i is found by evaluating the local gradient operator (3.20).

$$\nabla C_i = \sum_j \frac{m_j}{\rho_j} \nabla W_{ij} \qquad 3.20$$

The discrete shifting distance $\delta \mathbf{r}_{a_s}$ for a particle is thus given by (3.21) using the kernel gradient $\nabla \mathrm{C_a}$, and the shifting diffusivity $\mathrm{D_s}$ – which in turn is a function of the particle velocity magnitude $\|\boldsymbol{u}\|_i$, and timestep dt (3.22) as proposed by Skillen et al. [177]. A is a dimensionless parameter that controls the degree of shifting and maintains proportionality, allowing the operator to tune the degree of shifting as required by the problem being represented. In the full formulation, there is a free-surface detection procedure, however this was disabled as no free surface should be present in this problem (as this is used in vertically oriented simulations whereas this is formed as a horizontally arranged model), interested readers are directed to Lind et al. [176].

$$\Delta \mathbf{r}_{\mathrm{a_s}} = -\mathrm{D_s} \nabla C_a \tag{3.21}$$

$$D_s = Ah\|\boldsymbol{u}\|_i dt \tag{3.22}$$

For this modelling approach, the turbine is represented as a fluid-driven object, composed of multiple rigid bodies. As such, the forces f on each boundary (turbine) particle k from the fluid particles a is given by (3.23). Thus, for a body with mass M, composed of a set of boundary particles (BPs) the Newtonian motion $\boldsymbol{V}$ is derived from the sum of the contributions of the particle set (3.24). The inertia I, rotational velocity Ω, and centre of mass $\boldsymbol{R}_0$ are related under the same principle per (3.25).

$$f_k = \sum_{a \in WPs} f_{ka} \tag{3.23}$$

$$M\frac{d\boldsymbol{V}}{dt} = \sum_{k \in BPs} m_k f_k \tag{3.24}$$

$$I\frac{d\Omega}{dt} = \sum_{k \in BPs} m_k (\boldsymbol{r}_k - \boldsymbol{R}_0) \times f_k \tag{3.25}$$

The motion of the whole body is thus determined by integrating 3.24 and 3.25, and the motion of each boundary particle in the body is therefore calculated as shown in Equation 3.26. In the case used here, some external restraints, along with the solid body interactions are handled externally by the solid body solver Project Chrono [169], $\frac{d\boldsymbol{V}}{dt}, \frac{d\Omega}{dt}$ and Δt are passed from DualSPHysics to Chrono, which calculates the solid body interactions and returns $\boldsymbol{V}, \Omega,$ and $\boldsymbol{R}_0$, the connection between the two systems is fully described by Martinez-Estevez et al. [178]. The general passage of information between DualSPHysics and Chrono is shown in Figure 3.1.

$$\boldsymbol{v}_k = \boldsymbol{V} + \Omega \times (\boldsymbol{r}_k - \boldsymbol{R}_{\boldsymbol{0}}) \tag{3.26}$$

The Chrono library [169] includes several connection methods for bodies within the model, which here was used to appropriately connect the components of the turbine. The body was connected to the domain by a hinge which acted as an axle. The flaps were then connected to the body, and so hinged about their individual axles, and when in the closed position then transferred the forces through them to the body and thus turn the turbine as a whole.

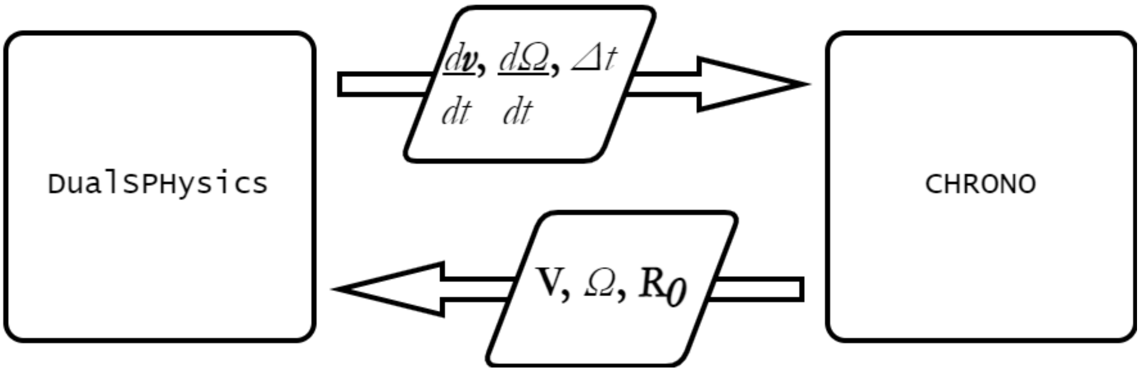

Figure 3.1: Interaction of DualSPHysics and CHRONO information passing.

DualSPHysics allows users the choice between two time-stepping algorithms, the computationally simple Verlet scheme [179], and the two-stage symplectic method – which is based on the Verlet scheme and is more computationally demanding but provides improved stability. As stability was a major factor in this study, the symplectic method of Leimkuhler and Matthews [180] was utilised, and so is presented here.

The symplectic method of Leimkuhler and Matthews [180] is an extension to the Verlet method, second-order accurate and reversible in time in the absence of diffusive terms. This makes it well suited to Lagrangian schemes. The Verlet scheme without dissipative forces is given in 3.27, showing the integration over the staggered time interval for a given particle *a*.

$$\begin{aligned}
\mathbf{r}_a^{n+\frac{1}{2}} &= \mathbf{r}_a^n + \frac{\Delta t}{2}\mathbf{v}_a^n \\
\mathbf{v}_a^{n+1} &= \mathbf{v}_a^n + \Delta t \mathbf{F}_a^{n+\frac{1}{2}} \\
\mathbf{r}_a^{n+1} &= \mathbf{r}_a^{n+\frac{1}{2}} + \frac{\Delta t}{2}\mathbf{v}_a^{n+1}
\end{aligned} \qquad 3.27$$

The inclusion of viscous forces and density changes in the Symplectic method dictates the need for velocity in the intermediate step ($\mathbf{v}_a^{n+\frac{1}{2}}$), this velocity Verlet half step is used in the calculation of the velocity, acceleration, and density changes in the intermediate, forming the system of equations in 3.28. The density evolution follows the half time-steps in the positioning scheme as given in 3.29, where the intermediate $\varepsilon_a^{n+\frac{1}{2}} = \Delta t \left(-R^{n+\frac{1}{2}}/\rho^{n+\frac{1}{2}}\right)$.

$$\begin{aligned}
\mathbf{r}_a^{n+\frac{1}{2}} &= \mathbf{r}_a^n + \frac{\Delta t}{2}\mathbf{v}_a^n \\
\mathbf{v}_a^{n+\frac{1}{2}} &= \mathbf{v}_a^n + \Delta t\mathbf{F}_a^n \\
\mathbf{v}_a^{n+1} &= \mathbf{v}_a^n + \Delta t\mathbf{F}_a^{n+\frac{1}{2}} \\
\mathbf{r}_a^{n+1} &= \mathbf{r}_a^n + \frac{\Delta t}{2}(\mathbf{v}_a^n + \mathbf{v}_a^{n+1})
\end{aligned} \qquad 3.28$$

$$\begin{aligned}
\rho_a^{n+\frac{1}{2}} &= \rho_a^n + \frac{\Delta t}{2}R_a^n \\
\rho_a^{n+1} &= \rho_a^n\left(\frac{2-\varepsilon_a^{n+\frac{1}{2}}}{2+\varepsilon_a^{n+\frac{1}{2}}}\right)
\end{aligned} \qquad 3.29$$

The variable timestep used in DualSPHysics is driven by Courant-Friedrichs-Lewy (CFL) condition, along with the forcing and viscous diffusion terms. A variable time step Δt is calculated based on the CFL number C_{CFL} and the minimum of two timesteps, Δt_f being the minimum stable forcing step over all the particles (where f_a is force per unit mass), and Δt_{cv} being the minimum timestep according to the CFL and Viscous time step controls per Monaghan and Kos [181].

$$\begin{aligned}
\Delta t_f &= \min_a\left(\sqrt{h/|f_a|}\right) \\
\Delta t_{cv} &= \min_a \frac{h}{c_s + \max_b \frac{|h\mathbf{v}_a \cdot \mathbf{r}_a|}{r_{ab}^2 + \eta^2}} \\
\Delta t &= C_{CFL}\min(\Delta \mathrm{t_f}, \Delta t_{cv})
\end{aligned} \qquad 3.30$$

3.2.2 DualSPHysics

DualSPHysics [182] was selected as a modelling solution for SPH based on a combination of factors. This software open-source (GNU Lesser General Public License) has been used in a multitude of situations including tsunami simulation [183], fluid-structure interaction [156], and the study of renewable energy devices [165, 184]. Some key advantages are the ability to improve performance by running the model on the Graphical Processing Unit (GPU) through the Nvidia CUDA programming language [182, 185, 186], open-source development, and a healthy community of users. Additionally, the solid body solver CHRONO [169, 178] is included within the model allowing for multi-physics problems to be accurately defined, and externally solved.

3.2.2.1 2D Plan Section

To minimise the computational cost, a 2D plan section was modelled through the turbine. This reduces the domain to a depth of one particle through, pinning all particles in the model to this plane. 2D SPH has been used typically with the plane being taken along a vertical axis, allowing for flows within it, vertical pressures, free surface dynamics and more. Examples of 2D SPH being used in wave-structure interaction [157–159], fluid mixing [187–189], dam break [190, 191], open channel flows [192] and more. The implementation here considers the plane in use to be a representative plan section through the device, with an isotropic turbulence formation. As such, gravitational forces were set to 0 along all axes, whereas a gravitational force would be used in the case of a vertically aligned 2D simulation.

3.2.2.2 Boundary Conditions

The boundary conditions in the model utilise fictitious-or-ghost particles to provide the relevant kernel support needed to boundary adjacent particles. The inflow and outflow buffer regions each use 8 layers of fictitious particles to properly develop the relationships between the entering and exiting particles. The inflow buffer generates particles and propels them into the domain at a pre-defined velocity, U_∞. The outflow buffer applied a velocity to the fictitious particles derived by extrapolating the velocity of the particles in the domain, with the intention of absorbing the internal velocity fluctuations generated by the device. To assess the degree to which the location of the upstream and downstream boundary impacted the model performance, a set of tests were conducted moving said boundaries farther from the device.

3.3 0D Tidal Range Scheme

0D models represent the activity of a tidal range scheme by calculating the internal water level based on the design characteristics and internal area. The model is primarily driven by the external water level, allowing calculation and application of the flow across the scheme at a given instance. This technique allows for a rapid operational assessment of a tidal range energy scheme without the need for an expensive full hydro-environmental modelling study. Due to the ease of construction and speed of operation, 0D modelling lends itself to optimisation of both the operation and physical design of the scheme during early-stage analysis as used by numerous prior studies [21, 22, 96, 121, 125, 127, 128, 193]. These models can incorporate (for flexible operation) or be wrapped in optimisation tools, such as grid-search, gradient-based, proximal policy, and genetic algorithms, for design and hyper-parameter analysis [194].

The 0D tidal range model used here was developed at Cardiff University, written in object-oriented C++. It is available for use under an MIT open license on GitHub in a repository[4].

3.3.1 Fundamentals

The tidal range scheme is represented in the 0D model by applying a continuity equation (3.31) where the volume of water held within the impoundment V (m³), over time- t (s) at a flow rate Q (m³/s). The impounded volume V is the sum of the $A(\eta)$ (m²) is the varying surface area of the scheme at a level η (m) from the minimum internal level to the water surface as shown in Equation 3.32.

$$\frac{dV}{dt} = Q \tag{3.31}$$

$$V = \int_0^{\eta} A(\eta)\, d\eta \tag{3.32}$$

$$\frac{d\eta}{dt} = \frac{Q}{A}, \qquad \frac{\eta_{up}^{n+1} - \eta_{up}^{n}}{\Delta t} = \frac{Q^n}{A^n} \tag{3.33}$$

---

[4] https://github.com/NHanousek/0D-Tidal-Range

Equation 3.31 can be decomposed and an Eulerian forward differencing scheme applied into Equation 3.33 where the upstream (or internal) water level η_{up} at a time $n + 1$ is determined based on Q at a time index n. Where Q comprises the incoming environmental flow Q_{In}^{n}, the flow through the sluices Q_{SL}^{n}, and the turbines Q_{TB}^{n} this becomes Equation 3.34.

$$\eta_{up}^{n+1} = \eta_{up}^{n} + \frac{(Q_{In}^{n} - Q_{SL}^{n} - Q_{TB}^{n})}{A(\eta_{up}^{n})} \Delta t \tag{3.34}$$

The flow through the sluice gates is calculated using the orifice equation, in the form as shown in Equation 3.35. Where ΔH (m) is the absolute head difference across the scheme shown in Equation 3.36 by the upstream and downstream (internal and external) water levels. A_{SL} (m²) is the total area of sluice gates C_D (-) *is* the dimensionless discharge coefficient, δ_{dir} (-) is a directional indicator described in Equation 3.37 and g (m/s²) is the rate of gravitational acceleration.

$$Q_{sl} = \delta_{dir} \cdot C_D \cdot A_{SL} \cdot \sqrt{2g \cdot |\Delta H|} \tag{3.35}$$

$$\Delta H = \eta_{up} - \eta_{down} \tag{3.36}$$

$$\delta_{\mathrm{dir}} = \begin{cases} -1, & \Delta\mathrm{H} < 0 \\ 1, & \Delta\mathrm{H} \geq 0 \end{cases} \tag{3.37}$$

The flow through and power produced/consumed by the turbines P_{TB} (MW) are calculated based on the head difference extracted from a provided hill chart. In the case that a turbine used is not the same size as the design turbine (9m Andritz Hydro Bulb Turbine as presented by Aggidis and Feather [29], and used in numerous tidal range studies), a scaling factor is applied based on the difference between their areas where D_{scaled} (m) is the diameter of the new turbine and D_{base} (m) is the original area Equation 3.38, based on the assumption that power and flow scale with cross sectional area.

$$Y_{scaled} = Y_{base} \times \frac{{D_{scaled}}^2}{{D_{base}}^2} \tag{3.38}$$

$$\text{where}, \mathrm{Y} \in \{Q_{TB}(\Delta H), P_{TB}(\Delta H)\} \tag{3.39}$$

To represent the time taken to open or close the turbines or sluices, a ramp function (Equation 3.40) is applied to the flow and power from the turbines and sluices to reflect their opening or closing at the appropriate time. Here t_{phase} and t_{ramp} are the phase time (amount of time since mode change) and a predefined ramping duration respectively – whose units must be the same. Increasing the flow up to the maximum when opening and decreasing when closing. This also has the secondary benefit of dampening large discontinuities in the flow, improving numerical stability by accounting for a physical effect. It is also assumed that the scheme will not change modes during this period.

$$RAMP = \frac{1}{2}\left(1 - \cos\left(\pi \frac{t_{phase}}{t_{ramp}}\right)\right) \qquad 3.40$$

$$\begin{cases} Q_{RAMP} = Q \times RAMP & ,Opening \\ Q_{RAMP} = Q \times (1 - RAMP) & ,Closing \end{cases}$$

3.3.2 Mode control

Operation of a tidal range scheme fundamentally requires a finite number of modes, whose differences in operational characteristics allow the development of a head difference, generation, and the eventual equalisation of the water levels across the impoundment as the tides move. These modes are summarised in Table 2.3, the process for moving from one to another can be based on duration – mapping the operation to the time elapsed, the head difference, or some alternative decision-making process. In the 0D model used here, the head difference between the external and internal levels was used. For two-way operation, the absolute head difference is used, and there is no discrimination between operations on the ebbing or flooding tides in terms of control (though differences to the flow scheme can be applied). Simplified code for this tree is given in Table 3.1 with the procedure when pumping is included in Table 3.2.

Table 3.1: Two-way control flow without pumping pseudocode.

```
switch (mode)
  hd = absolute(head difference)   // ebbing is the same as flooding
  case filling/sluicing:
    if (hd <= 0.01)                // mitigates oscillation at hd≈0.0
      mode = holding
    end
  case holding:
    if (hd >= head diff start)
      mode = generating
    end
  case generating:
    if (hd < head diff end)
      mode = sluicing
    end
  end
end
```

The pump control includes the option to separately control the pumps, via pre-determined levels (such as maintaining the original internal tidal range for each tidal cycle, or applying a specific duration of pumping). Through this, the model can be used to consider more complex motivations of operation if desired, as pumping opens the system up to an order of magnitude more decisions, particularly those pertaining to the environment of the impoundment and the nature of the energy generation profile.

Table 3.2: Two-way control flow with pumping pseudocode.

```
switch (mode)
  hd = absolute(head difference)
  case filling/sluicing:
    if (hd <= 0.01)
      mode = pumping                       // formerly holding
    end
  case holding:
    if (hd >= head diff start)
      mode = generating
    end
  case generating:
    if (hd < head diff end)
      mode = sluicing
    end
  case pumping
    if (pump control == head driven)       // head difference operation
      if (hd >= head diff pump)
        mode = holding
      end
    else if (pump control == levels)       // level-target operation
      if (target < mid-tide level)         // aiming for a low tide
        if (internal level < target)       // low tide reached
          mode = holding
        end
      else                                 // aiming for a high tide
        if (internal level > target)       // high tide reached
          mode = holding
        end
      end
    else if (pump control == time)         // duration-based operation
      if (phase time > max pump time)
        mode = holding
      end
    end
  end
end
```

3.3.3 Flexible Operation

Flexible tidal range scheme control underpins a large degree of the work carried out upon tidal range schemes, allowing the scheme to extract more energy, higher revenue, or maintain environmental constraints. Within the 0D model used here, the flexible operation is carried out using a repeated sampling procedure. Over a long duration run, testing every tide (or half tide) at every possible level, all within one branched system would grow the tree of options to a vast size very quickly which underpins the need for a lower cost flexibility identification process.

The repeated sample process takes the time domain, and identifies the periods at which a new set of start/end/pump levels are required – and demarcates these as 'flex points', these can be at constant time intervals 'flex intervals' such as every 24 hours (daily), or at certain hydrodynamic points – high/low water points or times of 'zero-crossing'. Then, at every timestep – the model identifies if this timestep is a flex point, and if so – carries out the flex procedure. First, the levels to be tested are determined (this can be the entire domain in the case of a grid-search, or the initial population for an evolutionary algorithm). For each set of control levels, a temporary instance of the model is run for a duration specified – the 'flex period'. This duration can be run with a different timestep to the main model to accelerate calculation at a reduced resolution of search. Once the temporary model reaches the end of the period the yield (as specified by the modeller – typically energy, or revenue if a value timeseries is provided) is recorded for each member of the population and (in the case of a grid search) the best performing configuration passed back to the main model to be used for the remainder of the interval. This process is adjusted when using a genetic algorithm as naturally the total set of flex runs is iterated populations of conditions – with limits on total flex runs based on convergence, or total simulation triggers.

Table 3.3: Flexible operation process pseudocode.

```
while (t < T)                                   // where T is the total time
  if (flex point)                               // either time or tide based
    initialise(control levels)                  // can be genetic or grid
    for control flex in control levels          // test each option
      t_flex = t                                // looking ahead from now
      yield[control flex] = 0
      while (t_flex < t + flex period)
        operate_trs(t_flex, control flex)       // use temporary variables
        yield[control flex] += yield flex       // track the desired parameter
        t_flex += dt                            // iterate temporary step
      end
    end
    control = control_levels[yield best]       // set global control from flex
  end
  operate_trs(t, control)
  t += dt
end
```

The balance between the flex period and interval can be critical as to how the model performs, Xue et al. [128] recommend having the period (or duration tested) be longer than the interval – such that the model uses a set of controls that ensure that not only will the tide in question produce the maximum amount of energy possible, the following tide will too. This compromises each tide to some degree but ensures that the tidal range scheme does not operate in some manner that results in the following tide being overly negatively impacted. In the case of assessing two tides for the operation of one – the name Every Tide Next (ETN) is used, with Every Half Next (EHN) being the same but for each half tide, these along with some other common options and a generalised case are shown in Figure 3.2. The best configuration of these flexibility parameters varies from scheme to scheme, since some are better at recovering from a given phase, and so allowing each period the opportunity to be greedy will result in a net increase – where some require a long-term view to be used at all times.

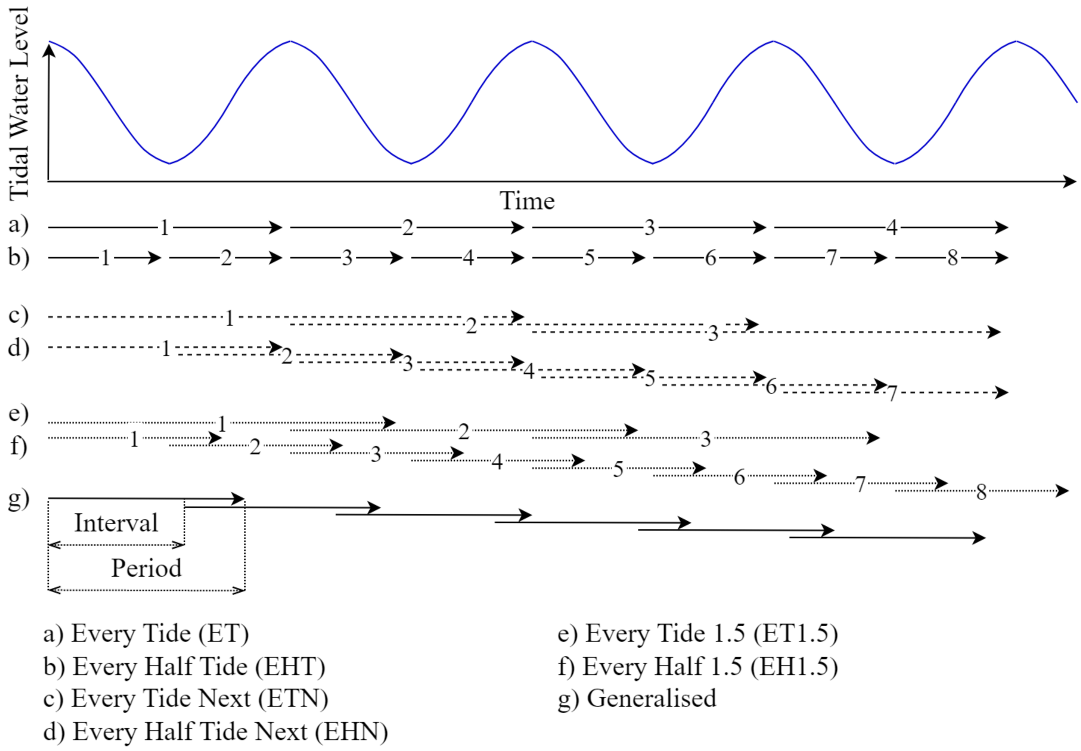

Figure 3.2: Diagram showing commonly used and generalised temporal progression of different flexible operation systems.

3.3.4 Model structure

The 0D tidal range scheme model, much like a real tidal range scheme is composed of a number of elements, each containing various components within them – shown schematically in Figure 3.3. The 0D model itself holds the numerical controls – time-step and duration. These are constant across however many tidal range schemes are included, along with this – the results are passed through the central model and the global energy value is mapped to the energy produced at this stage.

Each tidal range scheme has defined inflows, a water level area relationship, flexibility controls, and a scheme-specific energy value – this may be the same as the global energy value but can be an alternate, this could be a forecast with some degree of error or used to encourage generation at specific times by applying a time varying weighting. Each tidal range scheme also contains a number of turbine banks, at each of these there are a defined number of turbines and sluices and a specific water level trace. This can be used to assess the effect of having turbine banks in vastly different locations.

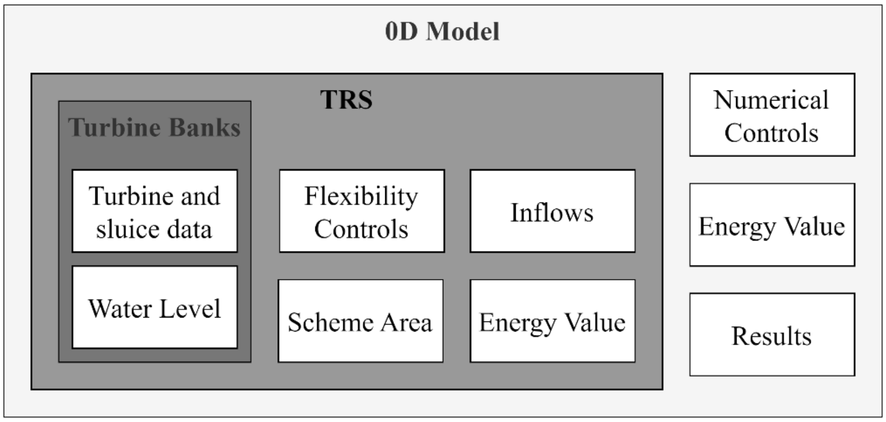

Figure 3.3: Object structure diagram of the 0D model.

3.3.4.1 Input and Output

The data regarding the operation of the 0D model is passed via text files, examples of the key files for the model as a whole in Figure 3.4, a specific tidal range scheme within a model in Figure 3.5 and the parameters controlling a genetic algorithm in Figure 3.6. Each uses a key-variable pair system, with the units being specified for dimensional parameters and the option to adjust the unit desired included for some variables where appropriate, with the 'End' key indicating the end of the data, allowing for additional comments to be stored below this line. The model file or configuration file for an example composition is shown in Figure 3.4, the first line is a comment or title that is ignored by the file reader, the model name determines the naming prefix of the output files, the timestep and maximum time (whose units can be specified as minutes or hours) are given, and the filenames of the singular scheme in question along with the energy value are given.

```
For DesignOpt of West Somerset Lagoon
modelName:     WSL-Fixed
schemeFile:    WSL-Fixed-SCHEME.dat
numSchemes:    1
printFull:     true
energyValue:   SSP-2018.dat
maxTime(hrs):  2190
timeStep(min): 5
End
```

Figure 3.4: Example of a configuration file for a single WSL 0D model.

The scheme file in Figure 3.5 would be pointed to by the configuration file and defines the majority of what is included within a tidal range scheme. Again, a commentary or title line precedes the data, the name is used in the data headers of the results file, and the turbine file contains the hill-chart and diameter of the base turbine which is then scaled into the turbine sizes declared at the given banks. The head differences to start and end are passed as two variables the minimum and maximum points to be used in the search procedure described in Section 3.3.3, with the 'delta's defining the step size to be used between these values. The flexType allows several keyword options for the timing of the flex points (or the 'flexInterval' can be specified) – here HighLow tells the model to test at every high or low tide of the external water level time series, and then to use a period of 12.4 hours. The minimum and maximum water level values instruct the model at what levels to limit the composition of the level-area curves from the data extracted from the scheme area file passed to the scheme, which can either be in a level-area paired list, or a .t3s (unstructured triangular element mesh file) of the scheme itself from which to ascertain the levels.

```
For DesignOpt of scheme
schemeName: WSL-300-60000.0
numBanks: 1
turbineFile: HQPTurbinesNew.dat
energyValue: SSP-2018.dat
turbineCentreLevel(m): -100
schemeArea: Scheme_Area_WSL.out
externalWaterLevel: WSL-Long-2018.ts1
numberTurbines(int): 300
turbineDiameter(m): 7.2
areaSluices(m2): 60000.0
inFlowFile: false
flexVariable: profit
midTideLevel(mD): 0.0
switchModeBuffer(hrs): 0.25
rampTime(hrs):         0.25
parrallelSluice: true
flexible:  true
operation: 2WY
pumping:   true
pumpControl: head
headDiffStart(m): 7.5 2.0
headDiffEnd(m):   3.5 0.5
pumpEndMax: 2.5
pumpEndMin: 0
pumpEndDelta: 0.1
headDiffStartDelta(m): 0.1
headDiffEndDelta(m): 0.1
flexType: HighLow
flexPeriod(hrs): 12.4
waterLevelMax(m): 10
waterLevelMin(m): -10
pumpEfficiency(0-1): 0.75
flexMethod: GRID
End
```

Figure 3.5: Example of scheme file defining a WSL model using flexible grid-search-based operation.

When a scheme is configured to use a genetic algorithm in the flexible operation procedure, by passing the variable GENETIC to the key flexMethod – or by including the key ‘geneticFile’ and the filename, a set of controls for the genetic algorithm will be read from a file such as the one in Figure 3.6. At the current state of development it is only numeric controls that define how the algorithm runs that can be declared – however adding alternative method choices such as different selection and, crossover and mutation mechanisms would be a good addition, as the choice of these can strongly impact the performance of the system, as discussed by Xue et al. [128]. The initial population is constructed as an n-dimensional Latin hypercube where n is the number of variables to be assessed. Some experimentation was carried out to ascertain the suitability of Bayesian Optimisation with Gaussian Process Regression to this process – as the method is reported as being well suited to optimising highly demanding methods by building a surrogate model to represent the search domain using the BayesOpt library [195]. However, the complexity in including the requisite back-ends required for the high-level mathematics behind Bayesian Optimisation in a manner that maintained the portability and simplicity of the 0D model led to this component being shelved.

```
Genetic Algorithm Control File
POPSIZE: 125
MAXGENS: 100
NVARS: 3
PXOVER: 0.5
PMUTATION: 0.35
End
```

Figure 3.6: Example of a configuration file for control of genetic algorithm for use in flexible operation analysis.

3.3.5 High Volume Usage

The nature of a 0D model is such that the best utilisation is reached when the model can be run a large number of times through a wrapping technique or automated model generation. For the vast majority of the 0D models run here, Julia script files were composed to automatically write text input files for the models, and run said models – and extracting the key parameters from the output data. An exemplum script is included in the repository, although it is a rather complex example of this process, the aim is for an interested user to look at this and see how the method could be applied to their uses in the language of their choice. This is particularly useful for processes such as sensitivity analysis of parameters [196], design space assessment [197], and mass model deployment [198].

3.4 openTELEMAC

The TELEMAC project [170] was launched in 1987 at the research and development branch of the French state-owned power company Electricite de France (EDF) to develop a free-surface focussed hydro-informatics solution for use in modelling the various aquatic environments that interact with the infrastructure of what was in 2009 – the largest electricity producer in the world [199]. This open-source (GNU General Public License) software boasts significant flexibility for the user, with an array of example models covering fluid problems from regional-scale tidal flows [200, 201], storm surges [202], oil spills and sea level rise [203], to river simulations [204, 205], and global oceanic simulation [206].

The operation of the TELEMAC suite allows users to modify code aspects to suit specific needs, with code compilation at time of execution. This has led to it being popular in the study of tidal renewable energy devices, both tidal stream [207] and tidal range [129]. Beyond this comes the ability to couple or extend the TELEMAC2D model to utilise the other solvers in the system, which provide a variety of extended functionality – notably GAIA/SISYPHE (sediment morpho-dynamics), TOMAWAQ (wave propagation in coastal areas), WAQTEL (water quality modelling tools), and KHIONE (ice processes) [208].

3.4.1 Fundamentals

To simulate the motion of a fluid in two dimensions, TELEMAC2D solves the Saint-Venant (or Shallow Water) equation, a form of depth-integrated Navier-Stokes equations of fluid motion using a finite element method. The partial differentials solved are, the continuity equation 3.41, momentum in the x direction (3.42), and momentum in the y direction 3.43. With the conservation of tracer(s) given in Equation 3.44.

$$\frac{\partial h}{\partial t}+\frac{\partial(uh)}{\partial x}+\frac{\partial(vh)}{\partial y}=S_h \qquad 3.41$$

$$\frac{\partial u}{\partial t}+u\frac{\partial u}{\partial x}+v\frac{\partial u}{\partial y}+g\frac{\partial \eta}{\partial x}=\frac{1}{h}\nabla(hv_e\nabla u)+F_x \qquad 3.42$$

$$\frac{\partial v}{\partial t}+u\frac{\partial v}{\partial x}+v\frac{\partial v}{\partial y}+g\frac{\partial \eta}{\partial y}=\frac{1}{h}\nabla(hv_e\nabla \mathrm{v})+F_y \qquad 3.43$$

$$\frac{\partial T}{\partial t}+u\frac{\partial T}{\partial x}+v\frac{\partial T}{\partial y}=\frac{1}{h}\nabla(hv_T\nabla_{\mathrm{T}})+S_T \qquad 3.44$$

Where h (m) is the water depth changing over time t (s), u and v (m/s) are the velocity components in the x and y directions respectively, and S_h represents a momentum source or sink. In the momentum equations η (m) is the free-surface height relative to the datum g (m/s²) is gravity, v_e (m²/s) the diffusion coefficient or eddy viscosity, and F_x, F_y are force sources/sinks in their respective directions (Coriolis, wind, etc.). T is the tracer concentration, v_T is the tracer diffusion, and S_T is a tracer source term.

TELEMAC has 6 base options for the modelling of turbulence, constant viscosity, an Elder model, a $k-\varepsilon$ model, Smagorinsky, mixing length, and Spalart-Allmaras models [208]. A comparison between these turbulence models in their suitability to hydro-environmental modelling of tidal regions – in particular, the wake effect behind small islands was carried out by Guo et al. [209], finding that the $k-\varepsilon$ model was the best performing in terms of comparison to field measurements, this was then paired with the conjugate residual solver for tidal range scheme modelling – and so is used herein, in aid of brevity the other methods are not presented here.

$k-\varepsilon$ turbulence treats the turbulent behaviour as a system of two isotropic components, the turbulent kinetic energy k shown in Equation 3.46, and the rate of turbulent energy dissipation ε (Equation 3.47), where the overbars represent averaging. These are used to determine the eddy-viscosity v_t (m²/s) Equation 3.45, based on the temporal fluctuations in velocity u_i' in the *x* direction and u_j', in the y direction through the vertical water column from Z_f (m) at the bed to Z_s (m) at the surface, as laid out by Hervouet [199].

$$v_t = C_u k^2/\varepsilon \qquad 3.45$$

$$k = \frac{1}{h}\int_{Z_f}^{Z_s} \frac{1}{2}\overline{u_i' u_j'} dZ \qquad 3.46$$

$$\varepsilon = \frac{1}{h}\int_{Z_f}^{Z_s} v \overline{\frac{\partial u_i'}{\partial x_j}\frac{\partial u_i'}{\partial x_j}} dZ \qquad 3.47$$

The k and ε variables can then be developed into transport equations similar to those for the water level and velocity components, giving the linked partial differential forms of the transport equations for k in Equation 3.48 and for ε in Equation 3.49:

$$\frac{\partial k}{\partial t}+u\frac{\partial k}{\partial x}+v\frac{\partial k}{\partial y}=\frac{1}{h}\nabla\left(h\frac{\nu_t}{\sigma_k}\nabla_k\right)+P-\varepsilon+P_{kv} \tag{3.48}$$

$$\frac{\partial \varepsilon}{\partial t}+u\frac{\partial \varepsilon}{\partial x}+v\frac{\partial \varepsilon}{\partial y}=\frac{1}{h}\nabla\left(hv_T\nabla_{\mathrm{T}}h\frac{\nu_t}{\sigma_\varepsilon}\nabla_\varepsilon\right)+\frac{\varepsilon}{k}\left(c_{1\varepsilon}P-c_{2\varepsilon}\varepsilon\right)+P_{\varepsilon v} \tag{3.49}$$

Where P denotes the production of turbulent energy given in Equation 3.50, and shear forces in the vertical for k and ε are P_{kv} and $P_{\varepsilon v}$ respectively based on the shear velocity u_* (m/s) from the velocity components. C_f is a dimensionless friction coefficient dependent on the chosen friction law. The remaining coefficients have been historically determined based on experimental data, and values used within TELEMAC are taken from Hervouet [199].

$$P=\nu_t\left(\frac{\partial u_i}{\partial x_j}+\frac{\partial u_j}{\partial x_i}\right)\frac{\partial u_i}{\partial x_j} \tag{3.50}$$

$$P_{kv}=C_k\frac{u_*^3}{h},P_{\varepsilon v}=C_\varepsilon\frac{u_*^4}{h^2},u_*=\sqrt{\frac{C_f}{2}\left(u^2+v^2\right)}$$

$$C_k=\frac{1}{\sqrt{C_f}},C_\varepsilon=3.6\frac{C_{2\varepsilon}\sqrt{C_\mu}}{C_f^{3/4}},C_\mu=0.09,C_{2\varepsilon}=1.92$$

3.4.2 Boundary Conditions

The nature of a physical boundary determines how it should be treated numerically, two fundamental boundary types are used in TELEMAC, those being solid – and liquid boundaries. In the case of a coastal model, the physical elements that should be treated as solid boundaries are the coastline and islands within the domain, whereas the ocean limit boundary of the model is a liquid bound.

Solid boundaries are by their nature impermeable and develop friction on the fluid flow around them – at a level in keeping with the assigned roughness of the boundary, and the turbulence law in use. The general method for determination of the friction effect is given by Hervouet [199] in the implicit form $\nu_t\frac{\partial u_t}{\partial n}=\alpha u_t$ where u_t is the velocity component that is tangential to the boundary at the point. To adequately develop the friction effect from the solid boundary on the fluid domain in the numerical scheme, a stronger effect is typically required. TELEMAC applies this in the form $\nu_t\frac{\partial u_t}{\partial n}=\alpha u$ and $\nu_t\frac{\partial v_t}{\partial n}=\alpha v$, this applies an artificial condition on the surface-normal component v_t. However, this is cancelled by the impermeability across the boundary ($v_t = 0$). In no-slip cases, u_t is also 0 at the boundary, and in either case limit or control of the free surface is enacted.

Fluid boundaries contain a significantly higher degree of nuance, their presence being fundamental to the assumption that a fluid domain exists beyond the model itself – whose nature is not numerically calculated but can influence the domain. Through these boundaries, flow can enter or exit the domain, and along a given boundary the direction and magnitude can vary both in time and space, prescribing conditions that propagate into the domain and develop the desired internal regime. There are several options for the prescription of flow conditions at a fluid boundary, depending on the formulation of the problem at hand, the velocities and water depth can be free or imposed (giving four options – free/free, imposed/imposed, free/imposed and imposed/free for velocity/depth respectively). The imposition of tracer values at a boundary is also possible through the same fundamentals.

In the modelling of a tidal range energy scheme, the tidal characteristics of the region modelled are the primary driver of the system. The inclusion of tidal boundaries in TELEMAC in this research was achieved through access to the global tidal databases of the TPXO project [43]. The TPXO condition is applied to a fluid boundary, defined as imposed velocity, and imposed water depths. This system was formerly a modification library that was added to the main TELEMAC version around the TELEMAC v6 release. This boundary system includes options to calibrate the incident tides as described in Section 5.3.2.

3.4.3 Tidal Range Scheme Module

To represent a tidal range scheme in TELEMAC, two primary options have been developed. Rtimi et al. [104, 105, 126] represented the Rance Tidal Barrage as two weir structures – one each for the sluices and turbines, each with their flow relationships modified to fit the desired structure – and variable in time to reflect the changing of operational modes. The alternate approach is to modify the culvert flow module (BUSE.f) initially developed by Smolders et al. [171], this method has the advantage of applying the flow and momentum transfer between nodes of the model at a customisable rate, whilst also providing the skeleton of the data input mechanism.

3.4.3.1 Timeline

The open-source nature of TELEMAC and the collective goal for it to be a tool with as much utility to the modelling of free-surface flows as possible. Users can make modifications to the code in local deployments – and with appropriate testing and validation, have these pulled into the trunk model for others to benefit from.

Original Culvert Treatment: BUSE.f

The BUSE.f module was initially constructed to represent flow across hydraulic structures in TELEMAC both 2D and 3D by C. Coulet, with developments to correct bugs, apply parallelism and other changes by a number of contributors (per the file header). A significant step was made by Smolders et al. [171] with an update to the existing model for culverts in TELEMAC-2D however this update included a variety of discharge configurations. A culvert is defined as a linked source/sink between two points, at which the discharges have opposite signs. The information about the culverts is passed to the TELEMAC system through a file containing descriptive information regarding the culvert such as area and discharge coefficients (a full listing of these parameters is given in Table 3.4). The module then calculates the flow through the culvert based on the categorisations of culvert flow described by Bodhaine [210], driven by the head difference between the nodes. This was used to simulate the ability of an engineered flood defence system to attenuate the flow volume due to a storm surge in the Scheldt estuary [202], and validated against laboratory models for a smaller section of the same system [211].

Guo: BUSE.f TRS Variants

Guo [172] used the ability of the BUSE.f module to apply a source/sink across two nodes, and overloaded the culvert flow procedures to apply the operation of a tidal range scheme to the culverts. Allowing the operation of a tidal range scheme by decomposing the regional mesh to separate the impoundment and the tide. Typically, a single tidal range scheme is represented as existing over multiple individual culverts to account for the spatial spread of a tidal range scheme compared to the mesh spacing required.

This adaptation to the module added the data required to classify the node types, and operate the tidal range scheme on a fixed or flexible operational schedule, critically – Guo et al. [140] investigated the effect of momentum transfer across the culverts, and included the numerical approach to doing so, as this has been found to have a significant affect on the hydrodynamic profile of the schemes [129]. This module however required user modification of the FORTRAN files to determine the operational type – be it fixed/flexible, two/one-way, and whether pumping was included. Further to this, the majority of the data regarding the nodes was passed through an external data file and mapped over the existing culvert data read by the BUSE module, negating the operation of the original BUSE functionality once included.

3.4.3.2 Current version: T2D-TRS.f

For this work, the BUSE module was expanded, and a new module T2D-TRS was added to support the operation of a tidal range scheme in the model. This was done with the long-term motivation of making the model more accessible to other users, and in a manner that would allow easy modification in the long term. Therefore, the key aims of the restructuring and expansion were as follows:

- Minimum user interaction with the code backend itself.
- Maximum flexibility in terms of operation and model construction.
- Easy to build inputs and comprehensible outputs.
- Full parallelism, maximising performance, and stability where possible.
- Expanded functions in combination with base BUSE features.
- Stability and robustness of the numerical modelling procedure for tidal range schemes.

The code for the tidal range scheme model is available for use and modification under an MIT open license on GitHub[5].

Structure

The 'user FORTRAN' for running a tidal range scheme with this system comprises three files, modified versions of the BUSE and LECBUS modules, and the new T2D-TRS module. The key variable denoting the inclusion of a tidal range scheme (or multiple) in a simulation, is in the flow control type variable CLPBUS, which previously had values of 0-3 denoting the possible directions of flow through the culvert. Values of 4-6 have been added denoting different types of tidal range scheme node pairings. This is read from the culvert data file specified in the TELEMAC steering file, and a trigger to load and consider tidal range operation is called if a culvert with a value indicating tidal range is present, a list of the variables in the culvert data, their base and new functions are given in Table 3.4.

---

[5] https://github.com/NHanousek/T2D-TRS

Table 3.4: Culvert file data prior use and tidal range scheme variables.

Name	Previous Use	New Use
I1	First culvert point	Internal culvert point
I2	Second culvert point	External culvert point
CE1	Head loss coeff at p1 as inlet	Ebb head loss coefficient generate/sluice
CE2	Head loss coeff at p2 as inlet	Flood head loss coefficient generate/sluice
CS1	Head loss coeff at p1 as outlet	Ebb head loss coefficient pumping
CS2	Head loss coeff at p2 as outlet	Flood head loss coefficient pumping
LRG	Width of the culvert	Turbine diameter, sluice width (if auto size)
HAUT1/2	Height of construction at p1/p2	Minimum water level for safe operation inside/outside
CLP	Flow control type (0 = both directions, 1 = from 1 to 2, 2 = from 2 to 1, 3 = none)	Added: Culvert types for TRS (4 = Control points, 5 = Turbine, 6 = Sluice)
LBUS	Linear head loss in culvert	Turbine Cd when operating as sluice
Z1/2	Level of inlet at p1/p2	Turbine draft tube area at node, or sluice area at node (0.0 = Auto)
CV	Loss coeff due to valve	Weighting of water level contribution to control
C56	Constant to determine flow type	Parallel sluicing setting (0 = False, 1 = True)
CV5	Correction for type 5 flow	Turbine type (1 = Turbine + Pump, 2 = Turbine only, 3 = Pump only)
C5	Correction for type 5 flow	Number of turbines or pumps at nodes
CT	Loss coefficient for trash screen	Tidal range scheme this culvert belongs to
FRIC	Manning Strickler coeff	Unused
LENGTH	Length of culvert	Unused
CIRC	Shape of culvert (1 = circle, 0 = rectangle)	Shape of sluice gate as before
D1/2	Angle of pipe-bottom at p1/p2	Unchanged
A1/2	Angle of pipe to x-axis at p1/p2	Unchanged
AA	Auto angles (1 = auto, 2 = user)	Added: 3 = Mean of group

The T2D-TRS module declares all the data that defines the operation of a tidal range scheme, such as the ramp time, whether or not the scheme is flexible or pumped, the water levels inside and out etc. It also contains a set of functions and subroutines used to drive the operation of the tidal range scheme, such as to determine the flow and power from the loaded hill-charts, load and write data, and identify the next operational mode of a given scheme. These are then all called at the appropriate time from the BUSE module.

The BUSE module is a modified version of that of Guo [172], fundamentally focussed on the momentum and liquid transfer across the nodes. Here the original flow type separation approach of Smolders et al. [171] is expanded to include the tidal range scheme models using the variables from the culvert data file.

As the culvert datafile includes the full node list, it inherently contains a list of all the tidal range schemes or other such structures present in the model, with the 'tidal range scheme number' of a culvert being stored in the CTRASH variable. Thus, if a tidal range scheme is found to be present on the loading of the culvert data, the LECBUS module calls the subroutines to load tidal range scheme data and initialise all the required arrays – from the T2D-TRS module.

Operation

In addition to the code-structure updates to the model, several operational expansions were included to better resolve some of the common issues encountered in tidal range scheme representations. These typically are stability issues that stem from the flows through the culverts being inconsistent with the hydrodynamics around the area, and unsteady conditions within and around the scheme due to the initial conditions.

The initial phase of operation, the warmup, is key to developing a stable set of conditions within the model as quickly as feasible. To do this, all the sluice and turbine culverts are assumed to be operating using the orifice equation (Equation 3.35) based on the cross-sectional area, with a specified discharge coefficient to magnify or reduce the flow, and with a ramp function (Equation 3.40) applied taking t_{phase} as the time to the end of the warmup. This, combined with a predetermined warmup duration paired with a suitable initial mode of operation, effectively prepares the scheme for operation. A typical example of a warmup period using this method is shown in Figure 3.7, with each turbine bank trace plotted separately – one can see the variation across the scheme due to the varied water level at the start of operation and how this oscillation propagates in a seicheing manner. The large flows at the final half-hour of warmup are caused by this variation – wherein the end of warmup is imperfectly matched to the external and internal levels balancing, resulting in varied head differences and thus flows across the scheme. Nonetheless, the aim of achieving a suitable internal water level at the appropriate time without undue numerical instability is realised through this approach.

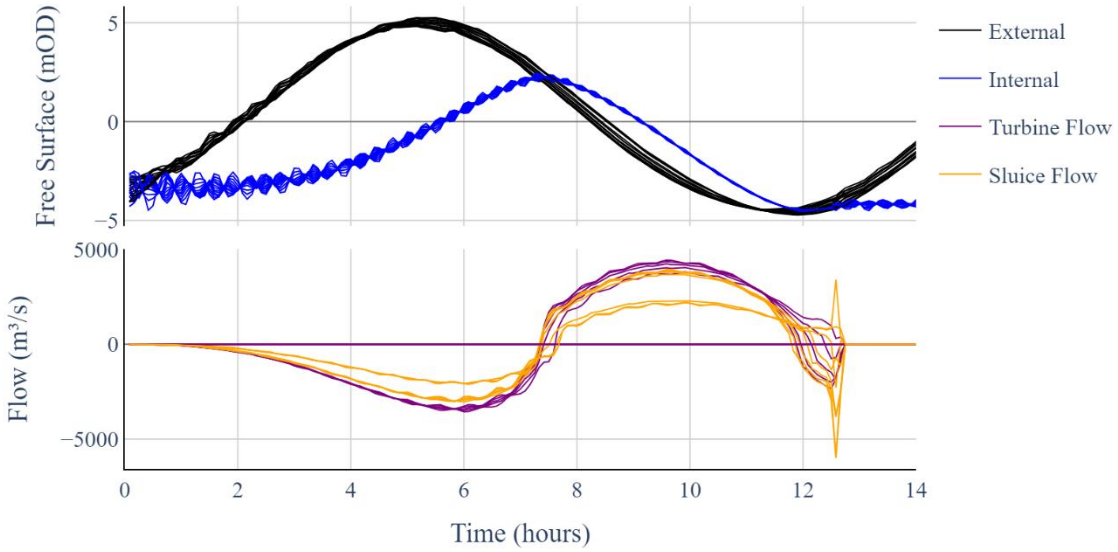

Figure 3.7: Initial warmup period of T2D-TRS based model with multiple turbine/sluice banks.

Guo [172] found that the representation of a tidal range scheme is stabilised by using control points to determine the flow across the scheme, as the water elevations at the nodes being treated can be unduly influenced by the flow passing through them. This principle was expanded in the current model to use both control nodes and the local nodes themselves, with a weighting applied to the nodal elevations to build a weighted mean water level (where the dimensionless weighting at a given node pair has a value CV_i), shown in Equation 3.51 for the nodes related to a given turbine bank. These weightings are applied to the nodes by the user via the CV value in the culvert file.

$$\bar{\eta} = \frac{\sum \eta_i CV_i}{\sum CV_i} \tag{3.51}$$

Physics

For a tidal range scheme model to be represented accurately the transfer of fluid momentum across the sluices and turbines must be accurately accounted for, and the location at which the exit velocity of the culvert is taken can influence the jet effect seen (both in 2D [129], and in 3D [149]). Sinks and sources of momentum in the TELEMAC system are described by Hervouet [199] as in Equation 3.52 and 3.53. Where u_{sce} (m/s) and v_{sce} (m/s) are the velocity components in x and y respectively due to the source velocity Sce (m/s).

$$F_x^q = \frac{1}{h}(u_{sce} - u) \cdot Sce \qquad 3.52$$

$$F_y^q = \frac{1}{h}(v_{sce} - v) \cdot Sce \qquad 3.53$$

If this source is the flow through a tidal range scheme culvert $Sce = TRS$, where the flow velocity for a given node pair is the culvert flow rate Q_i (m³/s) which can be either a sluice or turbine type exit node, TRS is calculated as Q_i/A_i. For best results in momentum conservation, the area taken at the end of the turbine diffuser is used – to account for energy losses in the turbine diffuser itself as found through 3D numerical modelling of the local hydrodynamics by Čož et al. [149] as shown in Equations 3.54 and 3.55.

$$F_x^q = \frac{1}{h}(u_{TRS} - u) \cdot \frac{Q_i}{A_i} \qquad 3.54$$

$$F_y^q = \frac{1}{h}(v_{TRS} - v) \cdot \frac{Q_i}{A_i} \qquad 3.55$$

Input/Output

The file input/output of the tidal range scheme module was re-configured to simplify the user experience and enable better model uptake. The data defining the governing principals of a given tidal range scheme bank of turbines or sluices is included in a ‘TRS’ file, a truncated version of which is shown in Figure 3.8 – and the information describing the physical and spatial characteristics in the culvert data file as tabulated in Table 3.4, a full example can be found in Appendix C.2.

The TRS files use a case-agnostic keyword–variable pair text format, with the capability for delimiter signs ":" and "=", or " " (space). Keywords are case-agnostic and can be used to declare the start of tabulated data such as hill charts and flexible operation data. Due to the nature of the FORTRAN backend – array data must be allocated with their appropriate length before loading, necessitating that the N_ and LEN_ variables be given ahead of their respective arrays.

```
RAMPTIME            0.25
PREV_SWITCH         0.0
MAX_GEN             48
MAX_HOLD            48
MAX_SLUICE          48
MAX_PUMP            48
IS2WAY              T
ISFLEXIBLE          TRUE
ISPUMPING           T
MODE_FIRST          4
N_HILLS_G           1
N_HILLS_P           1
LEN_HILLS_G         16
LEN_HILLS_P         16
N_FLEX              2
ORIG_DIAM_T         9
WARMUP              0.5
PUMPTOLEVEL         F
MODE                0
```

Figure 3.8: Sample TRS input file for a single bank of turbines.

The TELEMAC system prints information about the solver and numerical progress of the model at a user-determined rate, useful to modellers monitoring the progress of ongoing simulations. A printout of the tidal range scheme at that time is added to this as shown in Figure 3.9. This time interval is also used to print the operational data for each turbine bank within the model to a .csv file for expedited data analysis. The flow rate through the nodes is also stored in the private data array of the Selafin output file, which can be saved by the user if the relevant keywords are used in the steering file.

```
+++++++++++++++++++++++++++++++++++++++++++++++++++++++++++++++++++++++++++
         TIME(HRS):    96.750         TRS:         1
       HEADDIFF(M):     5.289     MODE(-):         2
        WL(mD) OUT:    -4.100          IN:     1.189
        PHASE(HRS):     2.038        RAMP:     1.000
       Q(m3/s)TURB: 11041.367      SLUICE:     0.000
         POWER(MW):   436.055    PTARG(-):     2.000
       H START (M):     4.900       H END:     2.500
+++++++++++++++++++++++++++++++++++++++++++++++++++++++++++++++++++++++++++
```

Figure 3.9: Example of console output during operation.

3.4.3.3 Scope for broader application

There are very few tidal range schemes in the world, and the timescale for constructing another is likely on the scale of decades – so one may rightfully question the utility of a module designed to represent these devices. There are however a variety of engineering scenarios that could be modelled through the expansion of the culvert modelling method to allow temporal control through usage of the flexible control system, custom head-flow relationships using the manual hill-chart reader, and automatic behaviour changes. Some simple cases of applications of this system to alternative engineering problems are described below.

Assessing the hydrodynamics in and around a dam over the course of an extreme scenario, such as a large volume of flow being incident from the upstream inlet – wherein the connection between the reservoir and the downstream river are governed by the TRS module. The hydrodynamics of coastal reservoirs, accounting for outlets to the water system, and natural flows around/into the impoundment. For dams or flood defences, including breaching conditions, the TRS controls could be used to expand on the previous studies using the BUSE.f module by Smolders et al. [202, 211].

3.5 Summary

Three methods for the simulation of marine renewable energy devices were presented, with their relative strengths weighed. These three methods are governed by continuity, with the Navier-Stokes equations being the basis for two of the three, and continuity alone for the 0D tidal range scheme method. These models were selected for various aspects of study in the assessment of marine renewables, with varying levels of track record in the field. In all cases assumptions are applied to reduce the dimensionality of complex engineering phenomena, to improve the ease of use and speed of calculation. Each of the models used is available under an open-source license, improving the availability of the methods to a greater range of researchers.

The SPH method is presented in its procedure of decomposing a domain into a set of particles with individual properties. The force interactions, and motions of the particles are determined by the Navier-Stokes equations – with a strength related to their relative positions as specified by a kernel function, truncated from the theoretically infinite region to an area of compact support. The DualSPHysics software was chosen for use as an SPH system due to its open-source nature, and inclusion of the solid body-solver CHRONO. This combination allows the construction of a 2D system wherein the physical components defining a vertical axis turbine can be modelled as free-moving bodies, hinged about the appropriate point(s). From this, the motion of a vertical axis turbine in-flow can be studied without the requirement for a predetermined motion pattern, a key feature in many such studies. The SPH method is also well documented as being suited to GPU-based acceleration, available in DualSPHysics through the Nvidia CUDA programming language.

0D modelling has been used in the study of tidal range schemes in a variety of forms, the model used here is presented in terms of the numerical backend, the operational control systems, and the mechanisms for implementing flexible operation. The code structure itself is laid out, guiding a prospective user through the components – enabling a clear understanding of the processes within the model. Examples of the input structure used are also provided. A summary of how the model can be wrapped and deployed in a mass form, as part of a multi-model study (as could be done for a sensitivity analysis or design assessment) is also provided. This model was used to study the way multiple operational choices impact operation in conjunction, and in the understanding of previously un-tested tidal range schemes.

The 2D finite element Shallow-Water-Equations solver TELEMAC-2D, a component of the openTELEMAC suite is described, along with the governing equations and turbulence modelling method. The bespoke module by which a tidal range scheme can be represented within a large hydro-environmental model is laid out in detail, and the motivation behind the development of the module is presented. The form and function of the model are then shown, from the elements controlling flows and momentum transfer within the model, to the code structure and input/output mechanisms. A brief note on potential further applications of the tools within the model to cases beyond tidal range energy is also provided.

4 Using Smoothed Particle Hydrodynamics to model a Vertical Axis Turbine

4.1 Introduction

Hydrokinetic energy can be found arising from various sources around the world. From rivers and streams transporting rainfall and snowmelt to the sea, to the tidal motion of the oceans themselves. This resource can be transformative when tapped into correctly, with reasonable degrees of predictability and reliability benefitting from the energy entrained within water. Hydrokinetic turbines are fundamentally classified by two parameters, axial or crossflow orientation, and being driven by one of two mechanics – drag, or lift. Significant investment and study have been carried out into the development of large axial flow turbines – as these have the potential to reach the highest power ratings when installed at suitable sites.

4.2 Vertical axis turbine – CarBine

There are, however, many sites where conditions are not suited to large singular devices, but where a small – low head and low power device may be sufficient. To this end, a drag-based crossflow turbine was conceptualised and developed at Cardiff University (namely CarBine). This uses the principals of a savonius turbine (Figure 4.1), where the convex shape of the side moving upstream against the flow results in a lower drag than that of the concave driving side thus developing a net rotational moment on the device. This is amplified in the CarBine concept by converting the arms to hinged flaps (in one or multiple points along the length of the arm) that are then pushed open or closed by the pressure differential across them created by the flowing water, the concept of which is shown in Figure 4.2.

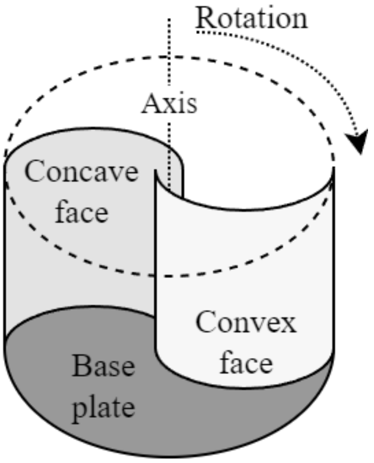

Figure 4.1: Schematic diagram of simple Savonius turbine.

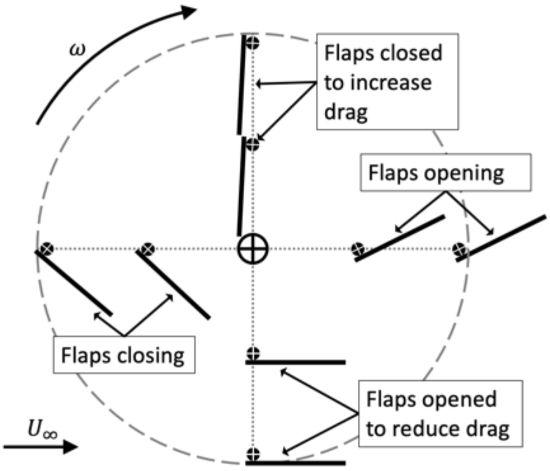

Figure 4.2: Cross-sectional diagram of CarBine key attributes.

The concept was developed, and initial testing carried out at Cardiff University, in the School of Engineering. Initial testing as part of MSc projects by Chrysafis [212] and Challans [213] involved determining fixed torque at intervals of position by measuring the forces required to restrain the turbine at various body angles and flow velocities, with some numerical modelling carried out using the same method models resulting in a $C_P/TSR = 0.25/0.64$ for a prototype with three arms. Further laboratory tests to determine the power output used through the use of a weight attached to a pulley, with the distance and time taken to lift the weight allowing for a power calculation [214]. From these tests a C_P of ~0.22 was achieved, though these tests could not provide detailed performance data, the proof of concept was established.

Ranabhat [215] carried out physical and numerical modelling (using ANSYS CFX) to develop understanding of the turbine motion when using flat and foiled blades in a number of configurations. A prototype rendering of a version for use in deeper water is shown in Figure 4.3. Much of the testing from Chrysafis [212], Challans [213], through to Harries [214], Brammer [216], Ranabhat [215] and this study was done in the NERC recirculating flume in the Cardiff University Hydro-environmental Research Centre, shown in Figure 4.4.

Figure 4.3: Rendering of CarBine.

Further study was then carried out by Harries [214] and Brammer [216] using both physical and numerical models. Physical modelling was used to compare the performance of the CarBine with a Savonius turbine [217], experimenting with the development of a hybrid CarBine-Savonius device, this was ultimately found to have inferior performance to both the Savonius and CarBine from which it was derived (with the constituent effects being detrimental rather than complementary). Both Harries [214] and Brammer [216] used Ansys CFX models to study various properties of the CarBine, with Brammer finding a good representation of the wake characteristics using an unsteady analysis. Harries found that although using two degrees of motion via nested moving reference frames, design variants where the flaps are to overlap in their regions of motion cannot be modelled – and noted that this eliminates the designs found to be most effective in lab testing. The subdomains were controlled by a user-inputted function, controlling when and where the flaps were to open and close – requiring prior physical model tests to develop the relationships.

These studies required application of a prescribed or empirically determined angular velocity, obtained through experimentation to develop the appropriate extracted, since a device converts energy from the flow only when it spins below the free-spin velocity. To calculate output torque from the design a reactive torque would need to be applied to the turbine via its shaft, at a variety of intensities to ascertain the true operational characteristics of the turbine. In this study, this was not possible due to the limitations of available restraints and as such only free-spin mechanics are examined. However, cold start driven solely by the hydrodynamic forces on the turbine was achieved.

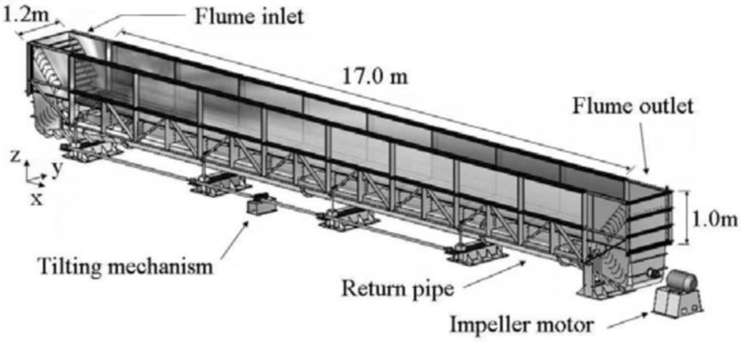

Figure 4.4: Cardiff University NERC flume, 3D perspective adapted from [218].

Physical modelling and field testing are important components in the development of a tidal turbine (or any turbine). However, they can be expensive, time consuming, and scaling assumptions are required where full size prototypes cannot be accommodated in the flume/basin [219]. Numerical models allow the designer to make changes and investigate performance changes across various scenarios without the limitations of scaling or physical lab space. There are many approaches available in the field of Computational Fluid Dynamics (CFD) for the analysis of hydro turbine behaviour. Židonis et al [23] compared a variety of Eulerian (mesh-based) and Lagrangian (mesh-free) methods/software used in the design of a Pelton turbine. Ansys CFX and Ansys Fluent were found to be most commonly used, with high accuracy and precision paired with a high computational cost, and noted that Lagrangian methods can be useful in the earlier design stages of such devices [220].

Large Eddy Simulation with an Immersed Boundary (LES-IB) has been used to predict the performance of vertical axis Darrieus turbine under both laminar and turbulent flow conditions by Ouro and Stoesser [221] wherein the Lagrangian turbine rotates at a prescribed constant rotational velocity (established through testing over a range of velocities) within an Eulerian fluid domain, again requiring a known motion of the body prior to modelling. Allmark et al. [73] demonstrated the process for testing a conventional style horizontal axis tidal turbine using both physical and numerical models, in the numerical study (carried out using Ansys CFX) where the turbine was represented in a Moving Reference Frame (MRF). A method whereby the turbine and adjacent space were modelled in a cylindrical region, that rotated at a prescribed angular velocity, determined from lab study or empirical analysis [222]. This method however required the rotational velocity of the turbine to be known in advance, and the turbine itself to not change shape within the MRF. To accurately represent the CarBine design using traditional methods would require nested MRF's whereby each flap is in a reference frame of its own, within the MRF of the body itself, and this would still require that the individual flaps are able to move into and out of the regions deemed belonging to other flaps. This is visible in Figure 4.2 , where the opening inner flap is in the space occupied by the closing outer flap. This nesting and cross-availability of systems would require a non-trivial model construction likely utilising dynamic remeshing, and as such would be unsuitable for explorative early-stage design modifications. Salehi et al. [223] used a flexible mesh to adjust the guide vanes of a Francis turbine over the process of a turbine shut-down using the open-source CFD solver OpenFOAM. This required a re-building of the mesh at every time-step to move the vanes at a predetermined angular velocity, while the runner maintains a constant rotational speed.

The Hunter turbine (patent No.GB9524439.8), shares some conceptual elements with CarBine [224, 225]. Yang and Lawn [224] ascertained geometric positions for the Hunter turbine at given body angles and used these positions to determine the forces across the blades and as such the turbine as a whole using a 2D Reynolds Averaged Navier Stokes (RANS) CFD model (using the commercial FINE™/Turbo code). Using these positions Hashemi et al. [225] developed equations to describe the flap positions based on the body angle and implemented these into a 2D model using Autodesk CFD where the mesh is deformed to form the predefined motion of the turbine over time.

CarBine design has a key complexity in that the turbine itself is composed of a set of linked but free moving components. The torque produced by the design in any position is not simply a factor of the fluid moving past it, as the positions of the flaps are constantly changing under the influence of the flow. A method to assess the performance of the design without a requirement for prior knowledge of the minutia of operation was deemed necessary, with the classical options each proving to lack some element. Additionally, a desire to mitigate costs both computationally and financially was fundamental to the analysis, as these costs can be seen as barriers to progression. Smoothed Particle Hydrodynamics (SPH), was identified as a methodology that could overcome the challenges faced with the modelling of this device, in a manner not excessively demanding in terms of computational power.

4.3 Model Details

A strength of representing the CarBine within DualSPHysics is the inclusion of the Project Chrono solid body solver suite [169], this allows the components to be included and connected in the same manner as they would be in prototype – with the body attached to the domain via an axle (or hinge) and the flaps attached to the body at their heads with hinges (laid out for the base design in Figure 4.5) with no torsional stiffness or damping applied. By ensuring the flaps are correctly oriented relative to their hinge points at particle generation, the device requires no further definition to start turning once the water begins to flow. The GenCase tool that is used to define the particle field within the domain operates on a cartesian grid system spaced at a spacing as defined by the modeller. This fills areas with particles of the appropriate type on a regular grid, for specific shapes, the 'freedraw' option can be used to provide a better form than the cartesian grid provides, as was used to generate the cylindrical hub component. The regular particle grid and adjusted circular particle positions can be seen in Figure 4.6, note that the circle drawn on the figure is to better delineate the particles for the viewer and not a model feature.

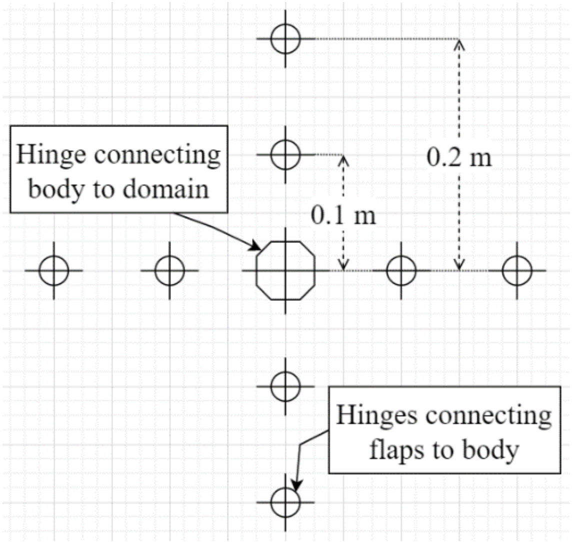

Figure 4.5: Chrono hinge setup for base design of CarBine model.

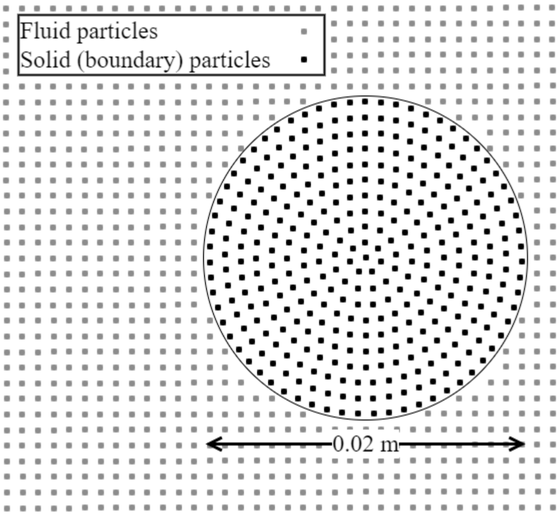

Figure 4.6: Initial particle spacing about central hub at dp = 1.0 mm.

The fluid domain was set up to mimic the conditions in the laboratory flume in which the testing was carried out, the tilting flume in the Cardiff University Hydro-environmental Research Centre (Figure 4.4), a 1.2 m wide, 17 m long flume allowing flow depths of up to 1 m, and with a flow rate capacity of 10-1000 l/s. Thus, a width of 1.2 m maintaining the blockage ratio reported by Ranabhat [215], contributing to flow acceleration around and behind the turbine, with the main axle on the centreline, and a length that was set at 2 m, with the CarBine placed with its central hub 0.5 m from the inflow buffer as laid out in Figure 4.7. The position of the upstream and downstream boundaries was tested as described in Section 4.3.1 below. In prototype, the device uses a pair of flat circular end-plates or radial arms to hold the flaps from above and below, connecting them to the central axle. The mass of these plates would have a further dampening effect on the motion of the turbine, however such components and their effect could be adjusted by changing the density of the central axle particles at an appropriate ratio to specify a given vertical height of turbine, however is excluded in this study.

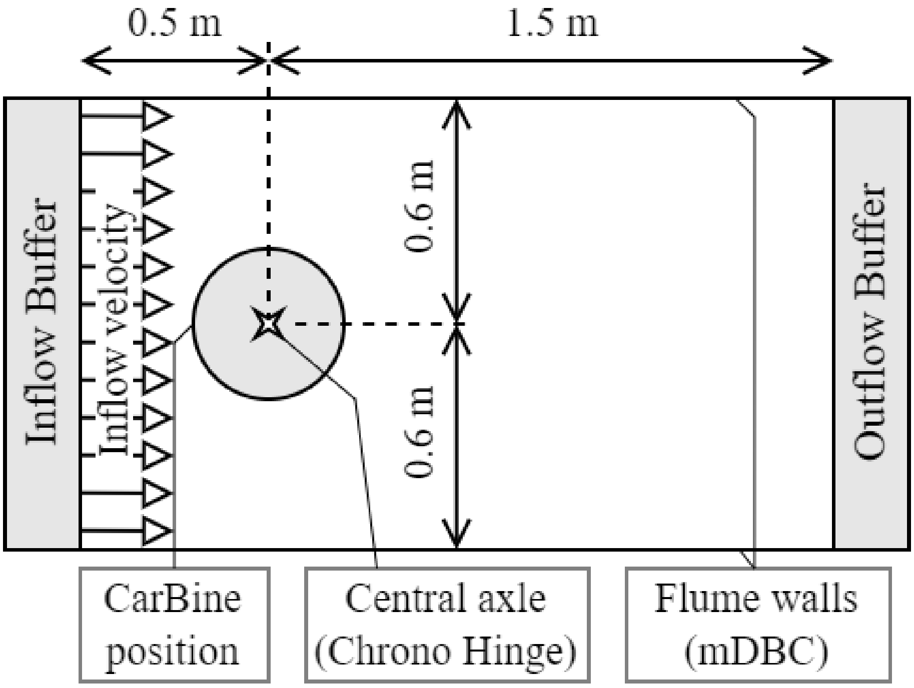

Figure 4.7: Schematic of numerical model layout of CarBine in flume.

The nature of particle-based methods has always yielded challenges in the aspect of boundary conditions, as particles within the domain require particles beyond the domain to resolve the SPH equations. To achieve this, methods utilising false particles or nodes beyond the modelled domain have been developed, and were used here to correctly treat the boundaries of the system. The flow inlet and outlet buffer zones were represented using the boundary method of Tafuni et al. [226]. The upstream end declared as an inflow buffer with a uniform velocity of U_∞, constant over the duration of the test, this was formed of 8 layers of fictitious particles whose properties are used to provide full support to the particles in the domain. The outflow also used 8 fictitious layers of fluid particles to develop an extrapolated pressure boundary – effectively absorbing the motions of the flow. The flume walls were configured using the impermeable Modified Dynamic Boundary Condition (mDBC) boundary described by English et al. [227], this uses ghost nodes mirrored across the boundary to provide compact support to particles within the fluid, with a free-slip condition applied through this mirroring of properties, as significant wall effects were not recorded at the test section, shown in Figure 4.8.

To ascertain the nature of the inlet velocity profile, an acoustic doppler velocimeter (ADV) was used to measure the flow velocity in the flume at a number of positions across the section and through the vertical profile, shown in Figure 4.8 and Figure 4.9. An average free-stream velocity was calculated using the combined profile. The velocity profile, shown in Figure 4.9 was found to be highly logarithmic [215], an average velocity was calculated over the area in which the model turbine is placed. For simplicity, the flume average was used as the input velocity for these tests.

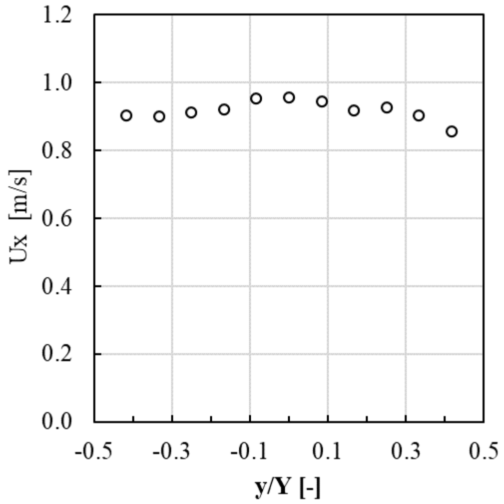

Figure 4.8: Measured flume flow velocity in the x direction across the width of the flume.

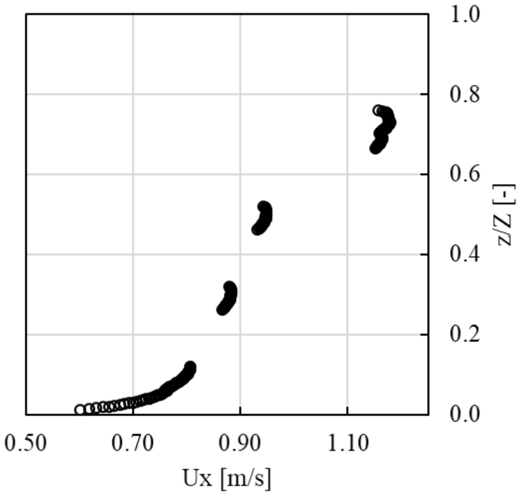

Figure 4.9: Measured flume flow velocity in the vertical (z) direction of the flume.

4.3.1 Numerical Setup

The SPH model was configured with no gravity (0 m/s^2) in any direction to simulate the 2D plan section, with fluid particles having a default density of 1000 kg/m^3. The polytropic constant for water in the state equation was set at 7 (default, used in Equation 3.11), maximum Courant-Freidrichs-Lewy (CFL) number of 0.2 [180], and speed of sound fixed at 15 m/s, limiting the compressibility of the fluid. The kernel length H and particle spacing dp were determined through a convergence study presented in Section 4.3.2, using a quintic Wendland kernel function [228]. The Symplectic-Verlet time stepping algorithm was used due to its numerical stability, at the cost of computational expense, with 40 (default) Verlet steps used to apply Euler time-stepping. The Fourtakas et al. Density Diffusion Term was used with (with δ_Φ set to the default value of 0.1) [174], though this becomes the Molteni and Colagrossi [175] term since the gravity is set to 0 in all directions. A summary of computational performance is given in Table 4.1.

The formation of voids was found to be highly problematic in the model, due to the meeting and separation of the floating components that make up the turbine itself. To mitigate this effect, the shifting algorithm of Lind et al. [176] was used with the 'A' shifting coefficient needing to be at the extreme value of -50 (default -2, with values of -20 used in some 2D example/benchmark cases). Smaller shifting magnitudes were tested and showed model instabilities, resulting in the extreme potential magnitude for the shifting rate. The method assumes that the model is a plan section of a deep flow, and so no free surface was expected to be developed, thus the free-surface detection parameter was set to 0, eliminating the free-surface check from the shifting algorithm.

Stabilising the models, whilst using an appropriate turbulence approach was one of the more challenging aspects of the study. The Laminar+SPS system of turbulence modelling is recommended for developed modelling with DualSPHysics, as the artificial viscosity does not inherently provide a turbulence model. Stability of the model with the Laminar+SPS method however was highly fragile, the meeting and separation of the floating bodies was liable to produce small voids, that when they propagated to either of the inlet or outlet boundary resulted in mass breakdown of the model, an example of this process beginning for a Laminar+SPS configured model is shown in Figure 4.10, with voids within the model domain highlighted in red. The tearing of the fluid domain from the corners of the inlet boundary can be seen in this figure. These voids developed and then shed by the flaps as indicated.

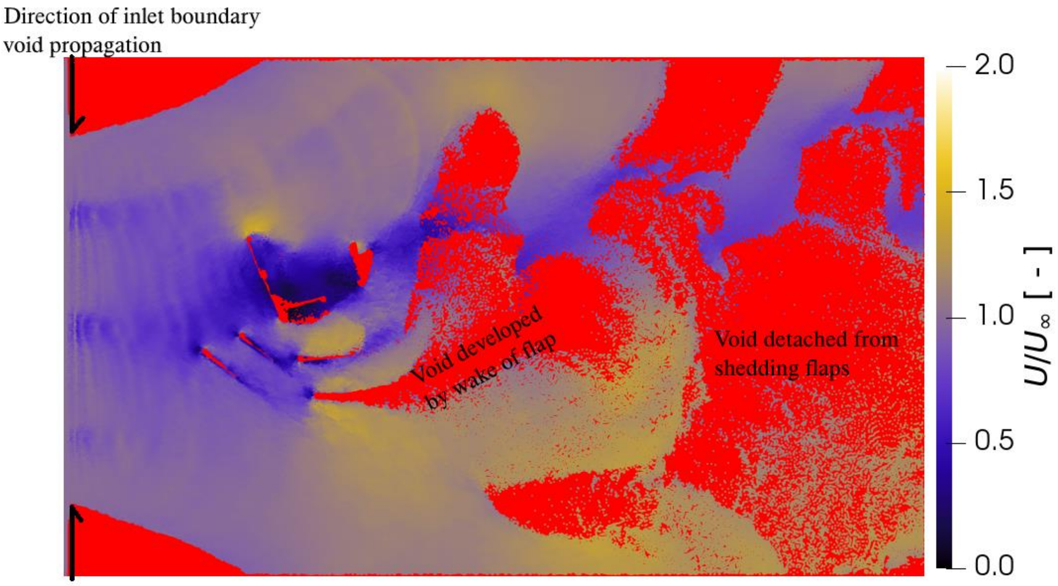

Figure 4.10: Development of domain rupture caused by voids and inlet boundary when using Laminar+SPS, and U∞ = 0.9 m/s.

Achieving direct numerical simulation of turbulence has long been a challenge in computational fluid dynamics, primarily due to the significant cost. It has been carried out with SPH both in the case of imposed turbulent conditions being allowed to dissipate [187, 188] in 2D simulations, and to the study of fluid-mixing devices in 2D representations where an encouraging agreement to prior studies was found [189, 229]. To achieve this, a high-resolution initial particle spacing was used in the studies, varying from 0.375 to 6.667 mm in Robinson et al. [229] and Robinson and Monaghan [188], respectively. Due to the challenge of stability, and the slender nature of some of the turbine components, a high resolution was used with the Artificial Viscosity formulation. The dimensionless α tuning parameter has been found to converge varyingly depending on the problem in question [230]. In this study, a value of $1e^{-3}$-$1e^{-6}$ was found to be stable, with $1e^{-5}$ producing the most stable operation.

A test duration of 10 seconds was deemed suitable for the achievement of steady-transience, with results saved every 0.02 seconds. A full example DualSPHysics xml file is available in Appendix A. The inlet boundary at U∞ = 0.9 m/s adds particles at a consistent rate of 1097100 particles per second, and the outlet boundary removes particles at a rate depending on the incident particle field. The balance of the inlet and outlet rates is seen in the total number of particles np (-) in the simulation over the test period. Plotted in absolute terms and with a secondary axis in Figure 4.11 showing values normalised with respect to the initial number of particles np_0. From an initial 2.51 million particles, np settles to between 2.35 and 2.365 million particles (0.93-0.94 np_0) after around 2.6 seconds. Small peaks in np can be seen for the rest of the duration, formed when turbulent vortices collect particles and then exit the domain.

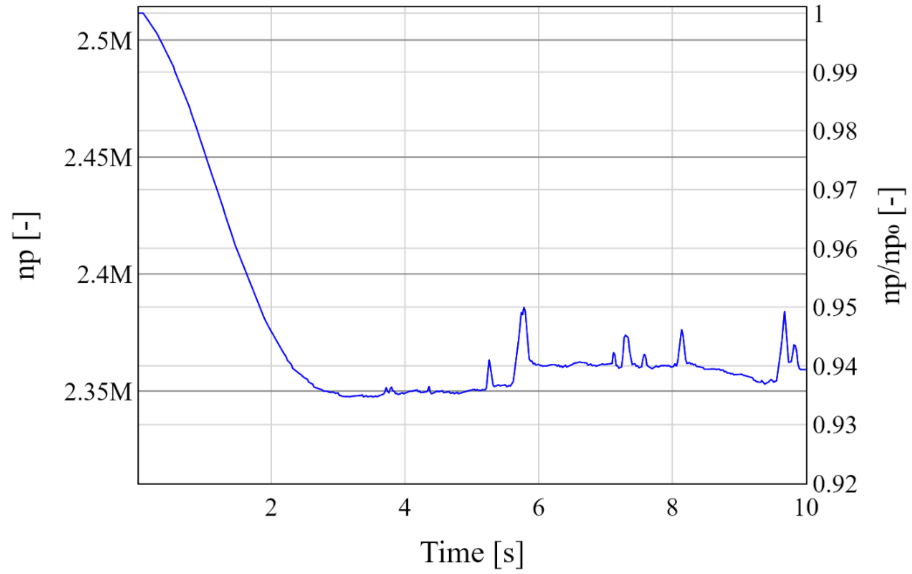

Figure 4.11: True and normalised number of particles in calibration model, U∞ = 0.9 m/s.

4.3.2 Convergence

A fundamental principle of using SPH to represent this turbine was the lack of prescribing motion to the turbine itself – as such, the motion of the turbine forms a suitable parameter by which to quantify the degree to which the model is able to represent reality in a free-spin scenario. Due to the disparity in sampling rates of angular velocity between the flume and SPH models – the net displacement (or average rate of displacement) beyond a 1 second assumed startup period was used, denoted by ϕ (rad). For a normalised accuracy, the L2 (-) error norm (Equation 4.1) was used as shown below:

$$L2(\phi) = \frac{1}{N}\sqrt{\sum_{i=1}^{N}\frac{(\phi_{Flume} - \phi_{SPH})^2}{\phi_{Flume}^2}} \qquad 4.1$$

Where the measured flume data is denoted ϕ_{Flume} and SPH data as ϕ_{SPH} over N timesteps. Quinlan et al. [231] found that the error in discretising from a continuum fluid domain to a particle field is driven by the inter-particle spacing dp and the ratio of spacing and kernel support dp/h, though error may grow if h is reduced below a critical value – dependant on the modelled scenario. Therefore, it is best practise to ensure that the model has converged both in terms of dp, and dp/h for the case at hand.

The slenderest aspect of the design is the flap blades, at 2 mm thickness, as such – a maximum spacing of 2 mm was necessary to ensure rendering of the feature. Spacings of 0.5, 1, 1.5 and 2 mm were tested at h/dp values of 1.5, 1.75, 2.0 and 2.25 (as suggested by Quinlan et al. [231]. For a 2D model, halving the inter-particle spacing results in four times the number of particles in the domain – increasing computational load to approximately the same degree. Increasing the h/dp value extends the kernel support (which in reality would be theoretically infinite) increasing the total number of particle interactions, but improving the stability of the calculation at each given particle.

At dp = 0.5 mm, the error was dominated by the smoothing length H, with worse accuracy than the coarser models – and so this spacing was excluded from further assessment. Figure 4.12 shows the rates of convergence for the h/dp ratio over the three remaining particle spacings, with power law least square equations fitted for each value. Here it can be seen that the L2 error norm based on the particle spacing is converging at a rate approaching third order, with the rate of convergence decreasing along with h/dp. Having reached a local solution at h/dp = 1.75, and diverging at h/dp = 1.5. Higher values of h/dp introduced an unexpected issue, due to the slenderness of the flaps – fluid particles were able to interact across the flap blades when using h/dp larger than 2.25 – this feature would likely be mitigated if seeking to model a device with bulkier components.

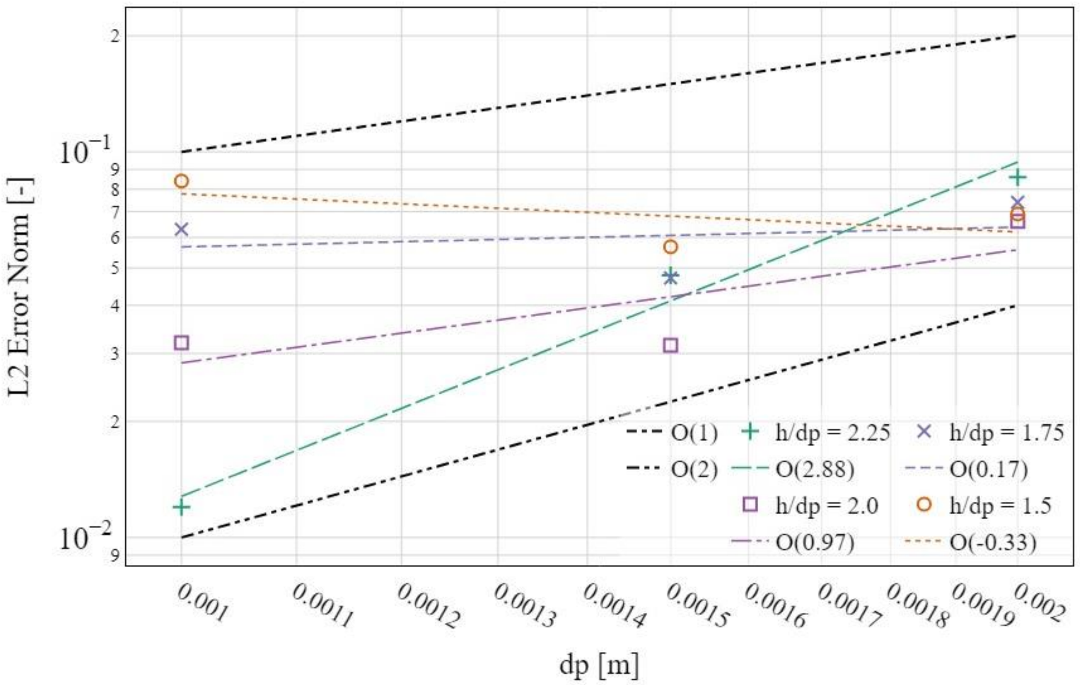

Figure 4.12: Model convergence to dp at $U_\infty$of 0.9 m/s.

Figure 4.13 shows the impact of dp/h (note this is the inverse of h/dp – used for plotting convention) on each of the spacings, the 1 mm spacing showing the highest order of convergence, in excess of 2nd order. Thus, a spacing of 1 mm, with a h/dp of 2.25 was used in all the remaining study of the turbine.

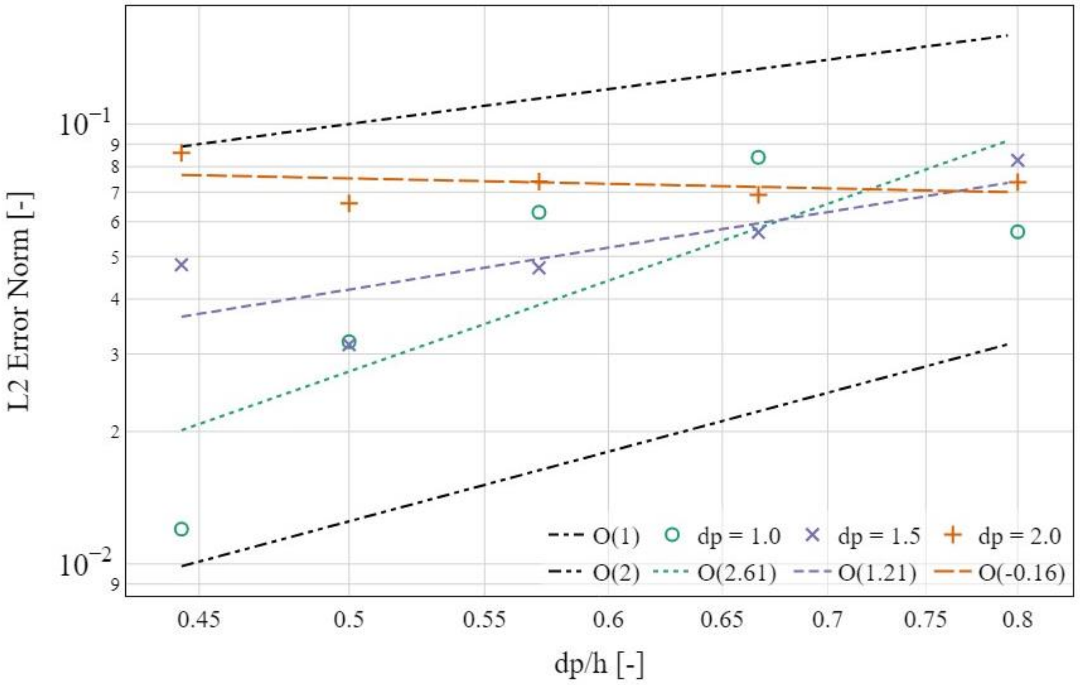

Figure 4.13: Model convergence to h/dp at $U_\infty$of 0.9 m/s.

4.3.3 Boundary Position

Although the turbulent wake effects were not the focus of this study, the interaction of the turbine wake and the downstream boundary were assessed for their potential to impact operation of the turbine during the tests. The aim of the study being to utilise a small domain to reduce computational expense, without the boundary affecting behaviour. A set of tests were therefore run, whereby the position of the boundary was varied from 1.5 – 7 m from the central axle (3.75 – 11.25 diameters). It was found that the position of the downstream boundary had a minimal effect on the displacement of the device (mean L2 error of 0.021). A domain of 7.5 m with the turbine 6.5 m from the inlet was also tested and found to have a marginally higher L2 error norm of 0.044, shown as case (i) in Figure 4.14. In order to reduce the computational cost, the smallest domain (a) was utilised in the remainder of the tests. A rendering of the boundary position tests at the end of the runtime is shown in Figure 4.14, with the angular displacement over time shown in Figure 4.15.

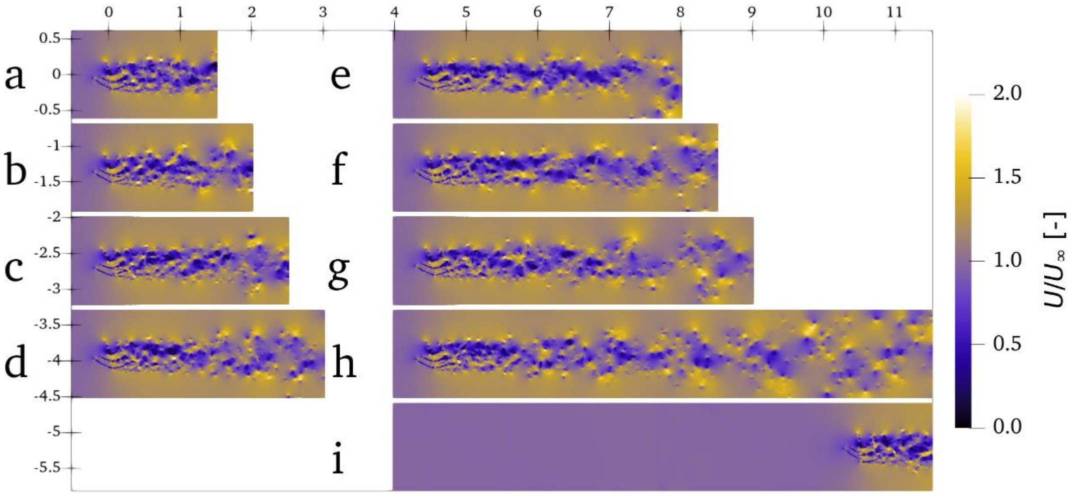

Figure 4.14: Flow velocity profiles at t=10 s using multiple domain lengths scale axes in metres, U_∞ = 0.9 m/s.

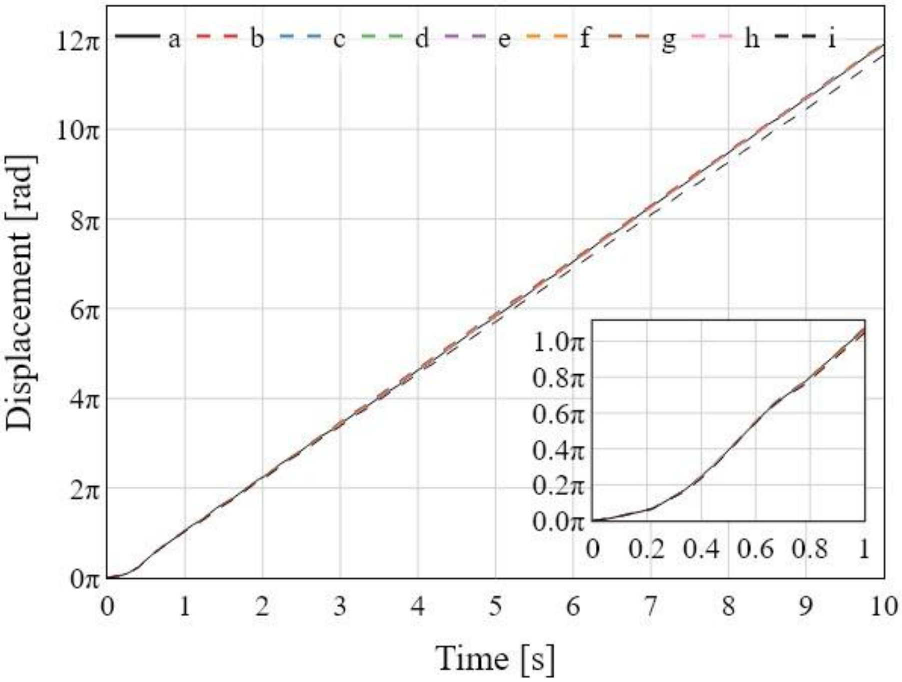

Figure 4.15: Body displacement using multiple domain lengths at U_∞ = 0.9 m/s..

4.3.4 GPU performance

The use of the Graphical Processing Unit (GPU) has been a significant step in the speedup of SPH models, due to the nature of the calculations carried out – GPU operation maps well onto the method. DualSPHysics uses the Nvidia CUDA programming language to carry out GPU based operation for some parts of the operation, and here was run on a variety of cluster mounted GPUs on the Supercomputing Wales High Powered Computer (HPC) 'Hawk' and on a desktop workstation GPU. To document the performance of these GPU's a brief performance test was completed.

The base model, with U_∞ of 0.9 m/s, dp of 1 mm, and h/dp of 2.25 was computed on three platforms to provide a variety of representative performance rates. The first was an Nvidia Quadro P2000 in a desktop workstation, the second and third being GPU enabled nodes on the Supercomputing Wales HPC – Hawk. These are equipped with either Nvidia Tesla P100 (Pascal architecture), or Tesla V100 (Volta architecture) processing units each with 16 GB of memory. This model configuration has on average – a maximum of ~2.5 million particles, and ~193 Tera Particle Interactions (TPIs). The Quadro P2000 desktop completed the simulation with an average of 10102 seconds of runtime per physical second (s/s), the P100 operated at 2870 s/s, and the V100 was the fastest at 1655 s/s. The Tesla V100 was used in the performance analysis carried out in [182] and found to be in excess of 200× faster than a 12 core CPU – highlighting the advantage of carrying out the calculations on a GPU enabled device.

Table 4.1: Computational performance comparison of desktop and HPC Nvidia GPUs.

GPU	System	Run time [s]	Speedup [-]
Quadro P2000	Desktop Workstation	101020	1
Tesla P100	Hawk HPC	28700	3.52 x
Tesla V100	Hawk HPC	16550	6.10 x

4.4 Method

Once a stable base model of the turbine had been composed, the scope of assessment was expanded to a number of aspects. Firstly, a validation of the model at additional flow velocities, also giving insight into the device behaviour in four additional flow conditions. All five conditions were then expanded to four variations on the base design, using the same components and principals, but with differing layout and number of flaps. Finally, a set of resilience tests were run on each of the base and alternative design configurations, removing in each case a single arm and assessing the behaviour in a post-damage scenario.

4.4.1 Design Variants

The Carbine concept in prior studies has been found to show best performance metrics in the base design, however alternate designs have been considered at most stages of the assessment. The alternate design cases with three and five arms (shown in Figure 4.16) – each with two flaps were tested under a variety of flow conditions by Harries [214], referred to as C3 and C5. Configurations using alternative flap lengths, and vertically offset-stacked flaps were also considered. For this study, only flaps within one plane were considered, with the offset arms of the 4-arm alternate being the major deviation to the existing options. The testing of the design variants was carried out in order both to gain an understanding of their potential and showcase the manner in which the SPH model can be easily modified in order to carry out such tests (as compared to the complex meshing procedure required for mesh-based methods).

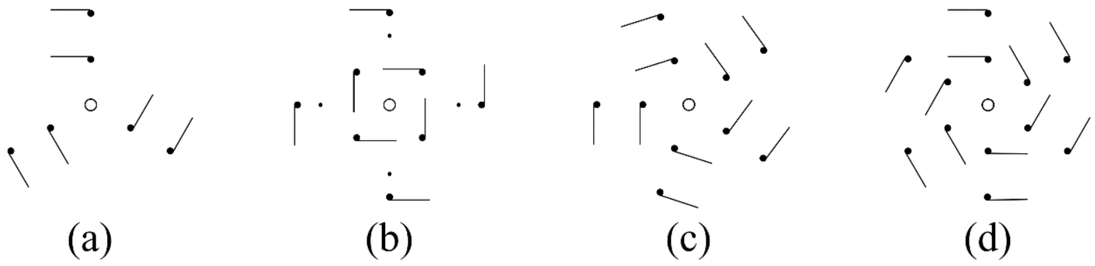

Figure 4.16: Design variants, (a) 3 arm, (b) 4 arm-alternate, (c) 6 arm, (d) 5 arm.

4.4.2 Resilience

The number of connected-moving parts within the CarBine concept is not only a challenge to numerical modelling for assessment but is arguably a design disadvantage. The number of components expected to be under stress as the device rotates, for a large number of cycles, suggests that there are likely to be component failures through the lifespan of the device. The motion of the device post failure is important from two perspectives: to a remote user of a CarBine to provide electricity, the ability to generate – even in a limited capacity could be critical. Further to this, the motion of the device in a damaged state is less consistent motion, and so is challenging to ascertain without a physical model – thus demonstrating the ability to assess this previously untested state using SPH.

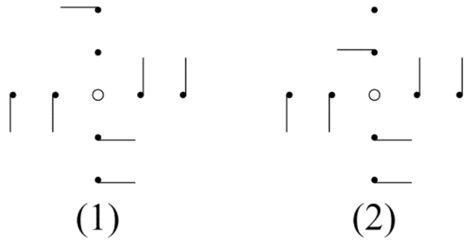

Figure 4.17: Base damage cases, 1 – loss of inner arm, 2 – loss of outer arm.

Resilience to damage was identified as a design motivator for small hydrokinetic devices by Kirke [31], such as impacts on riverine turbines from floating objects such as logs. To test the post-damage behaviour, two cases of damage were determined for each turbine, the loss of an inter flap – termed Case 1, or the loss of an exterior flap - Case 2. These can be seen for the base design in Figure 4.17. A comparison was also drawn between the two cases, allowing for the consideration to designers of which flap is likely to be more impactful if lost (assuming only one flap is damaged). This process was then carried out for the alternate designs – with schematics of the damage cases shown in Figure 4.18 - Figure 4.21. In each case, the missing flap was replaced with a simple cylinder, replicating the bolts attached to the turbine base and top plates that restrain the flaps in prototype.

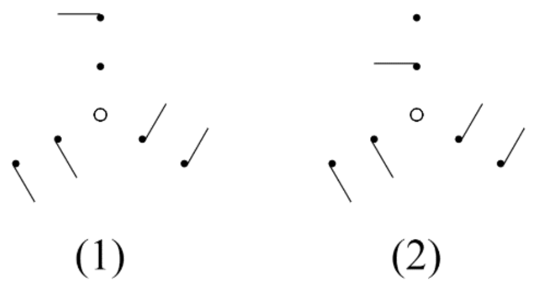
(1) (2)

Figure 4.18: 3 arm damage cases, 1 – loss of inner arm, 2 – loss of outer arm.

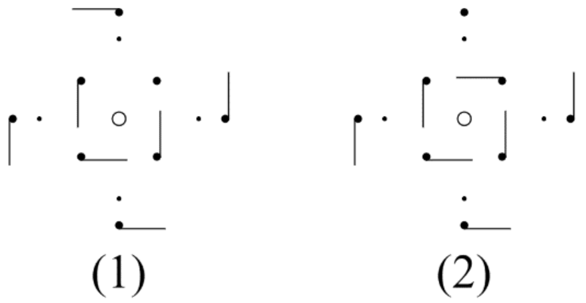
(1) (2)

Figure 4.19: 4 arm alternate damage cases, 1 – loss of inner arm, 2 – loss of outer arm.

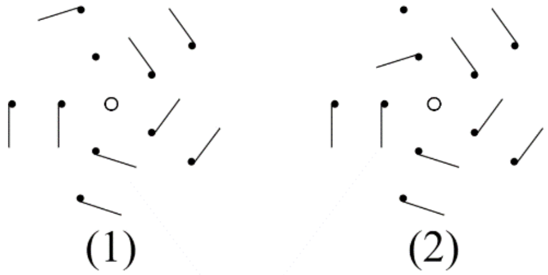
(1) (2)

Figure 4.20: 5 arm damage cases, 1 – loss of inner arm, 2 – loss of outer arm.

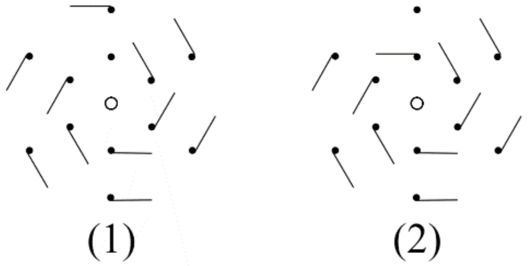
(1) (2)

Figure 4.21: 6 arm damage cases, 1 – loss of inner arm, 2 – loss of outer arm.

4.5 Results and Discussion

To provide an insight into the device behaviour at a temporal resolution that is available to the numerical model over the physical, the base four-arm model was placed in a flume with an incident velocity U_∞ of 0.9 m/s across the flume from an assumed start-up position. The free-wheeling flume model had a mean angular velocity of 3.87 rad/s over the tests, with the SPH model having a mean velocity of 3.825 rad/s excluding a 1 second warmup – this indicated a 1.2% difference in average rotational velocity. This relationship can be seen in Figure 4.22 (with the time averaged flume rotation rate is plotted as cold start data was unavailable). From this timeseries the ability of the SPH model to capture high frequency effects and self start mechanics is demonstrated, with the flume velocity being ascertained from a 1 Hz sampling rate, whereas the SPH model printed results at a 50 Hz rate demonstrating some high frequency periodic behaviour. The peak rotational speed was found within the startup behaviour, a previously unseen element of the turbine operation.

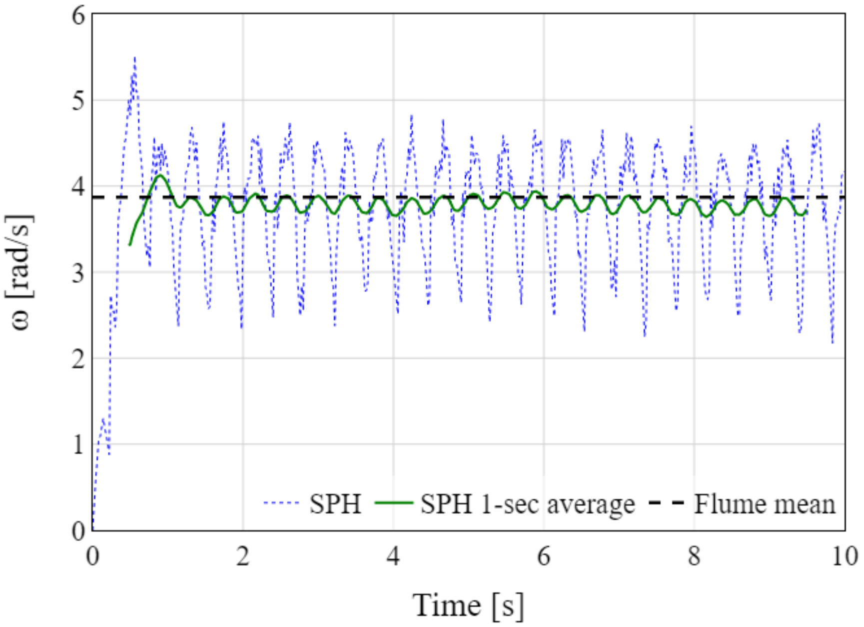

Figure 4.22: Mean flume (measured), 1 second moving average SPH, and detailed SPH model angular velocities over 10 second test.

In assessing the rotational speed of a tidal stream turbine across a variety of free stream velocities the dimensionless tip speed ratio λ is used, which is calculated as follows [217]:

$$\lambda = \frac{r_T \omega_{body}}{U_\infty} \tag{4.2}$$

where λ is the Tip Speed Ratio (TSR), r_T represents turbine radius (here the distance from the turbine centre to the outer hinge pin), ω_{body} is the mean angular rotation of the turbine (extracted from the rotation of the body object), and U_∞ is the free stream velocity.

To ascertain how the speed of the turbine varies as it rotates at a higher frequency, the tip speed ratio was calculated at every timestep and plotted against the body angle for the base condition, shown in Figure 4.23. Turbine motion is clockwise in this case and throughout this study. The start-up motion of the turbine is visible in the lower tip speed ratio point cluster around the 0-radian angle, after which the initial rotation of the turbine is shown by the set of points at higher TSR than the generally consistent in-operation motion. Once under motion, the turbine exhibits four-way symmetry as would be expected from a four-armed device, with a rapid acceleration as the blades fall into position followed by a mild acceleration, and finally a slowing once the turbine passes the optimal point. The rapid acceleration phases shown indicate a portion of the behaviour that could require additional study of the component interactions as this sudden acceleration due to the flaps impacting the body is indicative of a peak force occurring and thus the greatest potential for damage, these are however likely to be significantly damped and TSR reduced by a power take-off mechanism if one were to be attached to the turbine.

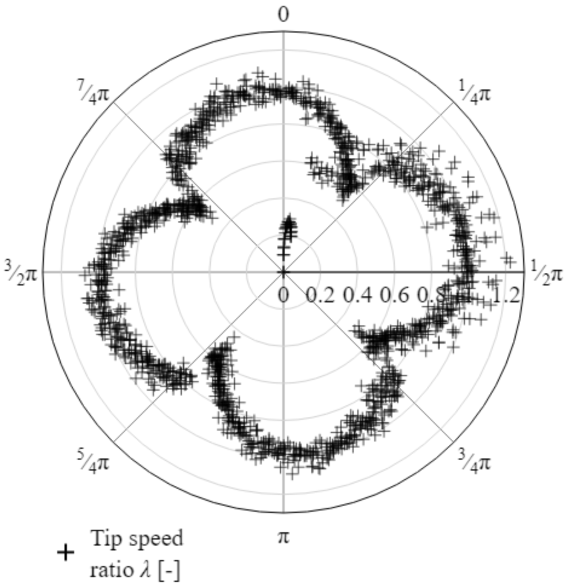

Figure 4.23: Base design free-spinning Tip Speed Ratio against body angle, U_∞ = 0.9 m/s.

Renderings of the particle field at the endpoint of the study (simulation time of 10s) are shown in Figure 4.24 - Figure 4.26. The normalised velocity field (Figure 4.24) shows how the upper side of the device extracts energy from the flow – with the lower velocity wake effect on the upper side of the flume (as viewed from above). The sections of increased velocity between the open flaps further demonstrating the CarBine concept functioning within the model.

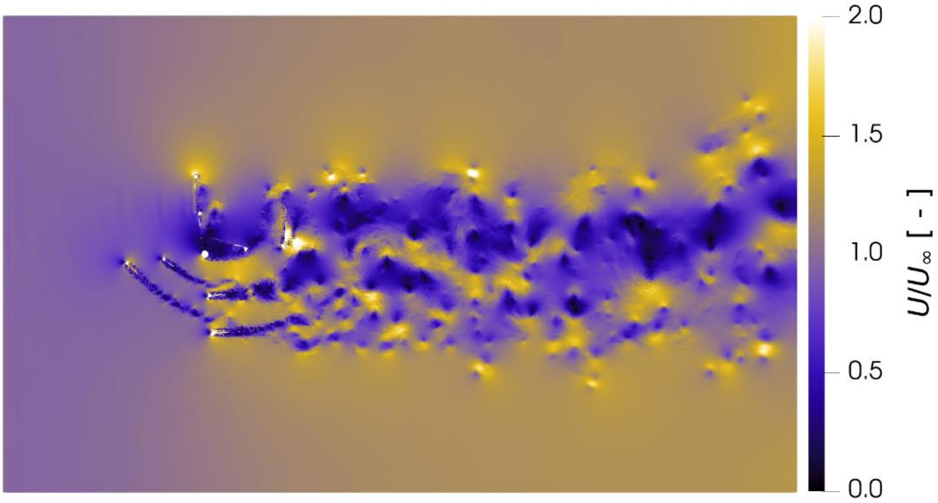

Figure 4.24: Base design, flow field (U_∞ = 0.9 m/s) at t = T.

The pressure field within the fluid, rendered in Figure 4.25 shows the pressure increase upstream of the turbine due to the turbine itself, and the lower pressure downstream of the turbine represent the blockage and energy abstraction effect of the turbine. The pressure differential across the closed blades is the effect driving the turbine to turn.

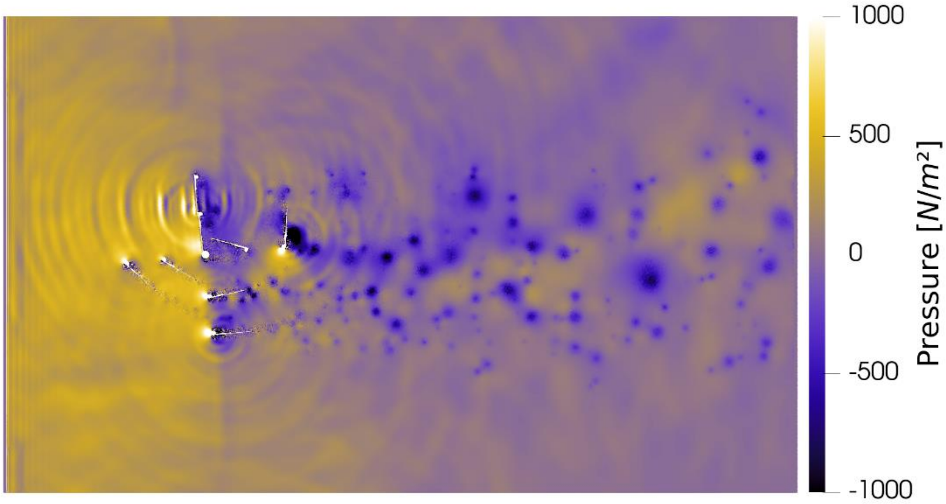

Figure 4.25: Base design, pressure field (U_∞ = 0.9 m/s) at t = T.

Although the nature of the turbine wake was beyond the scope of this study, the vorticity field formed by the turbine is shown in Figure 4.26, demonstrating the numerical simulation of the turbulent effects induced by the turbine. Notably the trailing wakes of the individual flaps on the returning side (below the central axis in these renders), along with the low vorticity channels between the flaps.

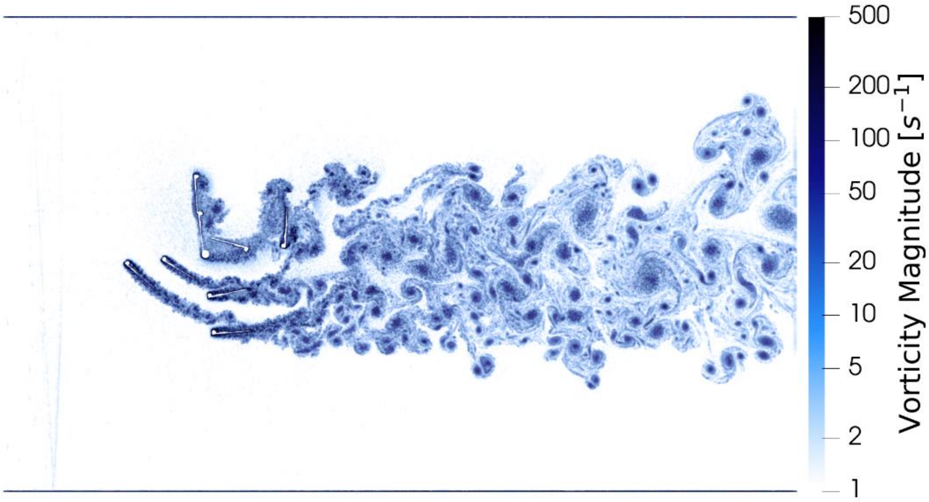

Figure 4.26: Base design, vorticity field (U_∞ = 0.9 m/s) at t = T.

4.5.1 Validation

As a turbine in reality would be required to operate in a variety of flow conditions, the ability of the numerical model to accurately portray the operation in said conditions is beneficial. The flume tests carried out at a variety of speeds allow for an insight into how the agreement of the numerical model and the flume measurements was impacted by changes to the flow. This is shown in Figure 4.27, with the L2 error of the net displacement excluding the warmup shown relative to the difference between the inflow velocity, and the inflow velocity of the convergence condition. The models show an increase in the normalised error magnitude as the inflow velocity deviates from the base condition, at a rate of O(1.47) determined using a least squares power law fit. With the fit and flow rates also shown in Table 4.2.

Table 4.2: Carbine free-spin displacement error at validation flow rates.

U_∞ **[m/s]**	**0.51**	**0.64**	**0.77**	**1.08**
SPH [rad/s]	2.191	2.741	3.138	4.540
Flume [rad/s]	1.991	2.656	3.182	4.321
L2 Error Norm [-]	0.100	0.032	0.014	0.051

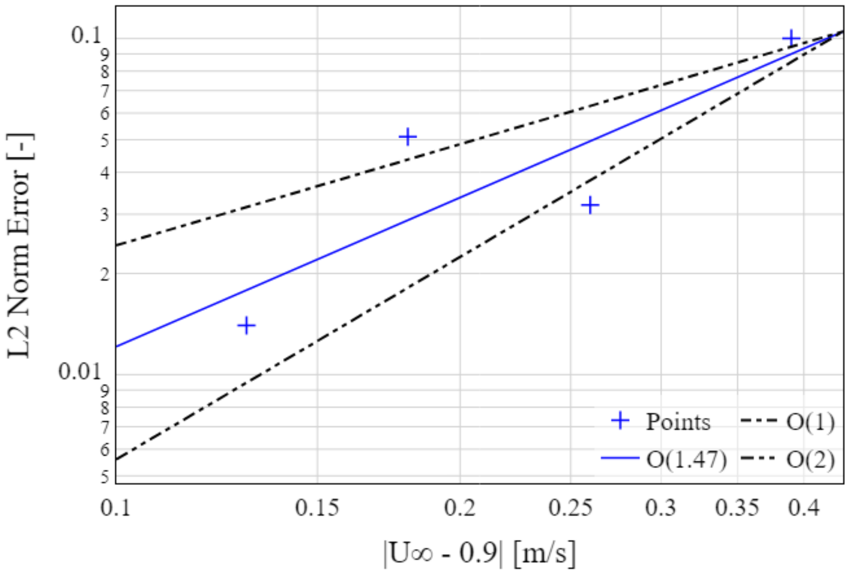

Figure 4.27: Model validation error levels at varied inflow velocities under free-spin condition.

The largest error was found to occur at the slowest inlet speed (U_{∞}= 0.51 m/s), this is not only the slowest flow condition, but also the farthest from the base – calibration condition (a free-spin turbine in a flow with an average inlet velocity of 0.9 m/s). This inlet flow condition was selected as this was found to be an optimal operating point for the device prototype, and as such has been the subject of greatest interest. This difference in behaviour is either due to the model poorly capturing an effect such as the turbulent behaviour about the device, the device being in a flow scheme where its own motion is beginning to undergo a transition, or the turbine becoming Reynolds dependant. This effect is visible on Figure 4.28, where the 0.51 m/s tip speed ratio is more spread than the remaining tests.

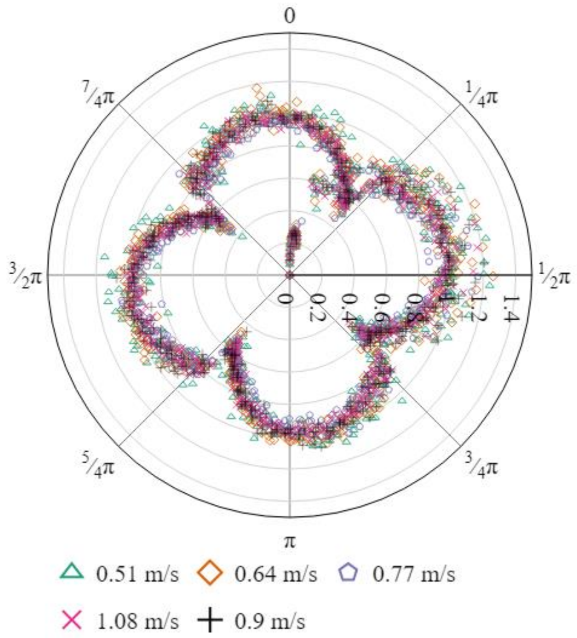

Figure 4.28: Tip speed ratio of base design at varied U_∞ levels.

4.5.2 Design Variants

The alternate designs shown in Figure 4.16 were initially tested at the base velocity, with the angular velocity over time shown in Figure 4.29. When some simple motion statistics are presented in Table 4.3, it is clear that the three-arm alternate model has both the highest maximum velocity, and the most varied, with a clear cyclic pattern of motion. The other designs exhibited typically lower variation in their motions, although this was accompanied by lower average velocities, which is likely a combination of both the increased inertia and the increased angles of activation from additional flaps. The tip speed ratios and indicative turbine wakes are shown for each alternate design in the following sections.

One element visible in each of these time series is the self-start behaviour. This varies across the design options, with the three-arm variant very quickly accelerating up to its long term behavioural pattern. The higher velocity achieved in the initial rotations of the five and six arm variants shown, is similar to that of the base design.

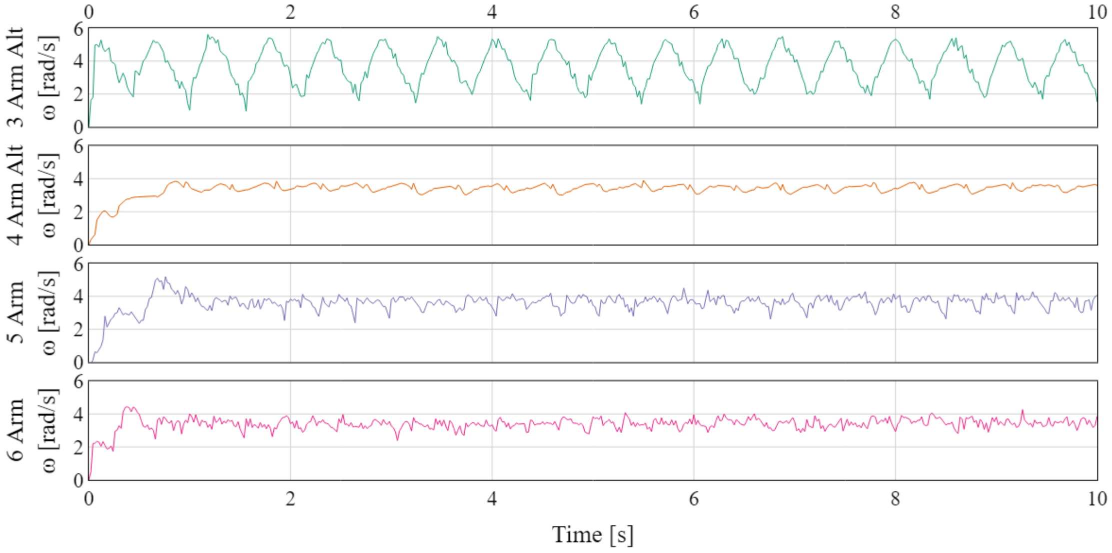

Figure 4.29: Angular velocities of design variants, at U_∞ = 0.9 m/s.

Table 4.3: Alternate design free-spinning angular velocity statistics at U_∞ = 0.9 m/s.

Model	**Mean Angular Velocity** [rad/s]	**Minimum Angular Velocity** [rad/s]	**Maximum Angular Velocity** [rad/s]	**Standard Deviation** [rad/s]
3 Arm Alt	3.708	0.953	5.615	1.101
4 Arm Alt	3.450	3.005	3.901	0.179
5 Arm Alt	3.651	2.392	4.513	0.337
6 Arm Alt	3.422	2.386	4.269	0.275
4 Arm Base	3.870	1.984	4.881	0.598

4.5.2.1 3 Arm Variant

The three-arm variant showed a continued high degree of variation across the range of velocities tested (Figure 4.30), suggesting that the motion of this design relative to the flow velocity is consistent within this range. Figure 4.31 shows a rendering of the velocity field of the test at the end of the simulated period. The tight spread of the tip speed ratios at a given body angle indicates the aforementioned consistency.

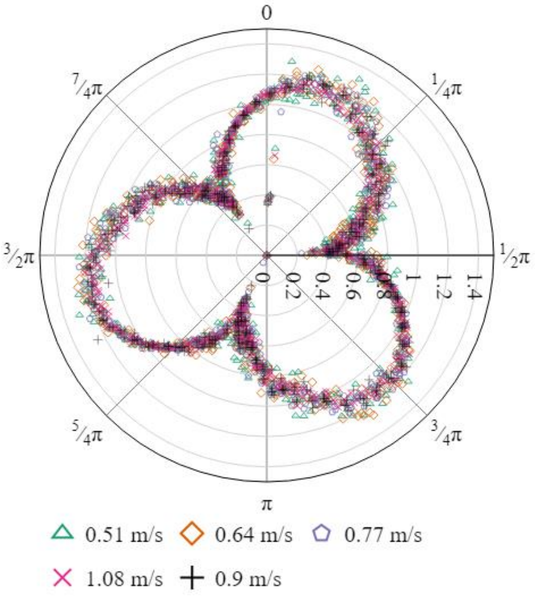

Figure 4.30: 3 arm variant TSR at varied U_∞ *levels.*

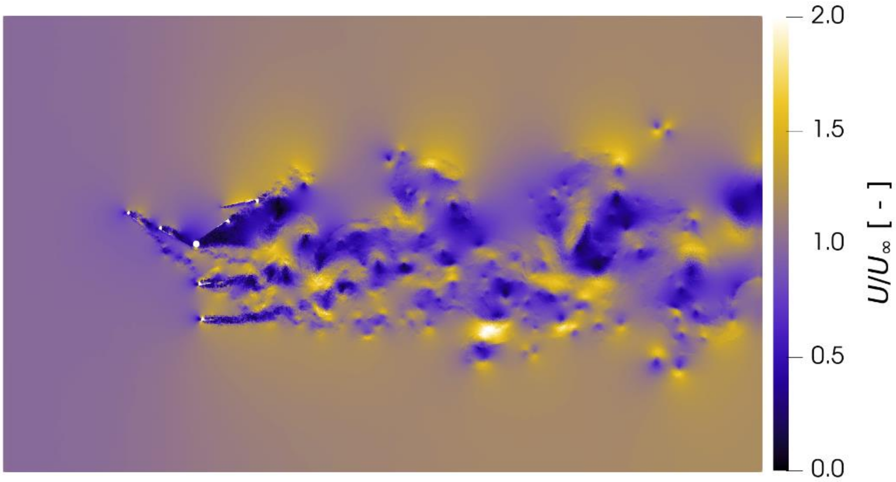

Figure 4.31: 3 arm final velocity field plot, U_∞ *= 0.9 m/s.*

4.5.2.2 4 Arm Alternative

The new four-arm design variant uses the same number of components as the base design, with the inner flaps offset by $\pi/4$ radians, extending the angles at which a flap is being activated by the flow and driving the turbine. This reduced variation in the angular velocity is seen in Table 4.3, with this being the design showing the lowest standard deviation. The tip speed ratio over a range of velocities is presented in Figure 4.32, where the consistency is visible within this range of flow velocities, as in the different flow velocities develop the same tip speed ration at the same body angle. The figure also shows the four-way rotational symmetry of the tip speed ratio. This, however, is the slowest rotating alternative, ~10 % slower that the base design on average.

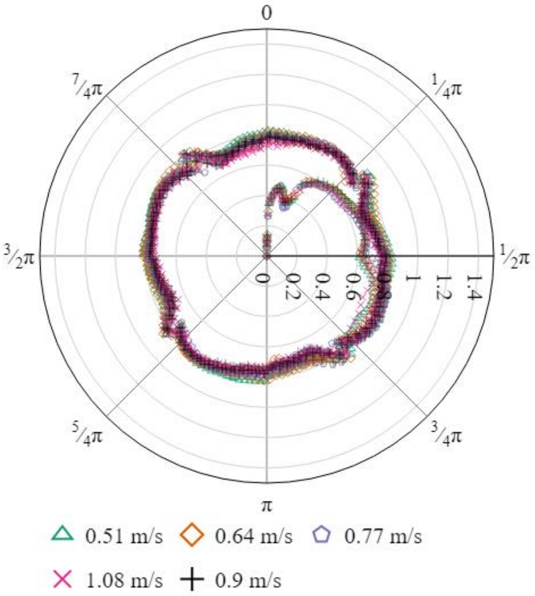

Figure 4.32: 4 arm variant TSR at varied U_∞ *levels.*

The flow field around the turbine in Figure 4.33 shows the increased small wake elements on the returning side of the turbine from the pins required to restrain the flaps. These would be less evident in the flume study, where this support is provided through small bolts or extrusions on the base and top plates.

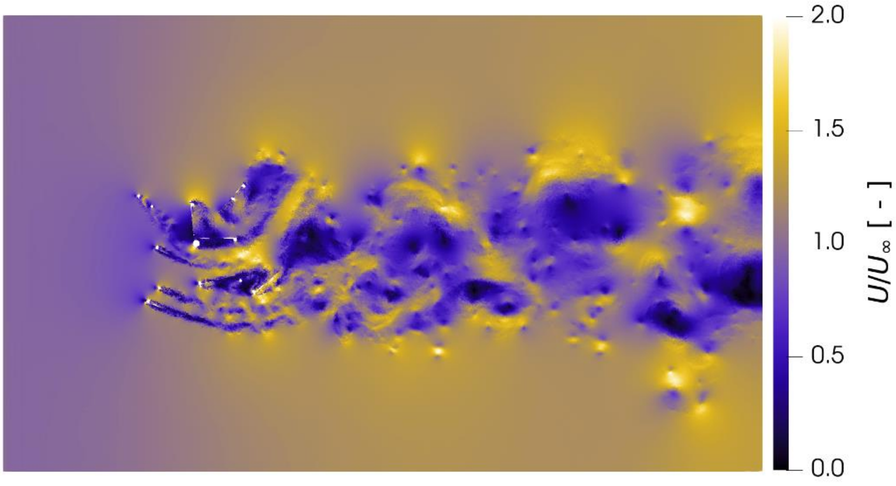

Figure 4.33: 4 arm final velocity plot, U_∞ *= 0.9 m/s.*

4.5.2.3 5 Arm Alternative

Five-way rotational symmetry in the turbine behaviour is shown when using five-arms in Figure 4.34, this design features an increase in net components over the base design – but with generally worse performance metrics based on this study. The wake structure in Figure 4.35 shows larger areas of low velocity in the wake than the other designs.

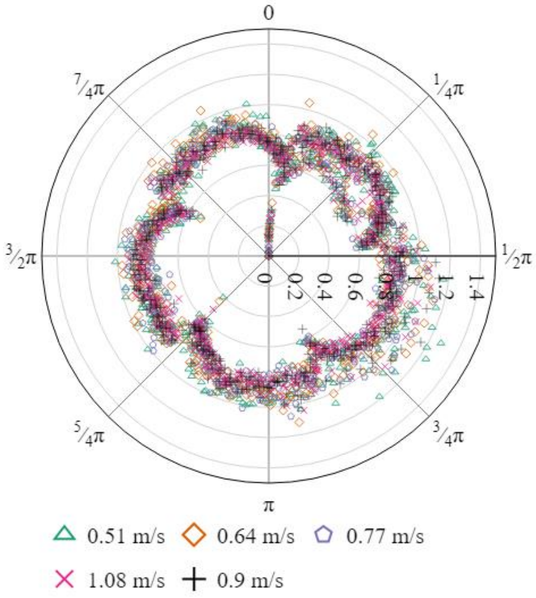

Figure 4.34: 5 arm variant TSR at varied U_∞ *levels.*

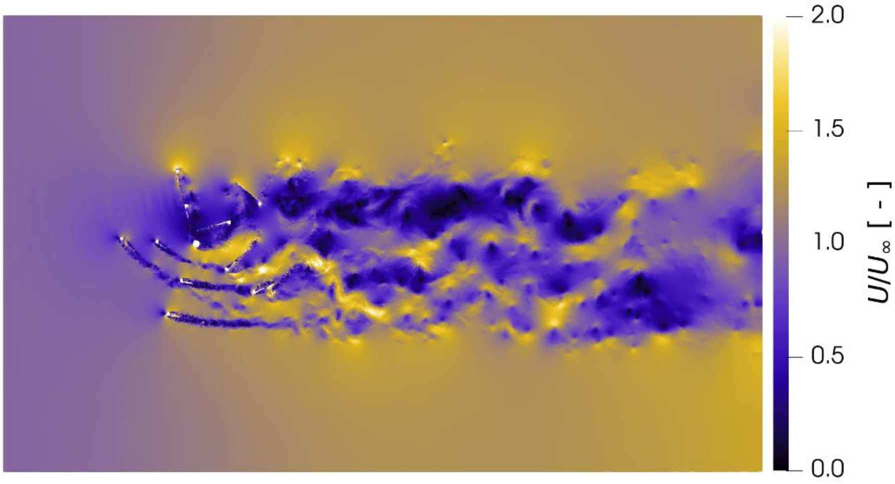

Figure 4.35: 5 arm final velocity plot, $U_\infty = 0.9$ *m/s.*

4.5.2.4 6 Arm Alternative

The six-arm alternative design showed statistical similarity to the five-arm, with less than 10 % difference between their mean, maximum and minimum velocities. This design had a lower variance in motion than the five arm, but the higher expected production cost and reduced mean velocity. This design exhibits six-way rotational symmetry in its motion pattern in Figure 4.36.

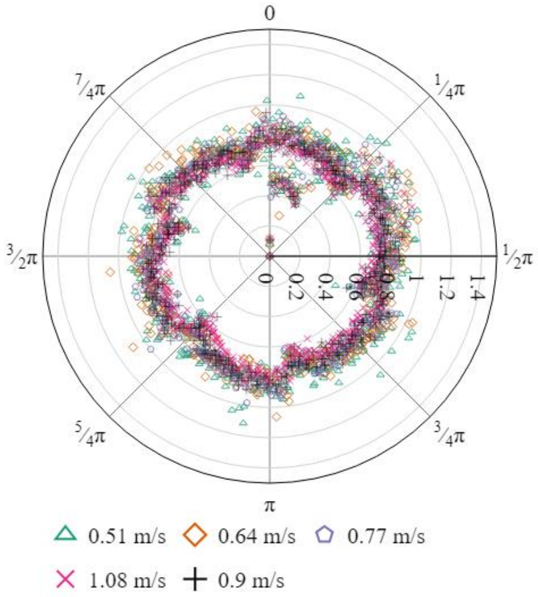

Figure 4.36: 6 arm variant TSR at varied U_∞ *levels.*

The velocity field (Figure 4.37) shows that here where the angle between the flaps is smaller allows for adjustments to some behaviour, such as the flaps on the returning side following in the wakes of the arm ahead of them to a greater degree than the prior models.

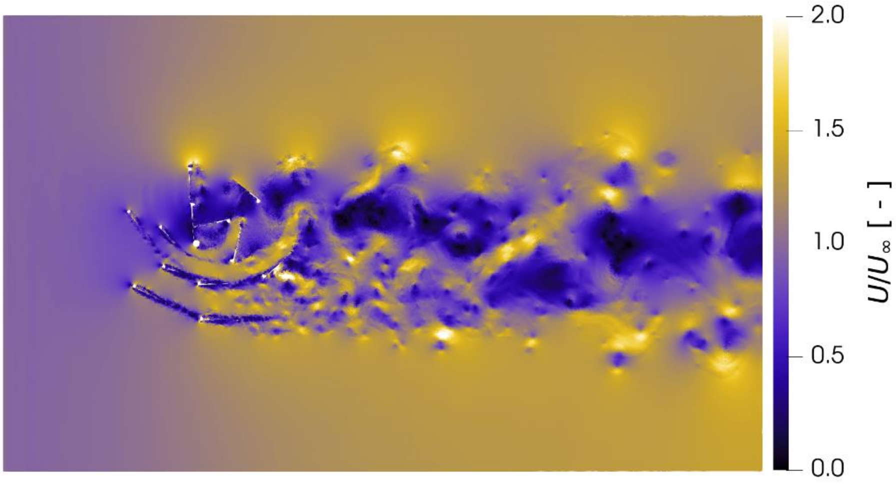

Figure 4.37: 6 arm final velocity plot, $U_\infty = 0.9$ *m/s.*

4.5.3 Resilience

The resilience of the design options to partial damage is assessed here through simulating the loss of a single arm per design. This simulates the scenario whereby a singular component has been damaged or corroded, but the device is still required for electricity generation for a period until repairs are available. An ability to operate having lost a flap or arm is something that is typically beyond the scope of axial flow turbines and can be a potential advantage of turbines such as CarBine. Naturally the loss of an arm is liable to be more impactful to a variant with fewer total flaps, since each is required to drive the motion for a greater proportion of the time. Throughout the process, the loss of an inner flap is referred to as Case 1, and the loss of an outer flap as Case 2. All resilience tests were conducted using U_∞ = 0.9 m/s.

4.5.3.1 Base Design

The base design showed very similar affects when missing an inner or outer flap, with the $\frac{3}{2}\pi$ body angle showing a significant drop in tip speed from the undamaged model (Figure 4.38). This is the section of the rotation where the missing flap would have been driving the device – note that the loss of an inner flap is marginally less detrimental than the loss of an outer flap. The phase after the broken flap is interesting in that in both damage cases it results in a period of higher velocity than the undamaged model. The self-start behaviour is largely unchanged by the loss of either arm in this configuration.

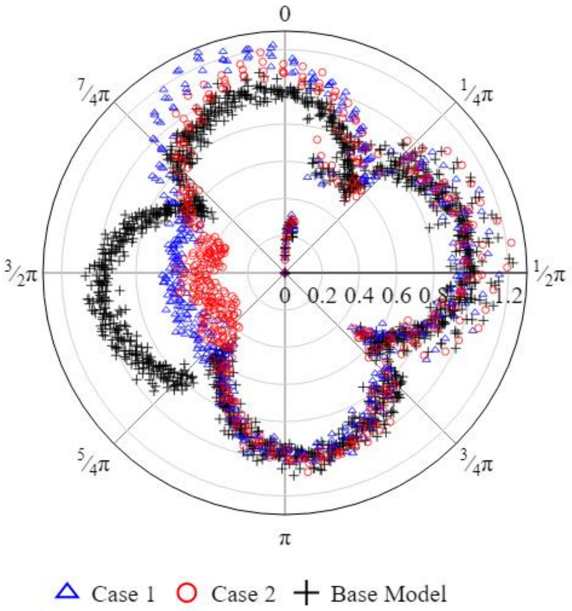

Figure 4.38: Base design damage behaviour at U_∞*=0.9 m/s. Compared to undamaged case.*

4.5.3.2 3 Arm Variant

The damaged three arm design (Figure 4.39) also saw a drop in rotational speed in the phase of the rotation when the missing flaps are in the active section. The loss of the outer flap again was more impactful than the loss of the inner flap. The velocity increase on the post-damage section is also seen with this design, although to a lesser degree. The self-start behaviour is largely unchanged by the loss of either arm in this configuration.

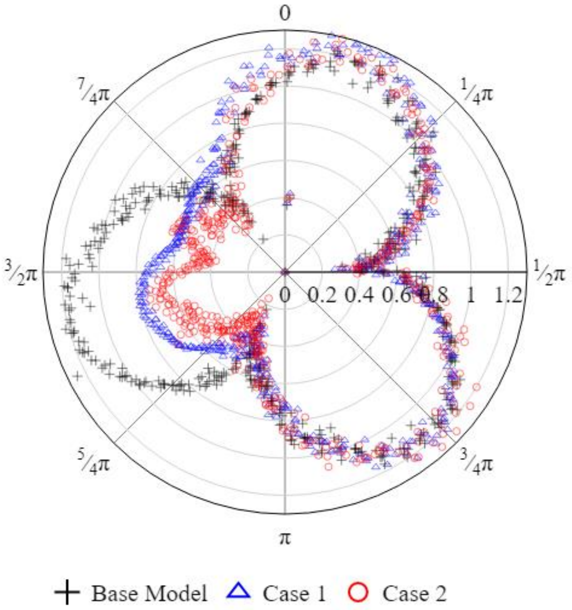

Figure 4.39: 3 arm design post-damage behaviour at U_∞*=0.9 m/s. Compared to undamaged case.*

4.5.3.3 4 Arm Alternative

The offsetting of the arms in the four-arm alternate design aimed to generate drive to the turbine over a greater range of angles, which is seen to be beneficial to the damaged case where an inner flap is lost (Case 1 on Figure 4.40). This design does not show the post-broken flap acceleration of the base and three arm models, this is predominantly due to the offsetting of the arms. The other designs have two flaps per notional arm – whereas this design is in effect an eight-arm single-flap design.

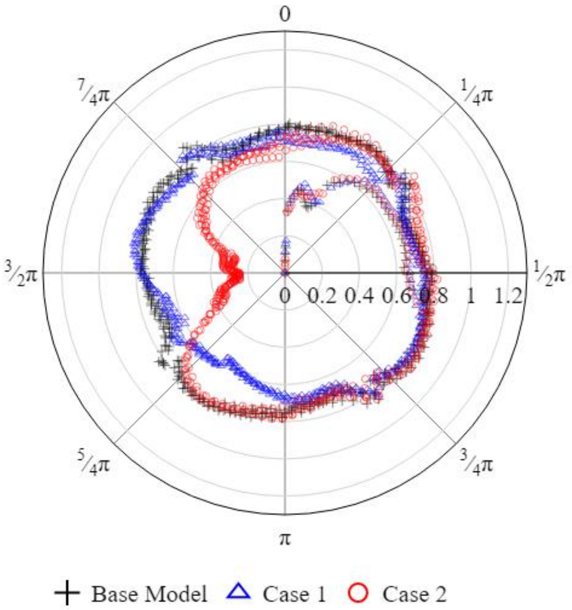

Figure 4.40: 4 arm alternative design post-damage behaviour at U$_\infty$*=0.9 m/s. Compared to undamaged case.*

4.5.3.4 5 Arm Alternative

The acceleration in the post-breakage phase is seen again in the five-arm damaged models in Figure 4.41. Here it is also visible that the convention of losing an inner flap is less impactful than an outer flap still holds.

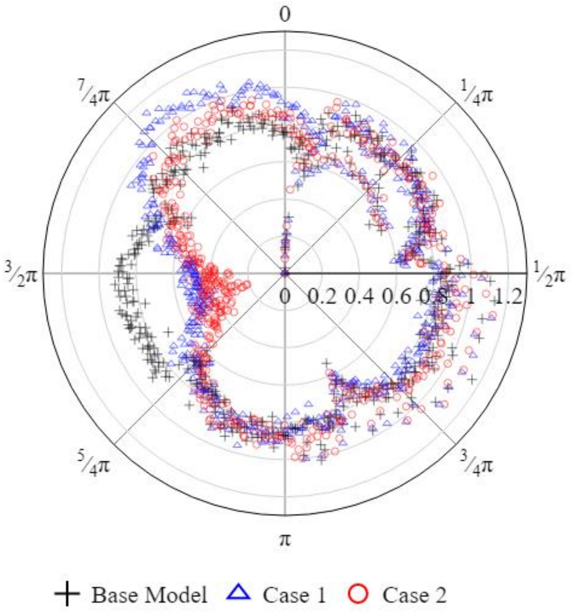

Figure 4.41: 5 arm design post-damage behaviour at U$_\infty$*= 0.9 m/s. Compared to undamaged case.*

4.5.3.5 6 Arm Alternative

The six arm alternat showed the largest acceleration of motion in the post-damage period when an inner flap is removed (Figure 4.42), though this is not seen for the removal of an external flap. This may be due to the dense nature of the inner flaps, having a smaller space within which to operate (note the two inner flaps making contact on the driving side of the device in Figure 4.37).

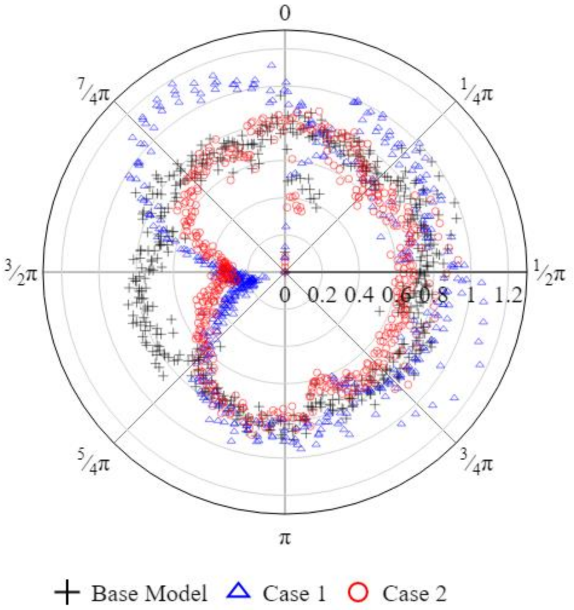

Figure 4.42: 6 arm design post-damage behaviour at U_∞ *= 0.9 m/s. Compared to undamaged case.*

4.6 Summary

In order to gain insight into the motion of a vertical axis turbine with a design that is challenging to model using meshed numerical modelling tools, an SPH modelling method was developed whereby the turbine is modelled via a plan cross section in a 2D model. This was carried out on the turbine developed at Cardiff University – referred to as CarBine, using the open-source SPH modelling software DualSPHysics. Modelling was carried out on the HPC Wales supercomputer ‘Hawk’ and on a GPU enabled desktop. This turbine design could be used in riverine flows, tidal currents, or potentially in the jet regions developed by a tidal range scheme when water is entering and exiting the impoundment to extract more energy from the hydrodynamics of the scheme.

A key aspect of the SPH model over alternative numerical modelling processes for turbines is the lack of a prescribed turbine velocity, the device is hinged to the domain, and only the fluid forces drive rotation. One novel element achieved by this approach is the representation of self-start due to only hydrodynamic forces, which is challenging with mesh-based methods, and was demonstrated for all variants including the damaged (resilience) tests which showed limited change to startup from the loss of a singular arm. This was further demonstrated by removing a single flap from each of the turbine designs and investigating how the device operates in a damaged state (also a potential design driver for small hydrokinetic devices such as this).

To achieve stability within the model (which was typically prone to the development of voids leading to full breakdown), a large shifting coefficient (-50) was required alongside the artificial viscosity model approaching direct numerical simulation of turbulence in the tests. Done by using a very fine particle spacing, which is partially necessitated by the nature of the device designs tested. The tests themselves were designed to mimic prior flume studies at Cardiff University, providing data against which to calibrate and test the SPH model.

SPH solutions have been found to converge to two key parameters, the initial inter-particle spacing dp and the kernel support H. For these tests convergence in excess of second order was found for dp of 1 mm, and H/dp of 2.25. The model was found to be insensitive to the position of the downstream boundary of the system.

The model process was applied to the base design in free-spin conditions of the turbine at a variety of flow velocities to provide validation of the ability of the setup to predict turbine behaviour beyond the calibration condition. A set of alternate designs were conceived and some initial behavioural information about them ascertained through modified models of the turbine, highlighting the relative ease of modifications to a design through the lack of a meshing process. The study is limited at this stage by the inability to adequately apply a restraining torque to the device, and as such power output metrics and the behaviours of the turbine when connected to a generator could not be developed.

5 Tidal Range Schemes and Net Zero

5.1 Introduction

The classical image of a tidal range scheme, from proposals to existing examples has typically been to construct a large impoundment, at a scale equivalent or in excess of a large commercial port. A scheme this size has the ability to generate large amounts of electricity, along with providing auxiliary benefits to the surroundings. These auxiliary benefits include flood protection, tourism, and space for recreational or industrial activities, however per current legislature – for an electricity generating project to receive state funding it must be financially viable in terms of operation solely as an electrical generator. The large size of these schemes also has the potential to result in vast changes to the hydro-environment in which they are constructed, a factor that has halted many tidal range developments in years prior – as such, an awareness of the environmental impact, and how any proposed changes would affect the environment is crucial throughout the development process. This chapter carries out a 0D based operational optimisation process assessing the individual and combined contributions of two processes to the ability of the scheme to yield revenue. The design space is then re-examined in the wake of this optimisation, to develop a view as to how more or fewer turbines or sluices may impact performance. Finally, the potential environmental impact of the operational improvements is validated for one of the schemes using a 2D modelling approach.

5.2 Large Tidal Range Schemes

The power output P (W) of a tidal range scheme is proportional to the product of the tidal range ξ (m) and the impounded area A (m^2) as developed by Prandle [232], shown in Equation 2.5. As such, the majority of tidal barrages and lagoons have been proposed (and built) around locations with large tidal ranges. Complementary bathymetry, flood protection potential, tourism, grid connection points, and adjacent population centres can all provide supporting motivation, however, the fundamental ability of the scheme to self-sustain as an electrical generation facility is critical to developers receiving state support.

To provide a demonstration of the processes carried out here, two lagoon schemes in the UK have been chosen for a design/operation assessment using a 0D approach, with one being carried on to a 2D hydro-environmental assessment and model comparison. The analysis is carried out on the West Somerset Lagoon (WSL) and North Wales Lagoon (NWL). These two schemes, along with some major works carried out regarding them are presented in Section 2.5.3. The two schemes are similar in size and represent two options considered likely for further development due to their generating capacity, flood protection, and proximity to major population centres. The work carried out here could nonetheless be applied to similar scaled schemes either within the UK or abroad.

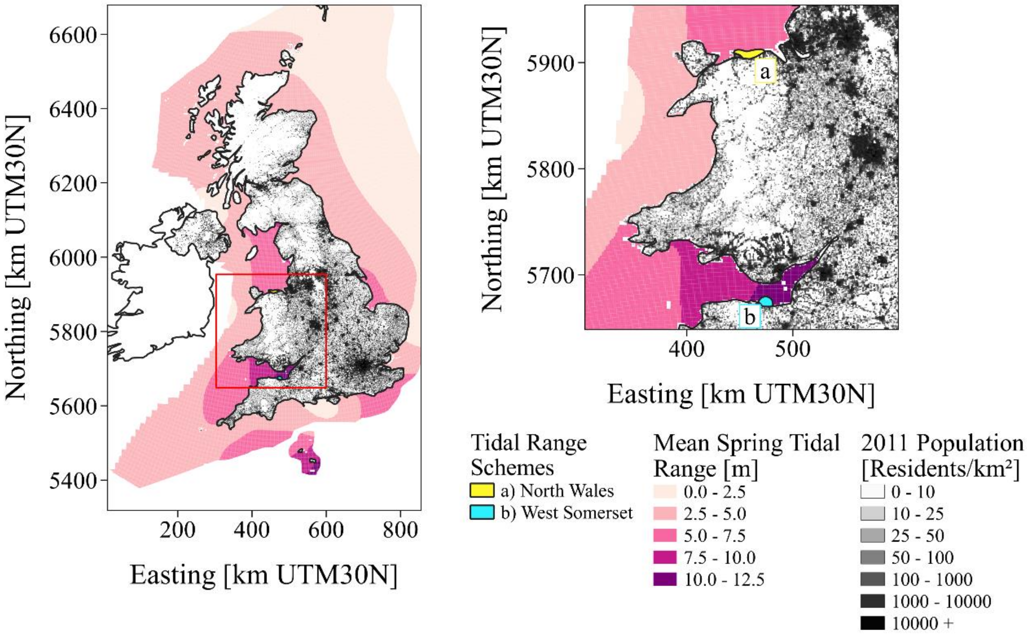

Figure 5.1: Population and tidal range map up the UK with studied schemes identified, tidal range data from [52] and population from 2011 UK census [53].

It should be noted that North Wales has a ~4 hour tidal phasing to the Severn Estuary/Bristol Channel, thus schemes spread across this location operate at a range of times across a given day, as shown for the two points on a sample day of mean tide in Figure 5.2 and for the entire Irish Sea in Figure 5.3, where the water levels for North Wales and West Somerset are taken at Llandudno and Hinkley respectively. This phasing is consistent over the tidal cycle for the two regions,

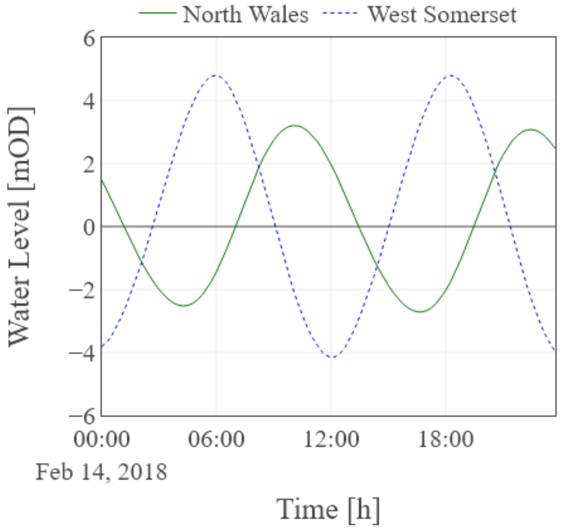

Figure 5.2: Comparison of tidal phasing and magnitude on a sample day (mean tide) at North Wales and West Somerset tidal lagoons, measurements from BODC.

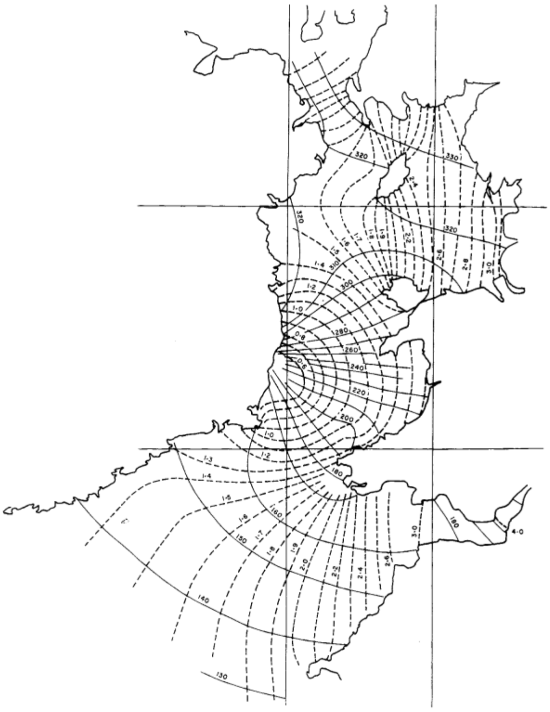

Figure 5.3: M2 cotidal map where solid lines are cotidal phase relative to equilibrium tide at Greenwich meridian, and dashed lines are co-amplitude lines with (m), reproduced from Robinson [233].

5.3 Method

The role of the 0D study in this case was to enable lightweight modelling of the two schemes in a number of operational systems, identify an ideal operation – and explore how well this operation is suited to modifications to the design of the schemes in terms of number of turbines and sluiced area. For the two schemes, a combination of operational choices were assessed in terms of the potential to increase financial return on investment – using 0D modelling. These choices were operating the schemes purely based on the cost-of energy changing over time, the inclusion of parallel sluicing, and then the combined impact of the two.

Some initial elements of the environmental impact of these changes is then assessed at West Somerset Lagoon to quantify the degree to which the operational changes will impact the hydro-environment of the schemes, along with providing a comparison to the 0D model from a physically representative model.

5.3.1 0D Study

5.3.1.1 Operational Optimisation

The operation of a tidal range scheme is shown in Figure 5.4; the switch between modes of the scheme is dictated by one of a few factors, including time of day and internal water level; the most commonly used however is the head difference across the scheme ΔH. The parameter ΔH_{start} is the water level that must be reached to end holding and begin generation, with ΔH_{end} being the level at which sluicing commences. These can be seen in Figure 5.4.

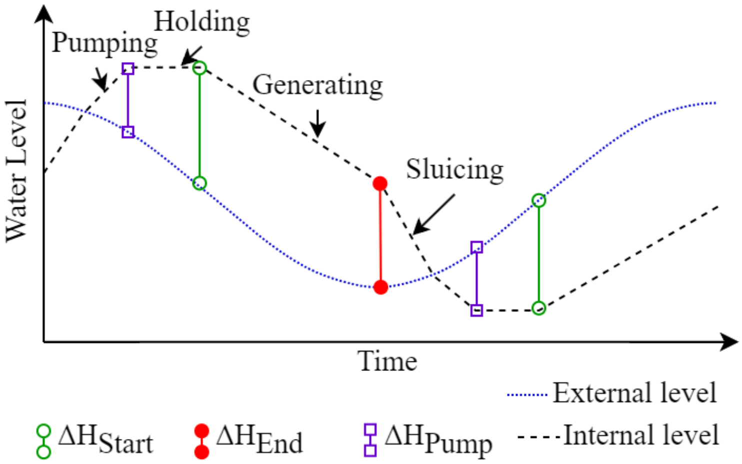

Figure 5.4: Schematic diagram of pumped tidal range scheme operation.

Parallel sluicing, as presented by Moreira et al. [127] was found to increase energy generation for the Swansea Bay Lagoon by opening the sluices before closing/shutting off the turbines, thus creating an additional period of energy generation, with an increased flow rate through it. The key advantage of this method is that again no additional cost is incurred when potentially aiming to increase generation. The gains come from the additional rate of emptying/filling and the extended generation period. Here this option is tested at two large schemes, to ascertain how this increased flexibility in operation could provide an advantage to the generation of energy and revenue.

Finally, to increase energy generation the turbines can be operated as pumps to increase the head difference by driving the internal water level past the natural range at times of low head [21]. Figure 2.23 provides an example of how the internal and external levels move over this cycle for two-way operation both with and without pumping, where ΔH_{Pump} is the target head difference to be reached by pumping.

The control parameters ($\Delta H_{Start}, \Delta H_{End}$ and ΔH_{Pump}) were assumed to be constant in early studies [232], however, varying these points (referred to as flexible operation) allows the operators to capitalise on one of the key abilities of tidal range energy – namely a degree of dispatchability that wind and solar (the predominant renewables in the UK) are unable to deliver. This being the ability to delay or expedite the start and end of generation, in order to improve performance [22], note that this dispatchability is at this stage of assessment still below the ability of technologies such as gas turbines or pumped hydro schemes. As the demand for energy and the supply of energy from intermittent sources (wind and solar) vary throughout the day, the price of energy in the wholesale energy market varies in response. At times of high demand (or when demand exceeds supply), the price is typically higher and vice versa. This demand pattern can be seen for 2012-2018 in Figure 2.2 (where each point is the mean energy price at that time of day, for a given year) with the annual average price at a given time of day normalised to the mean price of energy that year. By anticipating this effect, a tidal range scheme can operate to move generation to times of greater energy value, resulting in a revenue yield that is greater than that of the average value of the energy [22]. This is here referred to as ‘revenue-based operation’, with prices extracted from the Elexon Data Portal [17] and assumed to be accurately forecastable within a 24-hour window. The demand patterns and energy mix are taken for the UK in this study but are seen to be similar to the demand pattern in other developed energy markets. Without requiring any modification of the designs, the tidal range schemes were modelled for the full year under flexible operation aiming to maximise profit as opposed to energy output.

By combining this flexible operation method with pumping, the scheme can pump water to create an artificially high or low level inside the impoundment. This artificial water level difference is effectively an energy storage method, following the principals of a pumped-storage hydro powerplant. This way the tidal range scheme is operating both as an electricity generation facility, and a large-scale energy storage facility. This storage potential alleviates the need for the traditional storage needed to maintain a stable national grid, as is increasingly needed with the rise in intermittent renewables on the path to net zero [15]. This can be done either to produce optimum revenue (energy arbitrage) or to meet a balancing demand when there is a significant imbalance in the system.

Table 5.1: Operation choices assessed for case study tidal range schemes.

Case Name	Operation	Goal	Sluice Method
0	Fixed 2 Way	-	Serial
1	Flexible 2 Way	Energy	Serial
2	Flexible 2 Way	Revenue	Serial
3	Flexible 2 Way	Energy	Parallel
4	Flexible 2 Way	Revenue	Parallel

5.3.1.2 Design Optimisation

The design of a tidal range scheme is an iterative process, with the design in terms of layout, number of turbines, and sluices, alternating in process with the operational choices. With an optimised operation ascertained for the prior design, an updated range of design options is developed by varying the number of sluices and turbines (with the general layout assumed to be the same) and calculating the revenue yielded. Additional turbines and sluices are likely to be more costly than the amount of wall replaced, so a variety of combinations may be the most cost-effective depending on costings of components, or the future expectations of stakeholders, and is beyond the focus of this study. Both schemes were tested with the number of turbines ranging from a minimum of 25 to a maximum of 300 (double that of the larger NWL), and a sluiced area ranging from 0 to 60,000 m² (double the baseline of NWL); these ranges are presented in Table 5.2.

Table 5.2: Design parameter ranges for WSL and NWL used in the expanded design study.

Design Parameter			**Scheme**	
			WSL	**NWL**
Number of turbines	**[-]**	**Minimum**	25	25
		Maximum	300	300
Area of sluices	**[m²]**	**Minimum**	0	0
		Maximum	60,000	60,000

5.3.2 2D Study

The key aim of the 2D component of the study is to assess the extent to which the changes to the operation that result in improved performance in the 0D study translate to a more comprehensive 2D model, along with quantifying how these choices affect the hydro-environmental impact of a scheme. To do this, the various cases of operation assessed in the 0D operational development were simulated in a 2D hydro-environmental model of the Severn Estuary (Bristol Channel), and run for a representative period in terms of energy generation.

5.3.2.1 Severn Estuary-Bristol Channel Model

To understand the impacts brought upon by a tidal range scheme, it is key to first derive a picture of the state of the location without the scheme. This region has been modelled extensively using a variety of models including DIVAST [130], EFDC [143], and Delft3D [149]. For this study, the Severn Estuary Bristol Channel (SEBC) model was used (using EDINA Digimaps bathymetry), with grid spacing calibrated by Guo [129] with a full description in [172], with the refinement to the model around the West Somerset Lagoon included. This mesh covers a region from Hartland point in Devon, along the English coast and up the River Severn to the tidal limit at Haw Bridge near Gloucester, and the Southern Welsh coast passing Newport, Cardiff, and Swansea – reaching to Stackpole Head in Pembrokeshire, with a boundary defined by the Ordnance Survey high water line data (resampled to a 500m minimum segment length). The ocean boundary of the model passes inside the position of Lundy Island, and features refined internal spaces to represent Caldey Island, Flat Hold and Steep Holm as described by Guo et al. [209]. The mesh has elements varying in size from 250 m^2 up to ~1 km^2 as shown in Figure 5.5 – coloured by area associated to each node, with the ocean boundary labelled ‘TPXO’.

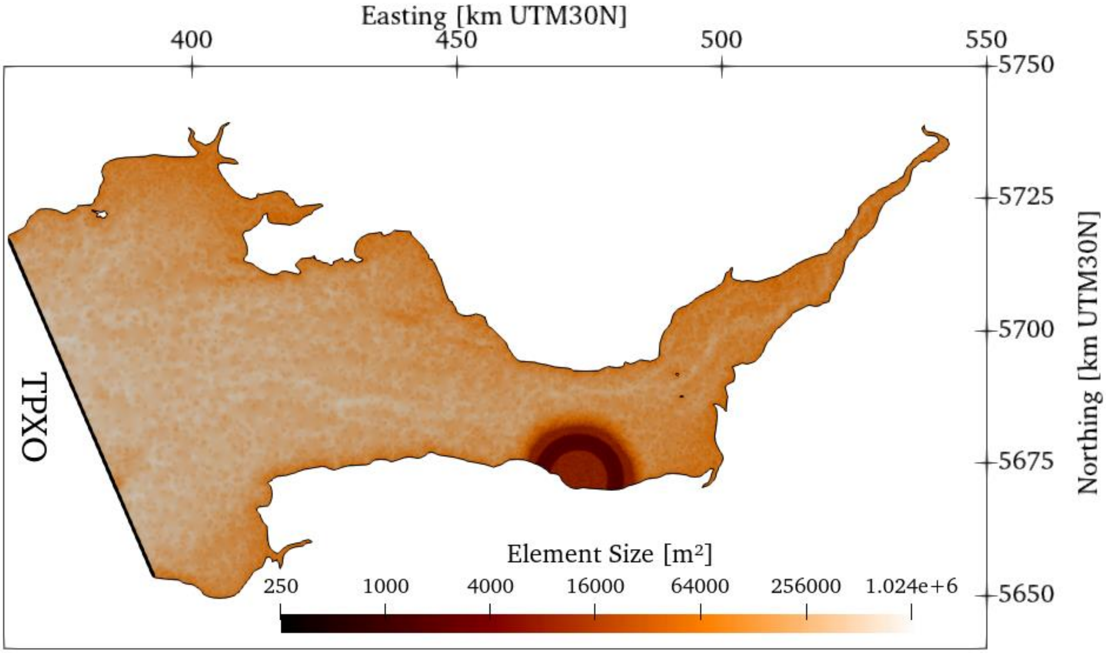

Figure 5.5: SEBC base model mesh density, with ocean TPXO boundary marked.

Within this region there are five BODC measuring stations, these are listed in Table 5.3 along with the respective Mean Spring-tidal Range (MSR) and Mean Neap-tidal Range (MNR) per the National Tidal and Sea Level Facility (NTSLF) [234]. They are also plotted in Figure 5.6, along with the bed level throughout the model – note the tail end of Lundy Island one third of the way up the oceanic western boundary. The Portbury station was historically referred to as Avonmouth, and is in approximately the same location (being on the opposite bank of the River Avon to the original gauge), however the Avonmouth gauge itself was decommissioned in 2011 [234].

Table 5.3: SEBC area BODC water level measuring stations used in model calibration, positions and mean tidal ranges for spring (MSR) and neap (MNR) conditions per NTSLF.

Location	Abbreviation	Easting [UTM 30N]	Northing [UTM 30N]	MSR [m]	MNR [m]
Hinkley	HIN	487112	5673373	10.91	5.32
Ilfracombe	ILF	417732	5674243	8.41	3.88
Mumbles	MUM	434061	5713197	8.46	4.03
Newport	NPO	501659	5708968	11.63	5.85
Portbury	PTB	516999	5705957	12.27	6.21

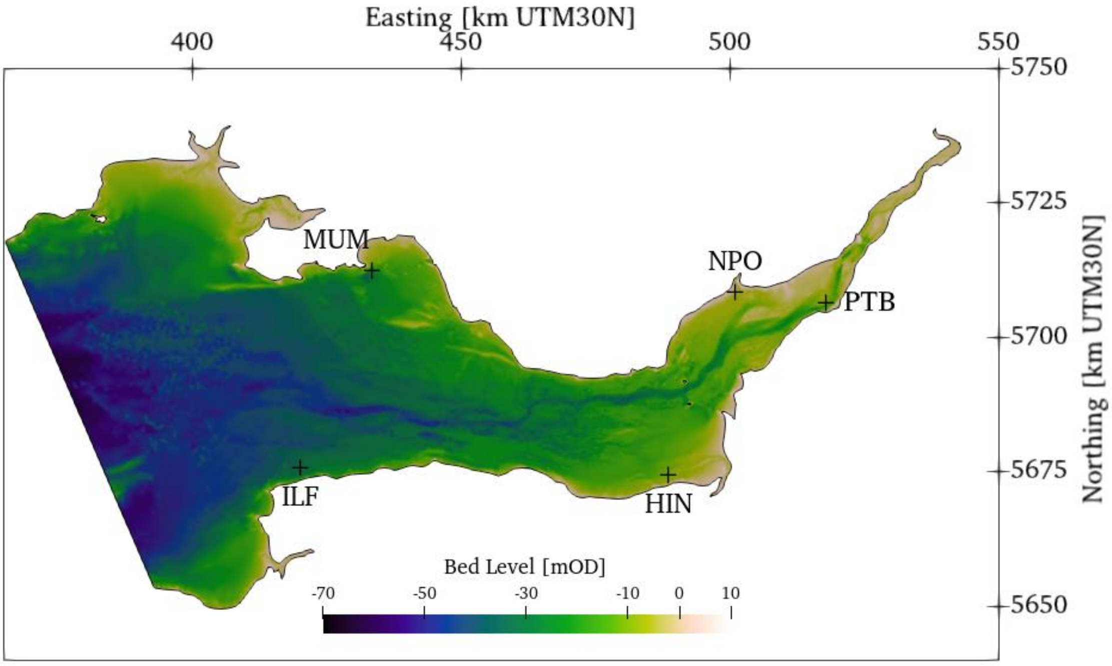

Figure 5.6: SEBC base model bathymetry (from EDINA Digimap), with BODC measuring points marked with abbreviations as listed in Table 5.3.

The quality of the outputs of a tidal range scheme model within a hydro-environmental model depends on the quality of the calibration of the hydrodynamics. To quantify the degree to which the model is able to represent the region, water level data from the BODC at the five gauges listed in Table 5.3 was compared to extracted water levels using two methods: statistical, and harmonic analyses. The Matlab package T_TIDE developed by Pawlowicz et al. [50] was used to ascertain the tidal constituents of the BODC data for the 01/01/2018 to the 31/03/2018 using a mesh of the region that had the elements whose removal separates the WSL impoundment re-included. The full timeseries of the water level at Hinkley is plotted for both the BODC and TELEMAC models in Figure 5.7, showing the multiple neap and spring cycles within the period, as is required for the calculation of multiple harmonic constituents. The tides within the TELEMAC model are controlled by the western boundary driven by the TPXO database [43], this boundary can be calibrated using three TELEMAC keywords, `COEFFICIENT TO CALIBRATE TIDAL RANGE` (dimensionless, default = 1) and `COEFFICIENT TO CALIBRATE TIDAL VELOCITIES` (dimensionless, default = 1), the initial water level across the domain is extracted from the same database and can be adjusted using the keyword `COEFFICIENT TO CALIBRATE SEA LEVEL` (meters, default = 0). A two-parameter search using the coefficients for tidal range and water level was carried out with the tidal range amplifier varied from 0.9 to 1.2 and the water level from -0.1 to 0.25. The best fitness based on harmonic and statistical analysis was found using:

```
COEFFICIENT TO CALIBRATE TIDAL RANGE       = 1.05
COEFFICIENT TO CALIBRATE TIDAL VELOCITIES  = 1.0
COEFFICIENT TO CALIBRATE SEA LEVEL         = 0.15
```

The results of which are presented below, plots of the water levels for the calibration period at the remaining sites are included in Appendix B.2.

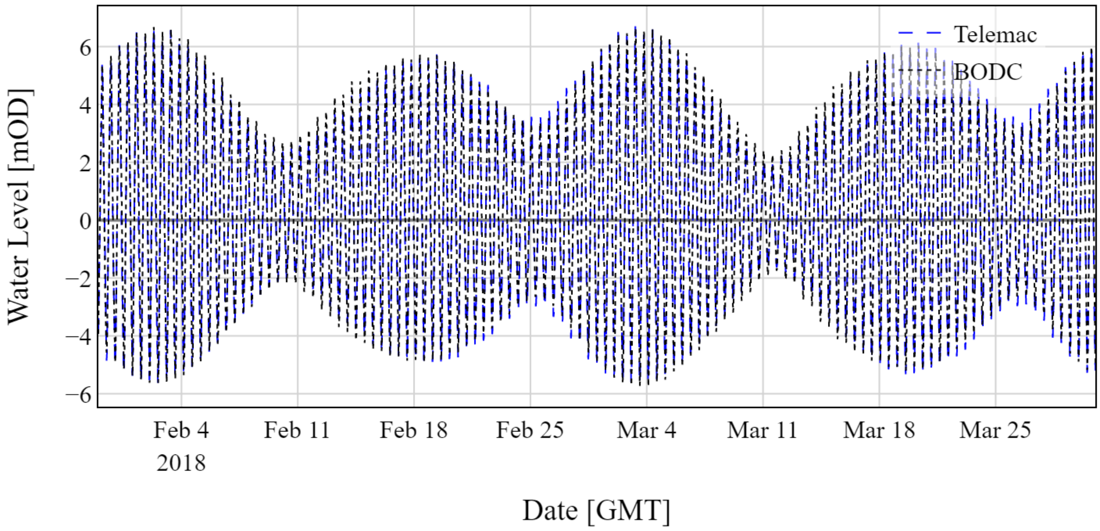

Figure 5.7: Hinkley water level comparison BODC and SEBC base TELEMAC model over full calibration period.

The first 8 major constituents based on the NOAA order [44] were selected for comparison to the measured extracted from the TELEMAC model at the corresponding locations, with an example of the constituents for Hinkley given in Table 5.4. 8 constituents being a recommended minimum for use in reconstructing signals based on constituents by Pappas et al. [193] for the prediction of tidal range energy scheme performance, and thus being a suitable number to determine quality of agreement. The remaining four constituent comparisons are given in Appendix B.1. To quantify the difference between the measured (BODC) and modelled (TELEMAC) tidal constituents, dimensionless errors in amplitude a_i and phase ϕ_i were developed per Equations 5.1 and 5.2 respectively, where a perfect match of amplitude would give an $E(a_i)$ of 1, and of phase $E(\phi_i)$ of 0.

$$E(a_i) = \frac{a_{i_{TELEMAC}}}{a_{i_{BODC}}} \tag{5.1}$$

$$E(\phi_i) = 1 - \cos\left(\phi_{i_{BODC}} - \phi_{i_{TELEMAC}}\right) \tag{5.2}$$

The comparison between the measured and modelled tidal constituents at Hinkley for the first quarter of 2018 in Table 5.4 show a good agreement between the two traces. The largest tidal constituent, the lunar semi-diurnal M2 phase having a 1 % difference in amplitude, and an absolute phase difference of less than 5° (note that the errors were calculated before rounding of results for display). For the two remaining semi-diurnal constituents (S2 and N2) the amplitude errors were 2.7 % and 9.1 % respectively, though at this location the M2 is more than double the amplitude of the S2, which in turn is more than double the amplitude of the N2 constituent. This configuration of the tidal condition within the model was thus found to be adequate based on the harmonic analysis.

Table 5.4: SEBC measured BODC and T2D model tidal constituents at Hinkley.

Constituent Name	**Amplitude**			**Phase**		
	BODC [m]	**T2D [m]**	**$E(a_i)$ [-]**	**BODC [°]**	**T2D [°]**	**$E(\phi_i)$ [-]**
M2	3.93	3.97	1.010	183.7	178.9	0.0034
S2	1.63	1.58	0.973	247.2	237.4	0.0147
N2	0.64	0.69	1.091	157.4	161.9	0.0031
K1	0.04	0.07	1.573	156.5	141.6	0.0336
O1	0.07	0.08	1.102	358.5	357.1	0.0003
M4	0.09	0.12	1.326	19.1	9.2	0.0149
M6	0.04	0.03	0.576	217.8	221.7	0.0023
MK3	0.01	0.01	0.920	203.2	205.7	0.0009

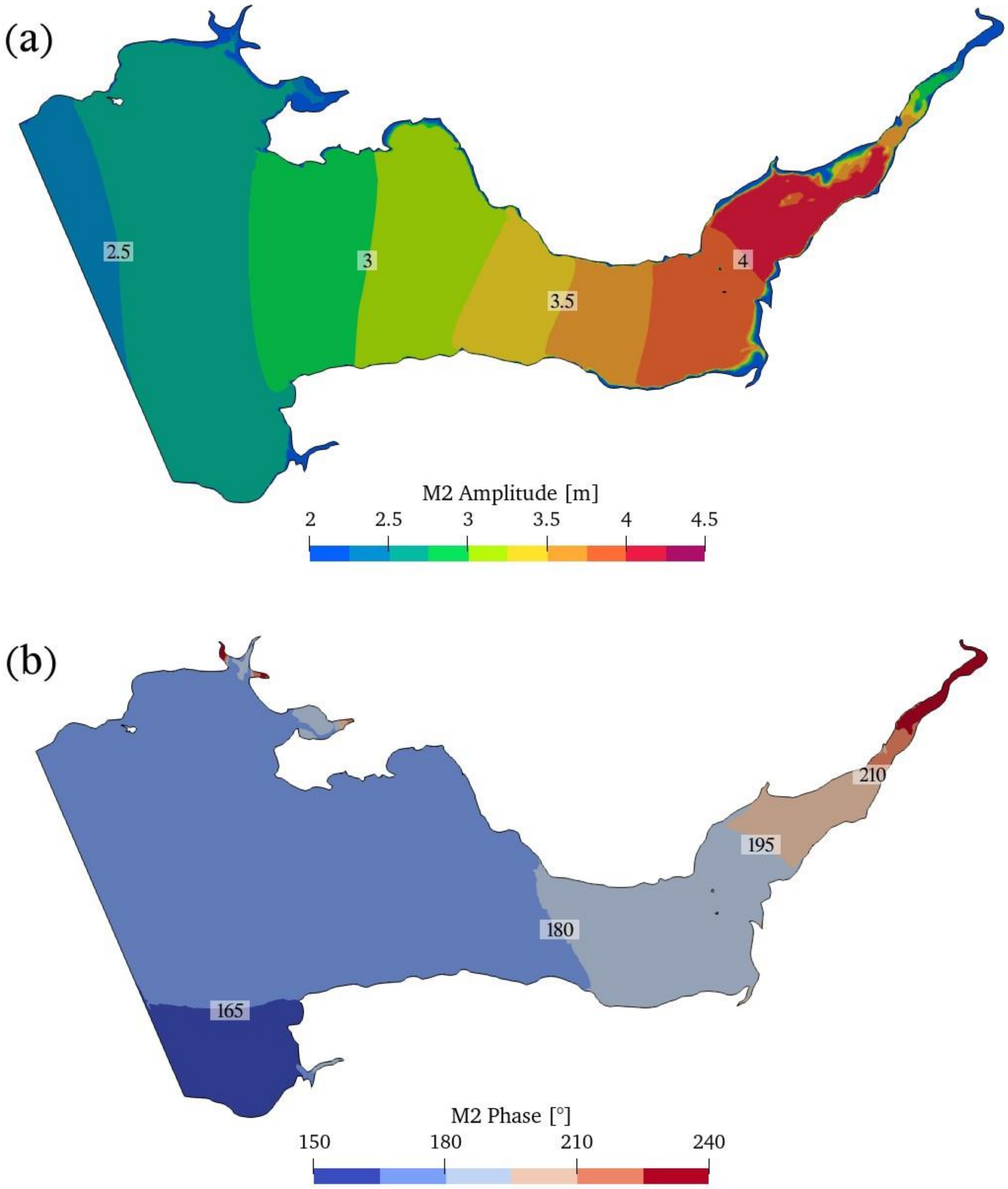

Figure 5.8: M2 tidal (a) amplitude and (b) phase within the SEBC model.

The largest two constituents in this region, the lunar and solar semi-diurnal constituents M2 and S2 respectively, are plotted in Figure 5.8 and Figure 5.9. These were extracted from the nodal timeseries at each point using the T_TIDE package [50]. Their contributions to the large tidal range particularly around Avonmouth can be seen where the M2 is in excess of 4 m and S2 in excess of 1.5 m.

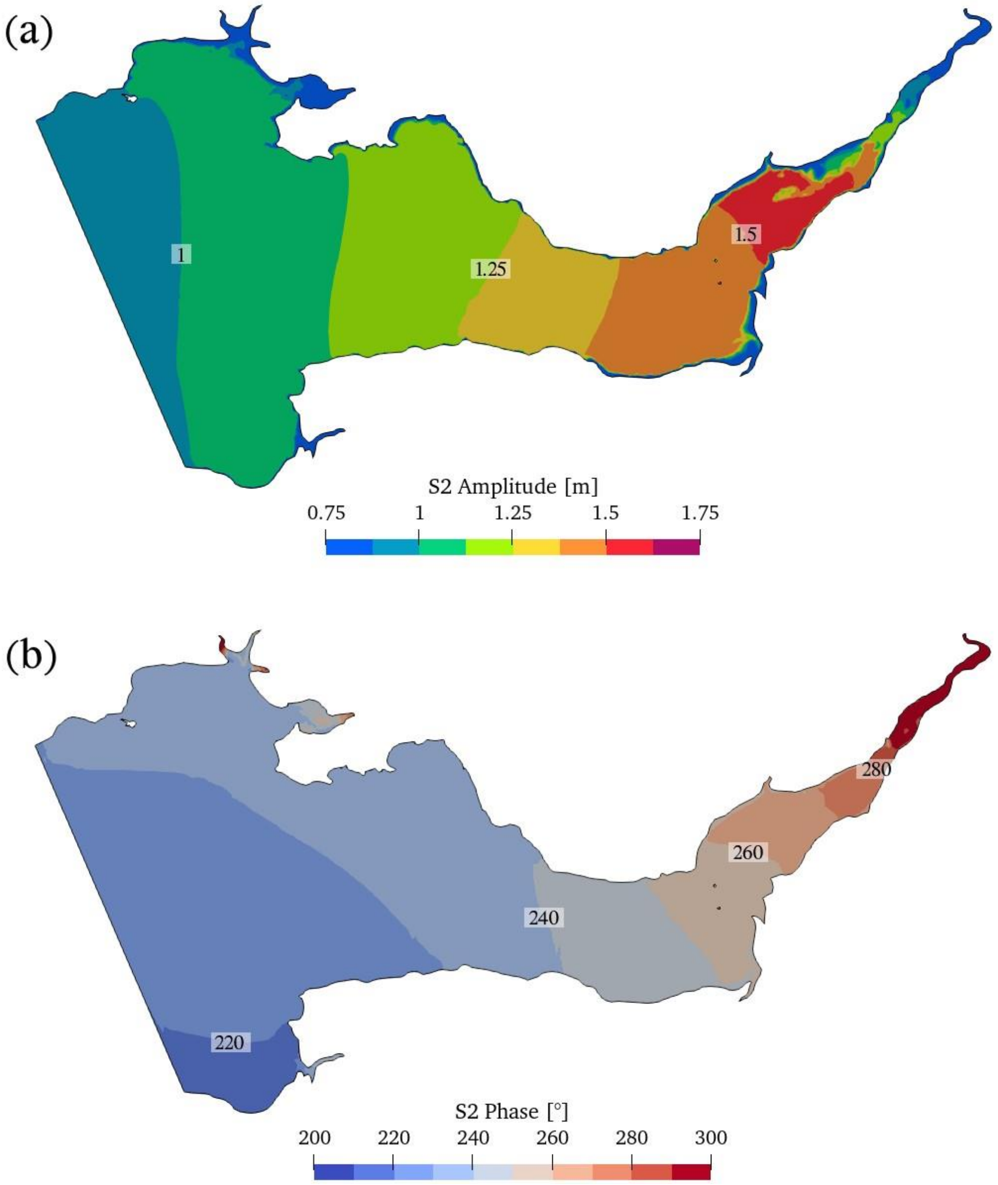

Figure 5.9: S2 tidal (a) amplitude and (b) phase within the SEBC model.

With the harmonic agreement established, a statistical check was carried out in addition to provide further assurance as to the data quality. Williams and Esteves [235] provide guidance on the setup and calibration of coastal models, they recommend a suitable match between measured data for water levels to be:

- Water levels:
    - To within ±0.1 m
    - OR 10 % of Spring AND 15 % of neap tidal range
- Timing of high water to within ± 15 minutes

From a duration of 1440 hours, with a 15 minute (0.25 hour) interval, containing 116 high tides, the fitness of the TELEMAC model to the BODC data at the five measurement sites is given in Table 5.5, the model can be seen to perform best at Ilfracombe and Mumbles by most metrics – being closer to the incident tides, with additional good match at the highly tidal Portbury (mean spring and neap tidal ranges for the sites are shown in Table 5.3). The weakest agreements are generally seen at Newport and Hinkley, where shallow water effects and large areas of intertidal space mean the measurement point in the numerical model needs to be farther from the point location of the gauge due to the resolution required for model stability. As a whole, the model shows a good match to the measured data based on the guidance.

Table 5.5: SEBC model water level calibration statistics, based on 116 high tides and the guidance of Williams and Esteves [235].

Location	**R^2** **[-]**	**Bias** **[m]**	$\overline{\Delta\eta} < 0.1MSR$ **[%]**	$\overline{\Delta\eta} < 0.15MNR$ **[%]**	$\overline{\Delta t_{HT}} < 0.25\ Hrs$ **[%]**
Hinkley	0.983	-0.086	100	98.6	96.5
Ilfracombe	0.992	0.017	100	100	98.3
Mumbles	0.992	-0.016	100	100	96.6
Newport	0.983	0.068	99.4	96.4	97.4
Portbury	0.986	-0.144	100	100	97.4

To ensure that no major underlying affect had been missed in the bulk statistical analysis of the water levels, the residuals ($\eta_{TELEMAC} - \eta_{BODC}$) were calculated over the duration, and plotted in histogram to ascertain their probability of occurrence, this is shown coloured by the contributions of the different sites to the whole in Figure 5.10. From this it is visible that the average underestimate of water level at Hinkley and Portbury comes from a spread of residual values, and that the largest maximum differences tend to come from the Newport station. A normal distribution for the combined residuals was fitted, with a mean of -0.061 m and a variance of 0.382 m.

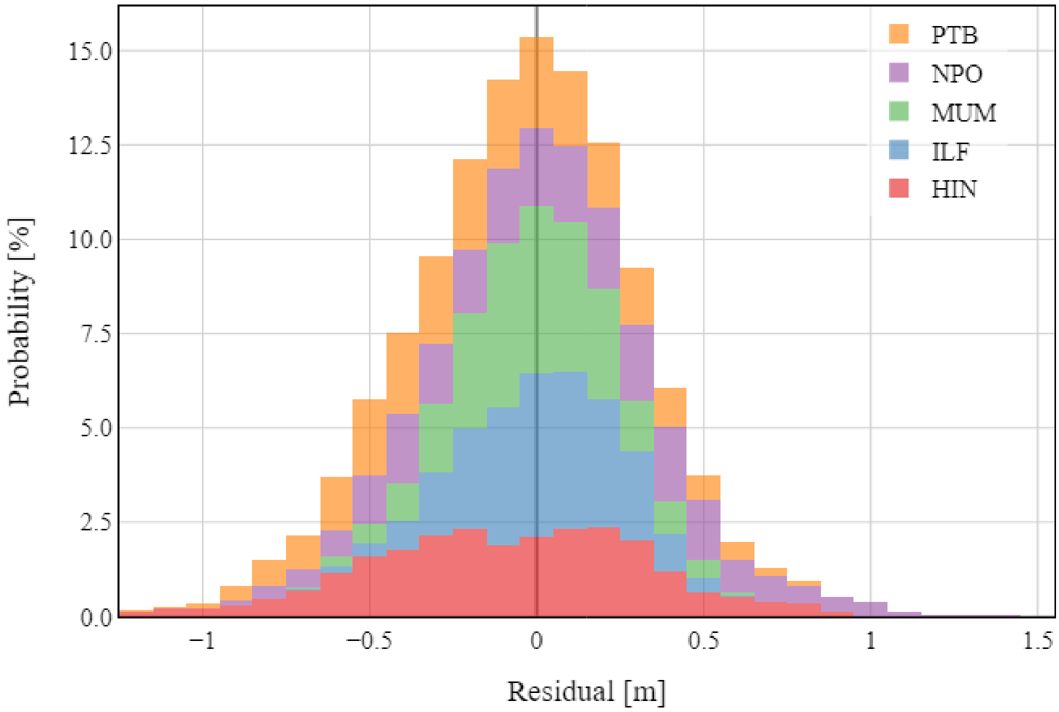

Figure 5.10: Distribution of residuals between BODC and Severn TELEMAC model at five gauging stations.

The piecewise correlation between the TELEMAC simulation and BODC measurements are further shown in Figure 5.11, including a line of best fit from a least squares regression. The plots for the four remaining calibration points are given in Appendix B.3. For Hinkley, it can be seen that the agreement is generally good, with a gradient marginally below unity.

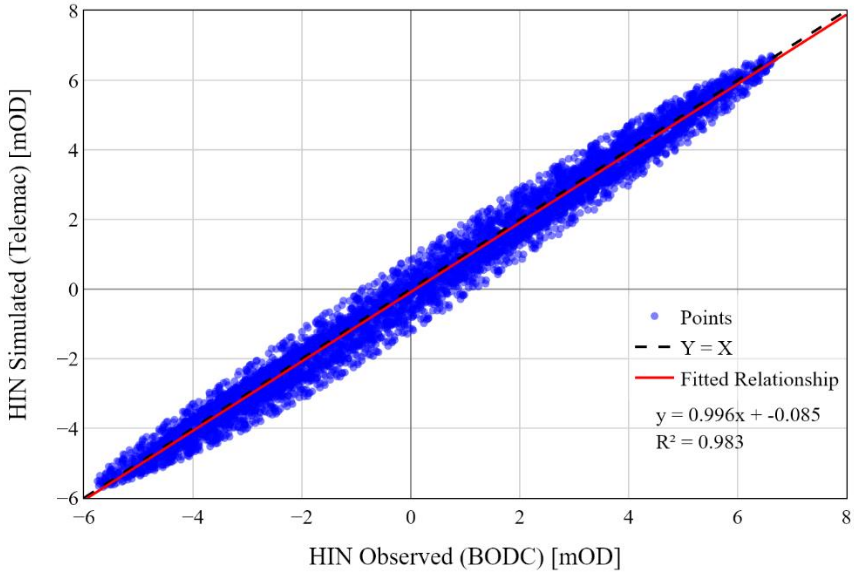

Figure 5.11: Scatter plot of simulated (TELEMAC) and observed (BODC) water levels at Hinkley over full calibration period.

5.3.2.2 Timeframe

A 0D model is computationally inexpensive in nature, not requiring the solution of multicomponent differential equations and so can typically be run for as long a duration as is required, a 2D model such as the TELEMAC model being used here is slower to run, and so requires a shorter time of operation. This allows for results to be calculated in a reasonable computational time-period and cost, and for the output files to be of a size that can be easily handled by standard software. To ensure that the effects of the changes to operation assessed in the 2D model provide an accurate image of the wider conditions, the selection of an appropriate timeframe for which to model the 2D region (with the West Somerset Lagoon in operation) required the identification of a period in which the scheme produced a representative amount of energy. To do this, the results of the 0D analysis were utilised.

The average power of the scheme using each specific operational mode $\overline{P^T}$(MW) over the year was calculated by using the net energy yielded. A start date of the 1st of February 2018 was chosen as this placed the start of the study two weeks (~1 neap spring cycle) ahead of the mean day of operation identified by Zhang et al. [236], the average power between this start point and any given moment thereafter $\overline{P^t}$ is the difference in net energy between the point being considered and the start, divided by the time between the point and the start. From these two variables, the dimensionless power error at time, namely $E(P^t)$ can be determined as presented in Equation 5.3:

$$E(P^t) = \overline{P^t}\,/\overline{P^T} - 1, \qquad \text{5.3}$$

$$where\ P = Energy\ /\ Time$$

For the single fixed, and four flexible cases described in Section 5.3.1.1 this error parameter is shown over the month of February in Figure 5.12, along with the sum of all the errors across the cases at each timestep. Here when the traces are above zero the scheme has extracted more energy than the average (or expected) up to that point, and vice versa. The sum is equal to approximately zero at four points in this period (to the nearest 15 minutes):

- 12th February 2018 at 12:00 (276 hours 10 minutes)
- 16th February 2018 at 09:00 (369 hours 00 minutes)
- 27th February 2018 at 02:45 (626 hours 45 minutes)
- 28th February 2018 at 07:15 (655 hours 15 minutes)

The seconds of these, 16/02/2018 09:00 was chosen as an endpoint as it is the shortest duration that is over the length of a neap-spring cycle 14.76 days (354.24 hours) [45]. The measured and modelled water level at Hinkley is shown for this period in Figure 5.13.

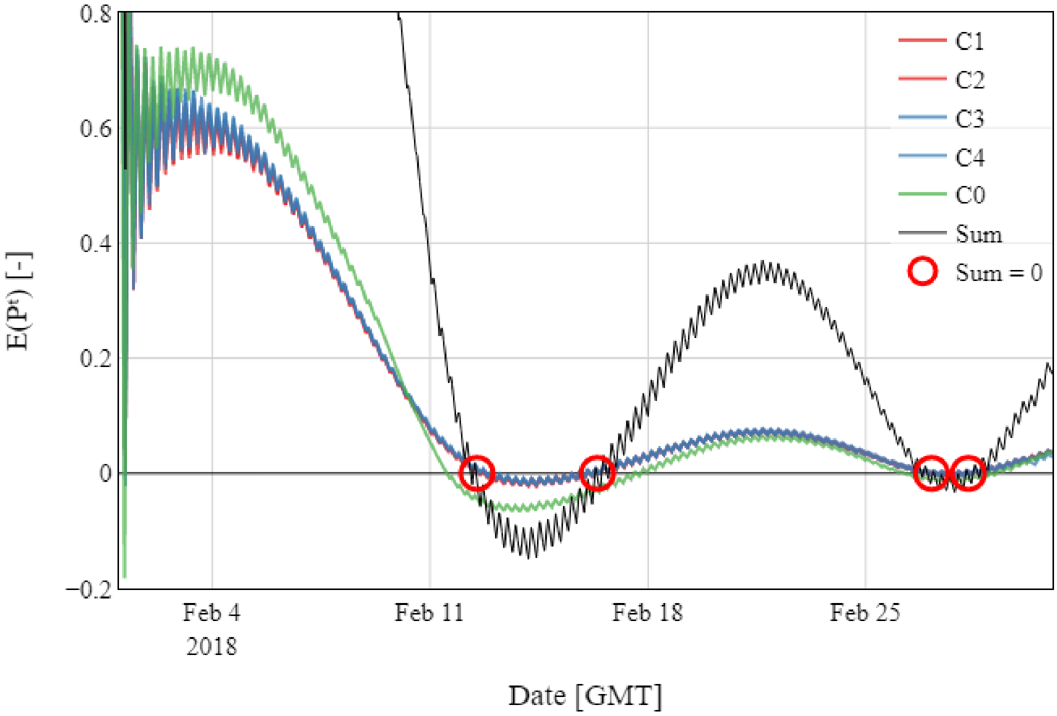

Figure 5.12: Development of representative period for WSL in February of 2018 using 0D model results, with times where the net error across models is zero indicated by the red circular markers.

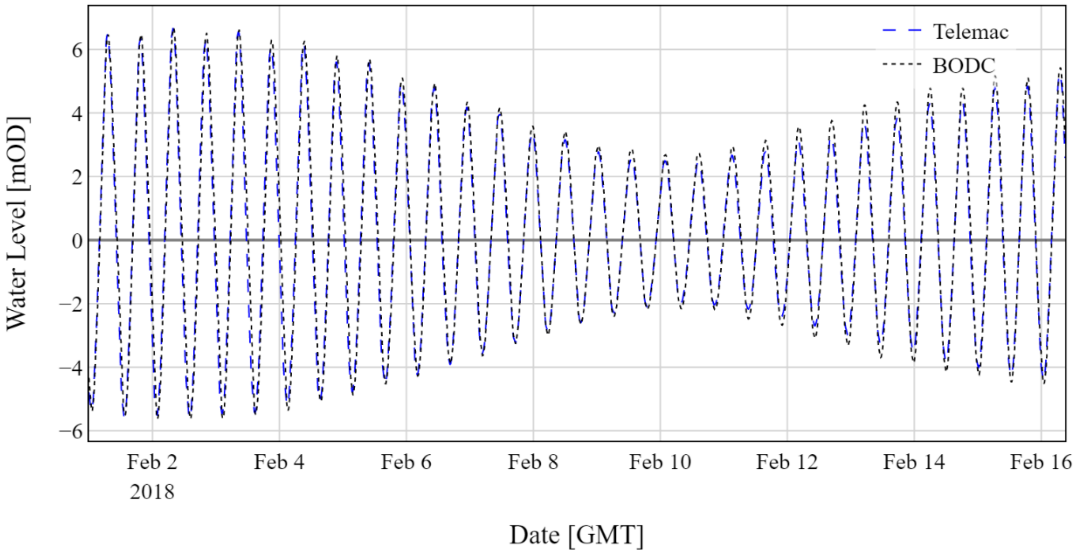

Figure 5.13: Tidal water level, both measured and modelled, at Hinkley over test period.

5.3.2.3 Pre-existing hydro-environment

With the appropriate data prepared in suitable formats, and the chosen timeframe ascertained, a baseline of the hydro-environment of the region needed to be established. The factors that are typically impacted by the operations of a tidal range scheme typically include changes to the maximum and minimum water level, which in turn connect to the intertidal area at locations where the maximum is raised over previously dry spaces, or the minimum lowered below previously wet areas and vice versa. The maximum water level across the domain in the period is shown in Figure 5.14, the funnelling and resonance effects amplifying the tidal range as the tide progresses up the estuary towards Gloucester is visible here, with the lines of equal maximum level being approximately perpendicular to the thalweg of the model.

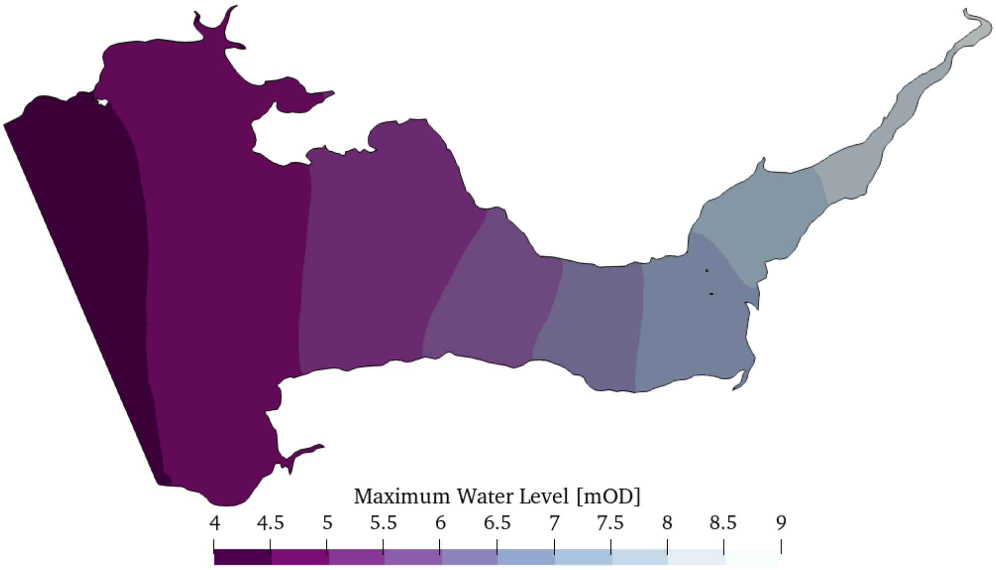

Figure 5.14: SEBC model maximum water level during representative period with respect to Ordnance Datum at Newlyn.

This increase in tidal range moving east (or upstream) is also visible in Figure 5.15 where the minimum water level is seen to decrease in elevation until the Newport-Avonmouth area. This plot also shows some of the areas where the minimum water level is ostensibly the bed level, and so the intertidal areas (isolated in Figure 5.17) can be identified. Figure 5.17 shows the intertidal flats, the areas where wetting and drying of areas occurs within the region. Notable are the large flats observed within the Bridgwater Bay, around the Gower peninsula, and between Newport and Avonmouth.

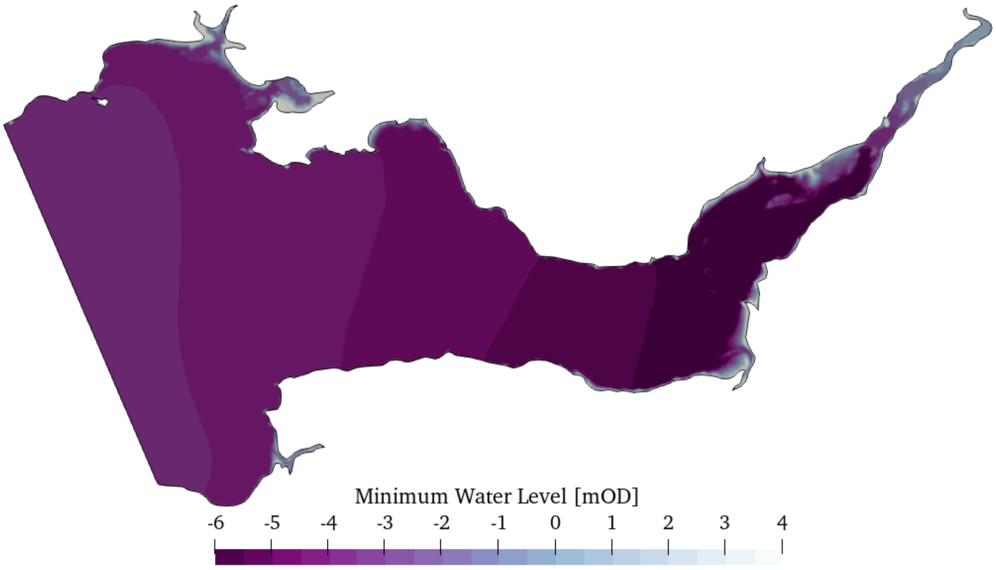

Figure 5.15: SEBC model minimum water level during representative period with respect to Ordnance Datum at Newlyn.

The contours of maximum water level, and minimum water level are broadly analogous to the progression of the tidal wave along the estuary. A cotidal chart showing the progression of the high tide peak for a typical average tide moving up the estuary is shown in Figure 5.16. The cotidal lines show a quarter hour breakdown of the tidal peak.

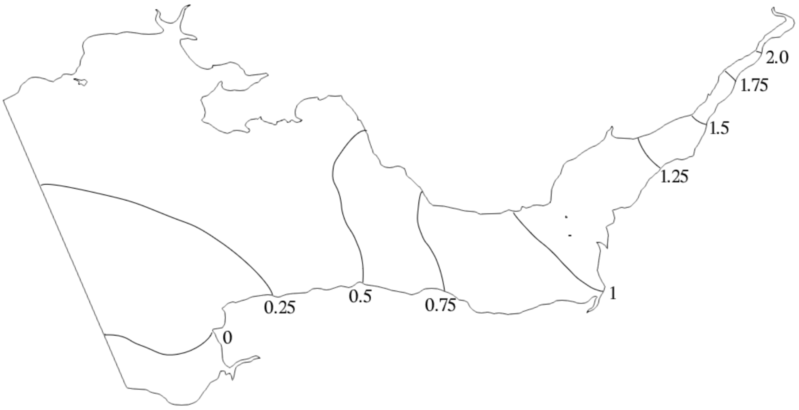

Figure 5.16: Cotidal chart of temporal lag (hours) in mean tidal high tide for SEBC model.

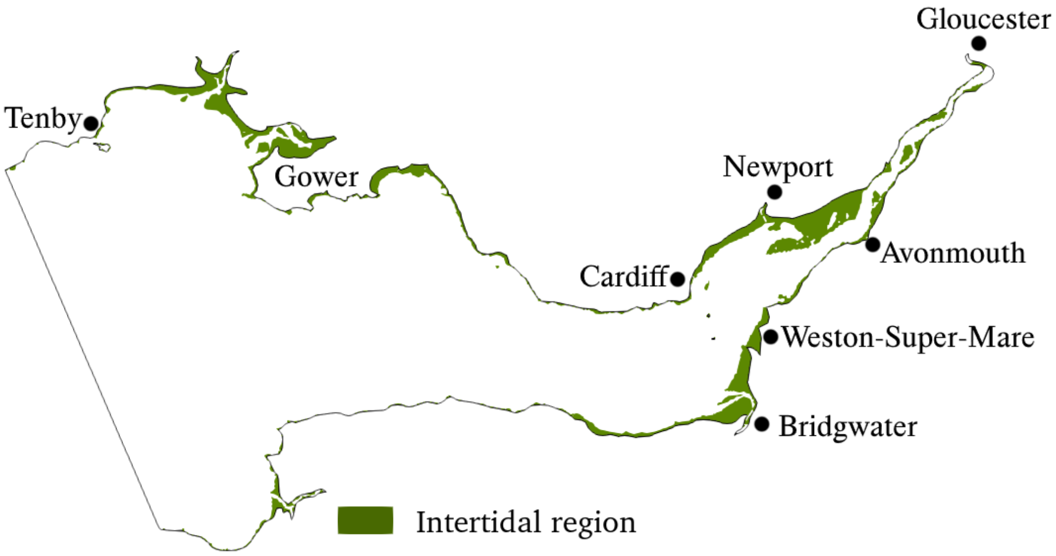

Figure 5.17: SEBC model intertidal area during representative period shown in green with major cities and towns marked.

The flow velocities in a macro-tidal estuary such as the Severn Estuary and Bristol Channel are significant both in their magnitude and degree of variation – exceeding 2 m/s in either direction around Flat and Steep Holm (between Weston and Cardiff) over the course of a tidal cycle [209]. To show the velocities in the region of the West Somerset Lagoon, snapshots of the flow field during the mid-flood (Figure 5.18a) and mid-ebb (Figure 5.18b).

Figure 5.19 shows (a) the maximum velocity magnitudes experienced in the region during the test period, and (b) the mean velocity magnitude for the same period. Note that in this region the maximum speed is largely between 1.5 and 2.25 m/s, and the mean between 0.5 and 1 m/s.

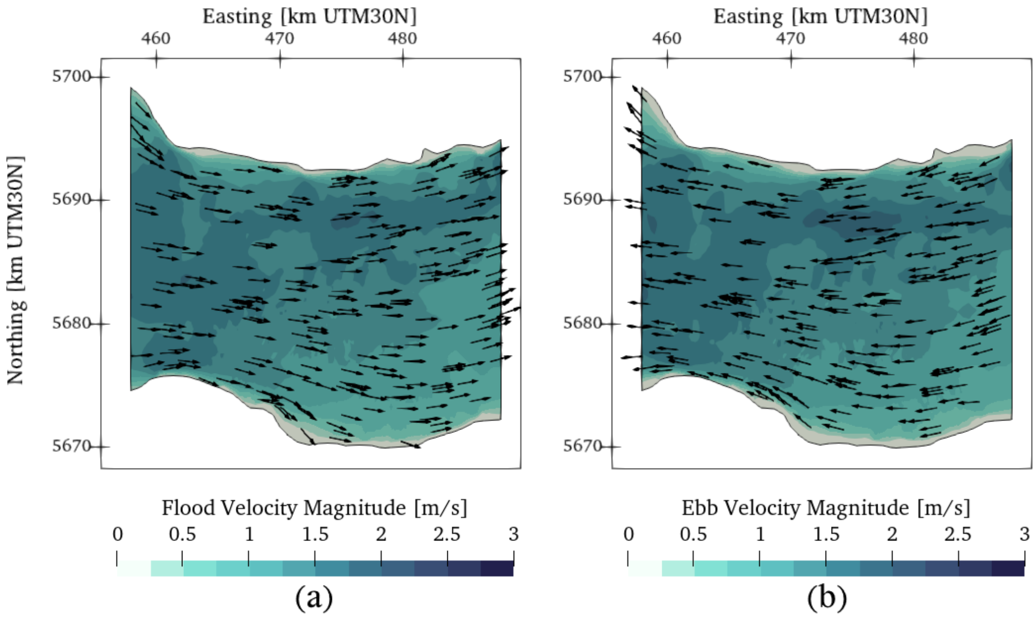

Figure 5.18: SEBC model instantaneous velocity at (a) 2018/02/16 03:45 (mid flood) and (b) 2018/02/15 22:00 (mid ebb) in the WSL region for a mid tide..

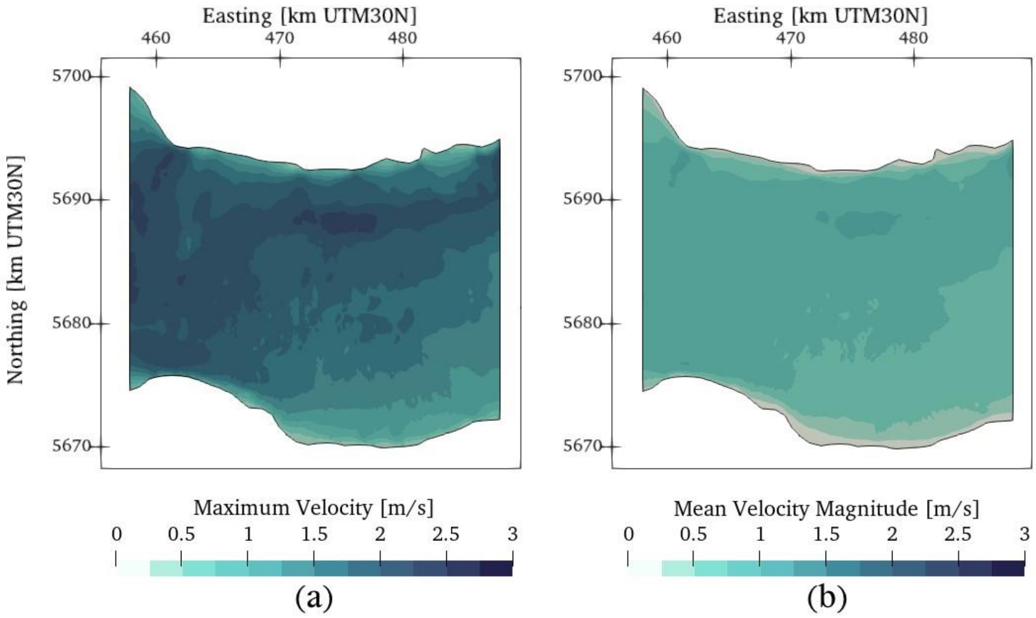

Figure 5.19: SEBC model (a) maximum and (b) mean velocity magnitude fields in the WSL region over test period.

5.3.2.4 WSL Model

The key physical element forming a tidal range energy scheme of any type is the boundary wall – this separates the internal (or impounded) area from the external – tidally driven region. In reality this is achieved via one of a few methods that amount to a physical barrier (discussed in Section 2.5). In a numerical model there are two common methods for separating the two regions, raising the elevation of the bed to physically represent a raised embankment, or removal of the elements that lie upon the embankment splitting the domain into two subdomains, termed domain decomposition. These two methods were compared by Guo [172], who found better numerical stability using the domain decomposition method – and thus this method was used here.

As the base mesh was constructed with the intent of modelling WSL, the nodal points sued to define the geometry of the scheme were included in the mesh itself, allowing for the elements that (in the base model) bridged between the interior and exterior of the WSL to be removed, separating the two sides. A detail of this around the junction of the WSL wall (vertical gap) and the existing coastline is shown in Figure 5.20, with the elements coloured grey, where the down sampling (reduction in resolution) of the coastline is also visible.

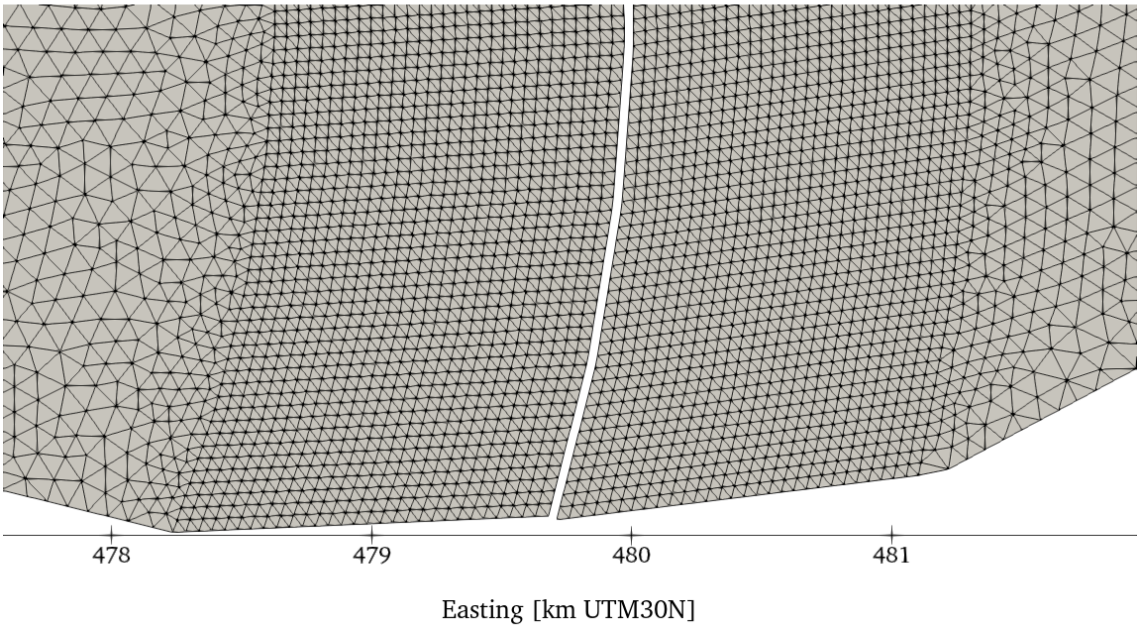

Figure 5.20: Detail view of mesh spacing, decomposition, and discretisation at junction of coastline and WSL at western landfall of lagoon bund wall.

With the internal and external regions adequately separated, the flow control structures that determined the operation must be positioned and their traits defined. For the West Somerset Lagoon, the design (number, size, and position of turbines and sluices) used here was that of Tidal Engineering Ltd[6]. This comprises 5 turbine blocks each with 25 turbines, and 8 sluice gate blocks with a total of 20 000 m² of sluice area, as was developed by Xue [130] and Guo et al. [129]. These are distributed about the boundary wall as shown in Figure 5.21, with each

---

[6] https://tidalengineering.co.uk/west-somerset-lagoon/engineering-design-and-construction/

bank being composed of 5 pairs of nodes, with the sluice or turbine nodes governed using the distributed control nodes in their radial array to mitigate instabilities due to taking water level at the node itself per the guidance of Guo [172], the node types are enumerated as follows:

- 4 - Control Nodes
- 5 – Turbine Nodes
- 6 – Sluice Nodes

A summary of the culvert numbers, turbine sizing is presented in Table 5.6, for the momentum conservation calculation through the turbines, the area of the draft tubes (diffusors) was 216 m² per turbine as recommended by Guo [129] who found this to have an impact on the wake effects developed by the flow through the turbines and sluices.

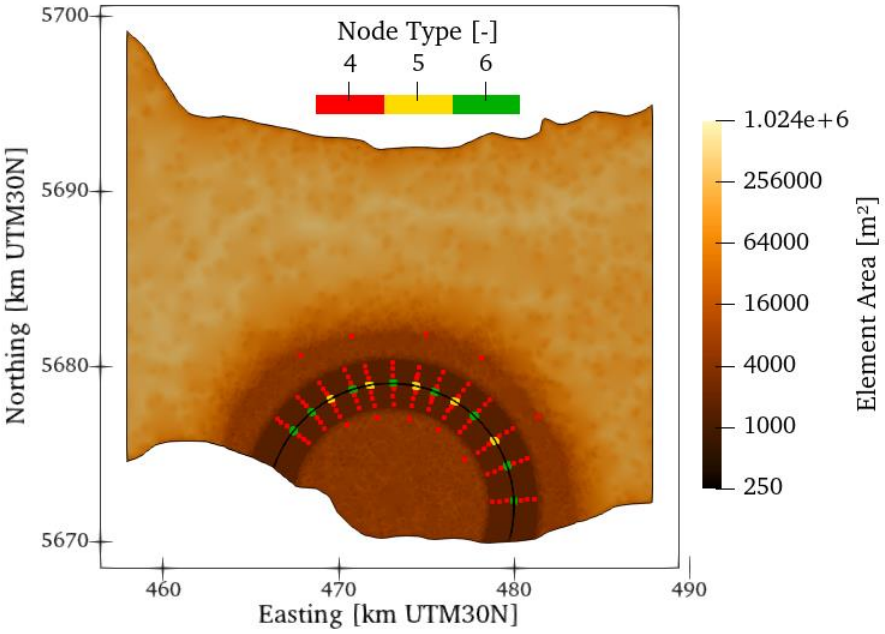

Figure 5.21: Severn WSL model lagoon nodal positions and mesh spacing.

Table 5.6: WSL model culvert specification summary.

Group	Culvert Numbers [-]	Type [-]	Turbine Diameter [m]	Combined Draft Tube or Sluice Area [m²]
1	1-5	Turbine	7.2	1080
2	6-10	Turbine	7.2	1080
3	11-15	Turbine	7.2	1080
4	16-20	Turbine	7.2	1080
5	21-25	Turbine	7.2	1080
6	26-30	Sluice	-	2860
7	31-35	Sluice	-	2860
8	36-40	Sluice	-	2860
9	41-45	Sluice	-	2860
10	46-50	Sluice	-	2860
11	51-55	Sluice	-	1900
12	56-60	Sluice	-	1900
13	61-65	Sluice	-	1900
1-13	65-109	Control	-	-

5.3.3 Model Data

To numerically represent the schemes, key physical characteristics needed defining. For the 0D model, the relationship between free surface water elevation and cross-sectional area determines how the water level will change as flow enters and exits the impoundment (Equation 3.31 to 3.34). The areas for the North Wales and West Somerset lagoons were extracted from bathymetric data, and can be seen Figure 5.22. In Figure 5.22 it is visible that the West Somerset lagoon displays a relatively uniform water level, where the highest and lowest astronomical tides are at 7.12 and -6.09 mOD (at Hinkley Point [234]). North Wales Lagoon on the other hand has an area that is over 80 % larger at the Highest Astronomical Tide (HAT) of 4.74 mOD than the Lowest Astronomical Tide (LAT) of -4.27 mOD. This is a design advantage of the WSL over NWL, as the degree to which the tidal prism is constant can be seen to affect performance – as is investigated in Section 6.4.5 for a set of disused dock basins.

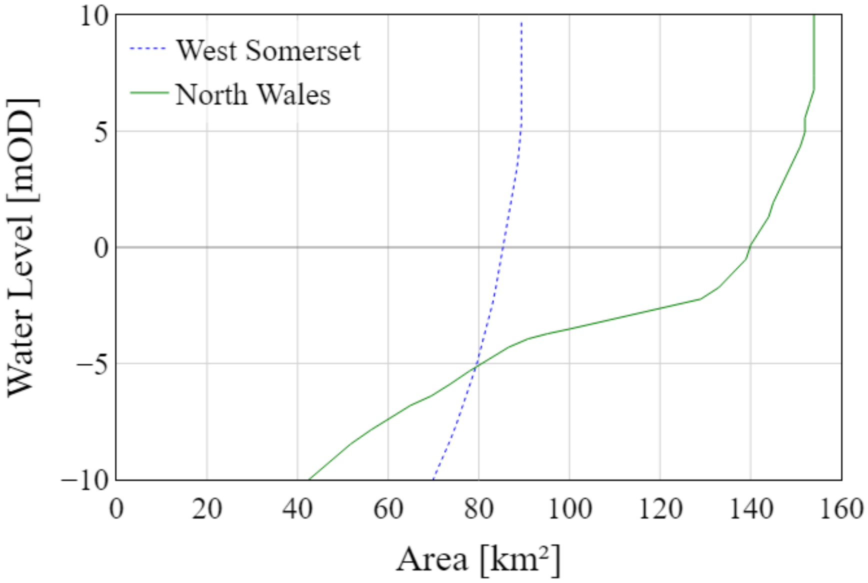

Figure 5.22: Area-water level curves for WSL and NWL.

In the majority of tidal range scheme assessments, the Andritz-Hydro two-way regulated bulb turbine, whose hill-chart can be found in Aggidis and Feather [29] has been used the peak efficiency curves for flow rate and power against head difference are shown in Figure 5.23. This turbine has a 9 m diameter, and so the scaling rule given in Equation 3.38 is applied to this to adjust the rating to the appropriate turbine size – 7.2 m diameter for WSL and 7.5 m diameter for NWL.

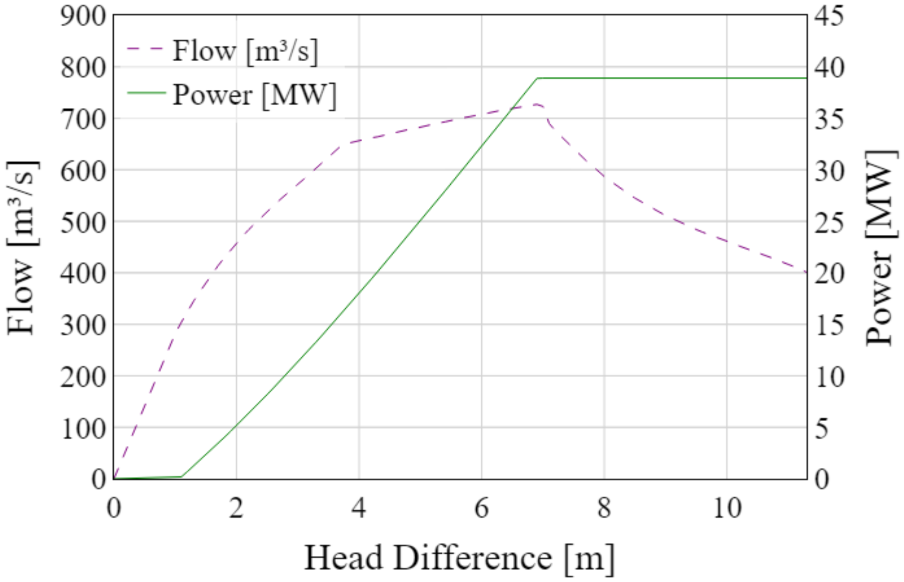

Figure 5.23: Extracted Hill-chart for 9m Andritz Hydro bulb turbine.

5.4 Results and Discussion

The 0D models were run for the duration of a year (2018) to establish the degree to which the models were able to agree to previously reported outputs for the sites when using the same operation, as recommended by Moreira et al. [194]. The year 2018 was chosen due to having a good data availability at the BODC measurement sites both at the locations of the two lagoons, and around the Severn Estuary-Bristol Channel (SEBC), which were used in the 2D component of the study in regard to the WSL scheme. Fixed operation was used for this application since the minutia of flexible control mechanisms tend to be underreported. These initial case (Case 0) models also provide an estimate to the energy and revenue yielded by these schemes over the course of the year from which proportional gains due to changes in operation can be ascertained. The control settings, and the yields associated from the two schemes, along with the degree to which the electricity generation agree with prior studies is presented in Table 5.7, with the impact these operational changes develop shown in Figure 5.24 and Figure 5.25 for WSL and NWL respectively.

Table 5.7: 0D fixed operation baseline results compared to prior studies with the control levels used, where C0 refers to the current study.

Scheme	Yield		C0/Prior Energy	Prior Study	H_{Start}	H_{End}	H_{Pump}
	[TWh/yr]	[£.m/yr]	[%]	[-]	[m]	[m]	[m]
WSL	5.968	347.5	95.7	[128]	4.9	2.5	0.0
NWL	3.837	222.5	99.9	[130]	3.7	1.3	0.0

The two schemes simulated here show a good agreement to the prior studies, with NWL having only a minimal difference between measured and reported energy extracted, and a < 5 % difference at WSL. This difference in energy yield is in both cases conservative, predicting a lower yield than the prior studies, and is due to differences in the tidal traces used (both in length and timing) along with potential discrepancy in internal model assumptions. A similar approach was used by Aggidis and Benzon [133] in comparing various configurations and models of the Mersey Barrage.

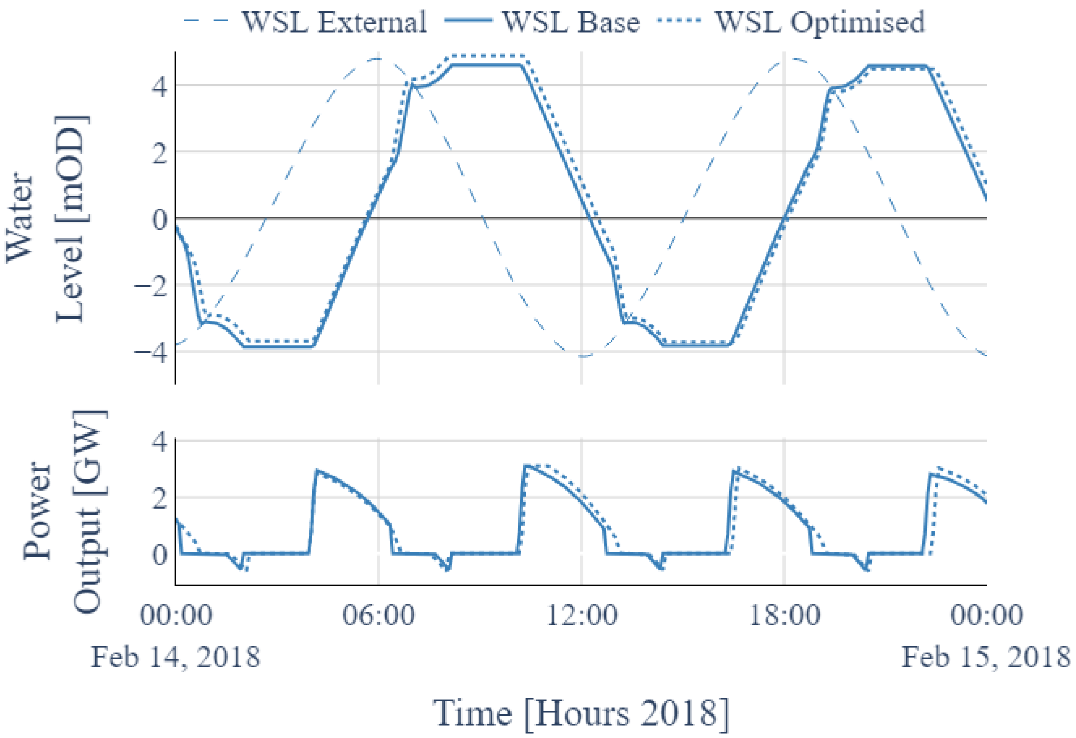

Figure 5.24: Impact of operational development at West Somerset Lagoon on sample day of mean tidal energy yield (mean tide).

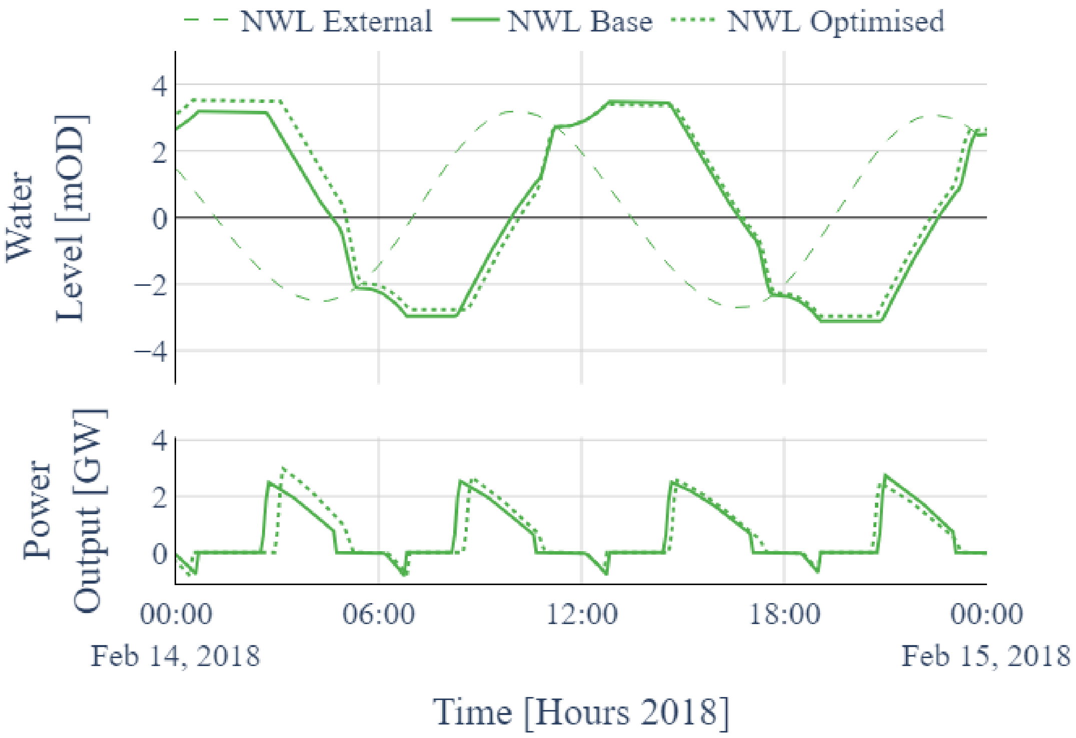

Figure 5.25: Impact of operational development at North Wales Lagoon on sample day of mean tidal energy yield (mean tide).

5.4.1 Operational Optimisation

The advantages of flexible generation over fixed control are well established, and so an improve starting point for the development of the operation is a 2-way fixed system. This was set to have $2m < \Delta H_{Start} \leq 7.5m$ with $0.5m < \Delta H_{End} \leq 3.5m$ and $0m < \Delta H_{Pump} \leq 2.5m$ using a grid search step distance of 0.1 m for all three variables. The scheme was flexed for a period of 12.4 hours at every high and low tide inflexion point (Every Half Next operation). These options were maintained for the remainder of the 0D modelling process.

5.4.1.1 Changes to flexible operation

The performance improvement due to the change to flexible operation aiming to maximise energy extraction can be seen in Table 5.8, where an increase of 20.9 % and 40.9 % in energy output can be seen for WSL and NWL respectively. This is in-line with the finding of Xue et al. [138] who found an increase of over 25 % at Swansea Bay Lagoon from the addition of flexible operation and pumping, and increases from 25-40 % energy output depending on the implementation of the flexible control system at WSL [128]. It is important to be aware that the degree to which the improvement to operation can be improved by moving from fixed to flexible operation is strongly governed by how well optimised the fixed operation schedule itself was, and how flexible the design (sizing and number of turbines and sluices) is in terms of operation.

This highlights the importance of utilising flexible operation at the earliest stage possible in the design of a tidal range scheme, with the wide difference in net energy yielded by fixed operations. As such, the remaining studies are compared to the base flexible scenario, using Case 1 as an updated starting point.

Table 5.8: Case 1 flexible energy (bold) operation results.

Scheme	**Energy**		**Revenue**	
	Yield [TWh/yr]	**C1/C0 [%]**	**Yield [£.m/yr]**	**C1/C0 [%]**
WSL	**7.219**	**120.9**	419.2	120.6
NWL	**5.408**	**140.9**	314.6	141.4

By considering the variability in the price of energy over both short and long terms (as shown in Figure 1.2 and Figure 2.2) tidal range schemes are able to expedite or delay generation, in order to increase the value of energy produced, though typically at a reduction in net energy produced. In these models the schemes were given a 12-hour forecast of the energy price (which was deemed reasonable, as energy is traded in a Day-Ahead-Market) from which to determine the best time to begin and cease generation so as to maximise revenue yield. This generation control was referred to as Case 2, with the results of this assessment listed in Table 5.9. Here the 2.7 and 3.0 % increases in revenue for WSL and NWL respectively are linked to reductions in net energy of 1.4 and 2.4 % a trend previously identified for Swansea Bay Lagoon by Harcourt et al. [22]. The greater degree of change at NWL between the two operational targets compared to WSL suggests that the NWL scheme is marginally more flexible, i.e. it can change its behaviour to a greater degree.

Table 5.9: Case 2 flexible revenue (bold) operation results.

Scheme	**Energy**		**Revenue**	
	Yield [TWh/yr]	**C1/C0 [%]**	**Yield [£.m/yr]**	**C1/C0 [%]**
WSL	7.118	98.6	**430.6**	**102.7**
NWL	5.278	97.6	**324.1**	**103.0**

5.4.1.2 Addition of parallel sluicing

Parallel sluicing was added to the energy driven flexible scenario (Case 1) to form Case 3. This allows the raw impact of this choice on the operation to be ascertained, as shown in Table 5.10. Here an increase in energy yield of 4.2 and 5.5 % was seen at WSL and NWL respectively, along with equivalent gains in revenue. Thus, it is apparent that although more energy was extracted by the schemes, this energy was wrought at a temporal distribution such that it maintained the mean value. Using parallel sluicing and an energy-based operation has the advantage that it does not require a forecast of the energy markets to be carried out, or changes to the physical make-up of the scheme, making it an effectively-cost free change. There may be changes to the hydrodynamic regime within the scheme due to this, with the sluices and turbines having different mechanics of flow.

Table 5.10: Case 3, energy-based operation results with parallel sluicing.

Scheme	**Energy**		**Revenue**	
	Yield [TWh/yr]	**C1/C0 [%]**	**Yield [£.m/yr]**	**C1/C0 [%]**
WSL	**7.522**	**104.2**	437.2	104.3
NWL	**5.704**	**105.5**	332.1	105.6

Finally, the two operational changes were combined to assess how they would work in conjunction, with a parallel sluiced operation looking to optimise revenue – Case 4. The results for Case 4 with comparison to the updated flexible baseline are given in Table 5.11. For both schemes, this resulted in the most revenue – with increases of 6.7 and 8.6 % for WSL and NWL, with reductions in the energy produced as compared to Case 3. The two independent additions to tidal range energy control can be seen to stack with each other, resulting in a best-case operation. For the two schemes assessed, this produced a net revenue gain of approximately £55 million, and 376 GWh of energy per year. In a year where the mean price of energy was 57 £/MWh this method increased the value of the energy extracted by the lagoons from ~58 £/MWh to 61 £/MWh.

Table 5.11: Case 4 flexible revenue operation results with parallel sluicing.

Scheme	**Energy**		**Revenue**	
	Yield [TWh/yr]	**C1/C0 [%]**	**Yield [£.m/yr]**	**C1/C0 [%]**
WSL	7.428	102.9	**447.2**	**106.7**
NWL	5.575	103.1	**341.6**	**108.6**

A comparison of Case 1 and Case 4 operations (termed ‘Base’ and ‘Optimised’ respectively) for the West Somerset and North Wales lagoons in terms of water level and power output are shown in Figure 5.24 and Figure 5.25. The chosen date was the 14th of February, as this was identified as the date where energy output was closest to the annual mean for the schemes in [236]. These plots show how the small changes between the operations occur over a given period, such as the NWL maintaining the higher internal level in the initial generation period with the updated operation, but still being able to empty to a comparable point, having produced a higher output over a shorter duration in that period. At 12:00 in the case of the WSL, the generation during the sluicing period is clearly visible, a key advantage of the parallel sluicing method, as this would otherwise have been a period of non-generation. The combination of the small differences between the base and optimised operational schemes improved revenue without requiring additional investment.

A comparison of how these generation profiles compare to the actual contributions to the National Grid from Feb 14th, 2018, is shown in Figure 5.26. This shows an example of the scale of the contribution that tidal range would form in comparison to the existing sources of electricity, with the traces stacked. As Figure 5.26 shows, the base level of demand is met by nuclear power (pink trace), with the level of output constant over the sample day. Wind, offshore and onshore (purple trace) increases as the day goes on, driven by the weather on the day. The gas contribution (red trace) shows a shape that is markedly similar to that of the average demand pattern in the country (shown in Figure 2.2) – suggesting that this energy source is the one most used to meet the variation in demand.

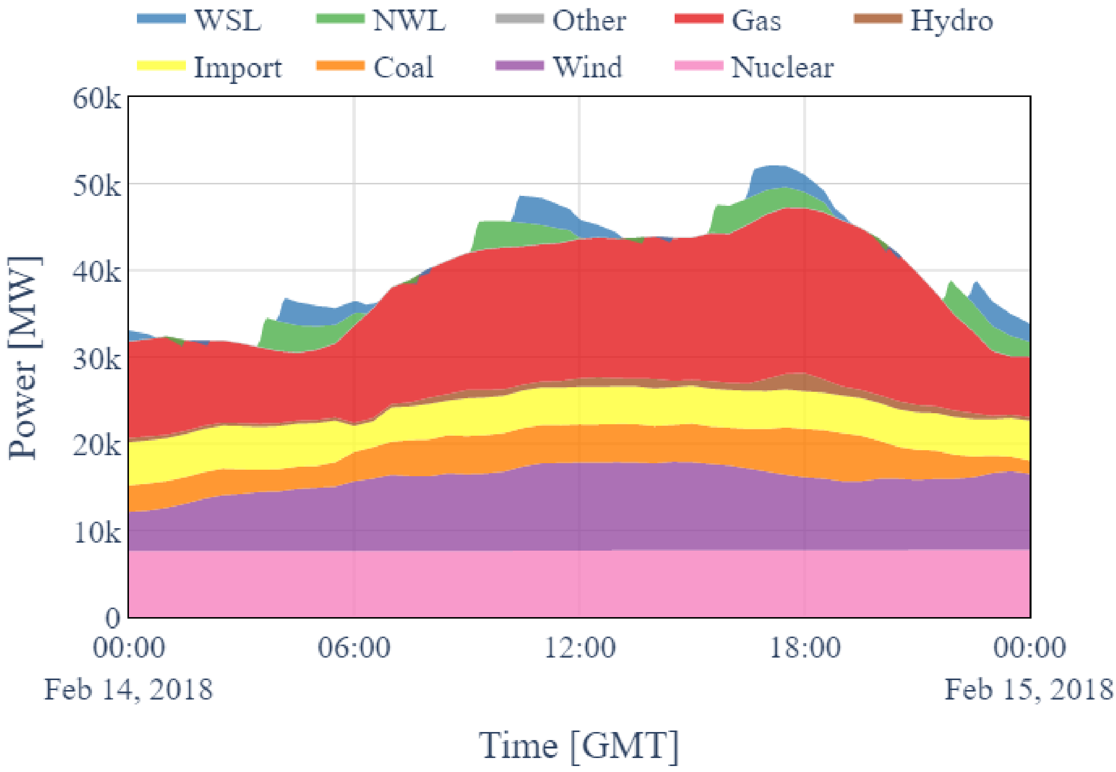

Figure 5.26: Theoretical contributions of optimised tidal range schemes to GB energy mix on sample day of mean tidal energy yield (mean tide).

As one of the majorly cited advantages of tidal range over other renewables is the dispatchability (option to control timing of generation to meet demand) this should place the technology in a position to reduce the need to use gas turbines, who fill this role currently. A simple image of how this might be developed is shown in Figure 5.27. In Figure 5.27 the electrical energy generated by tidal range over the day is removed from the energy required from gas, there is also an increase in the gas demand at times where the tidal range schemes are pumping, shown by the red extensions above the black 'original' line.

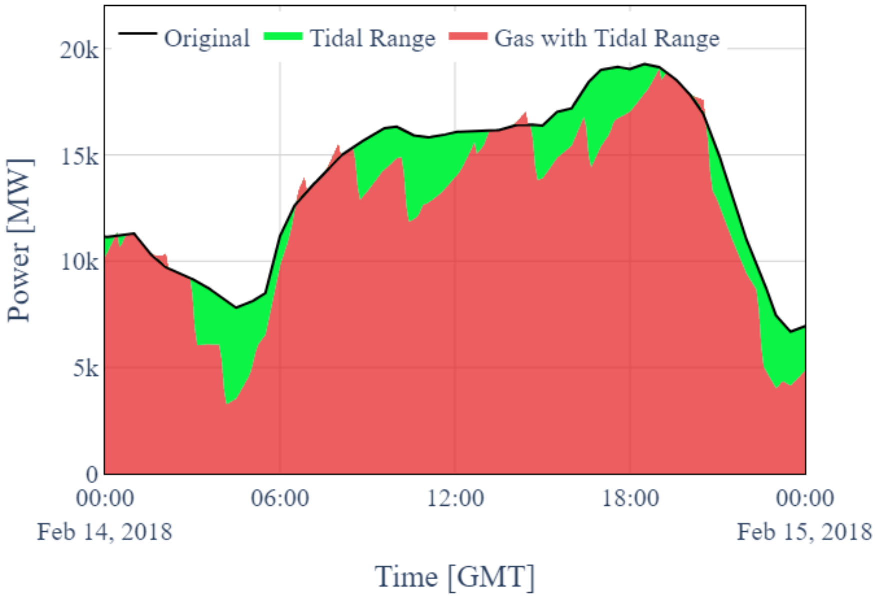

Figure 5.27: Potential reduction in gas turbine dependency due to tidal range on sample day of mean tidal energy yield (mean tide).

Combined Cycle Gas Turbine (CCGT) power plants have been estimated to produce approximately 350 $kgCO_2/MWh$ [237], whereas the operation of a tidal range scheme has been estimated to have a carbon emission of less than 0.05 $kgCO_2/MWh$ [238] during the operation period. Therefore, a tidal range scheme operating in place of a gas device would be effectively reducing the carbon contribution of the grid. For the two schemes using an optimised operation, the combined annual output of 13 TWh (7.428 TWh from WSL and 5.575 TWh from NWL) equates to a reduction of approximately 4.55 million tonnes of CO_2 per annum; there will of course be a capital carbon cost as the materials involved in large maritime construction alone have an inbuilt cost. The question of reduced carbon production ostensibly mirrors the financial situation surrounding the building of a tidal range scheme, with a large up-front cost and long-term returns. The development of sustainable construction methods could assuage this, also reducing the need for carbon-capture methods. This analysis assumes that the energy required to pump water would in turn result in an increased energy requirement during the pumping periods, as such even a full suite of tidal range schemes working in unison is unlikely to be able to provide the full coverage achievable through gas generation.

The schemes in this analysis use the price of energy as a control variable, operating to maximise revenue; this is taken as a surrogate for demand, however other options for control could be incentivised in a future energy scenario. One example of this would be operation to mitigate or absorb the energy imbalance between supply and demand. This would see the scheme operating to a greater extent as a pumped storage facility.

The examples of operation from Figure 5.25 through Figure 5.27 use a representative day to provide an image of how the operation of the two tidal range schemes combined on a sample day, however the timing of the tides varies throughout the year, and thus so will the electricity yielded by the tidal range schemes. Figure 5.28 shows the probability of exceedance of the power generated by the two schemes over the year, with ~20 % of the time being pumping, ~13 % of the time there being no power generated or required for pumping (3 Hours and 11 Minutes per day on average). And various levels above this, with an output of over 1440.2 MW being produced 50 % of the time.

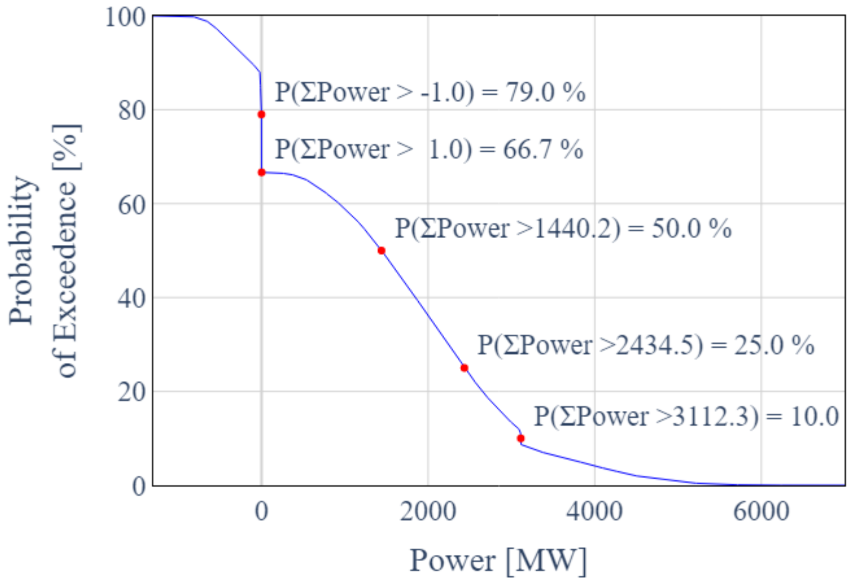

Figure 5.28: Probability distribution of combined schemes power when operated over full year under optimised operational system.

To see how this relates to the time of day, the annual combined operation, a 2D histogram partitioning the operation by the time of day and the power output is presented in Figure 5.29 (the occurrences being the number of days on which the schemes at this time produced this level). It can be seen that the most common state for the schemes at most times of day is no output or a small pumping demand (negative power). The flexibility of the schemes operating to produce at preferred times leads to increased energy output levels during the typical working hours (09:00-17:00) and a peak mean output at 19:00. This plot shows that the two schemes are able to work in a coordinated way to respond to high demand levels, but this is still not to the degree of gas turbines, with there still being periods of generation during the low demand periods (such as between 00:00 and 9:00).

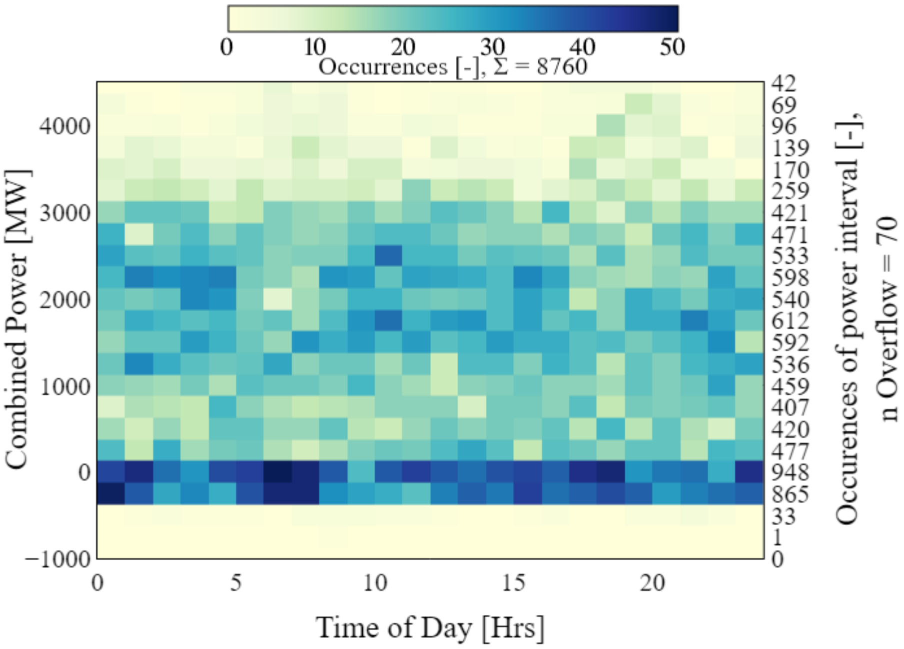

Figure 5.29: Number of days where combined energy production was at a given level at a given time, with totals for occurrence of each power output level.

The energy mix of the GB grid, along with many around the world, has evolved from 2018, driven by factors including changes in end-user behaviour, economic drivers, and meteorological variations both over long and short terms. In the first quarter of 2018, gas produced 36.0 TWh of electricity, approximately 39.9 % of the total electricity generated [239], and in 2022 gas contributed 28.0 TWh, or 33.3 % of the total electricity generated. Renewables in this period grew from 30.1 % to 45.5 % of the electricity generated, a result of the drive to reach net zero [240]. This trend is visible in the moving energy mix plots shown in Figure 1.1 and Figure 2.1. Therefore, although the role of gas is decreasing, grid operators continue to rely on gas to balance supply and demand. Considering the need to decarbonise the energy network further, and lack of existing grid-scale low carbon storage facilities, replacing reliance on gas and full decarbonisation of this component of the electricity mix is challenging. Subsequently, the role of tidal range in migration to net zero can be vital as tidal range schemes offer a mechanism by which to reduce gas-based generation in the UK by approximately 10 %, specifically looking to meet demand periods where the currently dominant renewable sources lack the degree of dispatchability of tidal range. Classical tidal range schemes are still constrained by their place in the environment and so are constrained by the physical limits of the surrounding environment. Therefore, they do not provide storage solutions, however through appropriate design and operation they effectively operate on a modified energy arbitrage principal in many places (buying energy to pump and selling it when generating at financially advantageous times), without the dependency on the rare earth metals used in many batteries.

5.4.2 Design Optimisation

With the understanding of an improved operation developed for a given design, the question of how alterations to this design could improve revenue can be assessed, in order to potentially exploit the areas where return on investment may have improved. To achieve this, the two schemes were run with a range of turbine numbers and sluice areas for the first quarter of 2018. The changes in revenue at varying configurations for WSL can be seen in Figure 5.30, and for NWL in Figure 5.31, with the optimised operation of the prior design (Case 4) marked with a ‘+’ symbol.

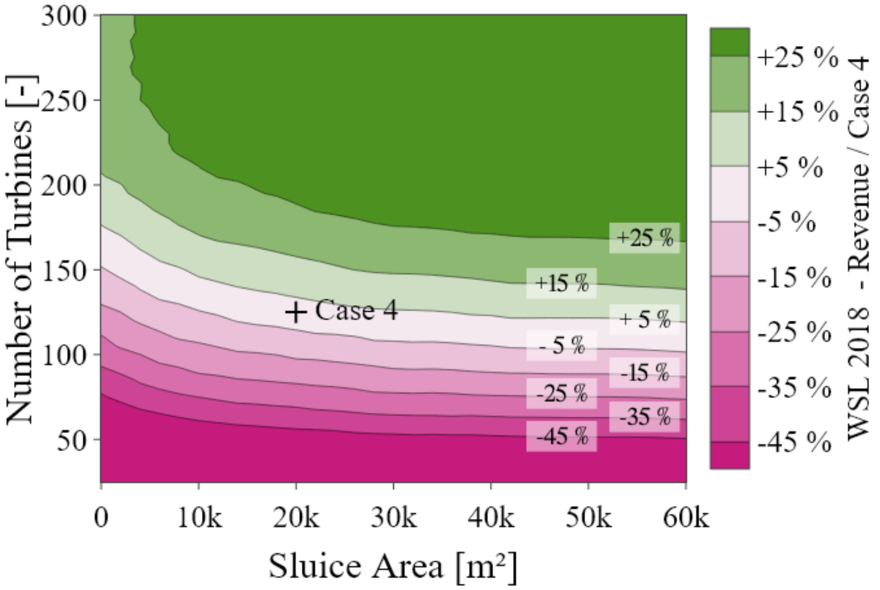

Figure 5.30: Revenue yield across WSL turbine and sluice number design space, with the initial design marked as a '+'symbol labelled Case 4.

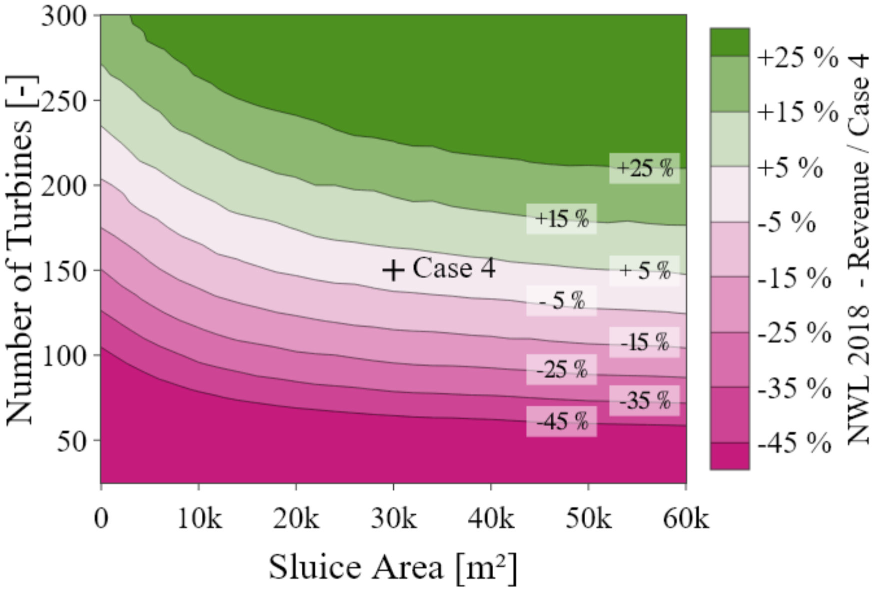

Figure 5.31: Revenue yield across NWL turbine and sluice number design space, with the initial design marked as a '+'symbol labelled Case 4.

5.4.3 Comparison of 0D and 2D Results

0D modelling has long been used to improve operational characteristics, but the simplification of a vast multi-faceted engineering problem to a non-physical model will inevitably yield some behaviour or effects that are less evident in a more thorough representation. For each of the cases of operation outlined in Table 5.1, the control limits (ΔH_{Start}, ΔH_{End} and ΔH_{Pump}) were extracted from the 0D model operation over the representative period and mapped into inputs for the 2D tidal range scheme model of the West Somerset Lagoon. The scheme was then modelled using these control limits and the difference between the energy extraction and revenue yielded compared for the two methods over the given period of time presented in Table 5.12. For all cases it can be seen that the 0D model over-estimates the energy and thus associated revenue yielded by the scheme using the given operation. The magnitude of the difference is broadly uniform across the operating conditions, at ~12 %. This tracks across from the energy produced to the revenue (which is a function of power).

Table 5.12: Comparison of 0D and 2D tidal range scheme performance metrics through representative period (factored up to annual output).

Case	Energy			Revenue		
	0D [TWh/year]	2D [TWh/year]	0D/2D [-]	0D [£.m/year]	2D [£.m/year]	0D/2D [-]
0	5.800	4.543	1.277	282.9	223.1	1.268
1	7.256	6.492	1.118	357.0	319.8	1.116
2	7.165	6.400	1.120	363.8	327.8	1.110
3	7.570	6.708	1.128	372.6	329.5	1.131
4	7.463	6.604	1.130	378.4	335.7	1.127

The differences seen between the two models applied here are not insignificant. The difference between two models doing a similar comparison was given by Guo [172], included here as Table 5.13 for reference. The largest contributor to the differences is undoubtedly from the external water level used in the 0D model as compared to that developed by the 2D model. This is shown in Figure 5.32 for the sample day. Note how the external 2D model water level has a lower tidal range, on the sample day this accounts for an example tidal range of 9.62 m in the 0D model and 8.55 in the 2D model, a 12.5 % difference. When this assessment is expanded to the entire modelled period, this becomes an 11.7 % overestimate in the tidal range at the site due to using the water level taken at the measuring station. For a scheme of this size there will also be an impact on the tidal range due to the constriction of the estuary by the impoundment itself. This would likely be lower in the case of the NWL – which sits on a more open section of coast, however the difference between the nearshore and offshore tidal levels would need accounting for in future assessment.

It can be seen that for the sample day shown in Figure 5.33, the tidal range input of the 0D model (the external water level) is greater than that of the modelled 2D scheme, and thus per the fundamentals of tidal range energy one should expect a lower energy yield. The development process of a tidal range scheme using tools such as this is an iterative and ostensibly cyclical process, whereby an operation can be obtained using a 0D mode, assessed with a 2D model, the inputs and assumptions refined, and the process repeated. In this case it is apparent that the match between the measured points on the existing estuary and the offshore position of the lagoon structures, combined with the impact of the structure itself on the hydrodynamics of the region (shown in Section 5.4.4) contribute to the 2D model yielding a 12 % lower energy and revenue than the 0D. Highlighting the need for complementary 0D and 2D modelling cycles.

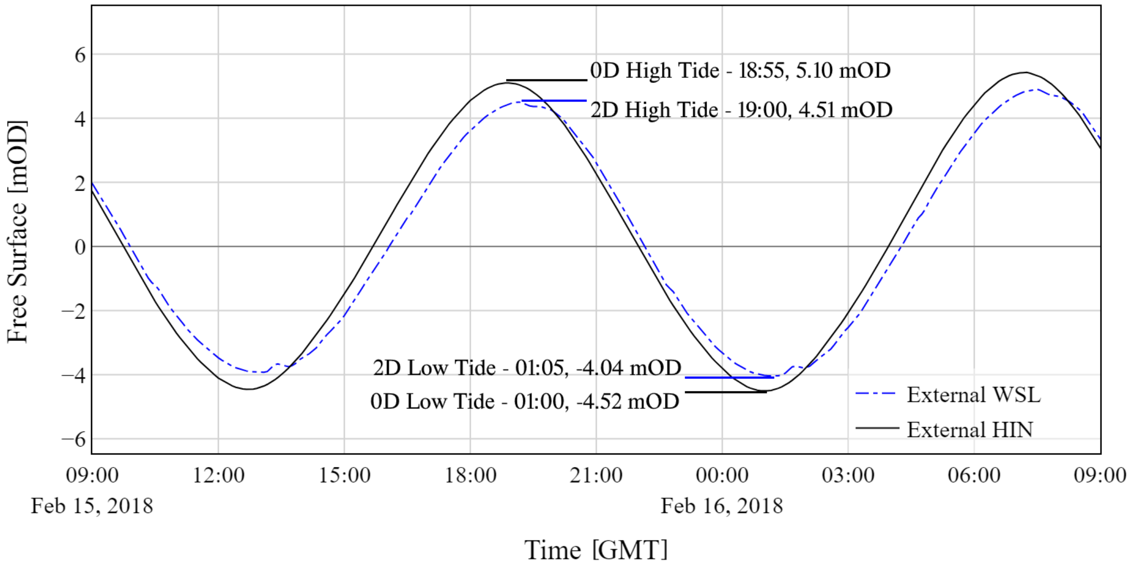

Figure 5.32: Comparison of measured and modelled water levels at Hinkley, and the WSL offshore location with and without the tidal range scheme (under operating Case 1, on mean tide).

This difference in 0D and 2D model predictions is mainly created by the selection of the water levels in the 0D model. The 2D model takes the water levels across each turbine bank and calculates the power at said bank and sums the output to calculate the power of the scheme. This way, water levels in the proximity of the turbine block is effectively used to calculate the flow and consequently power generated by the turbines at each time step. In the 0D model as used here, the tidal trace comes from a single position for both inside and outside the lagoon.

The outside water level was taken from a tidal gauge near the proposed scheme. Although, errors in available power were expected, this was done in order to create early-stage design of tidal range schemes where 2D models are not available.

Any single position will have a higher maximum and lower minimum than the mean of a set of points over the course of the tide. Per private communication, the 0D model used by Guo [172] utilised multiple water level inputs, and thus mitigated that error mechanism. Based on this, the multiple blocks method should be utilised when possible in the 0D modelling of tidal range schemes with large spatial distribution between proposed turbine banks – in line with the conclusions of Xue [130].

Table 5.13: Comparison of 0D and 2D tidal range scheme output for one tidal cycle (reproduced from Guo [172], Table 5.2).

Turbine Operation Head (m) (All in two-way generation)	**Energy Output (TWh) in one entire tidal cycle**		
	0D [TWh/year]	**2D [TWh/year]**	**0D/2D [%]**
H_start=4.9; H_end=2.5	0.196	0.198	99.0 %
Optimized flexible generation head	0.233	0.232	100.4 %
H_start=5; H_end=2.5; H_Pumping=2	0.247	0.249	99.2 %
Optimized flexible generation head and pumping head	0.269	0.270	99.6 %

The difference between the external water levels is exemplified in Table 5.14 which gives a statistical match for each of the key operational metrics of the schemes to the 0D model. Since the external water level is a primary driver to all the remaining operations of the scheme, the difference in the traces grows as the parameter under consideration is further abstracted from the water level. The internal level shows a fairly consistent degree of agreement, being a good metric for the extent to which the level-pond assumption is valid for this lagoon. The turbine flow in the majority of cases shows a statistical match in line with the product of the internal and external levels – being driven by the difference between the two, with a similar if worse match for the power output.

Table 5.14: R² statistical agreement of 0D and 2D tidal range scheme operational state.

Case Name	**External Water Level** [-]	**Internal Water Level** [-]	**Turbine Flow** [-]	**Sluice Flow** [-]	**Power** [-]
0	0.976	0.860	0.816	0.289	0.713
1	0.974	0.948	0.809	0.102	0.756
2	0.974	0.951	0.851	0.239	0.779
3	0.974	0.948	0.839	0.246	0.766
4	0.974	0.951	0.835	0.157	0.796

The sluice flow shows the weakest match across the board, however a when the data is plotted the reason for this becomes more apparent. Figure 5.33 and Figure 5.34 show a single day of operation (the final 24 hours of the representative period), here it can be seen that the nature of the sluice flow leads to this poor agreement, short duration peaks of high flow many hours apart. If the 0D and 2D model flow peaks are out of phase the statistical agreement becomes very poor since the scale of difference between them is large, even if the general behaviour is similar. Interestingly, the sluice phase is the period of the model where the two systems tend to converge in terms of water level the best – as small differences are naturally accounted for – higher head differences reducing faster – and thus mitigating themselves for example.

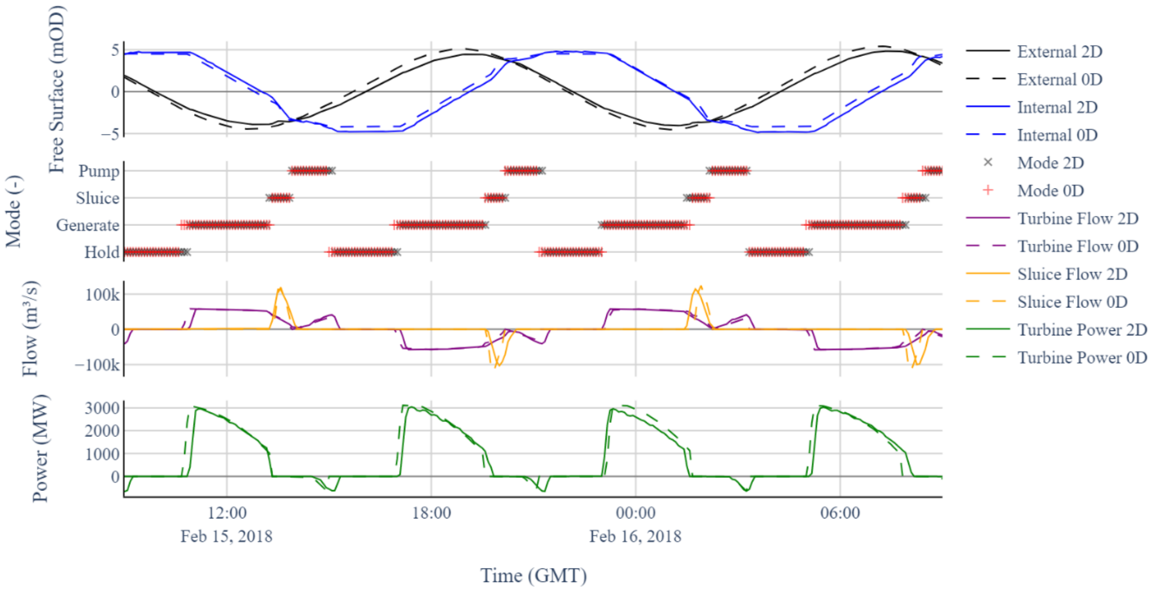

Figure 5.33: Comparison of 0D and 2D operation using energy based operating mode Case 1 over final 24 hours of 2D simulation (mean tide).

A key output from tidal range scheme models is the energy produced by the scheme over the selected period. This is calculated based on the head difference across the scheme, in Figure 5.33 and Figure 5.34 the way in which the difference in water levels propagates to the energy can be seen. The two models show good agreement at the start of generation, where the schemes have been in a holding phase and thus the internal regime of the 2D model has been able to settle – bringing it closer to the assumed flat surface defined in the 0D system.

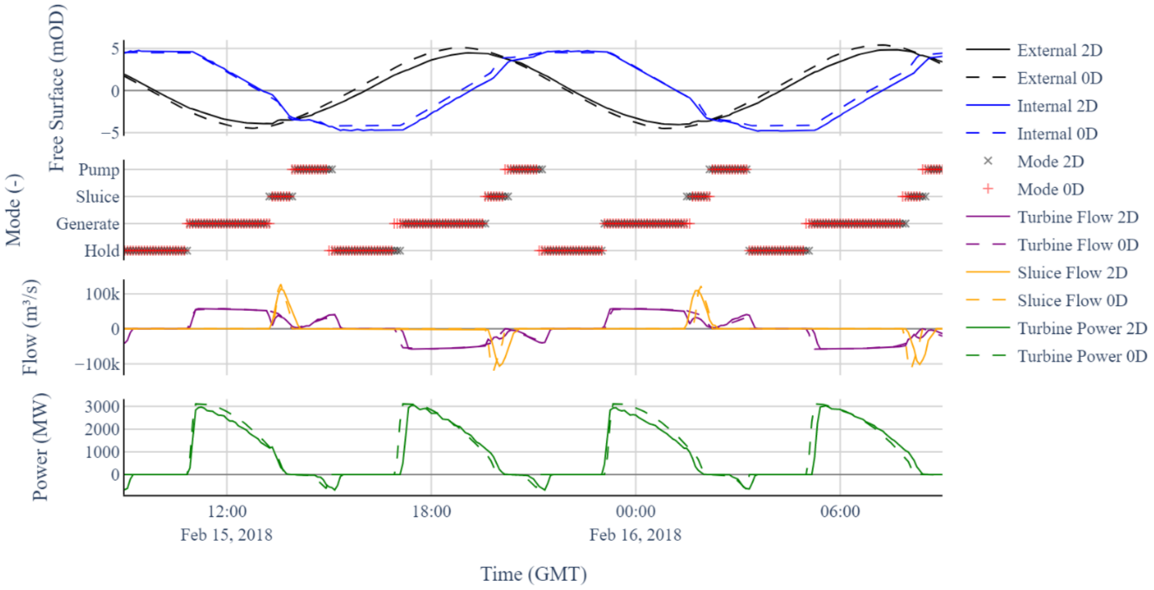

Figure 5.34: Comparison of 0D and 2D operation using flexible – revenue based and parallel sluiced operating mode Case 4 over final; 24 hours of 2D simulation (mean tide).

The key aim of the 0D study was to identify the way in which operational changes over the long term could improve performance. The improvements wrought over the course of a year are less evident in this shorter-term period, as compared to the corresponding 2D gains in Table 5.15. It can be seen that the change from a fixed generation cycle to flexible operation (Case 0 to Case 1) yields a significant increase in both 2D and 0D, as has been found to be the case in multiple prior studies. The difference between revenue and energy-based generations is also captured to broadly the same degree by the 0D and 2D models (Case 2 and Case 1 respectively) – with both showing the classical reduction in net energy and associated increase in revenue yielded, with the 2D model in fact showing a greater degree of improvement. The addition of parallel sluicing when considering only energy (Case 3 compared to Case 1) resulted in an increase in energy that was significant over the 2D and 0D models, this was then again improved in terms of revenue increase when the operation set to target times of high value (Case 4 produces more revenue in both 2D and 0D than Case 3). Making the parallel sluiced operation targeting =revenue the most profitable in the 2D model as expected from the 0D analysis, though not the configuration producing the most energy. This highlights a key aspect of tidal range that proponents have held for a long time, being the ability to generate at times of value – where traditional cost metrics for renewables are based solely around the energy output potential.

Table 5.15: Energy and revenue improvement from operational changes in 0D and 2D through representative period.

Cases Compared	**Energy Improvement [-]**		**Revenue Improvement [-]**	
	0D	**2D**	**0D**	**2D**
C1/C0	1.251	1.429	1.262	1.433
C2/C1	0.987	0.986	1.019	1.025
C3/C1	1.043	1.033	1.044	1.030
C4/C1	1.029	1.017	1.060	1.050

5.4.4 Environmental Impact

A key barrier to tidal range scheme development has historically been the negative environmental impacts associated with the schemes, the large man-made constructions in potentially environmentally/ecologically sensitive areas of coast can often overshadow the energy needs. 0D modelling can provide a minor degree of insight into the hydro-environmental effects a TRS may impose (such as changes to the internal water level, or mean velocities expected through the turbines and sluices), but for a more detailed picture a 2D model is fundamentally necessary.

The key elements a tidal range scheme is likely to impact are the high and low water levels (due to the volume of water impounded in the scheme itself at the time), which themselves link to the intertidal area within the region, and the near-field velocities developed by the scheme primarily developed by the sluices and turbines. To provide an insight into whether the operational changes proposed by the 0D study would have a detrimental affect on the hydro-environment of the region, the base (Case 1) and final (Case 4) hydrodynamic responses are presented here (with the corresponding plots for the remaining cases given in Appendix E).

As all the schemes use the same maximum and minimum head difference levels in their flexibility configuration, and the difference in energy produced through the alternative operations is only up to 5 % in the 2D model – the operational cases are unlikely to be very different. Figure 5.35 shows the change to the maximum free surface elevation over the sample period due to the operation of the West Somerset Lagoon using the base flexible case of operation. Here it can be seen that the scheme causes a decrease in the maximum water level around the scheme, with the impact reaching to the upstream end of the estuary model. The largest impact is in-fact within the impoundment itself where the maximum level is decreased by over 0.5 m. The changes to the regime within the scheme could be mitigated through an operation choice to maintain prior tidal levels – at a detriment to energy production. This ability to control the internal maximum water level is in-turn a key design driver in the case of some schemes such as the Sihwa Lake and could be valuable for the WSL as the area has experienced flooding in previous years.

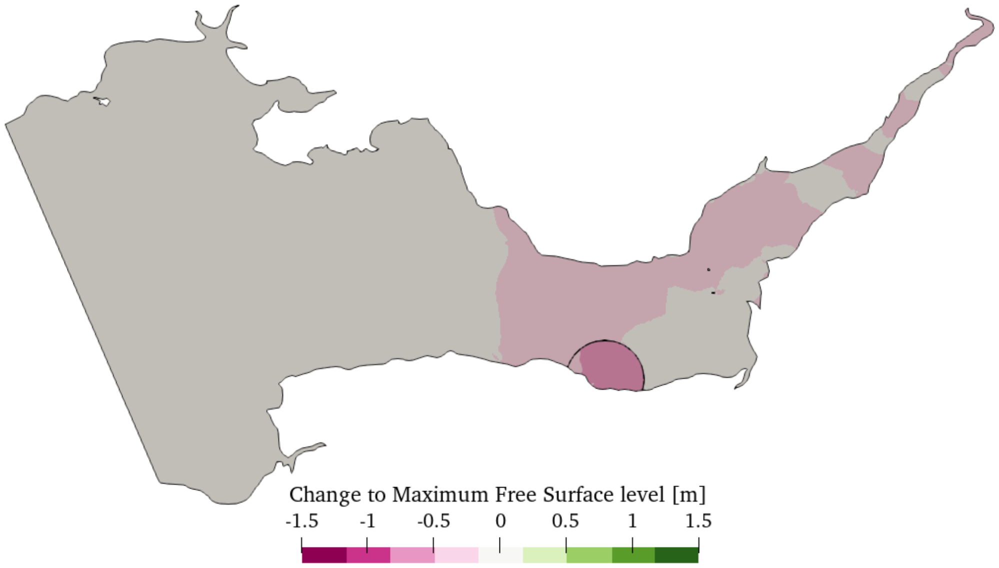

Figure 5.35: Change to maximum water level in SEBC model due to WSL using Case 1.

The change to a parallel sluiced revenue-based operation in Case 4 shows a similar general pattern in the region, with the largest reduction in maximum water level being within the lagoon itself – and a greater reduction than the base case being shown in Figure 5.36. This optimised case shows a smaller decrease in the maximum tidal water level to the north-east of the West Somerset Lagoon, although again a small decrease is visible at the tidal limit of the model.

The change to the low water level is unlikely to have a link to flood risk within the region, however it can have a large ecological effect. The minimum water level ties into the intertidal range – which itself determines the intertidal area, a key habitat in coastal areas. The change to the minimum water level due to the base flexible operation (Case 1) is shown in Figure 5.37, here a small (< 0.5 m) difference is shown in the area upstream (or north-east) of the tidal range scheme. The marginal increase in low water level is of limited impact in deeper water, however the intertidal areas around Newport can be seen in Figure 5.37 as broadly unchanged.

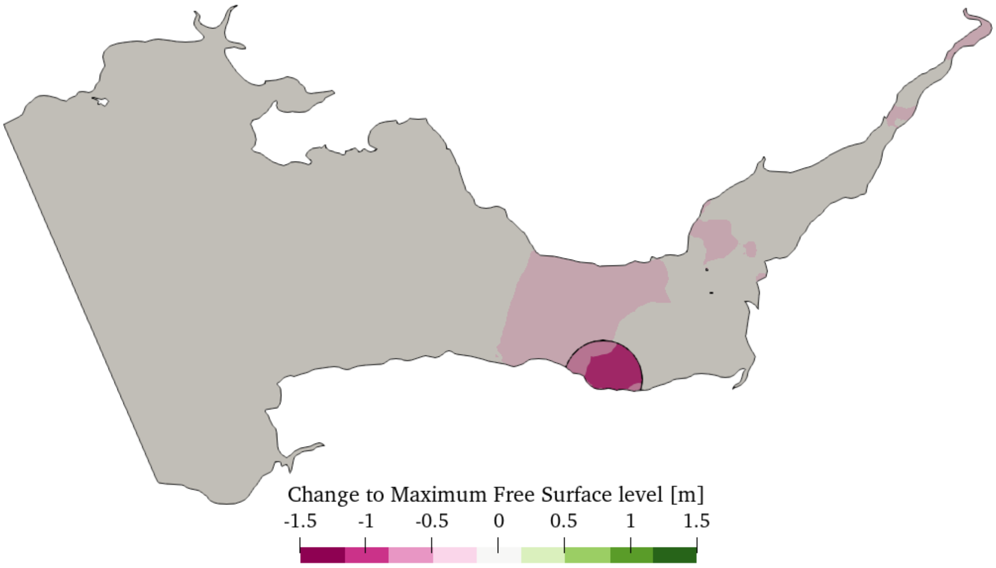

Figure 5.36: Change to maximum water level in SEBC model due to WSL using Case 4.

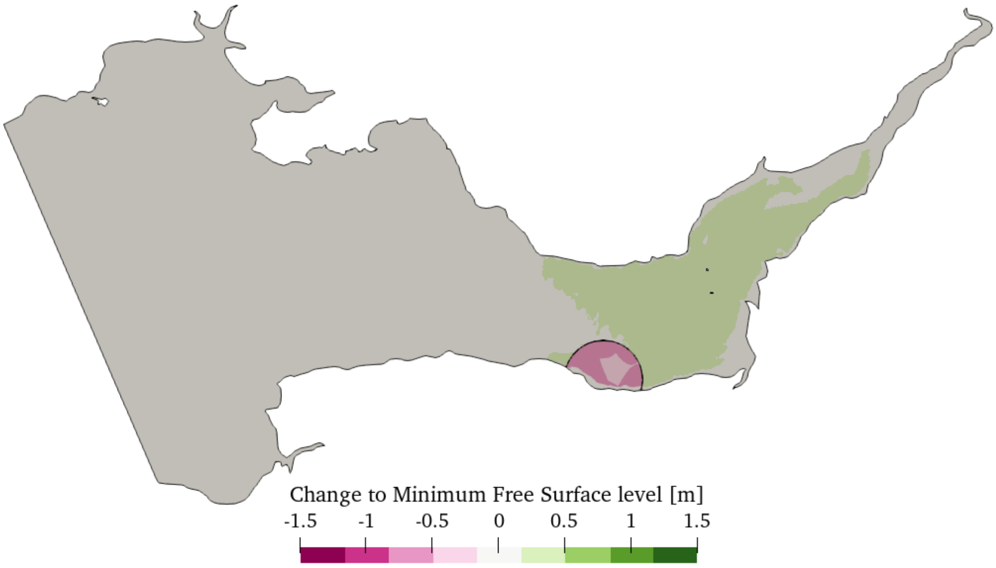

Figure 5.37: Change to minimum water level in SEBC model due to WSL using Case 1.

When using the Case 4 operation the low water level (Figure 5.38) is changed more significantly within the scheme, as is verified in the operational plots (such as Figure 5.34 for this condition), where the low-tide pumping phase empties the impoundment below the external tidal limit. This is potentially a product of the tidal prism – wherein the degree of vertical change achieved for the same energy expenditure in pumping is greater at low tide – where the surface area and thus volume change is smaller than the high-water equivalent. There is a ripple-type effect propagating away from the main grouping of turbines and sluices about the scheme – this is potentially due to the interaction of the outflows from the scheme at low water and the motion of the estuary. Note that the high and low water levels are the temporal maxima and minima over the sample period and so adjacent locations may have experienced these levels at different times.

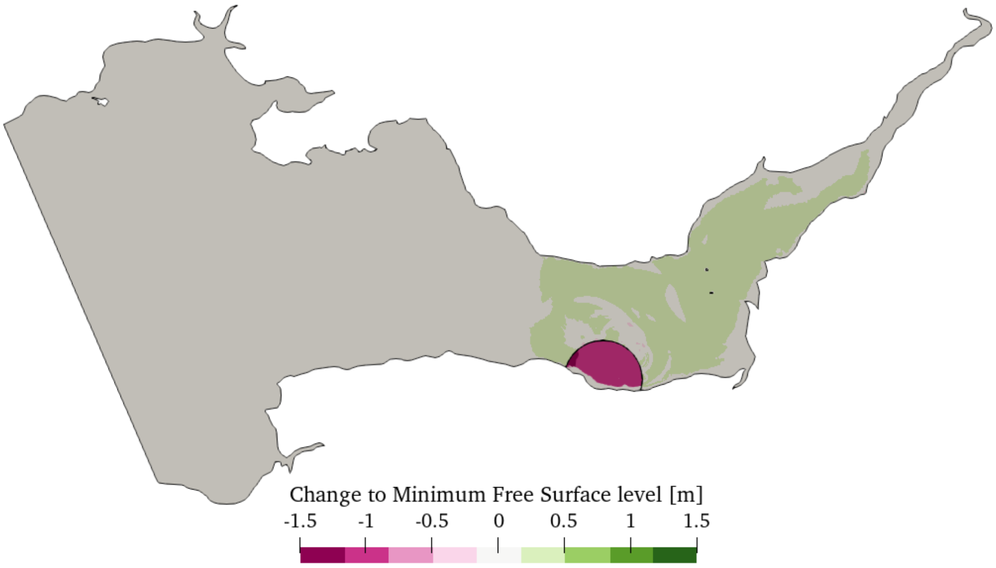

Figure 5.38: Change to minimum water level in SEBC model due to WSL using Case 4.

The change to the minimum water level $\Delta\eta_{min}$ (m) has been normalised to the mean water depth $\bar{d}$ (m), to show the sensitivity of the impact to the hydro-environment. Shown in Figure 5.39 for Case 1, and Figure 5.40 for Case 4, this develops parameter akin to engineering strain, wherein the same magnitude of absolute change in minimum water level is more impactful in shallower water depth areas than in deeper areas. As with the absolute change, the impact is largest within the lagoon, and is largely limited to within 1 centimetre per metre depth in the region downstream of the lagoon.

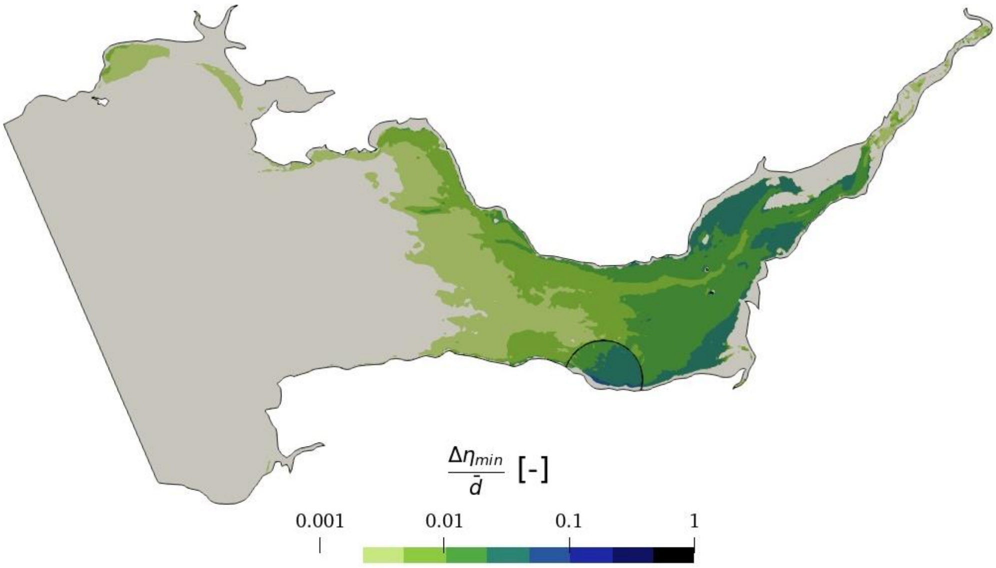

Figure 5.39: Average water depth normalised change to minimum water level in SEBC model due to WSL using Case 1.

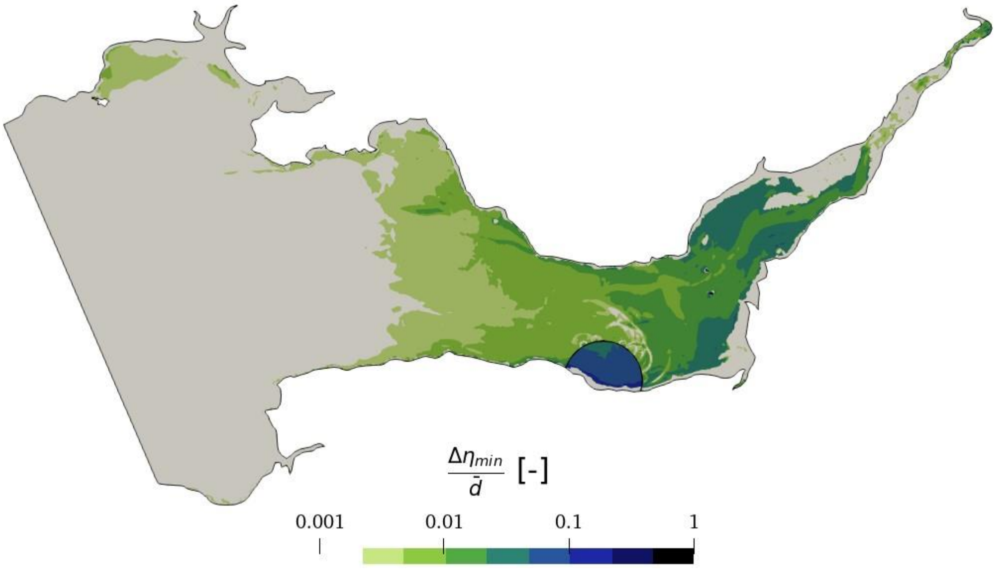

Figure 5.40: Average water depth normalised change to minimum water level in SEBC model due to WSL using Case 4.

Due to the nature of the tidal flats interpretation in TELEMAC model, a depth of 0.1 m was defined a dry element. The intertidal area was determined for the base condition (no tidal range scheme), and then again for each of the operating cases 1-4. For the base model an area of tidal flats within the region of 398.68 km² was identified. For cases 1 and 4 the change in the intertidal area due to the inclusion of the tidal range schemes are shown in Figure 5.41 and Figure 5.42 respectively. Here maintained areas are coloured orange, lost areas green, and new areas in red. In all the operational cases the difference was relatively minimal, with only a net loss of 1.5 % (6.2 km^2) of intertidal area for Case 1 and 1.2 % (4.8 km^2) for Case 4. Guo [172], found an area of 400.3 km^2 for post lagoon implementation (Equivalent to Case 1), this is 8 km^2 greater than the area identified here (though the different time period means different operational control limits). These differences are also a function of the incident tidal condition, with larger tides leading to a larger intertidal area. This parameter is also highly sensitive to the calibration of the mean water level to the bathymetry, relying on accurate measurements of an area that is typically difficult to capture due to being highly dynamic in the case of tidal flats.

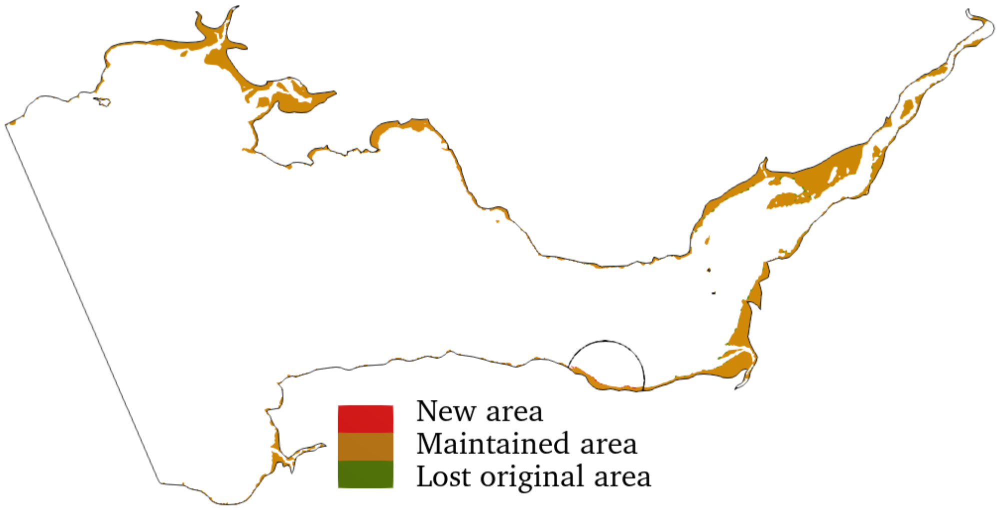

Figure 5.41: Change to intertidal area in SEBC model due to WSL operating using Case 1.

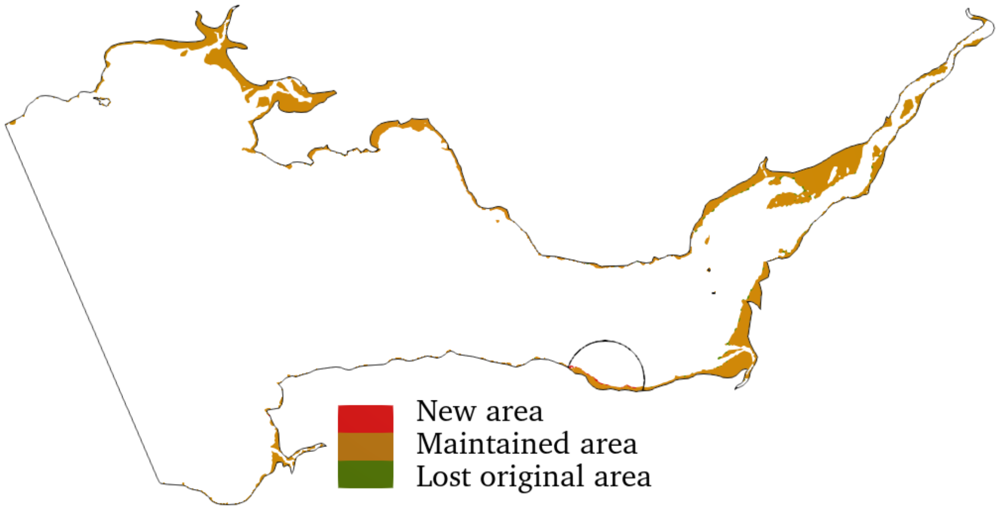

Figure 5.42: Change to intertidal area in SEBC model due to WSL operating using Case 4.

The velocity fields during two-hour periods of the final ebb and flood generation phases of the sample period were extracted from the model and time averaged to develop a mean velocity through the scheme over the period, as the flows are relatively high in their degree of variation compared to the base case so different individual snapshots will give different impressions of the system. The ebb generation period was defined as 15/02/2018 23:00 to 16/02/2018 01:00 and the flood-period as 16/02/2018 05:00 – 07:00.

The ebb generation profile for Case 1 and Case 4 are shown in Figure 5.43 and Figure 5.44 respectively. The differences between them are fairly negligible, with both showing the expulsion of water from the scheme into the relatively fast-moving water of the Severn in this area. The velocities peak around the turbine housings, particularly the eastern ones where the plumes are going contrary to the original flow direction (East to West). The velocities within the impoundment are and around the landfalls of the lagoon are reduced, a product of the wake effect of the boundary wall within the estuary, this may lead to water quality effects. This impact is potentially magnified however by the timing of the ebb generation phase, largely occurring around low water levels where the area west of the lagoon is shallow water or dry, reducing flows.

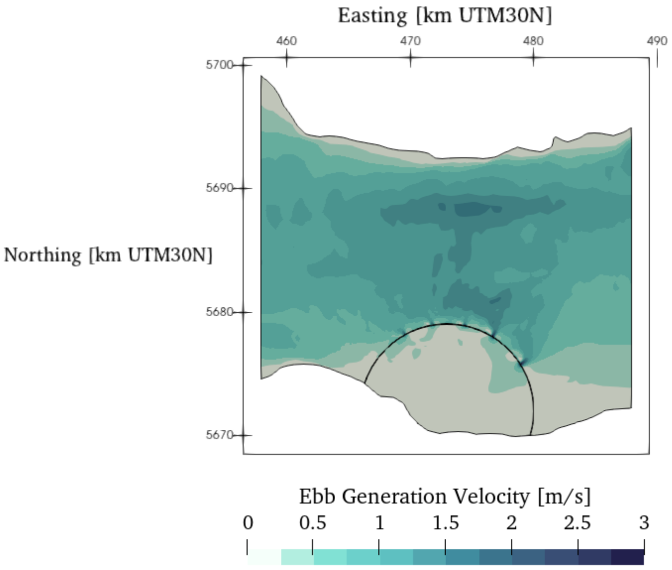

Figure 5.43: Mean ebb generating velocity around WSL when operating using Case 1.

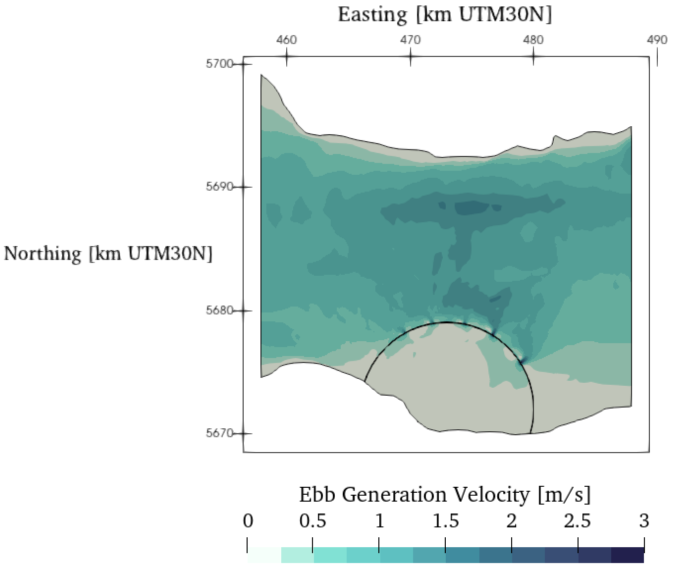

Figure 5.44: Mean ebb generating velocity around WSL when operating using Case 4.

The flood generation phase exhibits the same low velocity regions both within and around the lagoon; although since this occurs at higher water levels, the implication is that this is primarily driven by the obstruction of the estuary by the structure. The scheme also develops the customary radial jet pattern caused by the orientation and positions of the turbines. The jets differ only marginally from Case 1 (shown in Figure 5.45) to Case 4 (Figure 5.46), which was to be expected since the differences between the operations are focussed on adjustments to the start and end-point timings of generation.

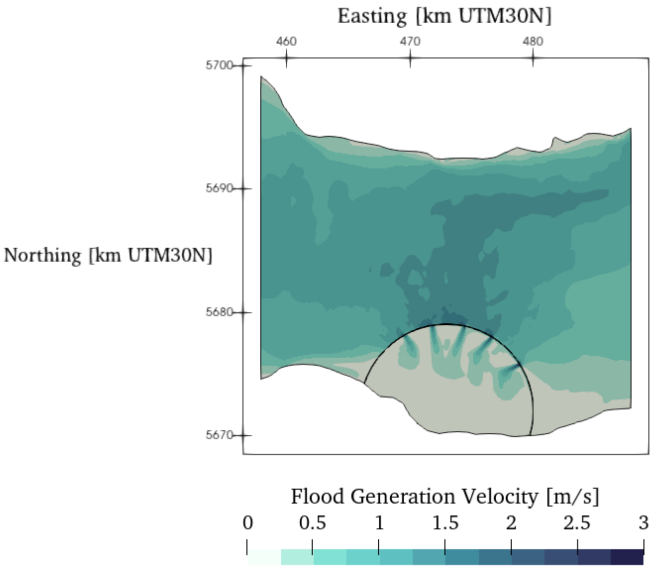

Figure 5.45: Mean flood generating velocity around WSL when operating using Case 1.

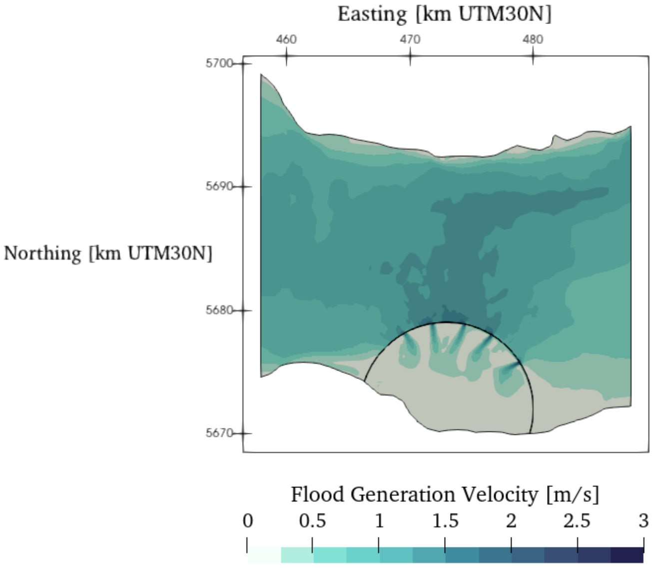

Figure 5.46: Mean flood generating velocity around WSL when operating using Case 4.

5.5 Summary

Developing understanding of the potential operation of tidal range energy schemes for the UK requires a combination of tools. 0D modelling is suited to operational changes being tested at a low cost – allowing a large number of variations of control decisions and design setups. These changes can then be confirmed through the use of a regional scale 2D model, also shining a light on the likely hydro-environmental impacts. Here the operational and design assessment was carried out for two schemes, the North Wales Lagoon, and the West Somerset Lagoon. The 2D analysis was continued for the West Somerset Lagoon.

The 0D assessment found that the change from an energy based flexible regime, can be combined with the usage of parallel sluicing for both the schemes. Demonstrating how the benefits of the two changes compound. This better positions tidal range within the GB energy mix as a potential electricity source to reduce the dependency on gas turbine methods, utilising the relative dispatchability of tidal range – a strength of tidal range over other renewables. The two large schemes could combine for a total of approximately 13 TWh per year, corresponding to an equivalent reduction in gas turbine generation – and better positioning the system to account for the variability in the major renewables being used. A statistical assessment of how the combined output of the two schemes would be mapped out over the year was developed, showing that they would generate 1.44 GW or more approximately half of the time. The cyclical nature of the tides results in the electricity generation having a broadly even spread across the time of day over the course of the year.

2D modelling confirms the performance improvements identified by the 0D process. The agreement of the 0D and 2D models was found to be strongly influenced by the assumed data trace for the 0D model, with a blanket overestimation occurring approximately 12 % of the energy output in this study. This stems from the difference between onshore and offshore measured tidal traces, the spatial distribution of the turbine housings being unaccounted for in the 0D model, and to lower extent the significant hydro-environmental impact of the lagoon structure itself. Highlighting the need for 0D and 2D modelling to be carried out in tandem through the development of a tidal range scheme. With the use of multi-trace external water levels where available in the 0D process for improved accuracy. Despite this difference, the improvements to energy and revenue produced, identified by the 0D study were evident in the 2D results. Through the 2D modelling process of West Somerset Lagoon the extent to which the environmental impact would be affected by the changes to the operation is evaluated. This was found to be minimal in comparison to the magnitude of hydro-environmental impact caused by a large tidal range scheme such as this. Environmental impact however is a highly nuanced concept to assess in terms of a tidal range scheme, and as such further study would be required were a scheme to be propelled further in the development process.

6 Disused Docks as Tidal Range Schemes

6.1 Introduction

The fundamental principles of a tidal range scheme require a few key elements; a tidally varying body of water, an adjacent non-tidal body of water, and a control structure between the two. Take the notion that the key advantages of tidal range when compared to other renewables – dispatchability, storage, and predictability – may have more value than the raw energy yield; the strengths of a very large scheme may be matched by an array of small schemes (as seen in distributed electricity generation [7] and battery storage [42]). The potential of using disused infrastructure elements is investigated here using the disused docks found around the coast of the United Kingdom as a test case. This design alternative should be far more cost effective than traditional schemes, with the further benefit of being close to centres of population or industry, with potential for inclusion in a redevelopment project. They could also serve as a testing site for novel technologies (such as new turbine designs or control schedules) before these are potentially applied to larger scale schemes. Through this the options for the use of tidal range are expanded to new physical forms.

6.2 Repurposing of Disused Docks

It is perhaps difficult to overstate the importance of water to human life, society has always clung to this resource from drinking fresh water, to fishing and aquaculture, and heavy industry, natural water bodies play a key role in our world. How we interact with the water varies depending on the task at hand: piers, jetties, harbours, docks, breakwaters and more, each developed to solve a location-specific challenge at a time of need or opportunity . How these structures are used is – like all things: subject to change over time, with some falling into disrepair. As both local and global industries and needs have shifted (such as the rise and fall of ‘harbours of refuge’ in the English Channel [241]), driven largely by the growth of global container shipping, and the requirement for facilities that can handle container ships the commercial usage of smaller and historic docks has seen a decline around the UK [242].

In 1999, Hawkins et al. [243] identified 11 ports in the UK with disused dock basins and eight sites of major redevelopment. The focus of this study has been on improving water quality and biodiversity through various methods to increase the mixing of water within the docks, and the introduction of aquaculture. The delicate nature of the terminology of restoration is also raised, implying an intervention to speed transition to a new state (especially where the original is unobtainable or unknown). The potential issues in water quality experienced at disused docks (particularly relating to algae and lack of water movement) are further discussed by Allen et al. [244] in the case of the Liverpool docks. This was also seen in the case of larger coastal impoundments, such as Cardiff Bay, a 202-hectare freshwater coastal reservoir, where dissolved oxygen levels and stratification are ongoing challenges [245], with aeration used to reduce their impacts. The impact of mixing systems and mussel populations on improving water quality and the restoration process over multiple decades is discussed by Hawkins et al. [132]. These works tend to discuss the state of docks and water quality from the perspective of typical dockland regeneration, as popularised in the 1980s following the success stories of the Baltimore and London Docklands restoration projects, wherein the housing, social and commercial needs were at the forefront of the development process [246, 247]. The dock basins themselves typically provide value in terms of the holistic and social benefits seen by developers of being water adjacent, or through the provision of additional ecological value.

The physical components of a disused dock basin, more so in the case of a former dry-dock as shown in Figure 6.1, are not too dissimilar to that of a very small tidal range scheme, with an internal impounded area (the dock basin) separated from the tide by a man-made structure. The cost of conversion would be primarily that of the turbines, generators, and electrical transmission systems – with much of the bund walling already being in-situ. It is likely in most cases that the opening would need to be re-built to allow the fitting of the turbines, however this is likely to be less than the equivalent cost rate of construction of a barrage or lagoon turbine house due to the lower depth of construction and immediate proximity to the harbour itself. Alongside this, the environmental costs are largely mitigated, with a reduced need to quarry rock or pour concrete to form a bund wall that is potentially kilometres long the carbon cost is much lower.

Figure 6.1: Disused dry dock in Govan, Glasgow – from Govan Voices [248].

The nature of a disused dock is such that the natural environment has long been primarily driven by human activity; there is minimal chance of impacting fish migration routes, or the habitats of marine creatures. On the contrary, the increased flow rates during generation periods may work to improve mixing and aeration rates within the dock and greater harbour area – although this would need to be balanced with the potential dangers to navigability for boats and the safety of water users. This hydrodynamic factor is likely to play a key point in the design and approval of such a scheme and would need to be assessed using 2D regional and likely 3D near-field modelling, however, was beyond the scope of this study.

Typically, harbours were built with multiple basins, allowing multiple vessels to dock at the same time (as seen in Figure 6.2). Having a combination of small tidal range schemes adjacent to each other has the potential to bring further benefits, such as sharing a portion of the construction costs, electrical components, and control facility. They could also be used as linked basins – a concept that has been considered in a number of ways over the years – wherein water is pumped or diverted between two impoundments to alter the timing of generation, Angeloudis et al. [145] found that for a spring-neap a linked system may be able to generate for 80-100% of the time however at a output energy reduction of over 70 % as compared to an equivalent single basin. An additional advantage of a set of small adjacent basins may be found in the project management aspect, with stakeholders being able to construct one basin (for a fractional part of the total cost of the set), appraise the operation, and make an informed decision as to whether to continue to develop neighbouring basins – allowing some return on the initial investment which may be more financially palatable to a local authority or investor.

Figure 6.2: Multiple adjacent disused basins in South Shields, River Tyne from Google Satellite Imagery (2022).

6.3 Method

The methodology proposed to identify disused infrastructures which can be used as tidal range schemes is laid out in generic terms in Table 6.1, and then broken down in detail later in this section, with an example of the process presented in Section 6.4.2. Considering a partially closed, tidally connected body of water as the basis for a tidal range scheme can mitigate the costs, both physical and environmental, of tidal range scheme construction, whilst offering an avenue for distributed small-scale electricity generation. Whereas historically the entirety of a scheme has been constructed from scratch, comprising some combination of coastline, caissons, and boundary wall extending into the undeveloped ocean, the use of existing engineered structures is the focus herein.

Table 6.1: Pseudocode method for initial assessment of small tidal range scheme.

```
1:   Identify potential region
2:   Define desired physical traits
3:   Set suitability parameter
4:   Identify basins in region
5:   For each basin in the region
6:       Measure physical parameters
7:       Acquire tidal trace
8:       Compose scheme design options
9:       For basin design in scheme designs
10:          Build 0D model with design parameters
11:          Run 0D model for suitability parameter
12:          If basin design is suitable
13:              Continue to in-depth design and analysis
```

6.3.1 Identification of basins

With an initial region (step 1) being identified as the UK coastline, and the desired physical traits defined as disused dock basins (step 2), the collation of a set of initial sites was carried out via an open-source intelligence gathering method. The suitability parameter here is the net energy extracted with operation aimed to maximise energy value (step 3). A combination of satellite and street view imagery was manually used to visually identify empty or unused basins at major coastal locations around the UK (step 4). This process is likely to yield a relatively high number of false positives where basins have changed usage since photographing, or have a usage that is not easily visible, and is liable to human error in missing what are in fact tidal basins where the imagery or coverage is poor, with an example of some common features shown in Figure 6.3 – including some that make various basins challenging or unsuitable for use. It does however yield a first-case dataset with potential developments at a variety of realistic sizes and feasible locations and could be applied to potential basins of a multitude of physical forms at minimal cost, only relying on the tidal water levels and a satellite image. This method aims to act as a precursor to a more detailed but costly engineering design and analysis process, to be carried out once a given dock is deemed suitable for development by the relevant stakeholders.

A. **Bute East Dock**
Isolated 19th Century dock, freshwater recreational fishing, adjacent residential developments.

B. **Roath Dock**
Multi-berth dock, access to Roath Basin, and accessed from Queen Alexandra Dock.

C. **Roath Basin**
Hospitality berth only, attached dry dock (south corner), access through Roach Dock.

D. **Queen Alexandra Dock.**
Multi-berth dock, access from estuary.

E. **Cardiff Bay**
Freshwater coastal reservoir [245], disused graving and dry docks.

Figure 6.3: Key features of the port of Cardiff, background from Google Satellite Imagery (2022).

6.3.2 Theoretical yield assessment

To determine the theoretical yield of each of the basins identified, the physical characteristics of the sites were required. With the intent to keep the process as accessible as possible – allowing this form of assessment to be available to the greatest possible number of people, the ‘measure distance’ feature on Google Maps was used to ascertain the basin areas (step 6). This open-source information was gathered with the knowledge that the exact area would need either a more detailed imagery system or on-site measurements, the cost of which is excessive at an initial stage of assessment.

Tidal water levels (step 7) can be freely obtained from a number of sources, due to their relevance to communities including those interested in fishing, sailing, surfing and other waterside activities. Many of these are derived from global tidal models such as the Permanent Service for Mean Sea Level data system [249], or TPXO [43]). In this study the tidal water levels were taken from the POLTIPS-3 software developed at the National Oceanography Centre, UK [250]. This uses a system of major sites where a trace has been measured and harmonic constants extracted, and minor sites, whose locations have been identified as being close enough to a major port to for the differences between them to be of limited significance to typical users. When contemplating a development of this nature, it is probable than an assumption of this nature will be needed at the assessment stage, until relevant funding has been secured for advanced modelling and study. From any water level data extraction method there will be some degree of error in the data, understanding how this error is likely to propagate into the model outputs is key, and a method for investigating it was utilised in this study, described in Section 6.3.5.

6.3.3 Local design study

For each basin a set of tidal range scheme design options (step 8) were composed based on an empirically derived Equation 6.1, based on the assumptions as laid out by Fay and Smachlo [251, 252].

$$2 \cdot D_{TB} \cdot n_{TB} + A_{SL}/\bar{\xi} \leq W_{Basin} \tag{6.1}$$

Here, a number of turbines n_{TB} (-), multiplied by twice their diameter D_{TB} (m), and area of sluices A_{SL} (m²) divided by the mean tidal range $\bar{\xi}$ (m) combined must be less than or equal to the total width of the existing opening W_{Basin} (m). This takes the assumption that for a turbine of diameter D_{TB} a width of the same amount is required for the housing and services required, shown in Figure 6.4. There are systems such as the Andritz HydroMatrix and StrafloMatrix [253] that use vertical and horizontal stacking in their design to improve the density of functional area within a space, and as such may be well suited to a tidal dock. In aid of consistency and comparability the bulb turbine described by Aggidis and Feather [29] scaled using Equation 3.38 to a diameter of 2.5 m, giving a power rating of 3 MW per turbine – installed at a level such that they can be safely operated through the entire tidal range expected at the site. The area of sluices was assumed to be either 0 or 100 m² at this stage, although could be modified later in the design process if space and need allowed. The turbine diameter and area of sluices were taken as an indicative first option. Smaller turbines would allow a greater depth of search, as would a varied sluice area.

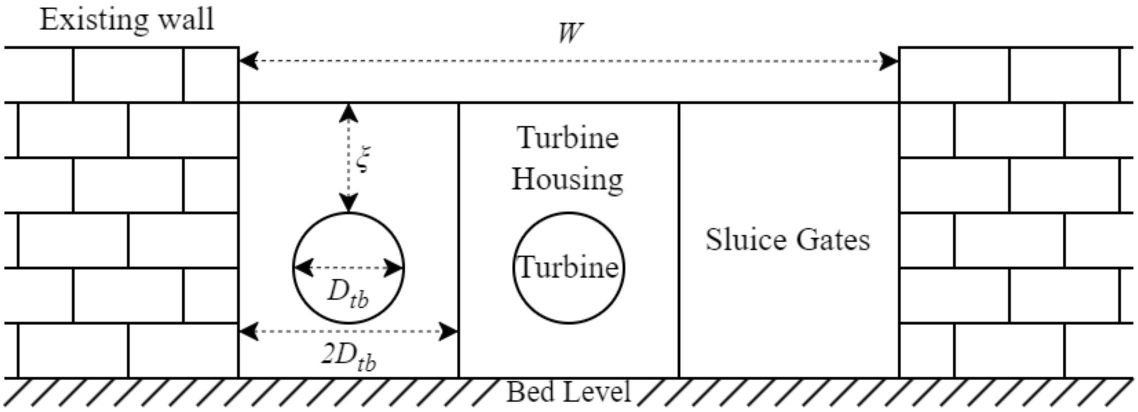

Figure 6.4: Tidal dock simple hydropower turbine (such as bulb) and sluice elevation, with spacing assumptions.

In a classical tidal range scheme, a number of other engineering facilities are required to allow operation. These include ship-locks, fish passes, access ways, and safety infrastructure. In the simple tidal dock model, these components are assumed not to be necessary, as ships would not be expected to enter the basin, and small boats could be craned or lowered in from the basin side (such as if required for maintenance activities). Fish movement into/from the basin would be possible through the turbines and sluices, as has been seen at many existing tidal range schemes [25, 102] and so a fish-pass allowing egress may be deemed necessary if monitoring suggests that this is occurring in a damaging manner. The wall of a tidal dock and the construction efforts needed for it will vary based on the specific site, with an appraisal of the structural integrity of the wall being needed to determine whether reinforcement or repairs are needed, along with this, the potential to extend the wall vertically using additional components could be considered, using a structure akin to a water tank – expanding the storage capacity of the basin were pumping to be used. As a base however the basins were assumed to have internal minimum and maximum water levels equal to the highest and lowest astronomical tides.

6.3.4 0D Modelling

Steps 11 and 12 in Table 6.1 define the construction of numerical model representations of all the potential designs for all the basins identified. For this, the 0D model described in Section 3.3 was utilised, with the parameter for the being the energy extracted (whilst controlling for maximal revenue to ensure the flexibility was utilised). The selected timeframe was the first quarter of the 2022 for all schemes, deemed long enough to provide a suitable sample length, whilst also being representative of the current energy market. The models were supplied with the energy value based on the system sell price of the national grid over that period, shown in Figure 6.5. There were two significant peaks in price during this period on the 14th and 24th of January – of 2950 and 4035 £/MWh respectively (related to the Russian invasion of Ukraine and the concerns over energy security). The operation was targeted to maximise revenue generation using this data, expanding on the intention of the schemes being highly flexible – and meeting the needs of the grid rather than operating in the manner of traditional intermittent renewables, with the net energy yield being taken as the output variable (step 3) at this stage as the true energy value is likely to be specifically agreed based on the schemes themselves. The price shown is highly variable, with the energy markets becoming increasingly varied over time due to the changing energy mix, and global energy market uncertainty [5, 17].

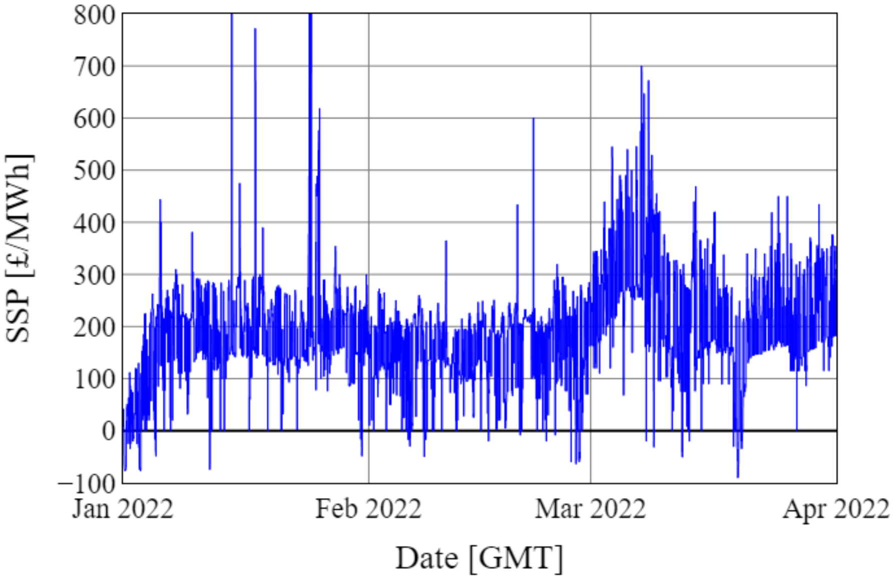

Figure 6.5: System Sell Price of energy for Quarter 1 of 2022.

The time-step used in the model was set to 2.5 minutes, with a convergence study confirming this step with tests of 1.25, 5 and 10-minute durations using a singular design configuration for each site. The timestep was found to be converging to a local solution below a timestep of 2.5 minutes, as shown in Figure 6.6, with a convergence rate below first order below a 7.5 minute timestep.

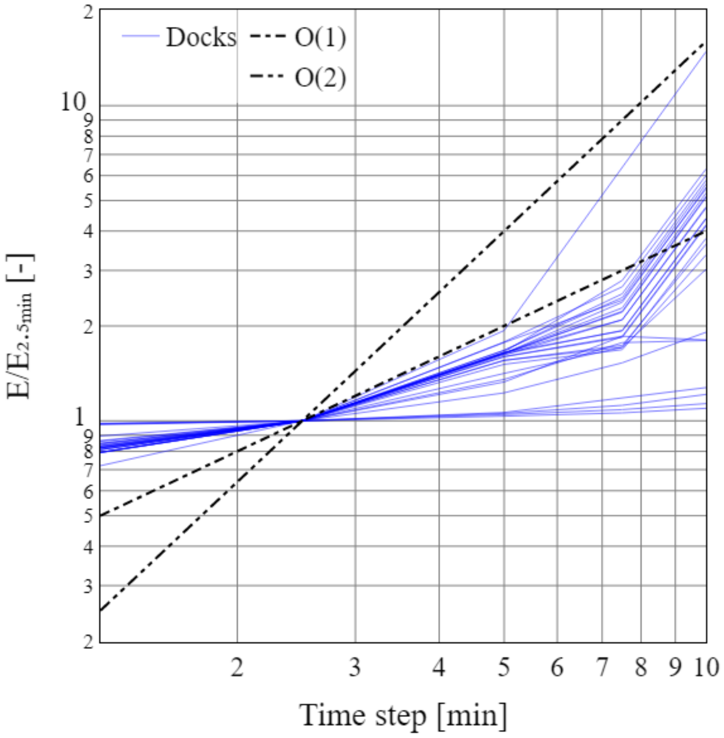

Figure 6.6: Convergence of net energy production to timestep for all basins considered.

6.3.5 Sensitivity analysis

The output of a tidal range scheme is primarily influenced by the tidal range at the site. Water levels here were extracted from measurement sites that are located close to the proposed locations. For more accurate results, these should be either extracted from a detailed hydrodynamic model of the proposed area, or measurements at the precise locations within the harbours being considered. The hydro-environment within a dock or harbour is likely to differ from the external regime, for example Yin et al. [254] found the aspect ratio of the harbour entrance to have a significant affect on the flushing characteristics and sediment regime. These effects can be beneficial, such as in the case of oscillating water column devices, where proximity to harbour walls has been found to enhance performance [255]. Therefore, an effort was made to quantify the degree of uncertainty present in the energy output assumptions for the docks on the understanding that there may be error in the inputs. As an approach to this, once an optimal design configuration for each site was identified (the design that produced the highest energy in the 0D model), the water level time series was multiplied by a bulk magnitude about the mean water level, increasing or decreasing the mean tidal range by an equal amount – shown in Figure 6.7. The range of magnitudes was set at ±15 %, giving traces that were felt to be close enough to the true data that they may represent that of a location adjacent to a given site. The model was then run again with a set of these new water levels for a range of magnitudes, and the impact on the net production determined.

The second key variable in determining the energy resource of the site is the surface area of the water (as this describes the impounded volume) or tidal prism. The area used in this study is taken from satellite imagery, and as such is the area at the maximum water, with on-site measurements being required to determine the geometry below this. In some cases – depending on the prior usage of the basin, the surface area is likely to reduce below this (as can be seen to be occurring in Figure 6.1). To investigate the potential impacts of variations to the wetted area, a set of tests were conducted with the previously ascertained optimal configuration wherein the area at the lowest water level was reduced (as shown in Figure 6.8), with a linear growth in area to the maximum, the lower bound of the area A_{min} was set at half the surface level A_0.

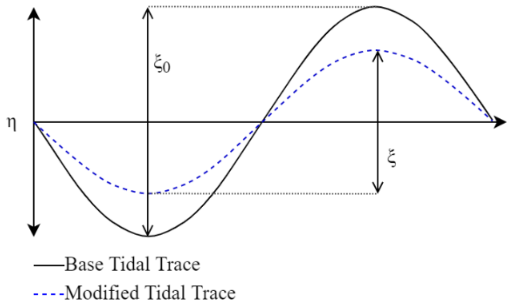

Figure 6.7: Tidal range sensitivity method conceptual diagram.

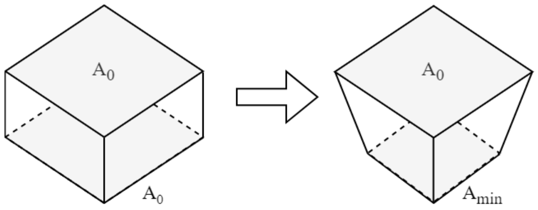

Figure 6.8: Concept diagram of impounded area sensitivity method.

6.4 Results and Discussion

6.4.1 Identified Sites

The process of finding disused dock basins around the UK coast, using open-source information yielded 28 basins spread through 13 cities, mapped in Figure 6.12. The three largest basins by surface area were identified in Cardiff (Figure 6.9), London (Figure 6.10) and Middlesborough (Figure 6.11). Some of the cities separated in Table 6.2 have been clustered in Figure 6.12 for visual ease. In the case of Cardiff this large basin coincides with one of the largest tidal ranges on the British coast, whilst in London the opportunity to have the scheme be very visibly located in a capital city may provide opportunities for gain beyond the tidal range operation itself.

The three largest basins by area are shown below, in Cardiff the Queen Alexandra Dock has an estimated area (blue hashing) of 203660 m² Figure 6.9, with a channel width of ~30 m connecting the South-West corner of the dock to the Bristol Channel. This channel is roughly 300 m long, and so a 3D assessment may find that additional engineering works are required in order to properly pass flows along it. The Millwall dock, shown in Figure 6.10 comprises two sub-docks, the 35000 m² inner (green cross-hatching) and the 95000 m² outer dock (blue hatching). These are in the case of this analysis treated as a continuous basin, they are currently connected by an opening with a raisable bridge, this could be utilised to form the two into a pair of linked basins allowing a two-stage operation. The entryway was deemed to be the 35 m wide former channel at the western end of the outer dock, this would require re-opening to fit sluices and turbines. The Middlesbrough dock shown in Figure 6.11 is adjacent to the Middlesbrough Football Club (M.F.C.) stadium, the main basin (blue hatching has an area of 68000 m², if the access channel were closed off in addition to this the total area of the system is raised to 100000 m².

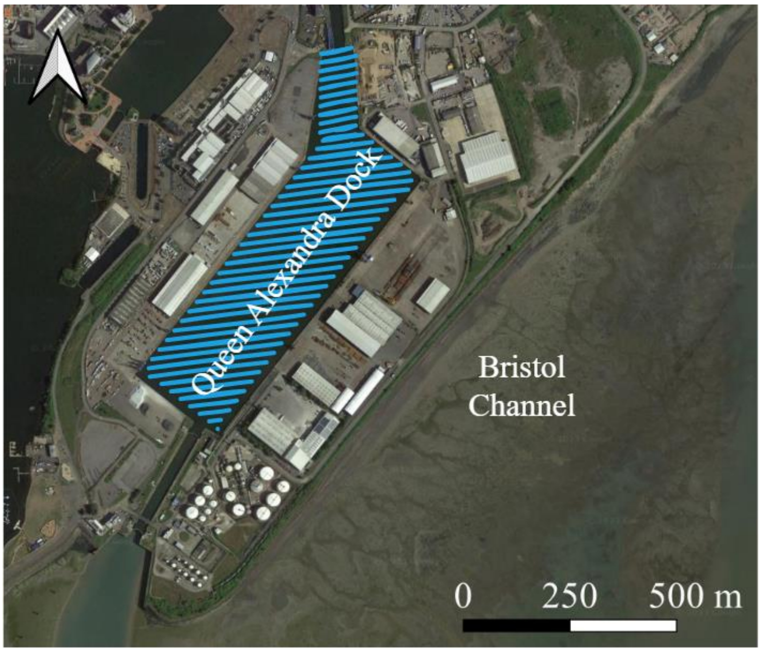

Figure 6.9: Queen Alexandra Dock in Cardiff, background from Google Satellite Imagery (2022).

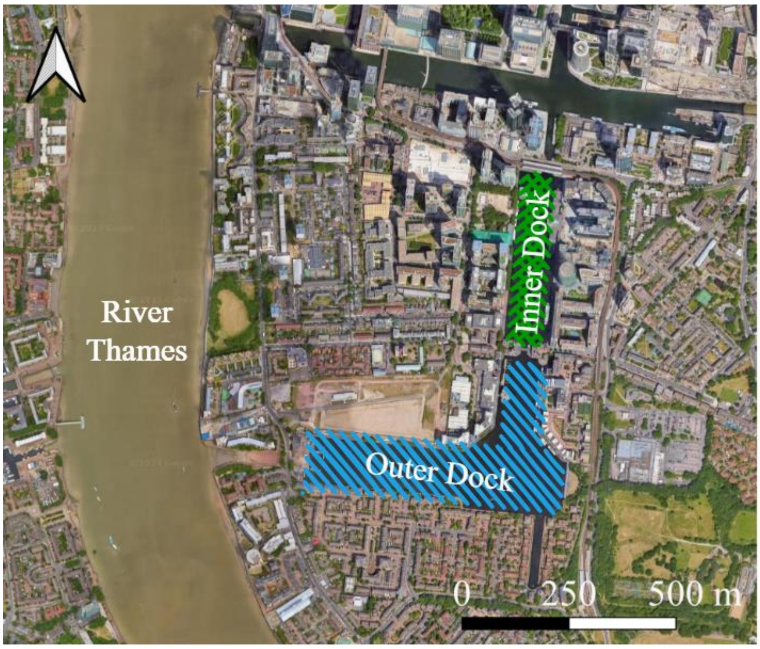

Figure 6.10: Millwall Dock connected basins, Isle of Dogs, London, background from Google Satellite Imagery (2022).

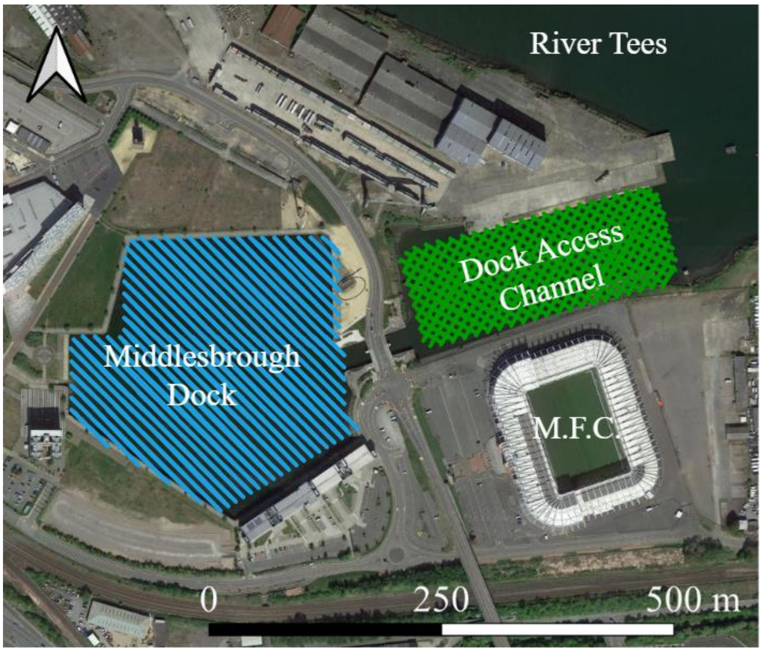

Figure 6.11: Middlesborough dock, access channel, and football stadium, background from Google Satellite Imagery (2022).

The largest number of potential basins in an area was 8 in Glasgow, with the River Tyne – predominantly Newcastle and South Shields – having 7 (such as the group of docks seen in Figure 6.2). Both of these being areas where industrial shifts have led to decline in the marine industry, with Glasgow seeing a transition from manufacturing to service based economy in the post-war period [256], and the Tyne seeing the steady closure of shipyards as recently as the early 21st century [257].

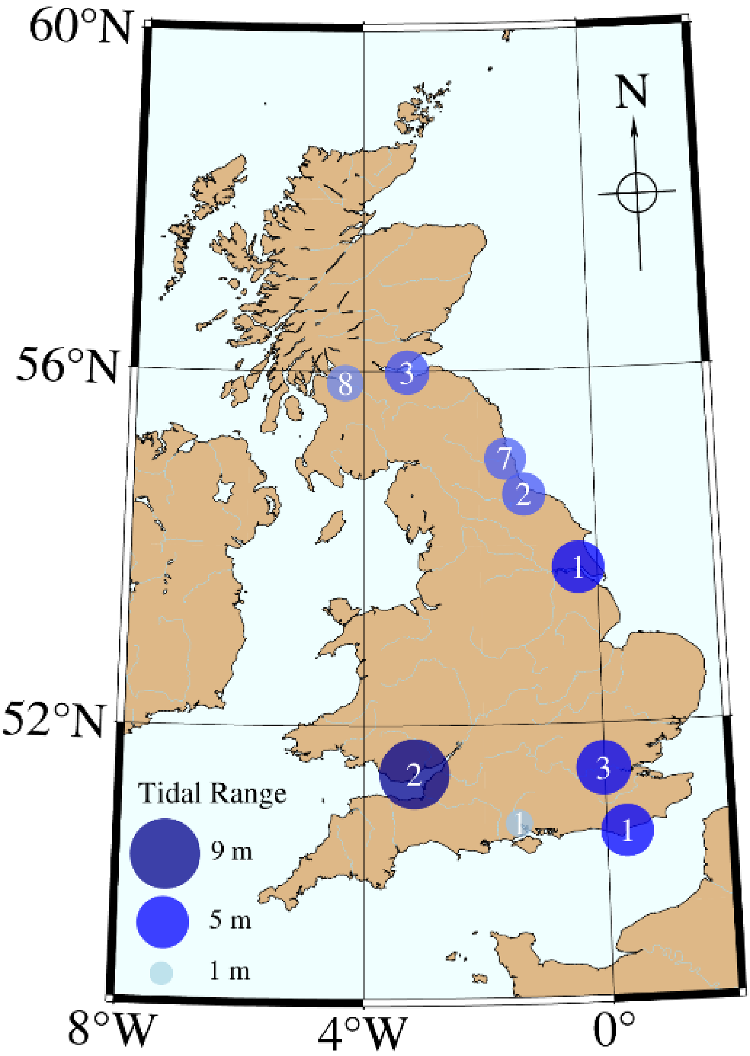

Figure 6.12: Number of basins identified around the UK, with positions sized and coloured by tidal range.

The variety in basin size (ranging from 4400 to 200000 m²), and geographical spread of sites provides a diversity to the studied basins with the potential value of both small and large basins being considered – and the spatial distribution providing a view of how a fully developed fleet of tidal docks would contribute not only to the local networks, but to the national grid as a whole. There is a notable gap in identified basins around the Irish sea, this region (particularly the Mersey) has been studied in reference to dockside regenerations [132, 244] and tidal range [116, 131, 133] schemes for many years. However a key feature of the regeneration and development efforts in the area was the walling off of many of the historic dock spaces [242] – disconnecting them from the tides of the region. These dock basins have since found use both as water-based recreational features and beyond, such as the construction of the new 52000 seat capacity Everton football club stadium in the Bramley Moore Dock [258]. Tidally adjacent – disconnected basins such as this were identified at a number of other locations (including in Cardiff as seen in Figure 6.3) however were excluded from further study as being outside the target design. These could however be converted to tidal or pumped storage features using a similar method, using pipe or culvert-based designs.

Table 6.2: Identified docks with area grouped by city.

City	Tidal Range [m]	Total Area [m²]	Count [-]
Cardiff	8.9	203660	1
London	5.4	133405	1
Middlesbrough	3.4	100000	1
Glasgow	2.5	60145	8
Eastbourne	5.1	47750	1
River Tyne	3.2	30125	7
Barry	8.9	27750	1
Southampton	1.4	16600	1
Rosythe	3.3	15500	1
Hull	5	10725	1
Edinburgh	3.5	6100	2
Grays	4.9	4850	2
Stockton-on-Tees	3.4	4400	1

6.4.2 Sample Site Procedure

The assessment process in detail is presented here for a sample location – the Barry Docks original entrance basin. This dock – constructed in the late 19th century was primarily constructed for the movement of coal from the area, and was the largest port for coal exports in the world in 1913 [259]. The basin in question has a rectangular shape, measuring 150 by 185 m encompassing an area of 27750 m², with an entrance channel width of 25 m, all shown in Figure 6.13. This area of the Severn estuary has significant tides with a mean tidal range of

8.9 m. This basin has the advantage of being large in size, with the adjacent Lady Windsor Lock (on the southwest side) being the primary route of passage for watercraft to the inner dock basins via basin 1 – the larger of the two.

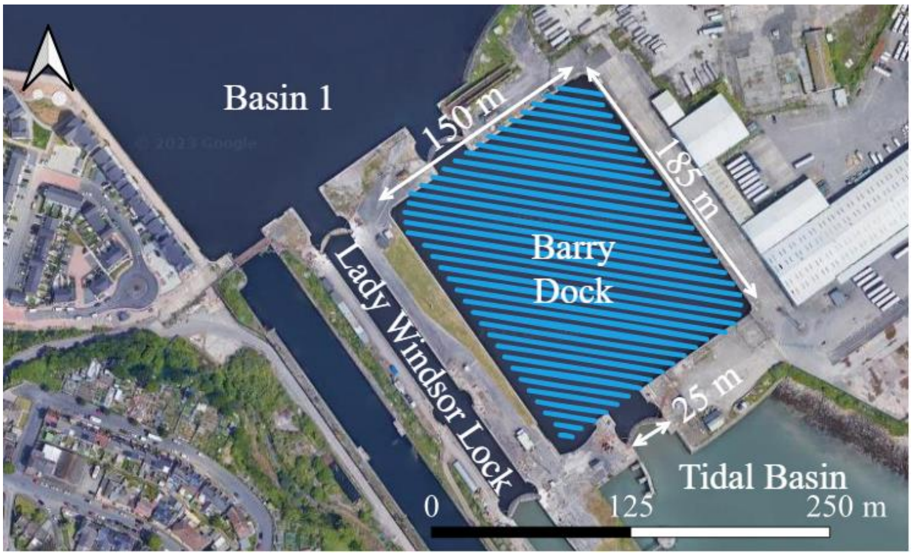

Figure 6.13: Measured impoundment dimensions at Barry Docks, background from Google Satellite Imagery (2022).

Due to the 25 m wide entryway, the design configurations defined were having 1 – 5 turbines with no sluices, or 1-2 turbines with 100 m² of sluices per Equation 6.1. Thus every combination of these options was modelled using the 0D approach as described in Section 3.3, using two-way generation to produce two generation periods per tidal cycle, with parallel sluicing (where sluices were included), and without pumping as defined in Section 6.3.3. As a flexibility scheme, the Every Half Next method was used (described in [128, 130]) – wherein on every high and low tide, the model identifies an optimal configuration that will produce the best yield for the next full tidal cycle. The estimated production from each of these configurations obtained using the 0D modelling process can be seen in Table 6.3. From this the one turbine – without sluices design was found to be the most productive, with one turbine also being the best producing option with sluice gates.

Table 6.3: Barry docks design option outputs.

n_{tb} [-]	**Energy [MWh/year]** 0 m² Sluice	100 m² Sluice
1	2900	2708
2	2828	2441
3	2780	-
4	2660	-
5	2568	-

The 14th of February was selected for demonstrating a view of the scheme operating on a representative day. This is shown in Figure 6.14, where the internal and external water levels, flow rates, and power output are all shown alongside the operating mode. Figure 6.14 shows that the dock typically delays operation until a large head difference has been established (where many tidal range proposals have sought to capitalise as much as possible over the tidal cycle through low-head devices). This then leads to a short duration 1-1.5 hour generation window as seen around 11:15 and 17:20. These short generation periods may be extended through the use of a turbine better suited for this situation; the dock could even be constructed with a combination of turbine sizes for under different conditions. The potential for the use of a tidal dock as a turbine testing facility may have additional value to developers, giving manufacturers a small controllable environment in which to operate hydropower devices.

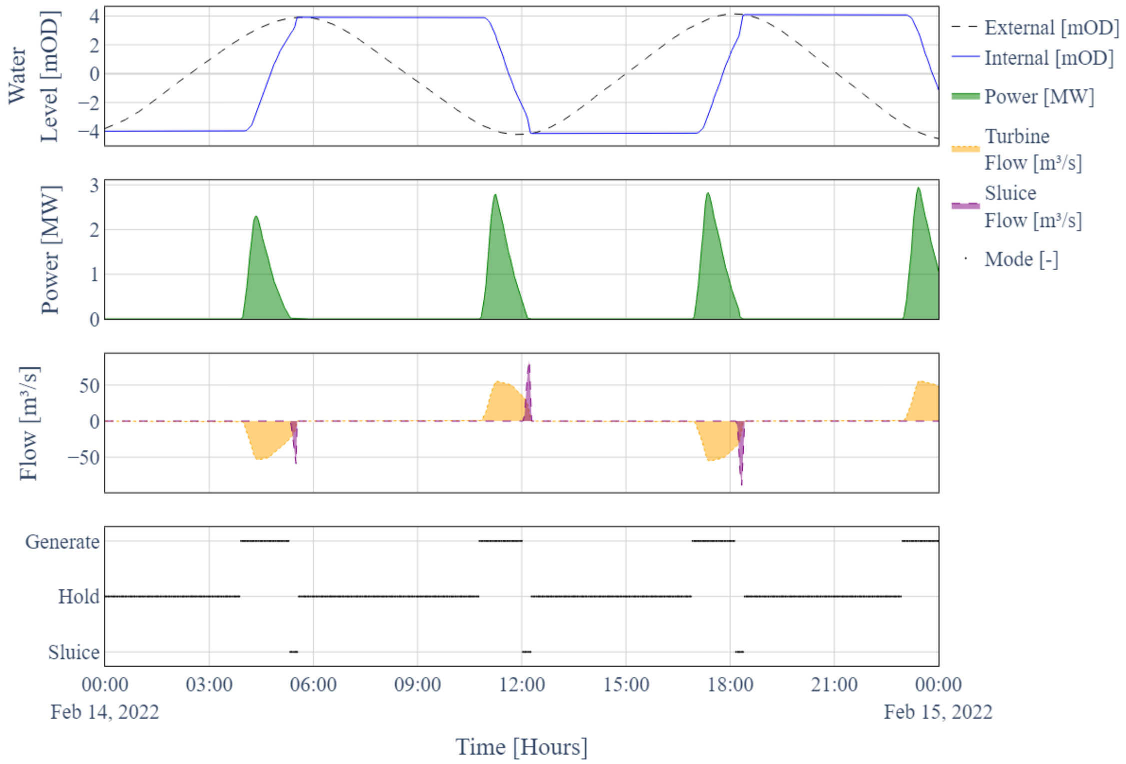

Figure 6.14: Day of operation for Barry Docks basin with single turbine and sluice gates (mean tide).

The maximum flow rates over the timeseries were 56.1 m³/s at the Barry site, through a single turbine, with a cross sectional area of 4.9 m². This equates to a peak flow velocity of approximately 11 m/s, being directed out into the Barry harbour at low tide, and into the basin during high tides – assuming no draft tube is used. A draft tube or housing would be a beneficial feature to include based on this analysis to reduce the flow velocities in the vicinity of the dock. Simply assuming a draft tube with a square opening with the width of the turbine housing – double the turbine diameter (per Figure 6.4) gives a 5 m by 5 m draft tube, a 25 m² area reducing the peak flow to 2.24 m/s, lower than the spring tidal velocities in the region (per Admiralty Chart 1182), assuming there is in fact topographical space for a draft tuber installation that maintains the required level of access.

The flows into the basin are unlikely to pose a hydrodynamic threat, however the high velocity flow into natural environment would require appropriate draft tubes, and possibly operation control to mitigate potential damage to the environment. For a simple threshold, ensuring that peak flows from the turbine are within that of the expected environmental flows can be used as a first case. In basins where the opening involves a long narrow section (such as the Queen Alexandra dock in Cardiff – shown in Figure 6.3) additional effort may be required to prevent the formation of seiche effects from the water level changing rapidly at one end and thus developing a water level gradient within the dock. This would require additional assessment using 2D or likely 3D models once a specific dock had been chosen for development.

6.4.3 Identified sites power generation

A total of 28 docks were identified by the search process, for each dock, the various design options were tested, and best-case configurations selected using the 0D modelling method as presented in Table 6.4. The tidal docks were found to produce a combined net energy of 34.26 GWh per year, with a maximum extracted energy ranging from 20392 MWh (Cardiff) to 12 MWh (Glasgow) per year, note that the small tidal range at Lowestoft (1.35 m mean) was found to be too small to produce energy under these conditions. The highest peak power output for the docks, 18 MW was found using 6 turbines at Cardiff. This classes the docks as ‘Small Power Stations (<50 MW)’ by GB National Grid guidance [34]. Only the largest docks were able to operate in a manner that had them reach close to their theoretical capacity however, with Cardiff and Barry achieving this level, and London coming close at a peak capacity of 3 MW per turbine. Eastbourne has a notably high energy capacity for the size of the basin and tidal range, stemming from a longer impoundment opening – allowing the largest number of turbines (28) per the design equation (6.1). This allows the scheme to produce a very short high power burst of generation – emptying the impoundment in a very short time, hence the more moderate energy yield of the scheme. The remaining docks had lost or gained enough water volume to bring the internal water level to below that of peak generation by the end of the warmup period, a better suited turbine could mitigate this effect.

The hydrodynamics of the schemes would vary depending on the basin areas, aspect ratios, and tidal ranges – with the strengths and weaknesses of the docks basins being a function of their prior uses. For example, former dry-docks or graving docks are designed to be fully emptied, with wall structures designed to accommodate this. Loading or transport docks may be found to have structural limits required on the internal regime, however accurate identification of these features would take place once the scoping use of a study such as this has been carried out.

In the majority of cases (20 of the 28 total) the best configuration was found to be the maximum number of turbines for the scheme opening space. Along with this, the option for not having a sluiced area was resoundingly the better configuration with all basins generating more electricity without sluices. This is likely a function of the flow rates that the turbines can provide relative to the impounded volume of water as compared to the far larger classical barrage or lagoon schemes. When considering the construction of a scheme such as this however it is important to bear in mind the relative costs of the components. Vandercruyssen et al. [24] found that turbines and generator systems were (in most cases) orders of magnitude more costly than sluice structures – and so the best configuration on an energy production basis may not be the most cost effective.

Table 6.4: Full docks output, generation, and configuration results.

City	Tidal Range	Area	Wall	Max Turbines	Best Annual Output	Peak Output Level	Best Config	
	[m]	[m²]	[m]	[-]	[MWh]	[MW]	n_{TB} [-]	A_{SL} [m]
Cardiff	8.9	203660	30	6	20392	18	6	0
London	5.4	133405	35	7	4296	10.2	7	0
Barry	8.9	27750	25	5	2900	3	1	0
Eastbourne	5.1	47750	150	30	2324	12.4	28	0
Middlesbrough	3.4	100000	25	5	1224	4.4	5	0
Hull	5	10725	20	4	468	2.4	4	0
Southampton	1.4	16600	40	20	452	5.6	14	0
Rosyth	3.3	15500	100	18	296	4.8	12	0
Newcastle	3.2	10000	55	8	272	3.2	8	0
Grays	4.9	3025	30	11	224	2.8	7	0
Glasgow	2.5	24700	90	5	168	2	5	0
Edinburgh	3.5	6100	25	6	156	2.3	6	0
Newcastle	3.2	6125	30	6	136	1.6	4	0
Glasgow	2.5	10000	65	13	124	4	10	0
Glasgow	2.5	9000	30	10	112	3.5	9	0
Stockton-on-Tees	3.4	4400	50	6	108	1.6	4	0
South Shields	3.2	4500	25	5	100	1.2	3	0
Grays	4.9	1825	25	5	96	2	5	0
Newcastle	3.2	3100	20	4	68	0.8	2	0
South Shields	3.2	2575	15	3	56	0.8	2	0
South Shields	3.2	2525	20	4	56	0.8	2	0
Glasgow	2.5	4350	55	11	56	1.6	4	0
Glasgow	2.5	3900	20	4	48	1.6	4	0
Glasgow	2.5	3600	35	4	44	1.6	4	0
Glasgow	2.5	3570	20	7	44	1.6	4	0
South Shields	3.2	1300	15	3	28	0.4	1	0
Glasgow	2.5	1025	20	4	12	0.4	1	0

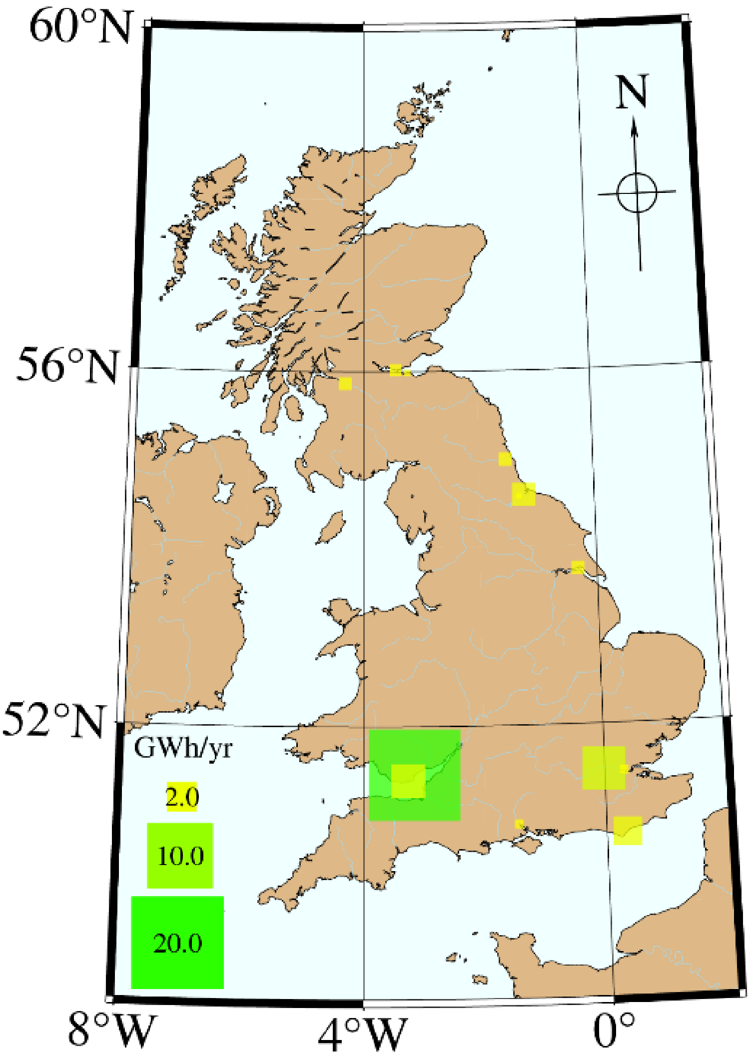

Figure 6.15: Mapped docks best annual energy extraction, markers scaled and coloured on best output.

6.4.4 Grid Impacts

Where a single dock as examined in Section 6.4.2 provides insight into some of the likely behaviour of a tidal dock, there is greater potential value to the grid of a fleet of tidal docks spread around the country providing energy over a range of times and locations. The operations of all 28 schemes, using the highest producing designs – laid out in Table 6.4 were combined in a stacked energy production plot in Figure 6.16. Here the impact of the neap-spring cycle can be seen over the three-month period, with all schemes showing higher levels of productivity during spring tides such as were seen in early February. The largest producing docks – Cardiff, London and Barry form the major proportion of the energy produced by the fleet of docks.

These three basins are notable in their size and large tidal range, as expected based on first principals (such as the assumptions developed by Prandle [124]).

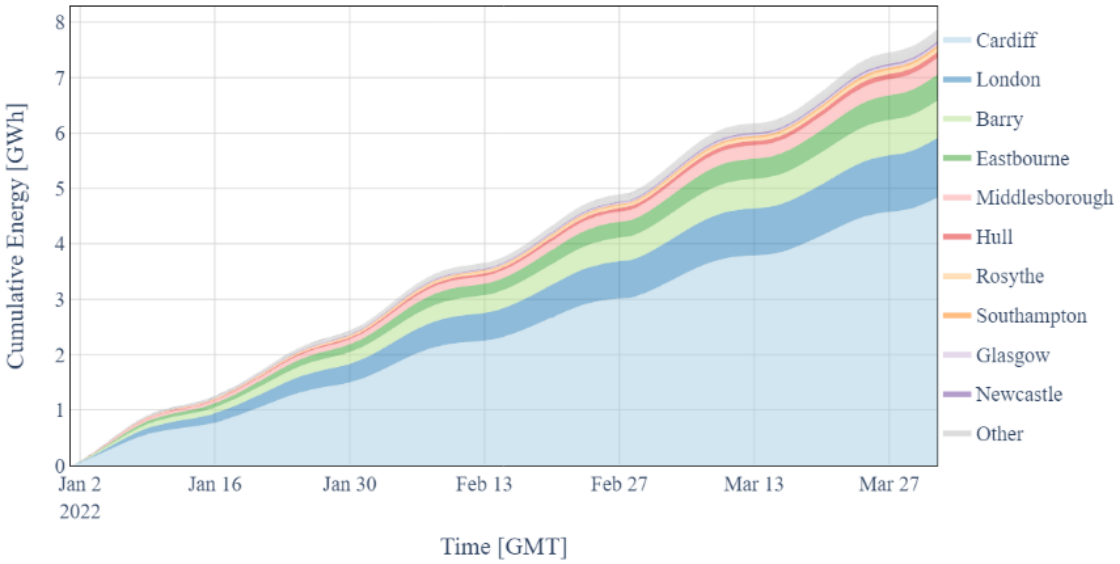

Figure 6.16: Q1 2022 – Combined energy yield of all docks considered.

Figure 6.17 shows a typical day of operation wherein all the energy extracted by the various schemes around the country is stacked together – with the varying energy price for the day shown below. On this day it is apparent that the energy price was above 0 £/MWh, with a key period of low value between 04:30 and 07:00, and high prices in the morning with peaks after 18:00. A pattern of this nature is typical for Great Britain, as shown in Figure 2.2. The tidal range schemes here use the spatial distribution and thus the temporal variation in tidal timings to spread the period of generation out over the day, generating 75.9 % of the time, and with a combined generation of over 5 MW for 18.9 % of the day (4 hours 32 minutes). This is a day of marginally lower production for the dock schemes combined as compared to the overall quarterly production, statistics of which are shown in Figure 6.18, where the schemes combine to generate 80.5 % of the time, and over 5 MW for 24.7 % of the time.

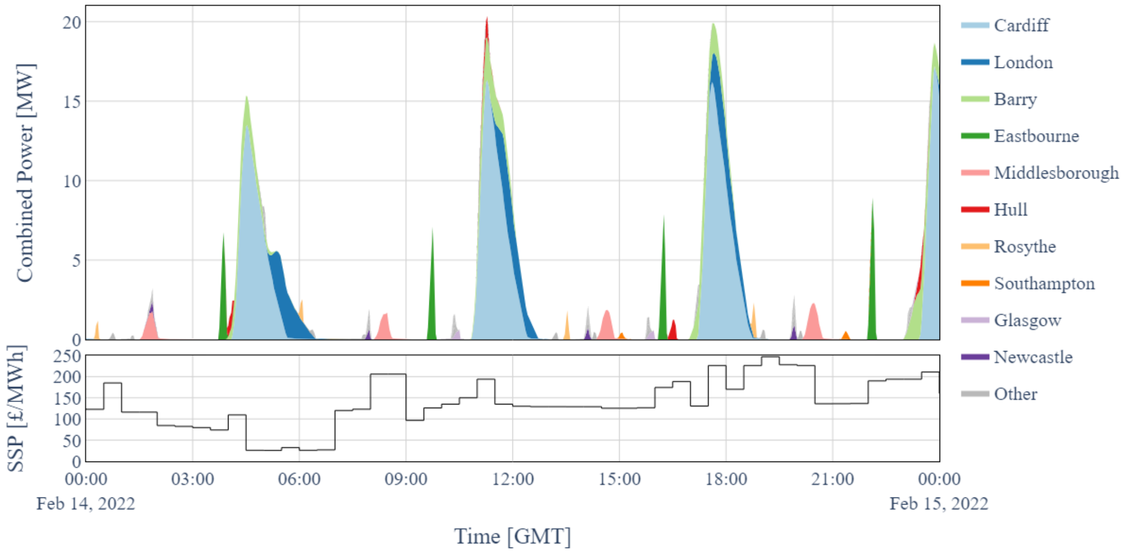

Figure 6.17: Power on sample day of combined output from docks (mean tide).

Continuous production has been considered in prior studies as a goal, however the intent of a small tidal dock would be more akin to that of a pumped storage facility, generating at times of need – or financial value. This is seen in Figure 6.17 at 11:00 and 18:00 where the largest basins all generate at the times of highest value based on System Sell Price (SSP). It is interesting to note that there is an electricity generation cluster during the low value period around 06:00, this is driven by the tides rather than the energy value – achieving an operation that returns some yield from a weak period, without excessively compromising the future generating potential of the schemes. These periods where the tides at the major locations do not align with the needs of the system are a fundamental drawback of the tidal range method, although many methods have sought to remedy this to some degree. This could be done by construction of a useable volume above the maximum water level of the area that can allow the scheme to function as a pure pumped storage system.

Over the 3 months, the optimal dock schemes reached a peak combined generation capacity of 40.4 MW. Figure 6.18 shows the probability distribution of the combined power output of the identified docks. This shows how the fleet of tidal docks combines in operation, generating more than 17.8 MW collectively over half the sampled time, and only generating no power 1.4 % of the time. Central control over the tidal range schemes could be used to augment this distribution, if a base load supply or equivalent target was held across the system.

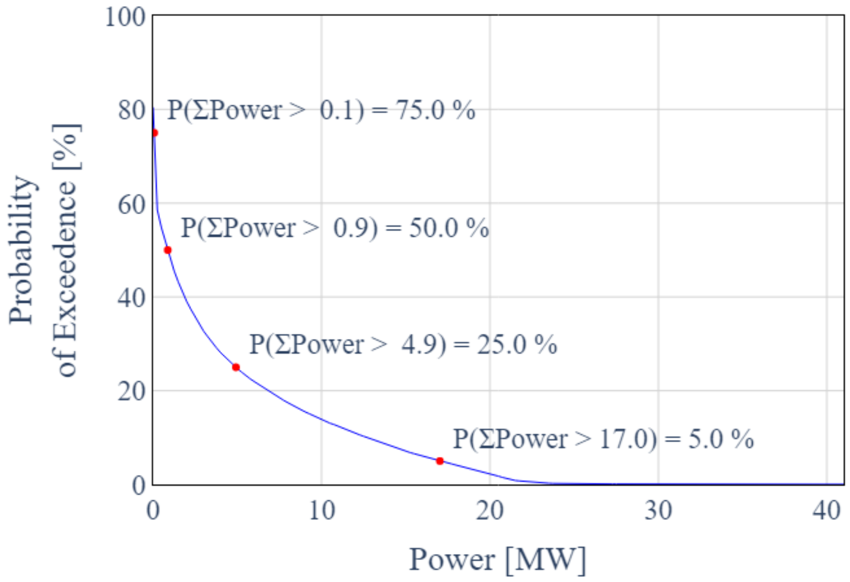

Figure 6.18: Probability distribution of power outputs for fleet of tidal docks.

6.4.5 Measurement Sensitivity

Due to the uncertain nature of the model's water level inputs, a quantification of the impact that this uncertainty induces was performed. To achieve this, the water level input traces were multiplied by a bulk magnitude of ± 5, 10 & 15 % about the mean water level, thus modifying the mean tidal range of the series (denoted by ξ) by the same degree. The models were then run using the best configuration determined in the prior assessment stage at a number of these levels and the energy E extracted by these modified inputs ascertained. These are shown below for the docks, normalised to the respective original tidal ranges (ξ_0) and energy outputs E_0 in Figure 6.19, along with a least-squares quadratic regression line, giving a very good degree of fit of that line to the data within this range.

Equation 2.5, derived from first principals by Prandle [232] defines the fundamental theory of tidal range scheme energy potential. The importance of the tidal range itself here is critical, and although using assumed tidal traces ascertained from harmonics at near to site locations provides a reasonable start-point, the potential impact of errors in this assumption cannot be ignored. Figure 6.19 represents an effort to quantify this potential error and shows how there is variation between the individual schemes . In general, however, it can be seen that for an assumed reduction in the tidal range of a given amount, there is a reduction in energy output of more than double the magnitude. Naturally, there is also an equivalent improvement of this order if the tidal range has been underestimated in the initial case. The sensitivity of the tidal range scheme to the variation of the surface area of the scheme through the tidal cycle was assessed, and it was found to follow a generally linear scheme, as suggested by Prandle [232]. This assumption showed a weaker correlation than that of the tidal range, however a reduction in the base area by a given magnitude did result in a reduced energy yield of a lower magnitude. These tests aim to provide an indicator of the performance changes associated with errors in the baseline data to those carrying out future assessments on these schemes.

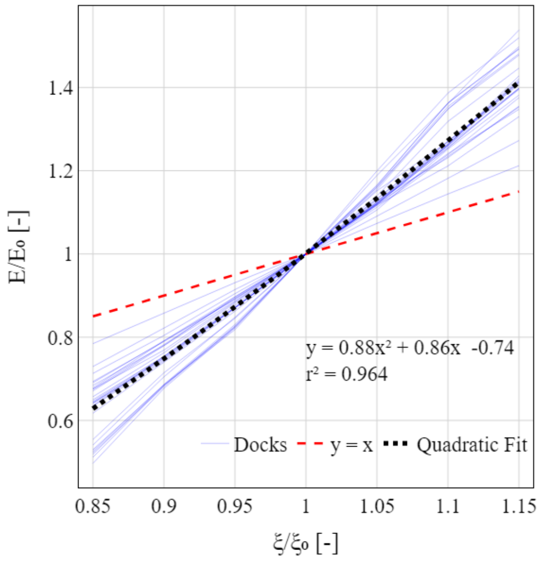

Figure 6.19: Sensitivity to water level input.

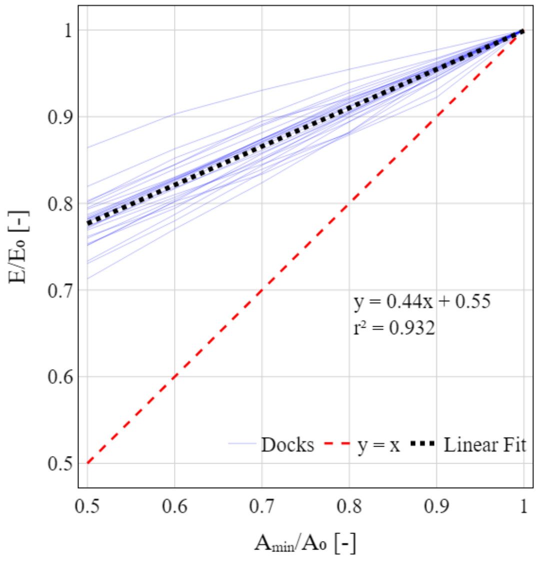

Figure 6.20: Sensitivity to basin area.

As the basin area is taken from satellite imagery, only the surface area can be determined without on-site measurements. The assumption used was that the surface area was constant through the tidal range, this however can only be viewed as a best-case scenario. In many cases there will be design aspects that reduce the area of the basin below this. To quantify the potential impact of this assumption, the area at the lowest natural water level A_{min} (km^2) is reduced from the original assumed area A_0 (km^2) creating a linearly trapezoidal volume, the impact of this upon the energy extracted is shown in Figure 6.20, along with a linear least-squares fit to the data, and the line of unity for reference.

There will be other hydrodynamic effects that influence operation that are in the case of these schemes, more influential than traditional schemes (which tend to be located at sites of generally open water with large natural flow velocities). The shape of an impoundment is likely to impact the extent to which the level-pond assumption can be held, with these docks often being particularly long and narrow. The likelihood of discharging into either a semi-enclosed area or a region of high navigational importance is also necessary to be considered in longer term understanding of the usage of a dock as a tidal range scheme.

6.5 Summary

The concept of using small basins to act as small-scale tidal range schemes whose operation is better suited to targeting high demand periods in the grid operation has been introduced to expand the potential scope of tidal range to contributing to a net zero energy mix for the UK. To do this, the option of retrofitting disused infrastructure with the engineering machinery typically associated with a tidal range scheme is considered based on the minimalization of the capital costs, reduced environmental value, and proximity to end-users. This system is expected to be cross-applicable to other small tidal range concepts – including regions with smaller tides than that of the UK. These tidal basins could provide some of the benefits of the tidal range mechanism, without the high costs of traditional scale schemes, along with a platform to carry out testing of novel approaches and technologies (such as turbines) in an environment with lower sensitivity to environmental effects.

To aid stakeholders in carrying out an assessment of this source of energy, a framework for determining an early-stage energy yield is presented, and then exemplified in detail for a single site (Barry docks older entrance basin), and then summarised for a total of 28 dock basins around the British coast, with particular attention paid to former areas of maritime industry. Tools used in this process were selected to be as inclusive as possible – minimizing the need for specialist software, expensive services, or large expertise in the field in hope of expanding the concept farther afield to developing or previously unconsidered areas, where the need for renewable energy is just as prevalent as the tidally blessed United Kingdom.

The 28 basins formed a set with varying size, and tidal range – yielding a combined 34.36 GWh of electrical energy per year. The tidal docks were found to have peak generation levels that classify them as Small Power stations per national grid guidance for the country, typically less than 50 MW.

A sample of how the identified tidal docks may interact with the energy network was presented and discussed in terms of how the operation may deviate from that classically associated with tidal range schemes. The short period generation profiles in the designs identified here were better suited to targeting the periods of high value as opposed to providing a baseload of power to the grid.

Tidal range and surface area, as with traditional tidal range schemes are still key to base production, and as such were sensitivity tested in order to provide a view as to how the production may be expected to vary if the base data were corrected using site measurements or higher resolution modelling study.

7 Conclusions and Recommendations

7.1 Conclusions

7.1.1 SPH modelling of vertical axis turbines

The CarBine turbine is a vertical-axis device that uses a set of hinged arms mounted about a central axis, that are moved by the flow through the device such that they have their drag reduced on the returning side and maximised on the generating side. To achieve net zero, regions where energy is available from flowing water, such as the tides around the UK, additional investigation into potential methods to extract this power will be required. This turbine could be applied to a range of operating conditions, including riverine flows, tidal flows, and potentially in the regions where jet effects from the discharge through a tidal range scheme incur large velocities. Unrestrained numerical representation of the CarBine has been a challenge due to the multiple moving components occupying the same space and the multi-faceted fluid-structure interactions required to drive the device. To understand the free-spin behaviour of the device when being operated in a scenario mimicking prior flume study, a Smoothed Particle Hydrodynamics model using a 2D representation of the turbine was developed. At this stage, no reactive force could be applied to the turbine, meaning that operation was limited to free-spin scenarios, which are not an operating mode that the turbine would be run in for any significant period of time in reality. Further to this, no determination of the power extraction characteristics could be yielded at this stage for the same reason, which would be required before any consideration of installation or suitability to generator connection could be made.

This method was able to model the turbine as a set of connected but otherwise free components, using the principles of the concept itself. The advantage of this is removing the need for a prior physical or empirical study to ascertain the behaviour of the device prior to simulation and thus allowing a calibrated and validated model to be modified to predict the behaviour of the device in unknown operating conditions. This was done using two 'damaged' cases for each of the five different design configurations. This resulted in an unsteady behaviour in all test cases, confirming the first-principles assumption that in a design wherein two flaps are mounted on the same radial arm, the loss of the outer arm is more detrimental to the device operation than the inner arm. In installation cases where the device is damaged, a 'limping along' type operation may be required if no other suitable sources of energy are available, and so replacing a lost outer arm with an inner arm could be used to provide better temporary operation. Representation of the self-start mechanism using only the hydrodynamic forces on the turbine was demonstrated for numerous design options including damaged turbine cases.

The relative positioning and number of flaps on a given CarBine design have been a key interest since the inception of the design. Recent studies tended towards a four-arm system with two flaps per arm. Four additional configurations were tested as part of this study, three-six arms each with two flaps and an alternate four-arm design with the inner flap array being mounted at a 45° offset to the exterior flaps. On simple merit the advantages of the four-arm base model were held up by the study, producing the highest rate of rotation and reduced variability in the rotation compared to the three-arm model. The four-arm alternate design showed the most consistent motion around the rotation and showed the best resilience to the loss of a single arm. The five and six-arm designs showed lower mean velocities than the designs with fewer arms, although the improved consistency of rotation may translate well to the application of a power take-off.

The development of a more widely applicable modelling method was an aim of the study, the SPH method was found to have both strengths and weaknesses in this usage. The speed of building, modifying, and running the simulations was very prevalent and natural. The ability to define all the bodies within the model, how they are connected, and a particle spacing makes for what can be vast changes very easy to make. Moving the position of elements or the position of a boundary ostensibly requires no re-formatting. The biggest challenge in this modelling was maintaining stability. A driver of this from the concept of this particular turbine, is how the flaps move apart from each other when transitioning between positions. This creates an area of low pressure – and if this action pulls the particles into too-disperse of a spacing such that compact support is lost between them, a void is liable to form. These voids had the propensity to propagate, and some formulations (notably the Laminar+SPS turbulence model) are highly unstable to this. As a result, a very large shifting correction and the artificial viscosity formulation were required to keep the model from coming apart. The extent to which this is required may vary with other turbine designs and should be investigated when testing other devices.

The SPH model was found to converge well to the particle spacing, and the length of compact support as suggested in the literature. The best balance was found to be with a particle spacing of 1.0 mm and a compact support distance of 2.25 mm. This allowed for a sufficiently detailed representation of the components (the flaps were slender by nature) and also provided a turbulence model using particle based direct numerical simulation. The turbulent wake effects were visible, but not a focus of the study at this stage. The downstream boundary condition, however, was found to be well suited to absorbing these turbulent effects, and the study found that the model operation was insensitive to the position of the downstream boundary, the benefit of this being the ability to minimise the domain when conducting study not related to the wake effects – reducing the cost of simulation.

7.1.2 Large tidal range schemes

To reach net zero goals in the UK, an expansion and diversification in the suite of renewable energy generators contributing to the system will be key. Tidal range has been considered for development in the UK for over a century, and this study looked at two existing proposals and carried out a multi-model study to investigate how changes to the operating schedule could improve the value of generated electricity, how the design space in terms of turbines and sluices looks, and what impact on the environment the operational changes would make. This was done to both further the state of knowledge on tidal range, gain an insight into how a well-developed tidal range network would contribute to the energy mix, and exhibit the tools used.

Through optimisation of the operational schedule alone - using two methods, the targeting of generation times of higher value, and the change to parallel sluicing - the two case study sites had their net revenue improved by a combined 7.5 %, or 55 million pounds per year. This demonstrates how two methods for operational improvement as previously tested can stack together and provide a consolidated gain. This was echoed in the two-dimensional modelling of the West Somerset Lagoon - where the degree of improvement from each stage as found in the 0D model was also seen in the 2D sample period. This adds validation to the simplified 0D methodology, as a physically based model can account for effects that may be used in 0D such as the extent to which the scheme follows the level pond assumption. 0D models have been in use for many years in the study of tidal range schemes, however, each user tends to develop their own (the author of this thesis included), to hasten the usage of 0D models for future studies the code used in this work has been made openly available for use and collaboration.

The electricity generated by the two schemes was directly compared to the National Grid energy mix on a sample day. The ability of the tidal range schemes to adjust operation to the peak demands is visible, as is the nature of the grid ecosystem itself. Currently, the grid is reliant on nuclear energy to form the base-load power (a steady level of constant usage), with gas turbines accounting for the major component of the difference between the demand and the energy produced by renewables. Tidal range with its dispatchability would be well suited to reducing the demand for gas turbines, meaning that the electricity generated by tidal range could account for a direct reduction in the electricity generated by gas. With the operation of the schemes developed, the design space of the two case studies is updated by a large dispatch of the 0D model at a variety of turbine numbers and sluice areas. Through this a set of design curves were composed - that could be used in conjunction with a cost function to find a point of best economical value for the schemes.

For the West Somerset Lagoon case study, the 0D modelling was validated by a 2D modelling study using a bespoke modified version of the TELEMAC suite of numerical modelling tools. These models used a 2D Shallow Water Equations method on a finite element grid of the Severn Estuary/Bristol Channel, driven by the open-source TPXO tidal boundary, showing good accuracy through the model based on modelling guidelines. The changes to the operation were found to have negligible environmental impact, this was broadly to be expected as the physical nature of the changes was small and iterative, with the largest being the parallel sluicing mode, acting hydro-environmentally as a lower velocity flow through the turbines. The TELEMAC subroutine used in the study has been shared for public use in the hope that it will make the study of tidal range easier for future users, along with the intention of developing the further scope of use for a system that allows temporal and model-state based control of flow structures, such as dams or reservoirs.

The 2D study found that the changes to performance in the 0D model were echoed in the 2D sample period (though for computational brevity the 2D model utilised a much smaller sample period). The magnitude of generation between the 0D and 2D models was larger than in some cited literature, possibly due to the selection method of the sample period, since the changes were of consistent degree. This highlights the need for further iterative optimisation processes using both 0D and 2D at relevant stages. A thorough 2D modelling study of a tidal range scheme is vital to understanding the impact these (large) structures would have on the regions in which they are constructed.

7.1.3 Disused docks as tidal range schemes

The classical image of tidal range in the UK has been to build a small number of large capacity installations, these would impound vast tracts of tidal areas, encompassing beaches, tidal flats, human infrastructure and more. This underpins the two great challenges of tidal range – cost and environmental impact. As a counterpoint to this, the concept of having (eventually) a large number of very small tidal range schemes around the country is developed. In this case through the idea of the tidal dock, sealing a disused tidal basin with a set of turbines and sluices. This concept mitigates the cost of construction – since the majority of the impoundment is in place, along with being much smaller (all identified were less than 1 km^2).

28 basins were identified around the UK using an open-source information-gathering approach, and 0D models were run for each of them to ascertain an ideal design configuration based on a simplified design space. This combination of basins combined to yield 34 GWh per year on average. Due to their relatively small size, the basins were found to empty in a short time, tending to target their generation to times of high energy demand in the period where available, indicating a strong possibility of their being operated more akin to pumped storage schemes than the classical tidal range operation we are used to seeing. The majority of the schemes were found in cities whose industrial role has shifted with the global economy, these areas are often redeveloped into housing as has been the case in London, Cardiff and Baltimore. In developments such as these, water is a feature that is desired by stakeholders, and the novelty of being beside an unusual electricity generation system may be a valuable selling point. The environmental impact of the schemes is also reduced, firstly by the scale of the development. Secondly, the area is already industrialised; thus, the ecosystems in place are likely to be less sensitive, and in some cases may benefit from the increased variation in water caused by a tidal basin. These tidal docks could also be well positioned for use as testing facilities for turbine manufacturers and other engineering devices, providing controllable impoundments that a structure can easily be installed in – where making modifications to a 10m turbine operating in deep water multiple kilometres into the estuary is challenging both in terms of logistics and scale. The access via the existing dock infrastructure would be far better suited to replacing modules and may aid the development of other tidal range ventures through this capability.

As tides are a global phenomenon, a template method was laid out to allow researchers anywhere to consider their location for use as a tidal range energy scheme, this was done by using an open-source intelligence gathering method to build the models, and a low-cost model itself to run the analysis. The aim of this was to create a method that would be available to a wide variety of potential users – not just those with access to high-powered computing and expensive software or tools. Other options for the deployment of this could be sought wherever the tidal range is felt to be large enough – although the study carried out here shows that the tidal range can be relatively low, and the basin still produces meaningful energy. This could be applied to consider the deployment of tidal range in developing energy markets where the scope for low-carbon growth in capacity could accelerate the global transition towards net zero.

7.2 Recommendations for future research

As part of this work, the SPH method was applied to the study of a vertical-axis turbine. This was in large part due to the challenges associated with modelling this turbine using the traditional methods – multiple linked and moving components within the same regions. The result of this was a relatively low-cost approach to the simple behavioural analysis of the CarBine. One key aspect that could not be applied within the project was the inclusion of power take-off, limiting the analysis at this stage to free-spin characteristics. Development of the boundary treatment of the central hinge either through the DualSPHysics model, or the CHRONO backend would be very valuable, as the development of power is the fundamental purpose of a turbine. With the development of a power take-off, the method would be well suited to testing on alternate and better-understood devices, to provide further evidence of the scope of the method for the development of hydrokinetic turbines. This could be both through the study of other drag-based devices such as the classic Savonius turbine upon which CarBine was based, or the expansion to lift-based designs such as Darrieus. In the case of lift-based turbines, the convergence of the particle spacing in particular would be interesting to investigate due to the importance of developing the appropriate forces over the blades by the foils. Comparisons of the SPH method to mesh-based methods typically used in the study of these devices would be valuable in terms of furthering one of the key goals of the SPHERIC steering committee – to improve the commercial faith in SPH.

Additional expansion into 3D modelling of the device may yield interesting phenomena, and again performance comparisons both in terms of device and computation may be investigated. Ideally, further study of either this device or alternate devices would begin to investigate the topic of turbulence in the wake and how the model represents this turbulence, with the approach being close to direct numerical simulation – though a different turbine design may be suited to a coarser domain and thus one of the other turbulence models would be better suited in terms of computational cost.

Tidal range energy has had a long history of interest in the UK but has always been held back by the balance of cost and risk – to the environment and the investor. Due to the nascent state of the industry within the UK, and the low number of developments across the world, the costing themselves are ever in need of better clarity – though the commercially sensitive nature of much of this information makes the topic challenging. One method to begin the process of changing the view of tidal range would be to apply the disused docks concept to other small basins, reducing the cost both financially and to the environment. By reducing this cost, it would be valuable to expand the small-tidal range concept beyond the coast of the UK, there are countries around the world with a degree of tidal range resource, including those in emerging economies, where the previously prohibitive cost being reduced could be transformative. For brevity, pumping was excluded from the study of the disused docks, this would undoubtedly increase the electricity generation potential if the correct limits were applied, further transitioning these small tidal range schemes towards operating as pumped storage energy systems.

Finally, the ancillary services market of the GB national grid could pose an interesting avenue for tidal range schemes to enter into, the ability of a tidal range scheme to develop an energy potential, hold that potential, and generate on command is akin to that of a pumped storage system. Developing a behavioural control system for a tidal range scheme to operate as an ancillary services provider to the grid could determine whether a tidal range scheme could be more valuable in this market. This would likely be better suited to small tidal range schemes, with the significant departure from the environmental flows that ancillary services-based operation would incur. This could shift the view of tidal range from being an alternate form of tidal turbine to that of a pumped storage battery – aided by the tide.

References

1. IPCC (2022) Climate Change 2022 - Impacts, Adaptation and Vulnerability - Summary for Policymakers. In: Portner H-O, Roberts DC, Poloczanska E, et al (eds) Contribution of Working Group II to the Sixth Assessment Report of the Intergovernmental Panel on Climate Change. Cambridge University Press, p 37
2. Briggs H (2021) What is the Paris climate agreement and why did the US rejoin ? In: BBC News - Sci. Environ. https://www.bbc.co.uk/news/science-environment-35073297. Accessed 27 Jul 2021
3. European Commission (2019) Communication on The European Green Deal
4. International Energy Agency (IEA) (2021) An Energy Sector Roadmap to Carbon Neutrality in China
5. International Energy Agency (IEA) (2022) World Energy Outlook 2022
6. Masson-Delmotte V, Zhai P, Pörtner H-O, et al (2018) IPCC, 2018: Global warming of 1.5°C. An IPCC Special Report on the impacts of global warming of 1.5°C above pre-industrial levels and related global greenhouse gas emission pathways, in the context of strengthening the global response to the threat of cli. Geneva, Switzerland
7. Alstone P, Gershenson D, Kammen DM (2015) Decentralized energy systems for clean electricity access. Nat Clim Chang 5:305–314. https://doi.org/10.1038/nclimate2512
8. United Nations Department of Economic and Social Affairs Population Division (2019) World population prospects 2019
9. Gielen D, Boshell F, Saygin D, et al (2019) The role of renewable energy in the global energy transformation. Energy Strateg Rev 24:38–50. https://doi.org/10.1016/j.esr.2019.01.006
10. Ember (2021) Global Electricity Review 2021 - Global Trends
11. HM Government (2009) The UK Low Carbon Transition Plan. London
12. Department for Business Energy & Industrial Strategy (2020) Energy White Paper - Powering our Net Zero Future. London
13. Department for Business Energy & Indutrial Strategy (2023) Powering Up Britain: The Net Zero Growth Plan. London
14. Department for Business Energy & Indutrial Strategy (2023) Powering Up Britain: Energy Security Plan. London
15. Cárdenas B, Swinfen-Styles L, Rouse J, et al (2021) Energy storage capacity vs. renewable penetration: A study for the UK. Renew Energy 171:849–867. https://doi.org/10.1016/j.renene.2021.02.149
16. International Hydropower Association (2021) Hydropower status report 2021
17. Elexon (2020) Electricity Pricing. In: Elexon Knowl. Base. https://www.elexonportal.co.uk/
18. Neill SP, Haas KA, Thiébot J, Yang Z (2021) A review of tidal energy - Resource, feedbacks, and environmental interactions. J Renew Sustain Energy 13:. https://doi.org/10.1063/5.0069452
19. European Marine Energy Centre (2021) Tidal Clients: Orbital. In: Eur. Wind Energy Cent. LTD. http://www.emec.org.uk/about-us/our-tidal-clients/orbital-marine-power/. Accessed 2 Aug 2021
20. Sustainable Development Commission (2007) Turning the Tide: Tidal Power in the UK. London
21. Yates N, Walkington I, Burrows R, Wolf J (2013) The energy gains realisable through pumping for tidal range energy schemes. Renew Energy 58:79–84. https://doi.org/10.1016/j.renene.2013.01.039
22. Harcourt F, Angeloudis A, Piggott MD (2019) Utilising the flexible generation potential of

tidal range power plants to optimise economic value. Appl Energy 237:873–884. https://doi.org/10.1016/j.apenergy.2018.12.091

23. Charlier RH, Menanteau L (1997) The saga of tide mills. Renew Sustain Energy Rev 1:171–207. https://doi.org/10.1016/S1364-0321(97)00005-1
24. Vandercruyssen D, Howard D, Aggidis GA (2023) A model of the costs for tidal range power generation schemes. Proc Inst Civ Eng - Energy 00058:1–10. https://doi.org/10.1680/jener.22.00058
25. Fisheries and Oceans Canada (DFO) (2019) Review of existing scientific literature pertaining ot fish mortality and its population-level impacts at the Annapolis Tidal Hydroelecitric Generating Station, Annapolis Royal, Nova Scotia. Dartmouth
26. International Energy Agency (IEA) (2023) Global Gas Security Review 2023
27. Mettam C (1978) Environmental effects of tidal power generating schemes. Hydrobiol Bull 12:307–321. https://doi.org/10.1007/BF02259192
28. Institution of Civil Engineers (Great Britain) (1982) Severn Barrage: proceedings of a symposium organized by the Institution of Civil Engineers. Thomas Telford, London
29. Aggidis GA, Feather O (2012) Tidal range turbines and generation on the Solway Firth. Renew Energy 43:9–17. https://doi.org/10.1016/J.RENENE.2011.11.045
30. Ridgill M, Neill SP, Lewis MJ, et al (2021) Global riverine theoretical hydrokinetic resource assessment. Renew Energy 174:654–665. https://doi.org/10.1016/j.renene.2021.04.109
31. Kirke B (2020) Hydrokinetic turbines for moderate sized rivers. Energy Sustain Dev 58:182–195. https://doi.org/10.1016/j.esd.2020.08.003
32. Natural Resources Canada (2022) Clean Energy for Rural and Remote Communities Program
33. O'Rourke F, Boyle F, Reynolds A (2010) Tidal energy update 2009. Appl Energy 87:398–409. https://doi.org/10.1016/j.apenergy.2009.08.014
34. Department for Business Energy & Industrial Strategy (2020) GB Electricity Market Implementation Plan
35. Department for Business Energy & Industrial Strategy (2019) Capacity Market Five-year review (2014-2019)
36. Hughes A (2020) We need long-term storage to keep the lights on. BHA Spotlight 14
37. Department for Business Energy & Indutrial Strategy (2020) The Ten Point Plan for a Green Industrial Revolution. London
38. Department for Business Energy & Indutrial Strategy (2021) Net Zero Strategy: Build Back Greener. London
39. Department for Business Energy & Industrial Strategy (2022) British Energy Security Strategy. London
40. Department for Business Energy & Industrial Strategy (2019) Statistical Press Release: UK Energy Statistics 2018 and Q4 2018. 9
41. Green R, Vasilakos N (2011) The Long-term Impact of Wind Power on Electricity Prices and Generating Capacity. Birmingham
42. Seward W, Qadrdan M, Jenkins N (2022) Quantifying the value of distributed battery storage to the operation of a low carbon power system. Appl Energy 305:117684. https://doi.org/10.1016/j.apenergy.2021.117684
43. Egbert GD, Erofeeva SY (2002) Efficient inverse modeling of barotropic ocean tides. J Atmos Ocean Technol 19:183–204. https://doi.org/10.1175/1520-0426(2002)019<0183:EIMOBO>2.0.CO;2
44. Parker BB (2007) Tidal analysis and prediction (NOAA Special Publication NOS CO-OPS 3). Silver Spring, Maryland
45. Hicks SD (2006) Understanding tides (NOAA Report)
46. Uncles RJ (2010) Physical properties and processes in the Bristol Channel and Severn Estuary. Mar Pollut Bull 61:5–20. https://doi.org/10.1016/j.marpolbul.2009.12.010

47. Cartwright DE (1999) Tides: a scientific history. Cambridge University Press, Cambridge
48. Egbert GD, Bennett AF, Foreman MGG (1994) TOPEX/POSEIDON tides estimated using a global inverse model. J Geophys Res 99:. https://doi.org/10.1029/94jc01894
49. Vazquez A, Iglesias G (2015) Device interactions in reducing the cost of tidal stream energy. Energy Convers Manag 97:428–438. https://doi.org/10.1016/j.enconman.2015.03.044
50. Pawlowicz R, Beardsley B, Lentz S (2002) Classical tidal harmonic analysis including error estimates in MATLAB using T_TIDE. Comput Geosci 28:929–937. https://doi.org/10.1016/S0098-3004(02)00013-4
51. European Marine Energy Centre (2019) EMEC Fall of Warness Tidal Test Site lease extended to 2040. In: Press Release. http://www.emec.org.uk/press-release-emec-fall-of-warness-tidal-test-site-lease-extended-to-2040/. Accessed 7 May 2021
52. ABP Marine Environmental Research Ltd (2008) Atlas of UK Marine Renewable Energy Resources: Technical Report
53. Office for National Statistics (2011) 2011 UK Census
54. Ma Q, Adcock TA. (2020) Modification of tidal resonance in the Severn Estuary by a barrage and lagoon. J Ocean Eng Mar Energy 6:171–181. https://doi.org/10.1007/s40722-020-00166-8
55. Munson BR, Young DF, Okiishi TH (2006) Fundamentals of fluid mechanics, 5th ed. Wiley, New York
56. The Crown Estate (2012) UK Wave and Tidal Key Resource Areas Project - Summary Report. The Crown Estate 1–10
57. Coles D, Angeloudis A, Greaves D, et al (2021) A review of the UK and British Channel Islands practical tidal stream energy resource. Proc R Soc A Math Phys Eng Sci 477:. https://doi.org/10.1098/rspa.2021.0469
58. Kirke B (2019) Hydrokinetic and ultra-low head turbines in rivers: A reality check. Energy Sustain Dev 52:1–10. https://doi.org/10.1016/j.esd.2019.06.002
59. Kirby K, Ferguson S, Rennie C, et al (2022) Assessments of available riverine hydrokinetic energy: a review. Can J Civ Eng 49:839–854. https://doi.org/10.1139/cjce-2021-0178
60. Lin P, Pan M, Beck HE, et al (2019) Global Reconstruction of Naturalized River Flows at 2.94 Million Reaches. Water Resour Res 55:6499–6516. https://doi.org/10.1029/2019WR025287
61. Balat M (2009) A review of modern wind turbine technology. Energy Sources, Part A Recover Util Environ Eff 31:1561–1572. https://doi.org/10.1080/15567030802094045
62. Khan MJ, Bhuyan G, Iqbal MT, Quaicoe JE (2009) Hydrokinetic energy conversion systems and assessment of horizontal and vertical axis turbines for river and tidal applications: A technology status review. Appl Energy 86:1823–1835. https://doi.org/10.1016/j.apenergy.2009.02.017
63. Lissaman PBS (1974) Applied aerodynamics of wind power machines
64. Pudjianto D, Frost C, Coles D, et al (2023) UK Studies on the Wider Energy System Benefits of Tidal Stream. Energy Adv 2:12–33. https://doi.org/10.1039/D2YA00251E
65. Encarnacion JI, Johnstone C, Ordonez-Sanchez S (2019) Design of a horizontal axis tidal turbine for less energetic current velocity profiles. J Mar Sci Eng 7:. https://doi.org/10.3390/jmse7070197
66. Ebdon T, Allmark MJ, O'Doherty DM, et al (2021) The impact of turbulence and turbine operating condition on the wakes of tidal turbines. Renew Energy 165:96–116. https://doi.org/10.1016/j.renene.2020.11.065
67. Fraser S, Williamson BJ, Nikora V, Scott BE (2018) Fish distributions in a tidal channel indicate the behavioural impact of a marine renewable energy installation. Energy Reports 4:65–69. https://doi.org/10.1016/j.egyr.2018.01.008
68. Ahmadian R, Falconer RA, Bockelmann-Evans B (2012) Far-field modelling of the hydro-environmental impact of tidal stream turbines. Renew Energy 38:107–116.

https://doi.org/10.1016/j.renene.2011.07.005
69. Dirieh ND, Thiébot J, Guillou S, Guillou N (2022) Blockage Corrections for Tidal Turbines—Application to an Array of Turbines in the Alderney Race. Energies 15:1–18. https://doi.org/10.3390/en15103475
70. EMEC (2020) Tidal developers: European Marine Energy Centre. In: emec.org.uk. https://www.emec.org.uk/marine-energy/tidal-developers/
71. Masters I, Williams A, Croft TN, et al (2015) A comparison of numerical modelling techniques for tidal stream turbine analysis. Energies 8:7833–7853. https://doi.org/10.3390/en8087833
72. Enevoldsen P, Xydis G (2019) Examining the trends of 35 years growth of key wind turbine components. Energy Sustain Dev 50:18–26. https://doi.org/10.1016/j.esd.2019.02.003
73. Allmark MJ, Ellis R, Lloyd C, et al (2020) The development, design and characterisation of a scale model Horizontal Axis Tidal Turbine for dynamic load quantification. Renew Energy 156:913–930. https://doi.org/10.1016/j.renene.2020.04.060
74. Elkhoury M, Kiwata T, Aoun E (2015) Experimental and numerical investigation of a three-dimensional vertical-axis wind turbine with variable-pitch. J Wind Eng Ind Aerodyn 139:111–123. https://doi.org/10.1016/j.jweia.2015.01.004
75. Divakaran U, Ramesh A, Mohammad A, Velamati RK (2021) Effect of helix angle on the performance of helical vertical axis wind turbine. Energies 14:1–24. https://doi.org/10.3390/en14020393
76. Roy S, Saha UK (2013) Numerical investigation to assess an optimal blade profile for the drag based vertical axis wind turbine. In: ASME International Mechanical Engineering Congress and Exposition, Proceedings (IMECE). pp 1–9
77. Roberts A, Thomas B, Sewell P, et al (2016) Current tidal power technologies and their suitability for applications in coastal and marine areas. J Ocean Eng Mar Energy 2:227–245. https://doi.org/10.1007/s40722-016-0044-8
78. Alvarez EA, Rico-Secades M, Suárez DF, et al (2016) Obtaining energy from tidal microturbines: A practical example in the Nalón River. Appl Energy 183:100–112. https://doi.org/10.1016/j.apenergy.2016.08.173
79. Bryden IG (2006) Discussion: The marine energy resource, constraints and opportunities. Proc Inst Civ Eng Marit Eng 159:131. https://doi.org/10.1680/maen.2006.159.3.131
80. Neill SP, Angeloudis A, Robins PE, et al (2018) Tidal range energy resource and optimization – Past perspectives and future challenges. Renew Energy 127:763–778. https://doi.org/10.1016/j.renene.2018.05.007
81. Falconer RA, Xia J, Lin B, Ahmadian R (2009) The Severn Barrage and other tidal energy options: Hydrodynamic and power output modeling. Sci China Ser E Technol Sci 52:3413–3424. https://doi.org/10.1007/s11431-009-0366-z
82. Elliott K, Smith HCM, Moore F, et al (2019) A systematic review of transferable solution options for the environmental impacts of tidal lagoons. Mar Policy 99:190–200. https://doi.org/10.1016/j.marpol.2018.10.021
83. Vandercruyssen D, Baker S, Howard D, Aggidis GA (2022) Tidal range electricity generation: A comparison between estuarine barrages and coastal lagoons. Heliyon 8:e11381. https://doi.org/10.1016/j.heliyon.2022.e11381
84. Charlier RH (2007) Forty candles for the Rance River TPP tides provide renewable and sustainable power generation. Renew Sustain Energy Rev 11:2032–2057. https://doi.org/10.1016/j.rser.2006.03.015
85. Singal SK, Goel V, Nautiyal H, Papantonis DE (2023) Elements of small hydropower: mechanical equipment
86. Energy and Climate Change Committee (2014) A Severn Barrage? Second Report of Session 2013-14. London
87. Peters C (2010) Severn Estuary Tidal Power. Cardiff Bay

88. Department of Energy and Climate Change (2010) Severn tidal power - Feasability Study Conclusions and Summary Report. London
89. Hinson S (2018) Parliamentary Briefing Paper: 7940 - Tidal lagoons. London
90. Xia J, Falconer RA, Lin B (2010) Impact of different tidal renewable energy projects on the hydrodynamic processes in the Severn Estuary, UK. Ocean Model 32:86–104. https://doi.org/10.1016/J.OCEMOD.2009.11.002
91. Lin B, Ahmadian R, Falconer RA (2010) Hydro-environmental modeling of proposed Severn barrage, UK. Proc ICE - Energy 163:107–117. https://doi.org/10.1680/ener.2010.163.3.107
92. Ahmadian R, Olbert AI, Hartnett M, Falconer RA (2014) Sea Level Rise in the Severn Estuary and Bristol Channel and Impacts of a Severn Barrage. Comput Geosci 66:. https://doi.org/10.1016/j.cageo.2013.12.011
93. Fairley I, Ahmadian R, Falconer RA, et al (2014) The effects of a Severn Barrage on wave conditions in the Bristol Channel. Renew Energy 68:428–442. https://doi.org/10.1016/j.renene.2014.02.023
94. Department of Energy (1989) Central electricity generating board and Severn tidal power group, the Severn Barrage project: general report. London
95. Tidal Lagoon Power (2016) OURS TO OWN From first mover to mass manufacture Building a new British industry from our natural advantage. Swansea
96. Petley S, Aggidis GA (2016) Swansea Bay tidal lagoon annual energy estimation. Ocean Eng 111:348–357. https://doi.org/10.1016/J.OCEANENG.2015.11.022
97. Hendry C (2016) The Role of Tidal Lagoons Final Report
98. Tidal Lagoon Plc (2017) Environmental Statement Chapter 4. Project Description. Appl Dev Consent
99. Moreira TM, de Faria JG, Vaz-de-Melo POS, Medeiros-Ribeiro G (2023) Development and validation of an AI-Driven model for the La Rance tidal barrage: A generalisable case study. Appl Energy 332:120506. https://doi.org/10.1016/j.apenergy.2022.120506
100. Waters S, Aggidis GA (2016) Tidal range technologies and state of the art in review. Renew Sustain Energy Rev 59:514–529. https://doi.org/10.1016/j.rser.2015.12.347
101. EDF (2021) L'usine marémotrice de la Rance. https://www.edf.fr/usine-maremotrice-rance/presentation. Accessed 2 Aug 2021
102. Retiere C (1994) Tidal power and the aquatic environment of La Rance. Biol J Linn Soc 51:25–36. https://doi.org/10.1006/BIJL.1994.1004
103. Andre H (1976) Operating experience with bulb units at the Rance Tidal Power Plant and other French hydro-power sites. IEEE Trans Power Appar Syst 95:1038–1044. https://doi.org/10.1109/T-PAS.1976.32194
104. Rtimi R, Sottolichio A, Tassi P (2022) The Rance tidal power station: Toward a better understanding of sediment dynamics in response to power generation. Renew Energy 201:323–343. https://doi.org/10.1016/j.renene.2022.10.061
105. Rtimi R, Sottolichio A, Tassi P, et al (2022) Three-dimensional hydrodynamic model of the Rance estuary (France) influenced by the world's second largest tidal power plant. LHB Hydrosci J 108:1–8. https://doi.org/10.1080/27678490.2021.2016025
106. Andritz Hydro (2015) Large Hydro
107. Bae YH, Kim KO, Choi BH (2010) Lake Sihwa tidal power plant project. Ocean Eng 37:454–463. https://doi.org/10.1016/J.OCEANENG.2010.01.015
108. Kim JW, Ha HK, Woo SB, et al (2021) Unbalanced sediment transport by tidal power generation in Lake Sihwa. Renew Energy 172:1133–1144. https://doi.org/10.1016/j.renene.2021.03.088
109. Park YH (2017) Analysis of characteristics of Dynamic Tidal Power on the west coast of Korea. Renew Sustain Energy Rev 68:461–474. https://doi.org/10.1016/j.rser.2016.10.008
110. Pope A (2019) Testing the future of tidal energy in Nova Scotia. Can. Geogr.

111. Todeschini G (2017) Review of tidal lagoon technology and opportunities for integration within the UK energy system. Inventions 2:1–21. https://doi.org/10.3390/inventions2030014
112. Withers P (2021) Nova Scotia Power to pull plug on tidal station, seeks $25M from ratepayers. CBC News
113. Li Y, Pan DZ (2017) The ebb and flow of tidal barrage development in Zhejiang Province, China. Renew Sustain Energy Rev 80:380–389. https://doi.org/10.1016/j.rser.2017.05.122
114. Zhang YL, Lin Z, Liu QL (2014) Marine renewable energy in China: Current status and perspectives. Water Sci Eng 7:288–305. https://doi.org/10.3882/j.issn.1674-2370.2014.03.005
115. Ahmadian R, Hanousek N (2021) Exploring broader benefits of tidal range schemes. Hydrolink 79–82
116. Petley S, Starr D, Parish L, et al (2019) Opportunities for tidal range projects beyond energy generation: Using Mersey barrage as a case study. Front Archit Res 8:620–633. https://doi.org/10.1016/j.foar.2019.08.002
117. Chaineux MC, Charlier RH (2008) Women's tidal power plant Forty candles for Kislaya Guba TPP. Renew Sustain Energy Rev 12:2515–2524. https://doi.org/10.1016/j.rser.2007.03.013
118. Fedorov MP, Shilin MB (2010) Ecological safety of tidal-power projects. Power Technol Eng 44:117–121. https://doi.org/10.1007/s10749-010-0152-x
119. Kadiri M, Ahmadian R, Bockelmann-Evans B, et al (2012) A review of the potential water quality impacts of tidal renewable energy systems. Renew Sustain Energy Rev 16:329–341. https://doi.org/10.1016/J.RSER.2011.07.160
120. Hooper T, Austen M (2013) Tidal barrages in the UK: Ecological and social impacts, potential mitigation, and tools to support barrage planning. Renew Sustain Energy Rev 23:289–298. https://doi.org/10.1016/j.rser.2013.03.001
121. Neill SP, Hemmer M, Robins PE, et al (2021) Tidal range resource of Australia. Renew Energy 170:683–692. https://doi.org/10.1016/j.renene.2021.02.035
122. Clark G (2018) Proposed Swansea Bay tidal lagoon (Statement by Business and Energy Secretary). Dep. Business, Energy Ind. Strateg.
123. Ahmadian R, Falconer RA, Bockelmann-Evans B (2014) Comparison of hydro-environmental impacts for ebb-only and two-way generation for a Severn Barrage. Comput Geosci 71:11–19. https://doi.org/10.1016/j.cageo.2014.05.006
124. Prandle D (1984) Simple theory for designing tidal power schemes. Adv Water Resour 7:21–27. https://doi.org/10.1016/0309-1708(84)90026-5
125. Mackie L, Coles D, Piggott MD, Angeloudis A (2020) The potential for tidal range energy systems to provide continuous power: A UK case study. J Mar Sci Eng 8:1–23. https://doi.org/10.3390/jmse8100780
126. Rtimi R, Sottolichio A, Tassi P (2021) Hydrodynamics of a hyper-tidal estuary influenced by the world's second largest tidal power station (Rance estuary, France). Estuar Coast Shelf Sci 250:. https://doi.org/10.1016/j.ecss.2020.107143
127. Moreira TM, de Faria JG, Vaz-de-Melo POS, et al (2022) Prediction-free, real-time flexible control of tidal lagoons through Proximal Policy Optimisation: A case study for the Swansea Lagoon. Ocean Eng 247:110657. https://doi.org/10.1016/j.oceaneng.2022.110657
128. Xue J, Ahmadian R, Jones O, Falconer RA (2021) Design of tidal range energy generation schemes using a Genetic Algorithm model. Appl Energy 286:116506. https://doi.org/10.1016/j.apenergy.2021.116506
129. Guo B, Ahmadian R, Falconer RA (2021) Refined hydro-environmental modelling for tidal energy generation: West Somerset Lagoon case study. Renew Energy 179:2104–2123. https://doi.org/10.1016/j.renene.2021.08.034

130. Xue J (2021) Optimisation of Tidal Range Schemes (PhD Thesis). Cardiff University https://orca.cardiff.ac.uk/138538/1/2021XueJPhD.pdf
131. Bernshtein LB (1995) Tidal power development - a realistic, justifiable and topical problem of today. IEEE Trans Energy Convers 10:591–599. https://doi.org/10.1109/60.464887
132. Hawkins SJ, O'Shaughnessy KA, Adams LA, et al (2020) Recovery of an urbanised estuary: Clean-up, de-industrialisation and restoration of redundant dock-basins in the Mersey. Mar Pollut Bull 156:111150. https://doi.org/10.1016/j.marpolbul.2020.111150
133. Aggidis GA, Benzon DS (2013) Operational optimisation of a tidal barrage across the Mersey estuary using 0-D modelling. Ocean Eng 66:69–81. https://doi.org/10.1016/j.oceaneng.2013.03.019
134. Burrows R, Walkington I, Yates NC, et al (2009) Tapping the Tidal Power Potential of the Eastern Irish Sea
135. Lewis MJ, Angeloudis A, Robins PE, et al (2017) Influence of storm surge on tidal range energy. Energy 122:25–36. https://doi.org/10.1016/j.energy.2017.01.068
136. Angeloudis A, Ahmadian R, Falconer RA, Bockelmann-Evans B (2016) Numerical model simulations for optimisation of tidal lagoon schemes. Appl Energy 165:522–536. https://doi.org/10.1016/j.apenergy.2015.12.079
137. Yu P, Zhang B, Yang Z, Wang T (2019) Numerical Investigation on the Shallow Water Entry of Wedges. IEEE Access 7:170062–170076. https://doi.org/10.1109/ACCESS.2019.2954141
138. Xue J, Ahmadian R, Falconer RA (2019) Optimising the operation of tidal range schemes. Energies 12:2870. https://doi.org/10.3390/en12152870
139. Vandercruyssen D, Baker S, Howard D, Aggidis GA (2023) Tidal range power generation: case studies combining the Lancaster 0-D generation and cost models. Proc ICE - Energy. https://doi.org/10.1680/jgeot.22.00135
140. Guo B, Ahmadian R, Falconer RA (2019) Influence of Different Momentum Sources on Modelling Tidal Lagoons. 38th IAHR World Congr - "Water Connect World" 38:3946–3956. https://doi.org/10.3850/38wc092019-0461
141. Zhou J, Pan S, Falconer RA (2014) Effects of open boundary location on the far-field hydrodynamics of a Severn Barrage. Ocean Model 73:19–29. https://doi.org/10.1016/j.ocemod.2013.10.006
142. Zhou J, Pan S, Falconer RA (2014) Optimization modelling of the impacts of a Severn Barrage for a two-way generation scheme using a Continental Shelf model. Renew Energy 72:415–427. https://doi.org/10.1016/j.renene.2014.07.036
143. Bray S, Ahmadian R, Falconer RA (2016) Impact of representation of hydraulic structures in Modelling a Severn barrage. Comput Geosci 89:. https://doi.org/10.1016/j.cageo.2016.01.010
144. Kärnä T, Kramer SC, Mitchell L, et al (2018) Thetis coastal ocean model : discontinuous Galerkin discretization for the three-dimensional hydrostatic equations. Geosci Model Dev 11:4359–4382. https://doi.org/10.5194/gmd-11-4359-2018
145. Angeloudis A, Kramer SC, Hawkins N, Piggott MD (2020) On the potential of linked-basin tidal power plants: An operational and coastal modelling assessment. Renew Energy 155:876–888. https://doi.org/10.1016/j.renene.2020.03.167
146. Mackie L, Kramer SC, Piggott MD, Angeloudis A (2021) Assessing impacts of tidal power lagoons of a consistent design. Ocean Eng 240:109879. https://doi.org/10.1016/j.oceaneng.2021.109879
147. Pennock S, Coles D, Angeloudis A, et al (2022) Temporal complementarity of marine renewables with wind and solar generation: Implications for GB system benefits. Appl Energy 319:119276. https://doi.org/10.1016/j.apenergy.2022.119276
148. Baker AL, Craighead RM, Jarvis EJ, et al (2020) Modelling the impact of tidal range energy on species communities. Ocean Coast Manag 193:105221.

https://doi.org/10.1016/j.ocecoaman.2020.105221
149. Čož N, Ahmadian R, Falconer RA (2019) Implementation of a Full Momentum Conservative Approach in Modelling Flow Through Tidal Structures. Water 11:1917. https://doi.org/10.3390/w11091917
150. Rocha J, Abreu T, Felgueiras C (2020) Evaluation of potential tidal impoundment energy systems in Ria de Aveiro, Portugal. Energy Reports 6:226–230. https://doi.org/10.1016/j.egyr.2020.11.115
151. Jeffcoate P, Stansby PK, Apsley D (2011) Near-Field Flow Downstream of a Barrage: Experiments, 3-D CFD and Depth-Averaged Modelling. In: Proceedings of the ASME 2011 30th International Conference on Ocean, Offshore and Arctic Engineering. Rotterdam
152. Brammer J, Falconer RA, Ellis C, Ahmadian R (2014) Physical and numerical modelling of the Severn Barrage. Sci China Technol Sci 57:1471–1481. https://doi.org/10.1007/s11431-014-5602-5
153. Leech C (2022) An experimental study of the hydrodynamic impact of turbine layout and design considerations in tidal range schemes (PhD Thesis). Cardiff University
154. Gingold RA, Monaghan J (1977) Smoothed particle hydrodynamics: theory and application to non-spherical stars. Mon Not R Astron Soc 181:541–559
155. Lucy L (1977) A numerical approach to the testing of the fission hypothesis. Astron J 82:1013–1024
156. Majtan E, Cunningham LS, Rogers BD (2021) Flood-Induced Hydrodynamic and Debris Impact Forces on Single-Span Masonry Arch Bridge. J Hydraul Eng 147:1–15. https://doi.org/10.1061/(asce)hy.1943-7900.0001932
157. Altomare C, Crespo AJ., Domínguez JM, et al (2015) Applicability of Smoothed Particle Hydrodynamics for estimation of sea wave impact on coastal structures. Coast Eng 96:1–12. https://doi.org/10.1016/j.coastaleng.2014.11.001
158. Baines A, Watson P, Cunningham LS, et al (2019) Modelling shore-side pressure distributions from violent wave breaking at a seawall. Proc Inst Civ Eng - Eng Comput Mech 172:118–123. https://doi.org/10.1680/jencm.19.00007
159. Altomare C, Gironella X, Crespo AJ. (2021) Simulation of random wave overtopping by a WCSPH model. Appl Ocean Res 116:102888. https://doi.org/10.1016/j.apor.2021.102888
160. Altomare C, Tafuni A, Domínguez JM, et al (2020) SPH simulations of real sea waves impacting a large-scale structure. J Mar Sci Eng 8:1–21. https://doi.org/10.3390/jmse8100826
161. Fourtakas G, Rogers BD (2016) Modelling multi-phase liquid-sediment scour and resuspension induced by rapid flows using Smoothed Particle Hydrodynamics (SPH) accelerated with a Graphics Processing Unit (GPU). Adv Water Resour 92:186–199. https://doi.org/10.1016/j.advwatres.2016.04.009
162. Xenakis AM, Lind SJ, Stansby PK, Rogers BD (2017) Landslides and tsunamis predicted by incompressible smoothed particle hydrodynamics (SPH) with application to the 1958 Lituya Bay event and idealized experiment. Proc R Soc A Math Phys Eng Sci 473:. https://doi.org/10.1098/rspa.2016.0674
163. Zubeldia EH, Fourtakas G, Rogers BD, Farias MM (2018) Multi-phase SPH model for simulation of erosion and scouring by means of the shields and Drucker–Prager criteria. Adv Water Resour 117:98–114. https://doi.org/10.1016/j.advwatres.2018.04.011
164. Tagliafierro B, Mancini S, Ropero-Giralda P, et al (2021) Performance assessment of a planing hull using the smoothed particle hydrodynamics method. J Mar Sci Eng 9:1–19. https://doi.org/10.3390/jmse9030244
165. Tagliafierro B, Karimirad M, Martínez-Estévez I, et al (2022) Numerical Assessment of a Tension-Leg Platform Wind Turbine in Intermediate Water Using the Smoothed Particle Hydrodynamics Method. Energies 15:. https://doi.org/10.3390/en15113993

166. Tagliafierro B, Martínez-Estévez I, Domínguez JM, et al (2022) A numerical study of a taut-moored point-absorber wave energy converter with a linear power take-off system under extreme wave conditions. Appl Energy 311:118629. https://doi.org/10.1016/j.apenergy.2022.118629
167. Shadloo MS, Oger G, Le Touzé D (2016) Smoothed particle hydrodynamics method for fluid flows, towards industrial applications: Motivations, Current state, And challenges. Comput Fluids 136:11–34. https://doi.org/10.1016/j.compfluid.2016.05.029
168. Marongiu J-C, Leboeuf F, Parkinson E (2007) Numerical simulation of the flow in a Pelton turbine using the meshless method smoothed particle hydrodynamics: A new simple solid boundary treatment. Proc Inst Mech Eng Part A J Power Energy 221:849–856. https://doi.org/10.1243/09576509JPE465
169. Mazhar H, Heyn T, Pazouki A, et al (2013) CHRONO: A parallel multi-physics library for rigid-body, flexible-body, and fluid dynamics. Mech Sci 4:49–64. https://doi.org/10.5194/ms-4-49-2013
170. Galland JC, Goutal N, Hervouet JM (1991) TELEMAC: A new numerical model for solving shallow water equations. Adv Water Resour 14:138–148. https://doi.org/10.1016/0309-1708(91)90006-A
171. Smolders S, Leroy A, Joao Teles M, et al (2016) Culverts modelling in TELEMAC-2D and TELEMAC-3D. In: Proceedings of the 23rd TELEMAC-MASCARET User Conference. pp 11–13
172. Guo B (2022) Hydro-environmental Modelling and Interaction of Tidal Lagoons around the UK Coast (PhD Thesis). Cardiff University
173. Monaghan J (2005) Smoothed particle hydrodynamics. Reports Prog Phys 68:1703–1759. https://doi.org/10.1088/0034-4885/68/8/R01
174. Fourtakas G, Domínguez JM, Vacondio R, Rogers BD (2019) Local uniform stencil (LUST) boundary condition for arbitrary 3-D boundaries in parallel smoothed particle hydrodynamics (SPH) models. Comput Fluids 190:346–361. https://doi.org/10.1016/j.compfluid.2019.06.009
175. Molteni D, Colagrossi A (2009) A simple procedure to improve the pressure evaluation in hydrodynamic context using the SPH. Comput Phys Commun 180:861–872. https://doi.org/10.1016/j.cpc.2008.12.004
176. Lind SJ, Xu R, Stansby PK, Rogers BD (2012) Incompressible smoothed particle hydrodynamics for free-surface flows: A generalised diffusion-based algorithm for stability and validations for impulsive flows and propagating waves. J Comput Phys 231:1499–1523. https://doi.org/10.1016/j.jcp.2011.10.027
177. Skillen A, Lind S, Stansby PK, Rogers BD (2013) Incompressible smoothed particle hydrodynamics (SPH) with reduced temporal noise and generalised Fickian smoothing applied to body-water slam and efficient wave-body interaction. Comput Methods Appl Mech Eng 265:163–173. https://doi.org/10.1016/j.cma.2013.05.017
178. Martínez-Estévez I, Domínguez JM, Tagliafierro B, et al (2023) Coupling of an SPH-based solver with a multiphysics library. Comput Phys Commun 283:108581. https://doi.org/10.1016/j.cpc.2022.108581
179. Verlet L (1967) Computer "Experiments" on Classical Fluids. I. Thermodynamical Properties of Lennard-Jones Molecules. Phys Rev 159:98–103. https://doi.org/https://doi.org/10.1103/PhysRev.159.98
180. Leimkuhler B, Matthews C (2015) Molecular Dynamics With Deterministic and Stochastic Numerical Methods. Springer
181. Monaghan J, Kos A (1999) Solitary Waves on a Cretan Beach. J Waterw Port, Coastal, Ocean Eng 125:109–161. https://doi.org/https://doi.org/10.1061/(ASCE)0733-950X(1999)125:3(145)
182. Domínguez JM, Fourtakas G, Altomare C, et al (2021) DualSPHysics: from fluid dynamics

to multiphysics problems. Comput Part Mech. https://doi.org/10.1007/s40571-021-00404-2

183. Pringgana G, Cunningham LS, Rogers BD (2023) Mitigating tsunami effects on buildings via novel use of discrete onshore protection systems. Coast Eng J 65:149–173. https://doi.org/10.1080/21664250.2023.2170690
184. Brito M, Bernardo F, Neves MG, et al (2022) Numerical Model of Constrained Wave Energy Hyperbaric Converter under Full-Scale Sea Wave Conditions. J Mar Sci Eng 10:. https://doi.org/10.3390/jmse10101489
185. Harada T, Koshizuka S, Kawaguchi Y (2007) Smoothed particle hydrodynamics on GPU computing. Proc Comput Graph Int 40:63–70
186. Morikawa D, Senadheera H, Asai M (2020) Explicit incompressible smoothed particle hydrodynamics in a multi-GPU environment for large-scale simulations. Comput Part Mech 8:493–510. https://doi.org/10.1007/s40571-020-00347-0
187. Valizadeh A, Monaghan J (2012) Smoothed particle hydrodynamics simulations of turbulence in fixed and rotating boxes in two dimensions with no-slip boundaries. Phys Fluids 24:. https://doi.org/10.1063/1.3693136
188. Robinson M, Monaghan J (2012) Direct numerical simulation of decaying two-dimensional turbulence in a no-slip square using smoothed particle hydrodynamics. Int J Numer Methods Fluids 70:37–55. https://doi.org/10.1002/fld
189. Valizadeh A, Monaghan J (2015) SPH simulation of 2D turbulence driven by a cylindrical stirrer. Eur J Mech - B/Fluids 51:44–53. https://doi.org/10.1016/j.euromechflu.2014.11.002
190. Violeau D, Issa R (2007) Numerical modelling of complex turbulent free-surface flows with the SPH method: an overview. Int J Numer Methods Fluids 53:277–304. https://doi.org/10.1002/fld.1292
191. Crespo AJC, Gómez-Gesteira M, Dalrymple RA (2007) Boundary conditions generated by dynamic particles in SPH methods. Comput Mater Contin 5:173–184. https://doi.org/10.3970/cmc.2007.005.173
192. Federico I, Marrone S, Colagrossi A, et al (2012) Simulating 2D open-channel flows through an SPH model. Eur J Mech - B/Fluids 34:35–46. https://doi.org/10.1016/j.euromechflu.2012.02.002
193. Pappas K, Mackie L, Zilakos I, et al (2023) Sensitivity of tidal range assessments to harmonic constituents and analysis timeframe. Renew Energy 205:125–141. https://doi.org/10.1016/j.renene.2023.01.062
194. Moreira TM, Vaz-de-melo POS, Medeiros-ribeiro G (2022) Control Optimisation Baselines for Tidal Range Structures — CoBaseTRS. Softw Impacts 14:100356. https://doi.org/10.1016/j.simpa.2022.100356
195. Martinez-Cantin R (2015) BayesOpt: A Bayesian optimization library for nonlinear optimization, experimental design and bandits. J Mach Learn Res 15:3735–3739
196. Hanousek N, Ahmadian R (2022) Assessing the sensitivity of tidal range energy models to water level accuracy. In: Ortega-Sanchez M (ed) Proceedings of the 49th IAHR World Congress: From Snow to Sea. IAHR, Granada, pp 4688–4697
197. Hanousek N, Ahmadian R, Qadrdan M, Harrison J (2024) Enhancing financial viability of tidal range schemes through revenue optimisation (UNDER REVIEW). Renew Sustain Energy Rev
198. Hanousek N, Ahmadian R, Lesurf E (2023) Providing distributed electrical generation through retrofitting disused docks as tidal range energy schemes. Renew Energy 217:. https://doi.org/10.1016/j.renene.2023.119149
199. Hervouet J-M (2007) Hydrodynamics of free surface flows modelling with the finite element method. Wiley, Chichester
200. Brière C, Abadie S, Bretel P, Lang P (2007) Assessment of TELEMAC system

performances, a hydrodynamic case study of Anglet, France. Coast Eng 54:345–356. https://doi.org/10.1016/j.coastaleng.2006.10.006

201. Abu-Bakar A, Ahmadian R, Falconer RA (2017) Modelling the transport and decay processes of microbial tracers in a macro-tidal estuary. Water Res 123:802–824. https://doi.org/10.1016/j.watres.2017.07.007
202. Smolders S, Teles MJ, Leroy A, et al (2020) Modeling storm surge attenuation by an integrated nature-based and engineered flood defense system in the Scheldt estuary (Belgium). J Mar Sci Eng 8:. https://doi.org/10.3390/JMSE8010027
203. Lavine W, Jamal MH, Abd Wahab AK, Kasiman EH (2020) Effect of sea level rise on oil spill model drift using telemac-2d. J Water Clim Chang 11:1021–1031. https://doi.org/10.2166/wcc.2019.057
204. Li Z, Liu J, Mei C, et al (2019) Comparative analysis of building representations in TELEMAC-2D for flood inundation in idealized urban districts. Water (Switzerland) 11:1–21. https://doi.org/10.3390/w11091840
205. Broich K, Pflugbeil T, Disse M, Nguyen H (2019) Using TELEMAC-2D for hydrodynamic modeling of rainfall-runoff. In: XXVIth Telemac-Mascaret User Conference
206. Bourban SE, Turnbull MS, Cooper AJ (2017) The Earth by TELEMAC. In: Proceedings of the XXIVth TELEMAC-MASCARET User Conference. Graz
207. Joly A, Pham C-T, Andreewsky M, et al (2015) Using the DRAGFO subroutine to model Tidal Energy Converters in Telemac-2D. XXII TELEMAC-MASCARET User Conf 182–189
208. openTELEMAC (2022) TELEMAC-2D User Manual, v8p3. Chatou
209. Guo B, Ahmadian R, Evans P, Falconer RA (2020) Studying the wake of an island in a macro-tidal estuary. Water 12:. https://doi.org/10.3390/W12051225
210. Bodhaine GL (1988) Measurement of Peak Discharge At Culverts By Indirect Methods, Book 3. Denver, CO
211. Smolders S, Vercruysse JB, Spiesschaert T, et al (2019) Modelling culverts in TELEMAC: code validation with scale flume model of Doelpolder. 18_145_1: https://doi.org/10.13140/RG.2.2.21947.46887
212. Chrysafis N (2008) Feasability Study of New Turbine Concept (MSc Thesis). Cardiff University
213. Challans P (2009) Analysis and Modelling of a Tidal Stream Turbine (MSc Thesis). Cardiff University
214. Harries T (2014) Phyiscal Testing and Numerical Modelling of a Novel Vertical - Axis Tidal Stream Turbine (PhD Thesis). Cardiff University
215. Ranabhat B (2022) Parametric Optimisation of a Vertical Axis Hydrokinetic Turbine with Shallow Water Application (PhD Thesis). Cardiff University
216. Brammer J (2014) Physical and Numerical Modelling of Marine Renewable Energy Technologies , with Particular Focus on Tidal Stream and Tidal Range Devices (PhD Thesis)
217. Harries T, Kwan A, Brammer J, Falconer RA (2016) Physical testing of performance characteristics of a novel drag-driven vertical axis tidal stream turbine; With comparisons to a conventional Savonius. Int J Mar Energy 14:215–228. https://doi.org/10.1016/j.ijome.2016.01.008
218. Rauen W, Lin B, Falconer RA (2008) Transition from wavelets to ripples in a laboratory flume with a diverging channel. Int J Sediment Res 23:1–12. https://doi.org/10.1016/S1001-6279(08)60001-3
219. Maître T, Amet E, Pellone C (2013) Modeling of the flow in a Darrieus water turbine: Wall grid refinement analysis and comparison with experiments. Renew Energy. https://doi.org/10.1016/j.renene.2012.09.030
220. Židonis A, Benzon DS, Aggidis GA (2015) Development of hydro impulse turbines and

new opportunities. Renew Sustain Energy Rev 51:1624–1635. https://doi.org/10.1016/j.rser.2015.07.007

221. Ouro P, Stoesser T (2017) An immersed boundary-based large-eddy simulation approach to predict the performance of vertical axis tidal turbines. Comput Fluids 152:74–87. https://doi.org/10.1016/j.compfluid.2017.04.003
222. Lanzafame R, Mauro S, Messina M (2013) Wind turbine CFD modeling using a correlation-based transitional model. Renew Energy 52:31–39. https://doi.org/10.1016/j.renene.2012.10.007
223. Salehi S, Nilsson H, Lillberg E, Edh N (2021) Numerical Simulation of Hydraulic Turbine during Transient Operation Using OpenFOAM. IOP Conf Ser Earth Environ Sci 774:. https://doi.org/10.1088/1755-1315/774/1/012060
224. Yang B, Lawn C (2011) Fluid dynamic performance of a vertical axis turbine for tidal currents. Renew Energy 36:3355–3366. https://doi.org/10.1016/j.renene.2011.05.014
225. Hashemi SM, Moghimi M, Derakhshan S (2020) Experimental and numerical study of a flapping-blade vertical-axis hydrokinetic turbine under free surface deformation and blockage effects. Int J Environ Sci Technol 17:3633–3650. https://doi.org/10.1007/s13762-020-02642-y
226. Tafuni A, Domínguez JM, Vacondio R, Crespo AJ. (2018) A versatile algorithm for the treatment of open boundary conditions in Smoothed particle hydrodynamics GPU models. Comput Methods Appl Mech Eng 342:604–624. https://doi.org/10.1016/j.cma.2018.08.004
227. English A, Domínguez JM, Vacondio R, et al (2021) Modified dynamic boundary conditions (mDBC) for general-purpose smoothed particle hydrodynamics (SPH): application to tank sloshing, dam break and fish pass problems. Comput Part Mech. https://doi.org/10.1007/s40571-021-00403-3
228. Wendland H (1995) Piecewise polynomial, positive definite and compactly supported radial functions of minimal degree. Adv Comput Math 4:389–396. https://doi.org/10.1007/BF02123482
229. Robinson M, Cleary P, Monaghan J (2008) Analysis of mixing in a Twin Cam Mixer using smoothed particle hydrodynamics. AIChE J 54:1987–1998. https://doi.org/10.1002/aic.11530
230. Gómez-Gesteira M, Rogers BD, Dalrymple RA, Crespo AJ. (2010) State-of-the-art of classical SPH for free-surface flows. J Hydraul Res 48:6–27. https://doi.org/10.1080/00221686.2010.9641242
231. Quinlan NJ, Basa M, Lastiwka M (2006) Truncation error in mesh-free particle methods. Int J Numer Methods Eng 66:2064–2085. https://doi.org/10.1002/nme.1617
232. Prandle D (2009) Design of tidal barrage power schemes. Proc Inst Civ Eng Marit Eng 162:147–153. https://doi.org/10.1680/maen.2009.162.4.147
233. Robinson IS (1979) The tidal dynamics of the Irish and Celtic Seas. Geophys J R Astron Soc 56:159–197. https://doi.org/10.1111/j.1365-246X.1979.tb04774.x
234. National Oceanography Centre (2023) National Tidal and Sea Level Facility. https://ntslf.org/. Accessed 28 Mar 2023
235. Williams JJ, Esteves LS (2017) Guidance on Setup, Calibration, and Validation of Hydrodynamic, Wave, and Sediment Models for Shelf Seas and Estuaries. Adv Civ Eng 2017:. https://doi.org/10.1155/2017/5251902
236. Zhang T, Hanousek N, Qadrdan M, Ahmadian R (2022) A day-ahead scheduling model of power systems incorporating multiple tidal range power stations. iEEE Trans Sustain Energy 14:826–836. https://doi.org/10.1109/TSTE.2022.3224231
237. Popa A, Edwards R, Aandi I (2011) Carbon capture considerations for combined cycle gas turbine. Energy Procedia 4:2315–2323. https://doi.org/10.1016/j.egypro.2011.02.122
238. Bycroft U, Ball L (2010) Severn Tidal Power-SEA theme paper. Bristol

239. Department for Business Energy & Indutrial Strategy (2018) Energy Statistics: Q1 2018. London
240. Department for Business Energy & Indutrial Strategy (2022) Energy Trends: UK January to March 2022. London
241. Allsop NWH (2019) English Channel "harbours of refuge": A discussion on their origins and "failures." Proc Inst Civ Eng - Eng Hist Herit 174:32–44. https://doi.org/10.1680/jenhh.19.00034
242. Russell GR, Hawkins SJ, Evans L., et al (1983) Restoration of a Disused Dock Basin as a Habitat for Marine Benthos and Fish. J Appl Ecol 20:43–58. https://doi.org/10.2307/2403375
243. Hawkins SJ, Allen JR, Bray S (1999) Restoration of temperate marine and coastal ecosystems: Nudging nature. Aquat Conserv Mar Freshw Ecosyst 9:23–46. https://doi.org/doi:10.1002/(SICI)1099-0755(199901/02)9:1<23::AID-AQC324>3.0.CO;2-C
244. Allen JR, Hawkins SJ, Russell GR, White KN (1992) Eutrophication and urban renewal: Problems and perspectives for the management of disused docks. Mar Coast Eutrophication 1283–1295. https://doi.org/10.1016/b978-0-444-89990-3.50108-5
245. Falconer RA, Guo B, Ahmadian R (2020) Coastal reservoirs and their potential for urban regeneration and renewable energy supply. Elsevier Inc.
246. Jauhiainen JS (1995) Waterfront Redevelopment and Urban Policy: The Case of Barcelona, Cardiff and Genoa. Eur Plan Stud 3:3–23. https://doi.org/10.1080/09654319508720287
247. Jones A (1998) Issues in waterfront regeneration: More sobering thoughts-A UK perspective. Plan Pract Res 13:433–442. https://doi.org/10.1080/02697459815987
248. Govan Docks Restoration Trust (2019) Govan Voices - A community consultation on the future of Govan's historic dry docks. Glasgow
249. Holgate SJ, Matthews A, Woodworth PL, et al (2013) New Data Systems and Products at the Permanent Service for Mean Sea Level. J Coast Res 29:493–504. https://doi.org/10.2112/JCOASTRES-D-12-00175.1
250. National Oceanography Centre (2022) POLTIPS-3. https://www.ntslf.org/products/software
251. Fay JA, Smachlo MA (1982) The Performance of Small Scale Tidal Power. Cambridge, MA
252. Fay JA, Smachlo MA (1982) Capital Cost Of Small Scale Tidal Power Plants. NOAA, Cambridge, MA
253. Schlemmer E, Ramsauer F, Cui X, Binder A (2007) HYDROMATRIX® and StrafloMatrix™, electric energy from low head hydro potential. In: International Conference on Clean Electrical Power. pp 329–334
254. Yin J, Falconer RA, Chen Y (2004) Velocity and solute concentration distributions in model harbours. Proc Inst Civ Eng Marit Eng 157:47–56. https://doi.org/10.1680/maen.2004.157.1.47
255. Daniel Raj D, Sundar V, Sannasiraj SA (2019) Enhancement of hydrodynamic performance of an Oscillating Water Column with harbour walls. Renew Energy 132:142–156. https://doi.org/10.1016/j.renene.2018.07.089
256. Gómez M V. (1998) Reflective images: The case of urban regeneration in Glasgow and Bilbao. Int J Urban Reg Res 22:106–121. https://doi.org/10.1111/1468-2427.00126
257. Mah A (2010) Memory, uncertainty and industrial ruination: Walker riverside, Newcastle upon Tyne. Int J Urban Reg Res 34:398–413. https://doi.org/10.1111/j.1468-2427.2010.00898.x
258. Hakiman R (2022) Laing O'Rourke makes visible progress on Everton's new stadium. In: New Civ. Eng. https://www.newcivilengineer.com/latest/laing-orourke-makes-visible-progress-on-evertons-new-stadium-18-07-2022/
259. Minchinton WE (1969) Industrial South Wales, 1750-1914 : essays in Welsh economic

history. Cass, London

Appendix A. CarBine CaseDef XML File

```
<?xml version="1.0" encoding="UTF-8" ?>
<case app="GenCase4 v4.0.077 (14-08-2018)" date="13-09-2018 18:54:50">
    <casedef>
        <constantsdef>
            <lattice bound="1" fluid="1" />
            <gravity x="0" y="0" z="0” units_comment="m/s^2" />
            <rhop0 value="1000" units_comment="kg/m^3" />
            <hswl value="0" auto="true" units_comment="metres (m)" />
            <gamma value="7" comment="Polytropic const used in the state equation" />
            <speedsystem value="0" auto="false" comment="Maximum system speed" />
            <coefsound value="0" comment="Coefficient to multiply speedsystem" />
            <speedsound value="15" auto="false" />
            <hdp value="2.25" comment="Coef to calc smoothing length (H=hdp*dp)" />
            <cflnumber value="0.2" comment="Coefficient to multiply dt" />
        </constantsdef>
        <mkconfig boundcount="240" fluidcount="10" />
        <geometry>
            <definition dp="0.001" units_comment="metres (m)">
                <pointmin x="-1.0" y="0.0" z="-0.75" />
                <pointmax x="2.0" y="0.0" z="0.75" />
            </definition>
            <commands>
                <mainlist>
                    <!-- Dims and configs -->
                    <newvarcte
                        xini="-0.51" xsize="2.020"
                        zsize="1.220" zini="-zsize/2" _rem="Fluid domain" />
                    <newvarcte xoversize="0.090" zoversize="Dp*6"/>
                    <newvarcte fluidvel="0.9" />
                    <exportvar vars="fluidvel,zsize"/>
                    <setshapemode>actual | bound</setshapemode>
                    <!-- Cyclinder hub -->
                    <setfrdrawmode auto="true"/>
                    <setmkbound mk="50" />
                    <setdrawmode mode="full" />
                    <drawcylinder radius="0.01">
                        <point x="0.0" y="-0.1" z="0.0"/>
                        <point x="0.0" y="0.1" z="0.0"/>
                    </drawcylinder>
                    <shapeout file="Axle" />
                    <setfrdrawmode auto="false"/>
                    <!--Draw Flaps-->
                    <setshapemode>actual | bound</setshapemode>
                    <setmkbound mk="21"/>
                    <setdrawmode mode="full"/>
                    <drawfilestl file="Flap-CW.stl">
                        <drawmove x="0.105" y="-0.005" z="0.0" />
                        <drawrotate angx="0.0" angy="90.0" angz="0.0" />
                    </drawfilestl>
                    <fillbox x="0.105" y="0.0" z="0.0">
                        <modefill>void</modefill>
                        <point x="-0.5" y="-0.05" z="-0.5"/>
                        <size x="1.0" y="0.1" z="1.0"/>
                    </fillbox>
                    <shapeout file="Flap-1"/>
```

```
<setmkbound mk="22"/>
<setdrawmode mode="full"/>
<drawfilestl file="Flap-CW.stl">
    <drawmove x="0.2" y="-0.005" z="0.0" />
    <drawrotate angx="0.0" angy="90.0" angz="0.0" />
</drawfilestl>
<fillbox x="0.2" y="0.0" z="0.0">
    <modefill>void</modefill>
    <point x="-0.5" y="-0.05" z="-0.5"/>
    <size x="1.0" y="0.1" z="1.0"/>
</fillbox>
<shapeout file="Flap-2"/>

<setmkbound mk="23"/>
<setdrawmode mode="full"/>
<drawfilestl file="Flap-CW.stl">
    <drawmove x="0.0" y="-0.005" z="0.105" />
    <drawrotate angx="0.0" angy="0.0" angz="0.0" />
</drawfilestl>
<fillbox x="0.0" y="0.0" z="0.105">
    <modefill>void</modefill>
    <point x="-0.5" y="-0.05" z="-0.5"/>
    <size x="1.0" y="0.1" z="1.0"/>
</fillbox>
<shapeout file="Flap-3"/>

<setmkbound mk="24"/>
<setdrawmode mode="full"/>
<drawfilestl file="Flap-CW.stl">
    <drawmove x="0.0" y="-0.005" z="0.2" />
    <drawrotate angx="0.0" angy="0.0" angz="0.0" />
</drawfilestl>
<fillbox x="0.0" y="0.0" z="0.2">
    <modefill>void</modefill>
    <point x="-0.5" y="-0.05" z="-0.5"/>
    <size x="1.0" y="0.1" z="1.0"/>
</fillbox>
<shapeout file="Flap-4"/>

<setmkbound mk="25"/>
<setdrawmode mode="full"/>
<drawfilestl file="Flap-CW.stl">
    <drawmove x="-0.105" y="-0.005" z="0.0" />
    <drawrotate angx="0.0" angy="-90.0" angz="0.0" />
</drawfilestl>
<fillbox x="-0.105" y="0.0" z="0.0">
    <modefill>void</modefill>
    <point x="-0.5" y="-0.05" z="-0.5"/>
    <size x="1.0" y="0.1" z="1.0"/>
</fillbox>
<shapeout file="Flap-5"/>

<setmkbound mk="26"/>
<setdrawmode mode="full"/>
<drawfilestl file="Flap-CW.stl">
    <drawmove x="-0.2" y="-0.005" z="0.0" />
    <drawrotate angx="0.0" angy="-90.0" angz="0.0" />
</drawfilestl>
<fillbox x="-0.2" y="0.0" z="0.0">
    <modefill>void</modefill>
    <point x="-0.5" y="-0.05" z="-0.5"/>
    <size x="1.0" y="0.1" z="1.0"/>
</fillbox>
<shapeout file="Flap-6"/>
```

```
                <setmkbound mk="27"/>
                <setdrawmode mode="full"/>
                <drawfilestl file="Flap-CW.stl">
                    <drawmove x="0.0" y="-0.005" z="-0.105" />
                    <drawrotate angx="0.0" angy="180.0" angz="0.0" />
                </drawfilestl>
                <fillbox x="0.0" y="0.0" z="-0.105">
                    <modefill>void</modefill>
                    <point x="-0.5" y="-0.05" z="-0.5"/>
                    <size x="1.0" y="0.1" z="1.0"/>
                </fillbox>
                <shapeout file="Flap-7"/>

                <setmkbound mk="28"/>
                <setdrawmode mode="full"/>
                <drawfilestl file="Flap-CW.stl">
                    <drawmove x="0.0" y="-0.005" z="-0.2" />
                    <drawrotate angx="0.0" angy="180.0" angz="0.0" />
                </drawfilestl>
                <fillbox x="0.0" y="0.0" z="-0.2">
                    <modefill>void</modefill>
                    <point x="-0.5" y="-0.05" z="-0.5"/>
                    <size x="1.0" y="0.1" z="1.0"/>
                </fillbox>
                <shapeout file="Flap-8"/>

                <!-- Open bounds -->
                <setmkfluid mk="1" />
                <drawbox>
                    <boxfill>left</boxfill>
                    <point x="#xini" y="-0.1" z="#zini" />
                    <size x="#xsize" y="0.2" z="#zsize" />
                </drawbox>
                <setmkfluid mk="2" />
                <drawbox>
                    <boxfill>right</boxfill>
                    <point x="#xini" y="-0.1" z="#zini" />
                    <size x="#xsize" y="0.2" z="#zsize" />
                </drawbox>
                <!-- Solid Bounds -->
                <setmkbound mk="1" />
                <drawbox>
                    <boxfill>solid</boxfill>
                    <point x="#xini-xoversize" y="-0.1" z="#zini-zoversize" />
                    <size x="#xsize+xoversize*2" y="0.2" z="#zoversize" />
                </drawbox>
                <setmkbound mk="2" />
                <drawbox>
                    <boxfill>solid</boxfill>
                    <point x="#xini-xoversize" y="-0.1" z="#-zini" />
                    <size x="#xsize+xoversize*2" y="0.2" z="#zoversize" />
                </drawbox>
                <setdrawmode mode="full" />
                <!-- Fluid domain -->
                <setmkfluid mk="0"/>
                <fillbox x="0.5" y="0.0" z="0.0">
                    <modefill>void</modefill>
                    <point x="#xini" y="-0.1" z="#zini" />
                    <size x="#xsize" y="0.2" z="#zsize" />
                </fillbox>
                <!-- END -->
                <shapeout file="" />
            </mainlist>
        </commands>
    </geometry>
    <properties>
```

```
            <propertyfile file="Floating_Materials_2.xml" path="materials"/>
            <links>
                <link mkbound="50,21,22,23,24,25,26,27,28" property="aluminium" />
            </links>
        </properties>
        <floatings>
            <floating mkbound="50,21,22,23,24,25,26,27,28" rhopbody="2500"
property="smooth_aluminium" />
        </floatings>
        <initials>
            <velocity mkfluid="0" x="#fluidvel" y="0" z="0"/>
        </initials>
    </casedef>
    <execution>
        <special>
            <chrono>
                <schemescale value="1" comment="Scale for Chrono objects (default=1)" />
                <collision activate="true">
                    <distancedp value="0.5" comment="max collision overlap by Dp” />
                    <contactmethod value="0" comment=" 0:NSC (Non Smooth Contacts" />
                </collision>
                <bodyfloating id="Tbody" mkbound="50"
                    modelfile="[CaseName]_Axle_Actual.vtk"/>
                <bodyfloating id="Flap-1" mkbound="21"
                    modelfile="[CaseName]_Flap-1_Actual.vtk"/>
                <bodyfloating id="Flap-2" mkbound="22"
                    modelfile="[CaseName]_Flap-2_Actual.vtk"/>
                <bodyfloating id="Flap-3" mkbound="23"
                    modelfile="[CaseName]_Flap-3_Actual.vtk"/>
                <bodyfloating id="Flap-4" mkbound="24"
                    modelfile="[CaseName]_Flap-4_Actual.vtk"/>
                <bodyfloating id="Flap-5" mkbound="25"
                    modelfile="[CaseName]_Flap-5_Actual.vtk"/>
                <bodyfloating id="Flap-6" mkbound="26"
                    modelfile="[CaseName]_Flap-6_Actual.vtk"/>
                <bodyfloating id="Flap-7" mkbound="27"
                    modelfile="[CaseName]_Flap-7_Actual.vtk"/>
                <bodyfloating id="Flap-8" mkbound="28"
                    modelfile="[CaseName]_Flap-8_Actual.vtk"/>
                <!-- Link body of turbine to the domain -->
                <link_hinge idbody1="Tbody">
                    <rotpoint x="0" y="0.0" z="0.0" comment="Point for rotation" />
                    <rotvector x="0" y="1" z="0" comment="Vector dir for rotation" />
                    <stiffness value="0" comment="Torsional stiffness" />
                    <damping value="0" comment="Torsional damping" />
                </link_hinge>
                <!-- flaps to the body -->
                <link_hinge idbody1="Tbody" idbody2="Flap-1">
                    <rotpoint x="0.105" y="0.0" z="0.0" comment="Point for rotation" />
                    <rotvector x="0" y="1" z="0" comment="Vector dir for rotation" />
                    <stiffness value="0" comment="Torsional stiffness" />
                    <damping value="0" comment="Torsional damping" />
                </link_hinge>
                <link_hinge idbody1="Tbody" idbody2="Flap-2">
                    <rotpoint x="0.2" y="0.0" z="0.0" comment="Point for rotation" />
                    <rotvector x="0" y="1" z="0" comment="Vector dir for rotation" />
                    <stiffness value="0" comment="Torsional stiffness" />
                    <damping value="0" comment="Torsional damping" />
                </link_hinge>
                <link_hinge idbody1="Tbody" idbody2="Flap-3">
                    <rotpoint x="0.0" y="0.0" z="0.105" comment="Point for rotation" />
                    <rotvector x="0" y="1" z="0" comment="Vector dir for rotation" />
                    <stiffness value="0" comment="Torsional stiffness" />
                    <damping value="0" comment="Torsional damping" />
                </link_hinge>
                <link_hinge idbody1="Tbody" idbody2="Flap-4">
```

```
            <rotpoint x="0.0" y="0.0" z="0.2" comment="Point for rotation" />
            <rotvector x="0" y="1" z="0" comment="Vector dir for rotation" />
            <stiffness value="0" comment="Torsional stiffness" />
            <damping value="0" comment="Torsional damping" />
        </link_hinge>
        <link_hinge idbody1="Tbody" idbody2="Flap-5">
            <rotpoint x="-0.105" y="0.0" z="0.0" comment="Point for rotation" />
            <rotvector x="0" y="1" z="0" comment="Vector dir for rotation" />
            <stiffness value="0" comment="Torsional stiffness" />
            <damping value="0" comment="Torsional damping" />
        </link_hinge>
        <link_hinge idbody1="Tbody" idbody2="Flap-6">
            <rotpoint x="-0.2" y="0.0" z="0.0" comment="Point for rotation" />
            <rotvector x="0" y="1" z="0" comment="Vector dir for rotation" />
            <stiffness value="0" comment="Torsional stiffness" />
            <damping value="0" comment="Torsional damping" />
        </link_hinge>
        <link_hinge idbody1="Tbody" idbody2="Flap-7">
            <rotpoint x="0.0" y="0.0" z="-0.105" comment="Point for rotation" />
            <rotvector x="0" y="1" z="0" comment="Vector dir for rotation" />
            <stiffness value="0" comment="Torsional stiffness" />
            <damping value="0" comment="Torsional damping" />
        </link_hinge>
        <link_hinge idbody1="Tbody" idbody2="Flap-8">
            <rotpoint x="0.0" y="0.0" z="-0.2" comment="Point for rotation" />
            <rotvector x="0" y="1" z="0" comment="Vector dir for rotation" />
            <stiffness value="0" comment="Torsional stiffness" />
            <damping value="0" comment="Torsional damping" />
        </link_hinge>
    </chrono>
    <inout>
        <!-- INFLOW BUFFER -->
        <inoutzone>
            <refilling value="0" comment="Refilling mode. 0:Simple full" />
            <inputtreatment value="2" comment=" 2:Remove fluid (inlet)" />
            <layers value="8" comment="Number of inlet/outlet particle layers" />
            <zone2d comment="Input zone for 2D simulations">
                <particles mkfluid="1" direction="right" />
            </zone2d>
            <imposevelocity mode="0" comment="Imposed velocity 0:fixed value, ">
                <velocity v="#fluidvel" units_comment="m/s" />
            </imposevelocity>
            <imposezsurf mode="0" comment="Inlet Z-surface 0:Imposed fixed value">
                <zbottom value="#-zsize/2 units_comment="m" />
                <zsurf value="#zsize/2" units_comment="m" />
            </imposezsurf>
            <imposerhop mode="1" comment="Outlet rhop 1:Hydrostatic" />
        </inoutzone>
        <!-- OUTFLOW BUFFER -->
        <inoutzone>
            <refilling value="0" comment="Refilling mode. 0:Simple full" />
            <inputtreatment value="1" comment="1:Convert fluid (Outlet)" />
            <layers value="8" comment="Number of inlet/outlet particle layers" />
            <zone2d comment="Input zone for 2-D simulations">
                <particles mkfluid="2" direction="left" />
            </zone2d>
            <imposevelocity mode="2" comment=" 2:Extrapolated value" />
            <imposezsurf mode="0" comment=" 0:Imposed fixed value">
                <zbottom value="#-zsize/2" units_comment="m" />
                <zsurf value="#zsize/2" units_comment="m" />
            </imposezsurf>
            <imposerhop mode="1" comment=" 1:Hydrostatic" />
        </inoutzone>
        <!-- END BUFFERS -->
    </inout>
</special>
```

```
        <parameters>
            <parameter key="SavePosDouble" value="1" />
            <parameter key="Boundary" value="2" comment="Boundary method 2:mDBC" />
            <parameter key="StepAlgorithm" value="2" comment="2:Symplectic (default=1)" />
            <parameter key="VerletSteps" value="40" comment="(default=40)" />
            <parameter key="Kernel" value="2" comment=" 2:Wendland (default=2)" />
            <parameter key="ViscoTreatment" value="1" comment="1:Artificial" />
            <parameter key="Visco" value="0.000001" comment="Viscosity value" />
            <parameter key="ViscoBoundFactor" value="1" comment="(default=1)" />
            <parameter key="DensityDT" value="3" comment=" 3:Fourtakas(full)" />
            <parameter key="DensityDTvalue" value="0.1" comment=" (default=0.1)" />
            <parameter key="Shifting" value="3" comment=" 3:Full" />
            <parameter key="ShiftCoef" value="-50" comment="(default=-2)" />
            <parameter key="ShiftTFS" value="0.0" comment="Threshold for free surface" />
            <parameter key="RigidAlgorithm" value="3" comment="3:Chrono " />
            <parameter key="FtPause" value="0.0" units_comment="seconds" />
            <parameter key="CoefDtMin" value="0.05" />
            <parameter key="DtIni" value="0.0001" units_comment="seconds" />
            <parameter key="DtMin" value="0.000001" units_comment="seconds" />
            <parameter key="DtFixed" value="0" units_comment="seconds" />
            <parameter key="DtFixedFile" value="NONE" units_comment="milliseconds (ms)" />
            <parameter key="DtAllParticles" value="0" />
            <parameter key="TimeMax" value="10.0" units_comment="seconds" />
            <parameter key="TimeOut" value="0.02" units_comment="seconds" />
            <parameter key="PartsOutMax" value="1" units_comment="decimal" />
            <parameter key="RhopOutMin" value="700" />
            <parameter key="RhopOutMax" value="1300" />
            <parameter key="XPeriodicIncZ" value="0/>
            <simulationdomain >
                <posmin x="default" y="default" z="default" />
                <posmax x="default" y="default" z="default" />
            </simulationdomain>
        </parameters>
    </execution>
</case>
```

Appendix B. Severn Estuary-Bristol Channel model calibration and validation

B.1 Harmonic constituents

Table B.1: Constituent comparison at Hinkley

Constituent Name	Amplitude			Phase		
	BODC	T2D	E(a_i)	BODC	T2D	E(ϕ_i)
M2	3.93	3.97	1.010	183.7	178.9	0.0034
S2	1.63	1.58	0.973	247.2	237.4	0.0147
N2	0.64	0.69	1.091	157.4	161.9	0.0031
K1	0.04	0.07	1.573	156.5	141.6	0.0336
O1	0.07	0.08	1.102	358.5	357.1	0.0003
M4	0.09	0.12	1.326	19.1	9.2	0.0149
M6	0.04	0.03	0.576	217.8	221.7	0.0023
MK3	0.01	0.01	0.920	203.2	205.7	0.0009

Table B.2: Constituent comparison at Ilfracombe

Constituent Name	Amplitude			Phase		
	BODC	T2D	E(a_i)	BODC	T2D	E(ϕ_i)
M2	3.06	2.98	0.975	163.0	161.3	0.0005
S2	1.29	1.20	0.934	219.4	214.3	0.0041
N2	0.54	0.55	1.028	133.4	140.0	0.0067
K1	0.05	0.06	1.357	142.3	133.9	0.0108
O1	0.07	0.07	1.082	351.1	349.0	0.0007
M4	0.10	0.10	0.951	353.2	339.1	0.0302
M6	0.02	0.01	0.473	348.5	283.5	0.5769
MK3	0.00	0.00	0.686	165.8	178.1	0.0231

Table B.3: Constituent comparison at Mumbles

Constituent Name	**Amplitude**			**Phase**		
	BODC	**T2D**	**E(a_i)**	**BODC**	**T2D**	**E(ϕ_i)**
M2	3.12	3.16	1.013	172.8	170.9	0.0005
S2	1.31	1.27	0.964	229.6	224.7	0.0038
N2	0.54	0.58	1.064	142.6	149.6	0.0076
K1	0.05	0.06	1.340	152.4	138.4	0.0296
O1	0.07	0.07	1.085	355.4	353.3	0.0007
M4	0.07	0.08	1.125	15.3	4.1	0.0192
M6	0.04	0.02	0.610	9.8	327.3	0.2635
MK3	0.00	0.00	1.103	173.9	190.9	0.0434

Table B.4: Constituent comparison at Newport

Constituent Name	**Amplitude**			**Phase**		
	BODC	**T2D**	**E(a_i)**	**BODC**	**T2D**	**E(ϕ_i)**
M2	4.14	4.16	1.004	196.1	192.2	0.0024
S2	1.70	1.60	0.939	263.08	254.2	0.0119
N2	0.64	0.68	1.068	171.74	178.6	0.0072
K1	0.04	0.07	1.616	164.56	151.3	0.0269
O1	0.07	0.08	1.077	5.29	6.6	0.0003
M4	0.17	0.24	1.395	352.44	351.9	0.0000
M6	0.09	0.03	0.331	279.65	256.0	0.0839
MK3	0.02	0.02	1.147	233.75	246.8	0.0259

Table B.5: Constituent comparison at Portbury

Constituent Name	Amplitude			Phase		
	BODC	**T2D**	**E(a_i)**	**BODC**	**T2D**	**E(ϕ_i)**
M2	4.24	4.27	1.006	199.7	198.2	0.0004
S2	1.77	1.65	0.932	267.3	261.6	0.0048
N2	0.61	0.70	1.151	177.3	185.7	0.0106
K1	0.04	0.07	1.763	172.3	151.2	0.0672
O1	0.07	0.08	1.218	8.6	8.1	0.0000
M4	0.25	0.27	1.069	349.4	345.1	0.0027
M6	0.13	0.10	0.800	279.2	246.2	0.1614
MK3	0.01	0.02	1.621	226.7	244.2	0.0467

B.2 Water level timeseries comparisons

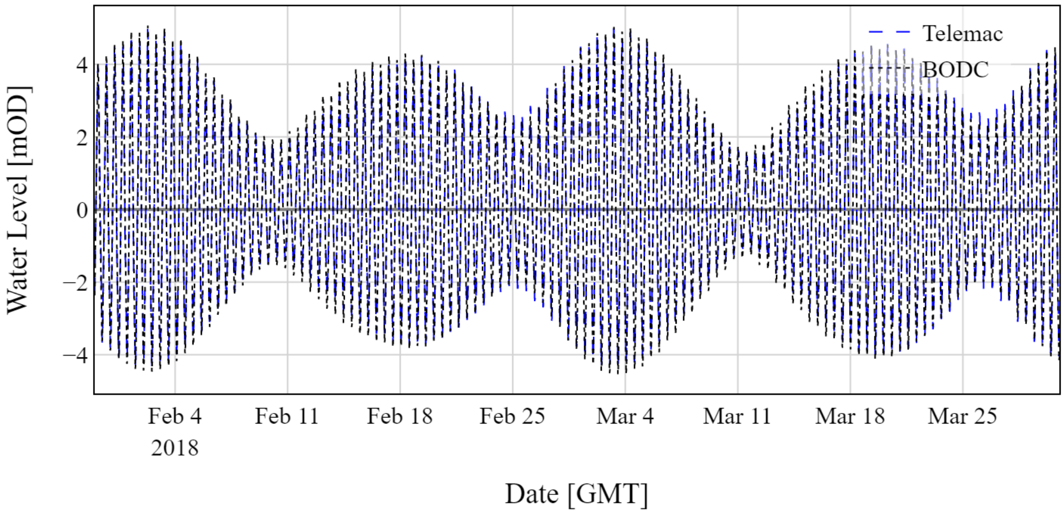

Figure B.1: BODC and TELEMAC water level timeseries comparison at Ilfracombe over full calibration period

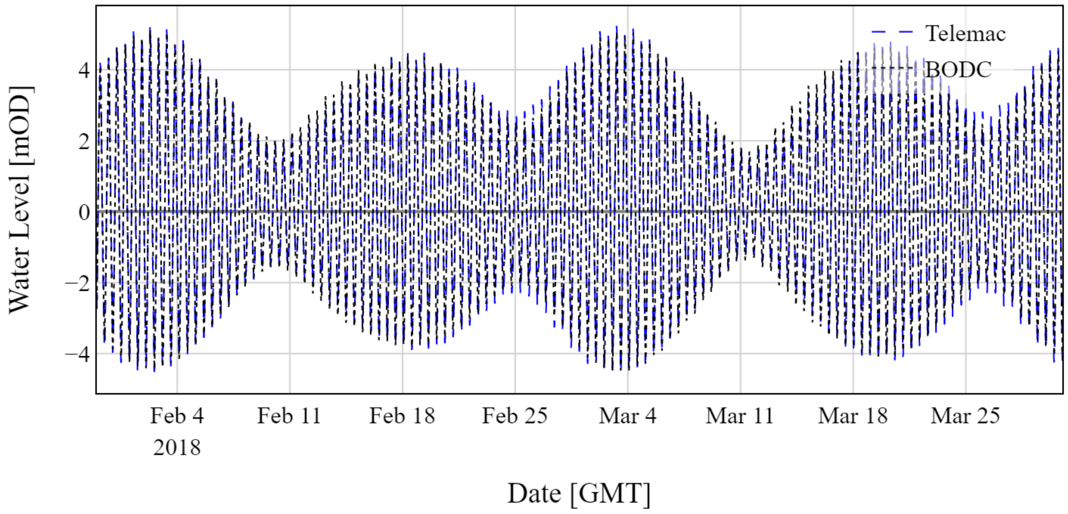

Figure B.2: BODC and TELEMAC water level timeseries comparison at Mumbles over full calibration period

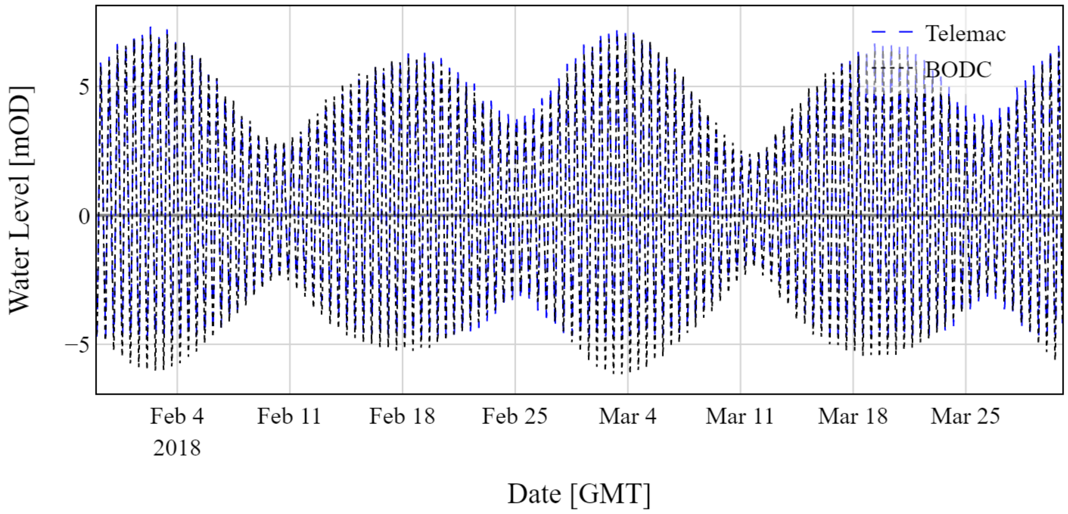

Figure B.3: BODC and TELEMAC water level timeseries comparison at Newport over full calibration period

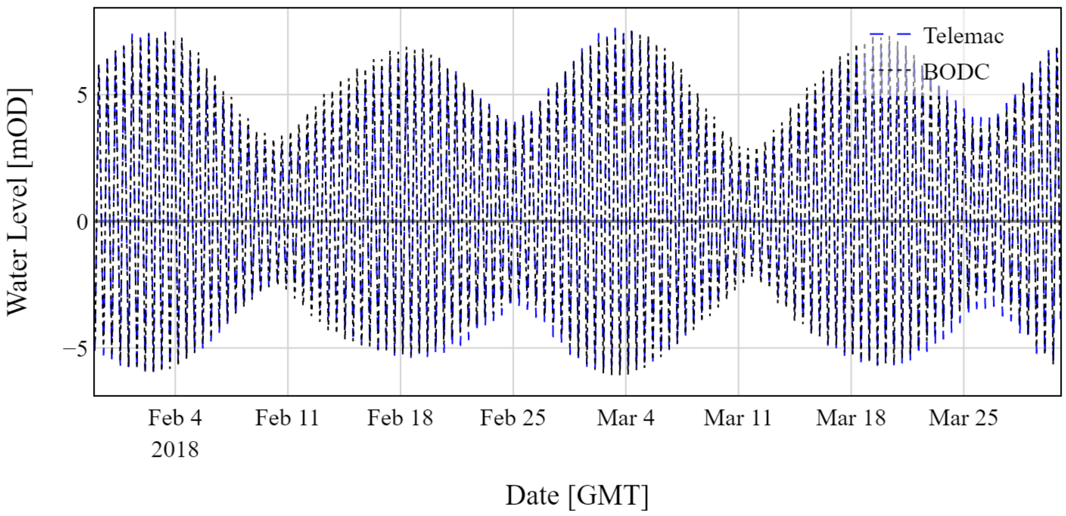

Figure B.4: BODC and TELEMAC water level timeseries comparison at Portbury over full calibration period

B.3 Water level scatter comparisons

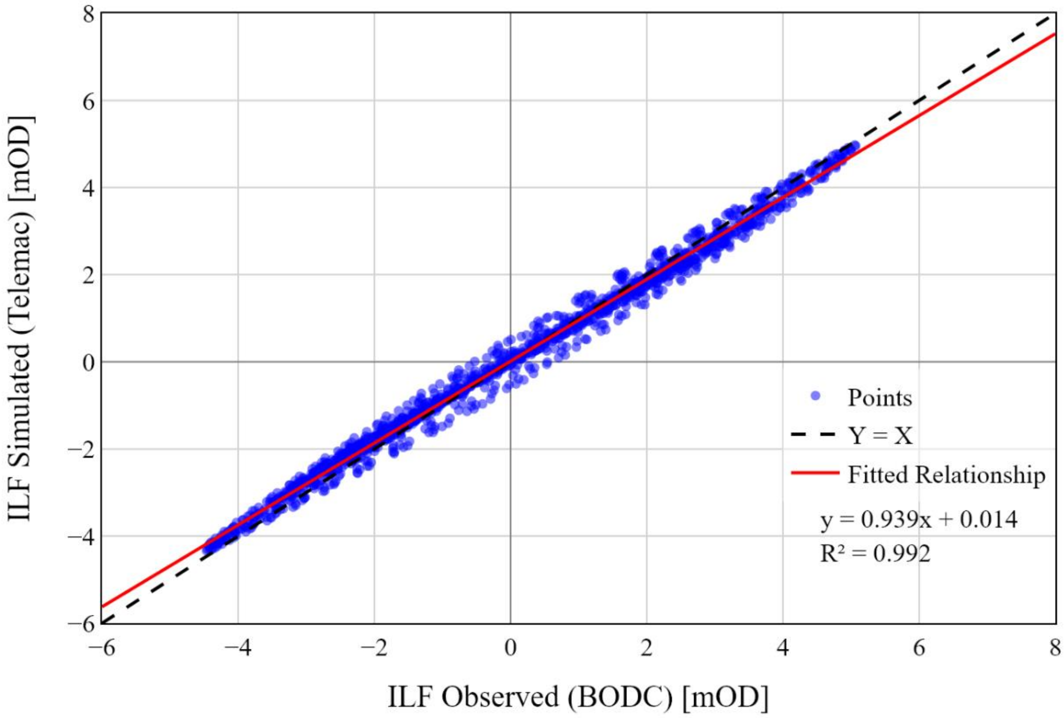

Figure B.5: BODC and TELEMAC water level scatter comparison at Ilfracombe over full calibration period

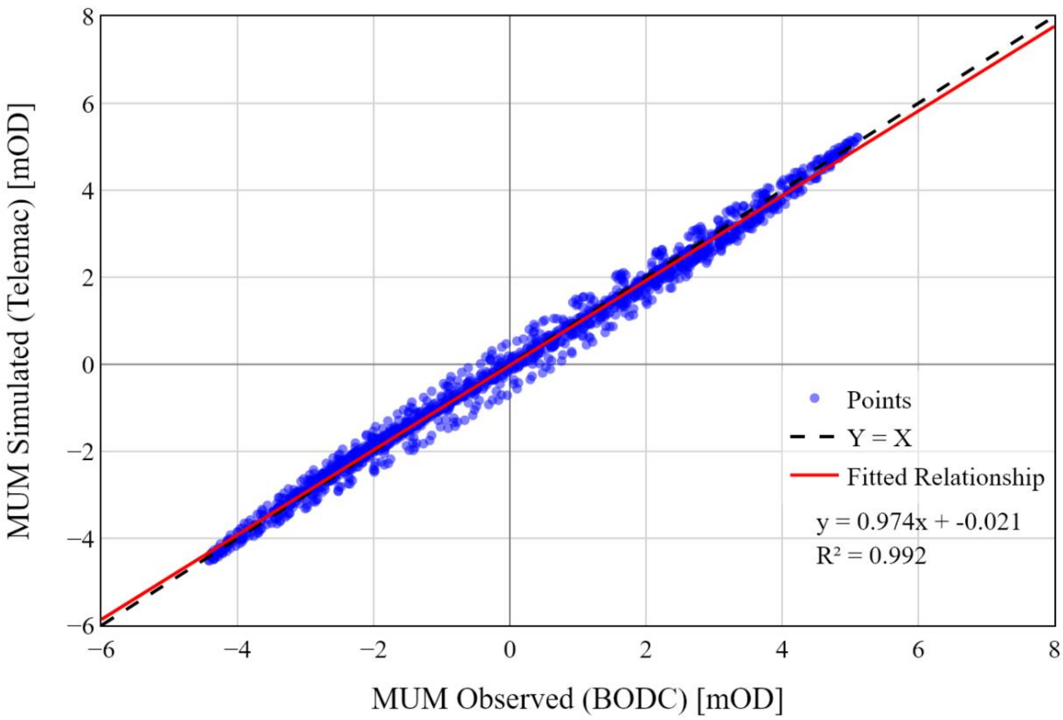

Figure B.6: BODC and TELEMAC water level scatter comparison at Mumbles over full calibration period

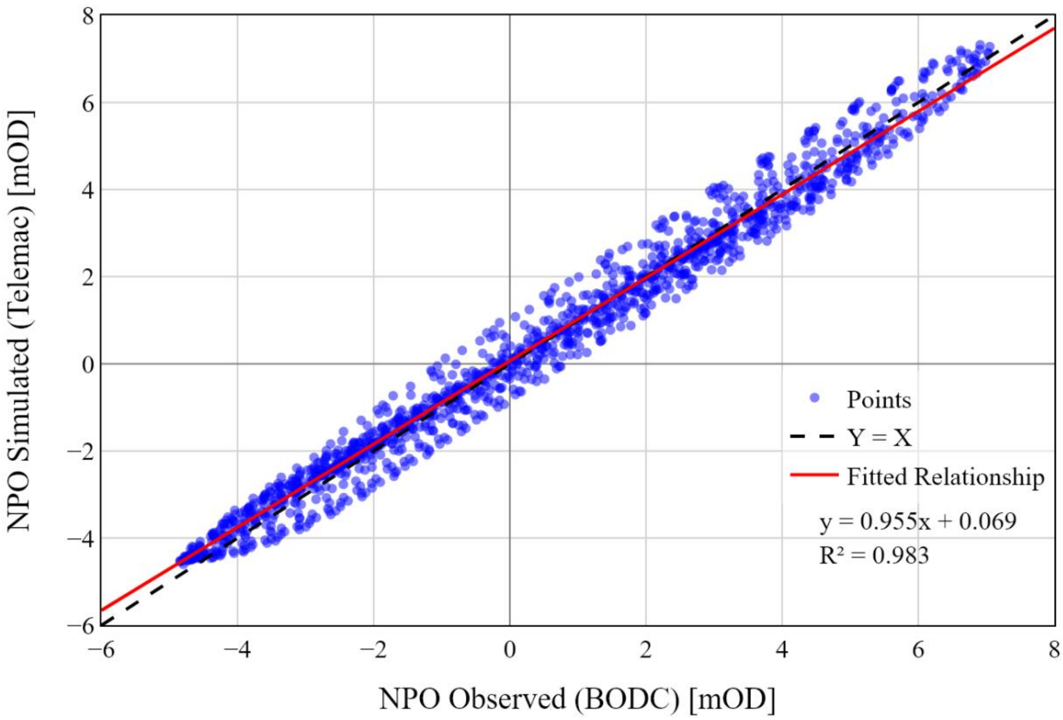

Figure B.7: BODC and TELEMAC water level scatter comparison at Newport over full calibration period

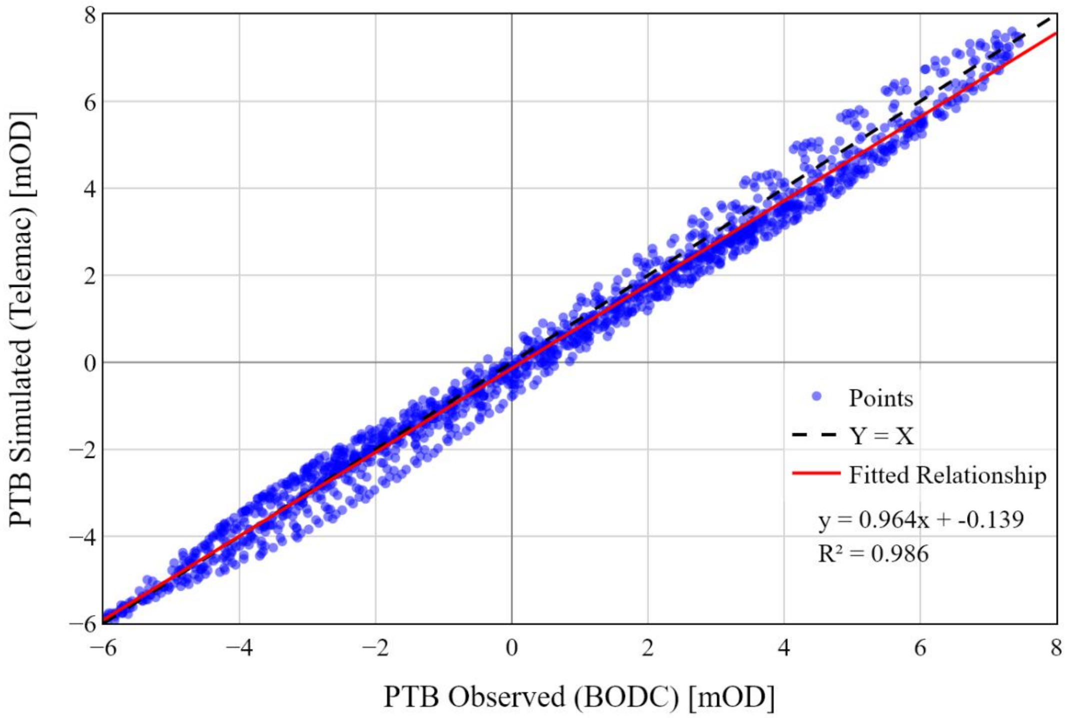

Figure B.8: BODC and TELEMAC water level scatter comparison at Portbury over full calibration period

Appendix C.TELEMAC input file examples

C.1 TELEMAC steering file

```
/---------------------------------------------------------------------
/ TELEMAC2D Version v8p3 22-Aug-2017
/ Severn WSL from Bins model configs - using TPXO boundary
/ Fixed operation, pumping, minimal cleverness
/---------------------------------------------------------------------

/---------------------------------------------------------------------
/ BOUNDARY CONDITIONS
/---------------------------------------------------------------------
STAGE-DISCHARGE CURVES                     = 0
MASS-LUMPING ON H                          = 1
VERTICAL STRUCTURES                        = NO
TREATMENT OF NEGATIVE DEPTHS               = 1
OPTION FOR THE TREATMENT OF TIDAL FLATS    = 1
/---------------------------------------------------------------------
/ EQUATIONS
/---------------------------------------------------------------------
AIR PRESSURE                         = true
LAW OF BOTTOM FRICTION               = 4
ROUGHNESS COEFFICIENT OF BOUNDARIES  = 0.025
FRICTION COEFFICIENT                 = 0.025
BOTTOM SMOOTHINGS                    = 1
TURBULENCE MODEL                     = 3
CORIOLIS                             = YES
/---------------------------------------------------------------------
/ EQUATIONS, BOUNDARY CONDITIONS
/---------------------------------------------------------------------
OPTION FOR TIDAL BOUNDARY CONDITIONS       = 1
TIDAL DATA BASE                             = 2
COEFFICIENT TO CALIBRATE TIDAL RANGE       = 1.05
COEFFICIENT TO CALIBRATE TIDAL VELOCITIES  = 1.0
COEFFICIENT TO CALIBRATE SEA LEVEL         = 0.15
GEOGRAPHIC SYSTEM                           = 1 /lat-long
SPHERICAL COORDINATES                       = YES
SPATIAL PROJECTION TYPE                     = 3
LATITUDE OF ORIGIN POINT                    = 00.0
LONGITUDE OF ORIGIN POINT                   = 00.0
RESULT FILE IN LONGITUDE-LATITUDE          = YES
BINARY DATABASE 1 FOR TIDE =
'/scratch/c.c1304433/TELEMAC/TPXO/h_tpxo9.v4a'
BINARY DATABASE 2 FOR TIDE =
'/scratch/c.c1304433/TELEMAC/TPXO/u_tpxo9.v4a'
/BINARY DATABASE 1 FOR TIDE='D:\TELEMAC\TPXO\DATA\hf.AO_2008.out'
/BINARY DATABASE 2 FOR TIDE='D:\TELEMAC\TPXO\DATA\uv.AO_2008.out'
/---------------------------------------------------------------------
/ EQUATIONS, INITIAL CONDITIONS
/---------------------------------------------------------------------
INITIAL CONDITIONS                  = 'TPXO SATELLITE ALTIMETRY'
/---------------------------------------------------------------------
/ INPUT-OUTPUT, FILES
/---------------------------------------------------------------------
GEOMETRY FILE            ='SLF_T100.slf'
RESULTS FILE             ='r2d_T100P.slf'
```

```
BOUNDARY CONDITIONS FILE ='CLI_T100.cli'
/---------------------------------------------------------------------
/ INPUT-OUTPUT, GRAPHICS AND LISTING
/---------------------------------------------------------------------
NUMBER OF PRIVATE ARRAYS         = 1
NAMES OF PRIVATE VARIABLES       = 'CULVERT M3/S'
MASS-BALANCE                    = true
VARIABLES FOR GRAPHIC PRINTOUTS = U,V,B,H,L,S,N
LISTING PRINTOUT PERIOD         = 300
GRAPHIC PRINTOUT PERIOD         = 900
INFORMATION ABOUT SOLVER        = true
/---------------------------------------------------------------------
/ INPUT-OUTPUT, INFORMATION
/---------------------------------------------------------------------
TITLE ='Severn, BASIC TRS, using TPXO'
/---------------------------------------------------------------------
/ NUMERICAL PARAMETERS
/---------------------------------------------------------------------
DISCRETIZATIONS IN SPACE       = 12;11
CHECKING THE MESH             = YES
CONTINUITY CORRECTION          = true
TIDAL FLATS                    = YES
ORIGINAL DATE OF TIME          = 2018;01;30
ORIGINAL HOUR OF TIME          = 00;00;00
TREATMENT OF THE LINEAR SYSTEM = 2
H CLIPPING                     = YES
TIME STEP                      = 1
/DURATION      =      90000                 /      90000 = 25 hrs
DURATION = 1501200    / Using end-date of 16-02-2018 09:00
/ this was found as representative
/ period when staring from 01-02-2018 00:00
SUPG OPTION                    =1;1;1;1 /(for -ve depths = 1)
PARALLEL PROCESSORS            =40
/---------------------------------------------------------------------
/ NUMERICAL PARAMETERS, SOLVER
/---------------------------------------------------------------------
SOLVER ACCURACY =1.E-5
/---------------------------------------------------------------------
/ NUMERICAL PARAMETERS, VELOCITY-CELERITY-HIGHT
/---------------------------------------------------------------------
IMPLICITATION FOR VELOCITY =0.6
IMPLICITATION FOR DEPTH    =0.6
/---------------------------------------------------------------------
/ PHYSICAL CONSTANTS
/---------------------------------------------------------------------
WATER DENSITY =1020.
/---------------------------------------------------------------------
/ TIDAL RANGE COMPONENTS
/---------------------------------------------------------------------
OPTION FOR CULVERTS  = 1
NUMBER OF CULVERTS   = 109
CULVERTS DATA FILE    = 'T100_culvertdata.txt'
FORTRAN FILE          = 'user_fortran'
MAXIMUM NUMBER OF ITERATIONS FOR SOLVER    =150
MAXIMUM NUMBER OF ITERATIONS FOR K AND EPSILON    =150
```

C.2 TRS control file

```
Turbine bank TRS file for WSL
RAMPTIME            0.25
PREV_SWITCH         0.0
MAX_GEN             48
MAX_HOLD            48
```

```
MAX_SLUICE          48
MAX_PUMP            48
IS2WAY              T
ISFLEXIBLE          TRUE
ISPUMPING           T
MODE_FIRST          4
N_HILLS_G           1
N_HILLS_P           1
LEN_HILLS_G         16
LEN_HILLS_P         16
N_FLEX              2
ORIG_DIAM_T         9
WARMUP              0.5
PUMPTOLEVEL         F
MODE                0
GENERATOR FLOW
0    0
1    282
1.5  381
2    458
2.5  519
3.7  650
6    708
6.5  719
7    723
7.1  690
7.5  641
8    587
8.5  545
9    511
9.5  484
11.3 401
GENERATOR POWER
0    0
1    0.1
1.5  2.3298
2    5.1731
2.5  8.1827
3.7  15.9697
6    32.2995
6.5  35.951
7    38.9
7.1  38.9
7.5  38.9
8    38.9
8.5  38.9
9    38.9
9.5  38.9
11.3 38.9
PUMP FLOW
0    0
1    282
1.5  381
2    458
2.5  519
3.7  650
6    708
6.5  719
7    723
7.1  690
7.5  641
8    587
8.5  545
9    511
9.5  484
11.3 401
```

```
PUMP POWER
0    0
1    0.1
1.5  2.3298
2    5.1731
2.5  8.1827
3.7  15.9697
6    32.2995
6.5  35.951
7    38.9
7.1  38.9
7.5  38.9
8    38.9
8.5  38.9
9    38.9
9.5  38.9
11.3 38.9
FLEX CONTROL
12.5 4.9 2.5 1 2 1
1000.0 4.9 2.5 1 2 1
!(START_TIME,H_START,H_END,TURBINE_CHART,PUMP_TARGET,PUMP_CHART)
```

Appendix D. Hydro-environmental impact of West Somerset Lagoon

D.1 Case 0

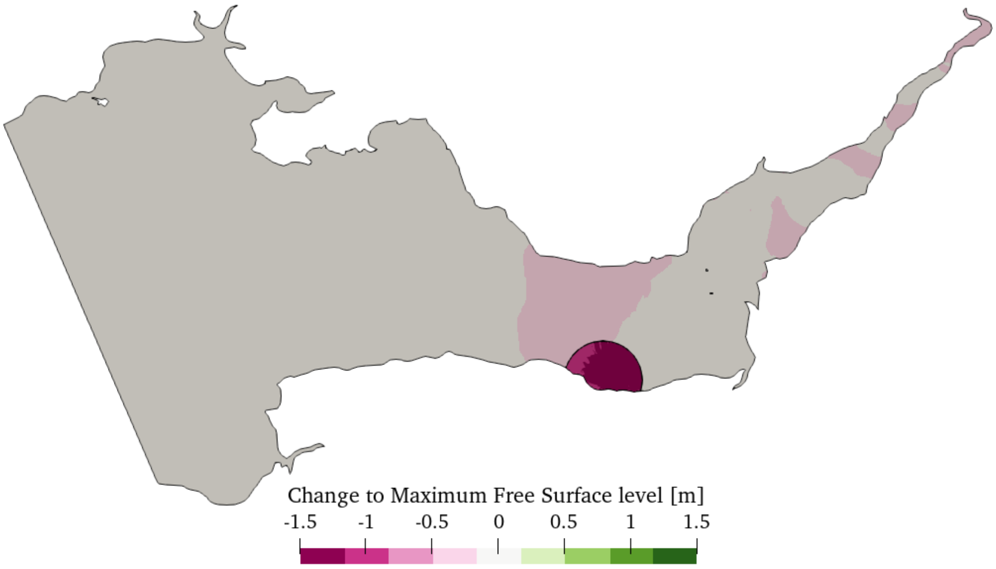

Figure D.1: Change to maximum water level in SEBC model when operating WSL using Case 0

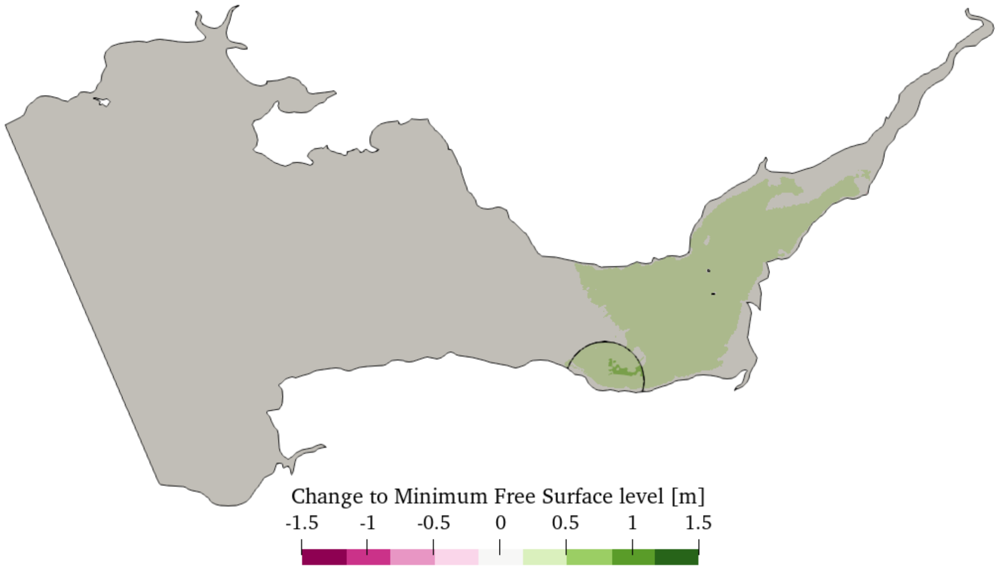

Figure D.2: Change to maximum water level in SEBC model when operating WSL using Case 0

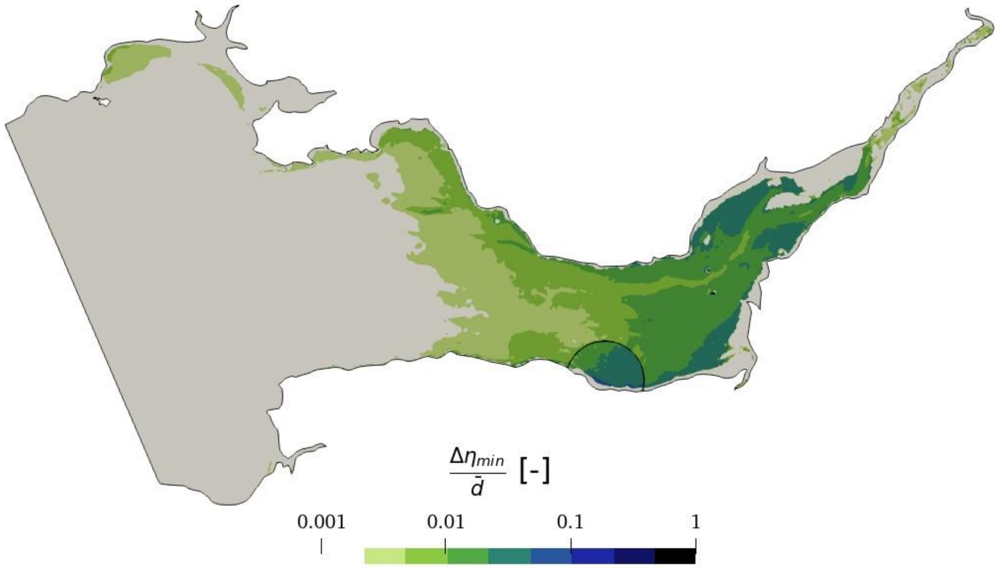

Figure D.3: Average water depth normalised change to minimum water level in SEBC model due to WSL using Case 0.

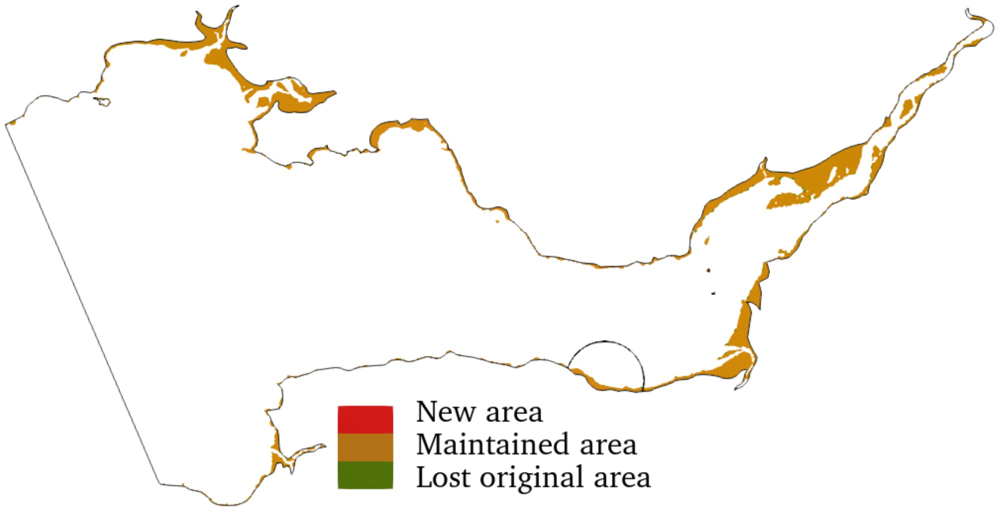

Figure D.4: Change to intertidal area in SEBC model when operating WSL using Case 0

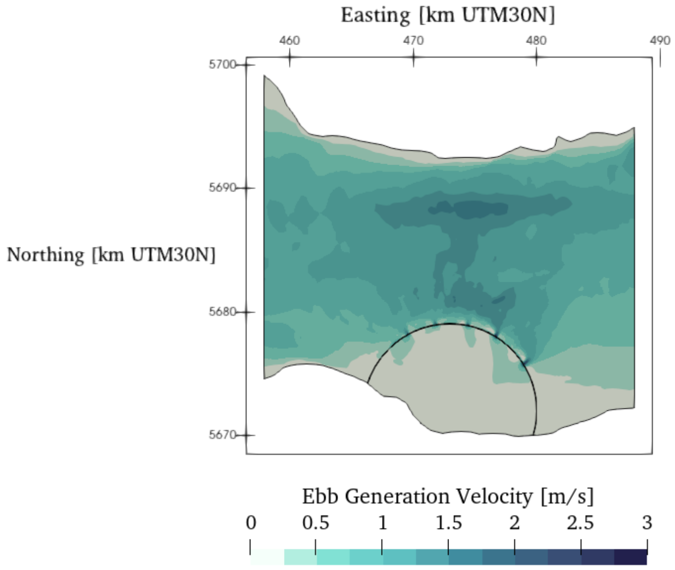

Figure D.5: Ebb generation average velocity field in SEBC model when operating WSL using Case 0

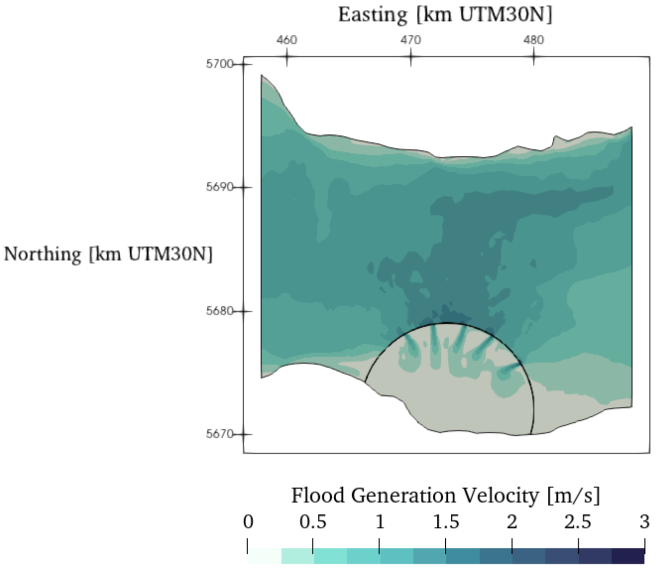

Figure D.6: Flood generation average velocity field in SEBC model when operating WSL using Case 0

D.2 Case 2

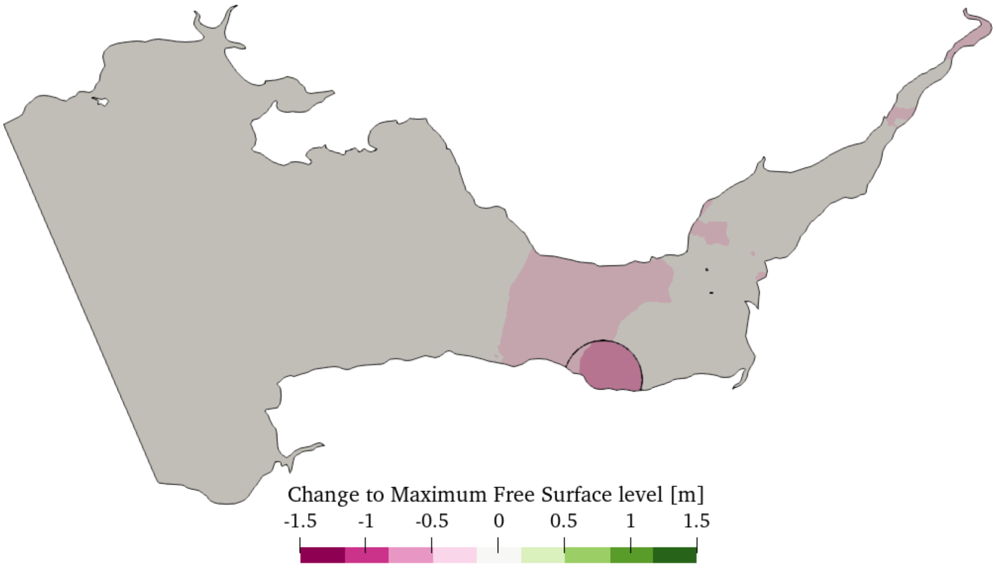

Figure D.7: Change to maximum water level in SEBC model when operating WSL using Case 2

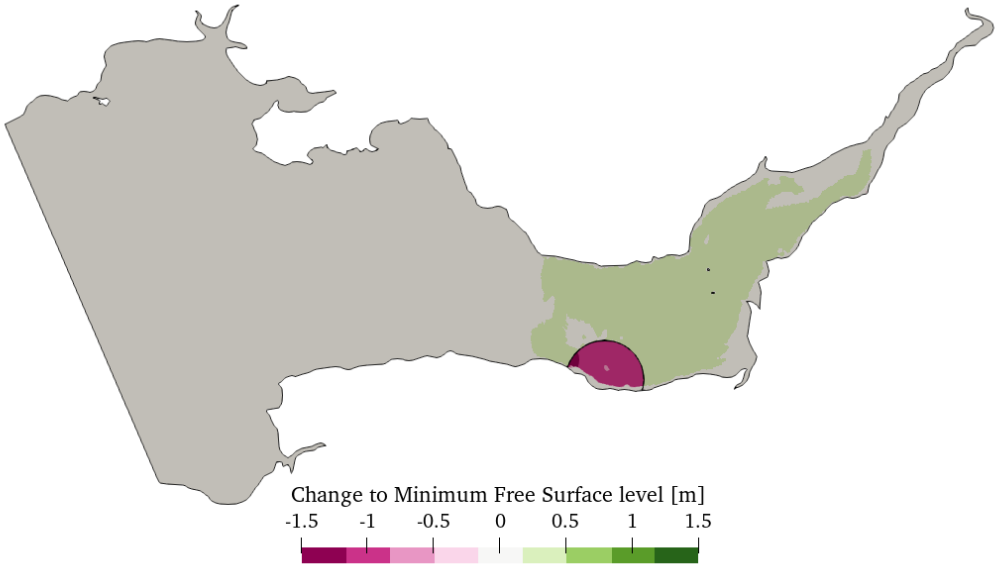

Figure D.8: Change to minimum water level in SEBC model when operating WSL using Case 2

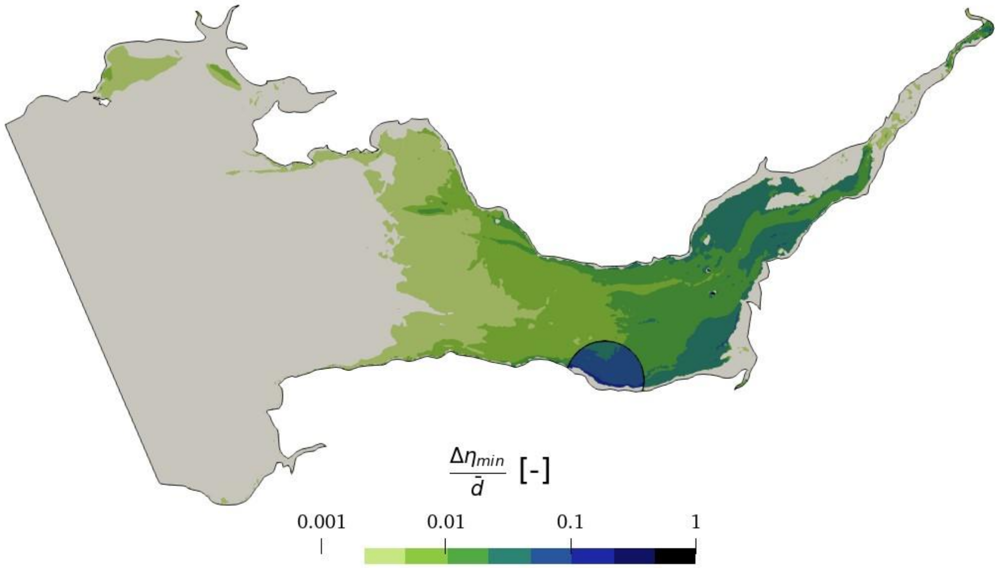

Figure D.9: Average water depth normalised change to minimum water level in SEBC model due to WSL using Case 2.

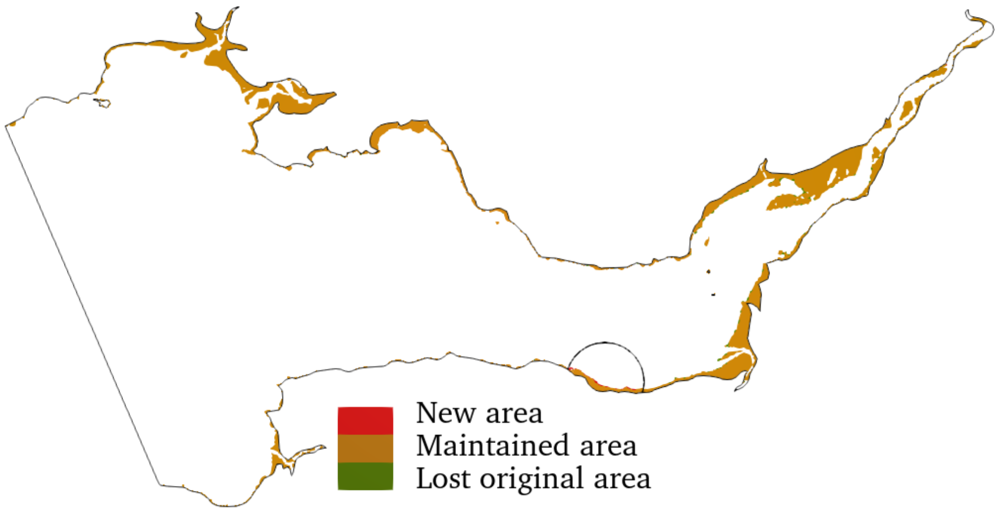

Figure D.10: Change to intertidal area in SEBC model when operating WSL using Case 2

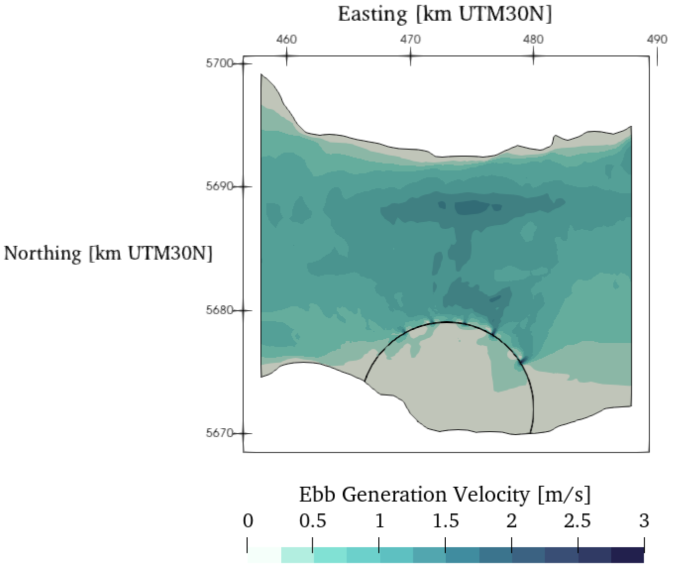

Figure D.11: Ebb generation average velocity field in SEBC model when operating WSL using Case 2

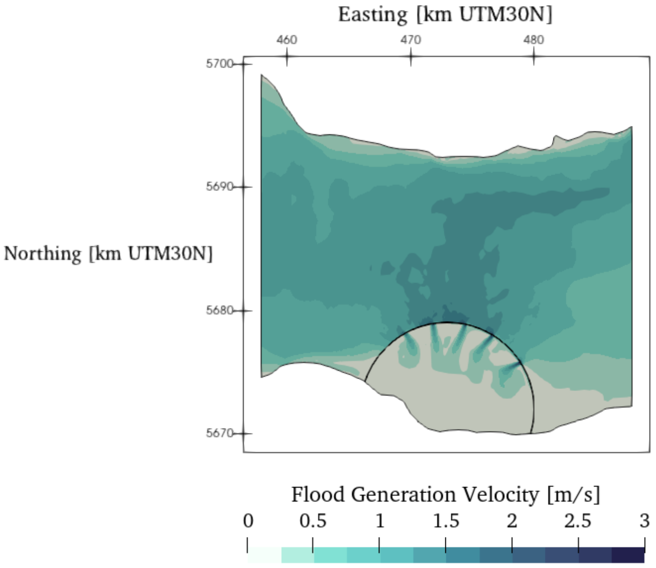

Figure D.12: Flood generation average velocity field in SEBC model when operating WSL using Case 2

D.3 Case 3

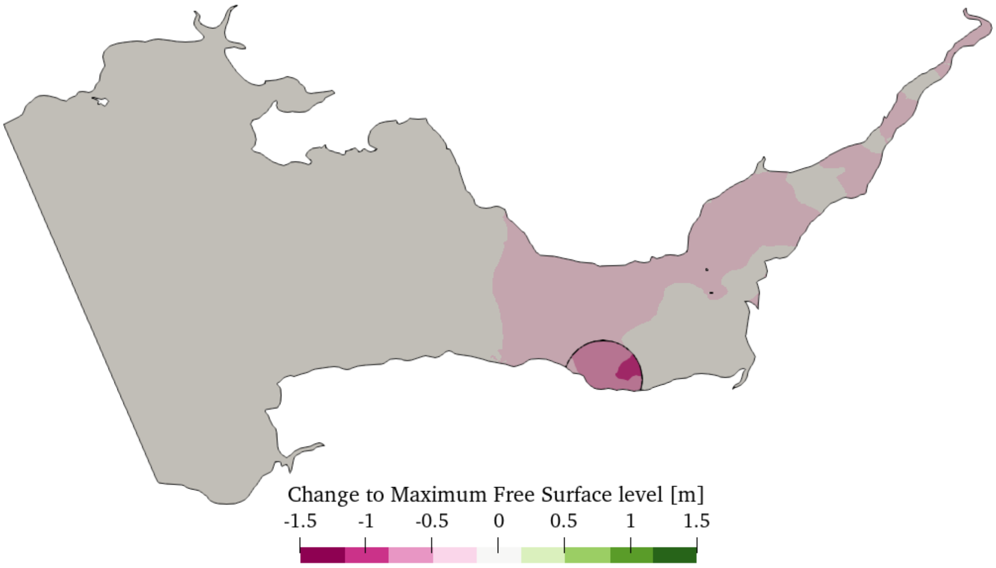

Figure D.13: Change to maximum water level in SEBC model when operating WSL using Case 3

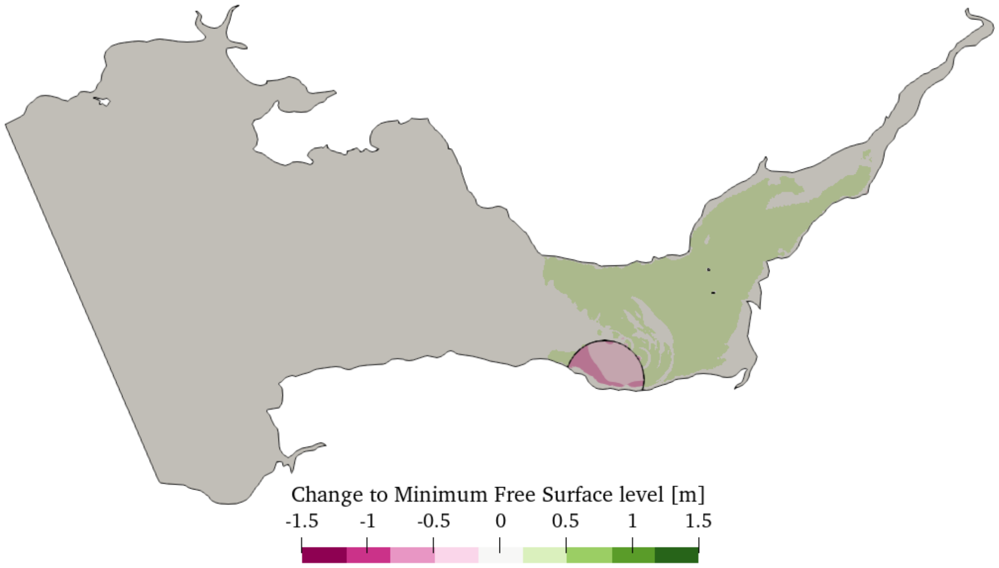

Figure D.14: Change to minimum water level in SEBC model when operating WSL using Case 3

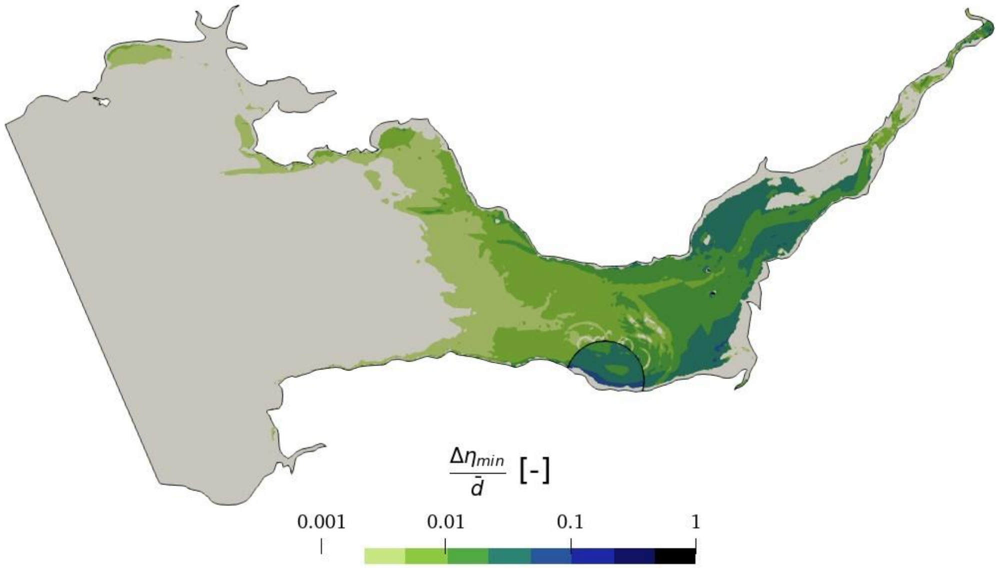

Figure D.15: Average water depth normalised change to minimum water level in SEBC model due to WSL using Case 3.

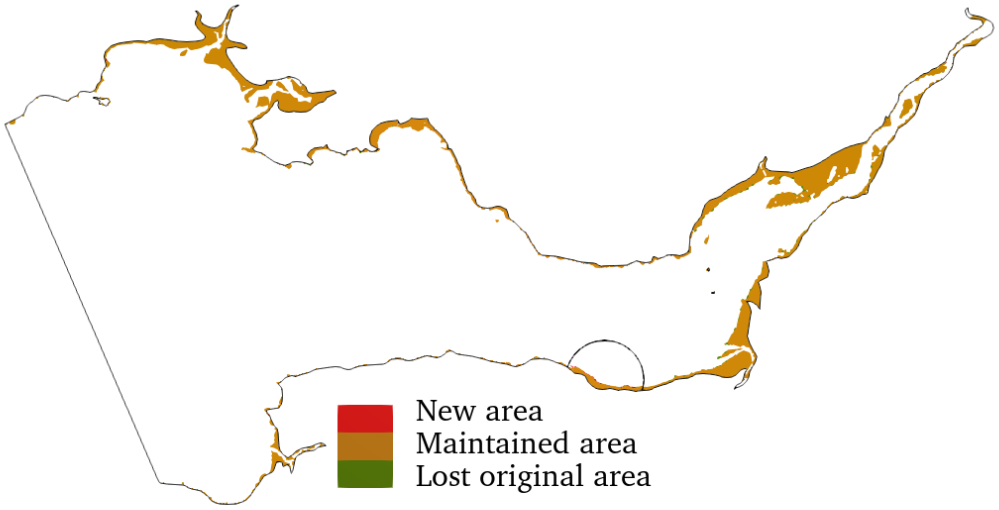

Figure D.16: Change to intertidal area in SEBC model when operating WSL using Case 3

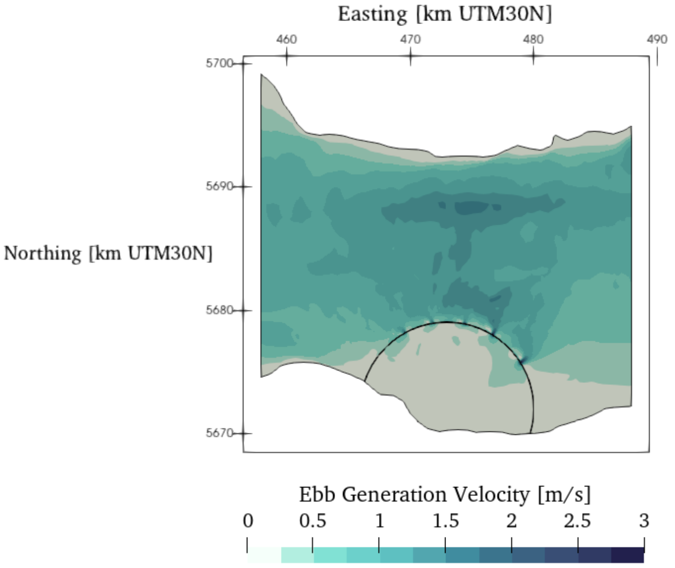

Figure D.17: Ebb generation average velocity field in SEBC model when operating WSL using Case 3

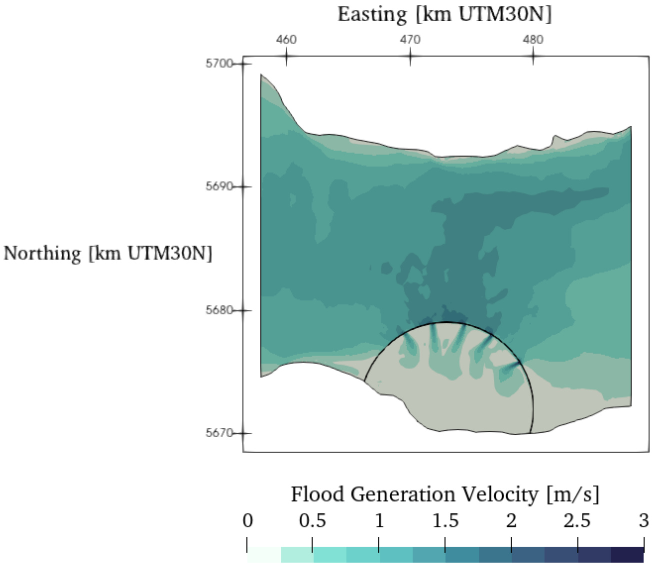

Figure D.18: Flood generation average velocity field in SEBC model when operating WSL using Case 3

Appendix E. Comparison of 0D and 2D behaviour at WSL

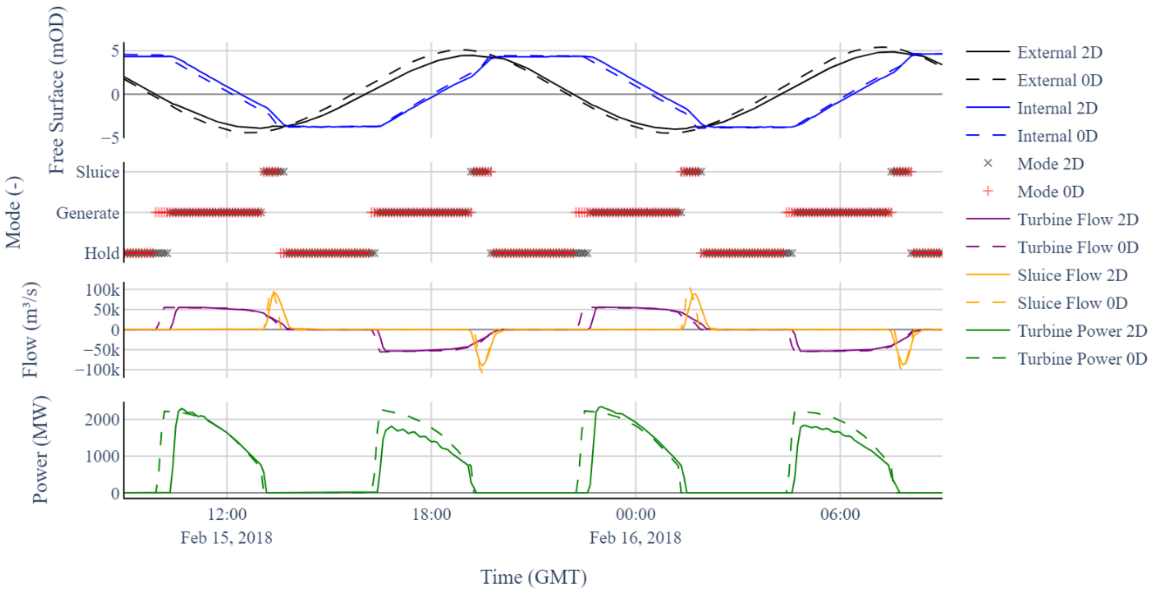

Figure E.1: Comparison of C0 behaviour between 0D and 2D in final 24 hours of 2D simulation (mean tide)

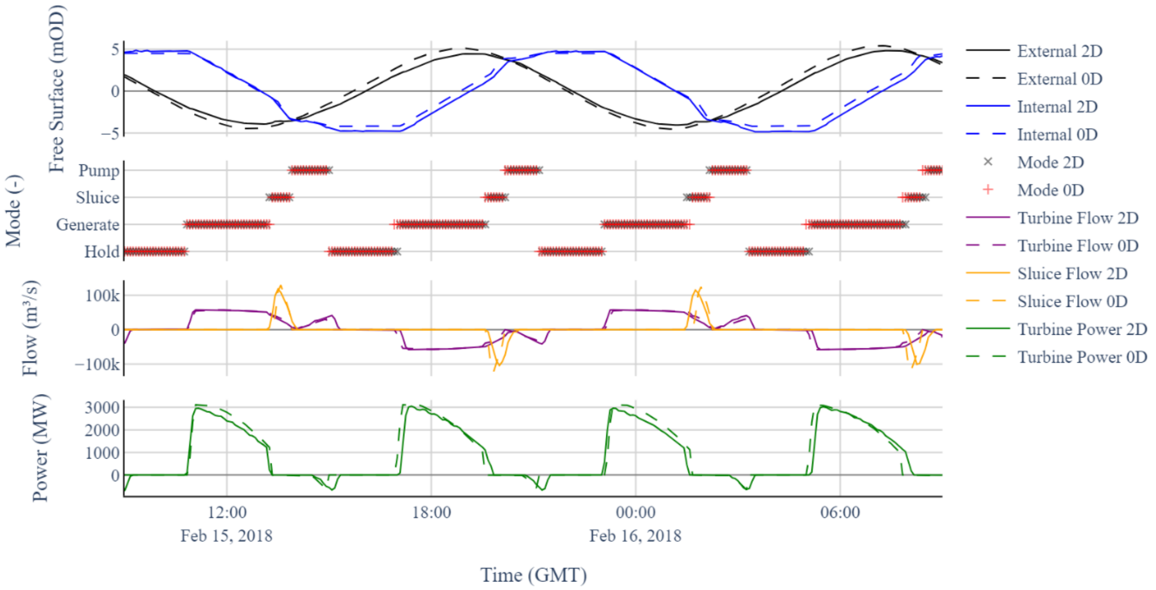

Figure E.2: Comparison of C2 behaviour between 0D and 2D in final 24 hours of 2D simulation (mean tide)

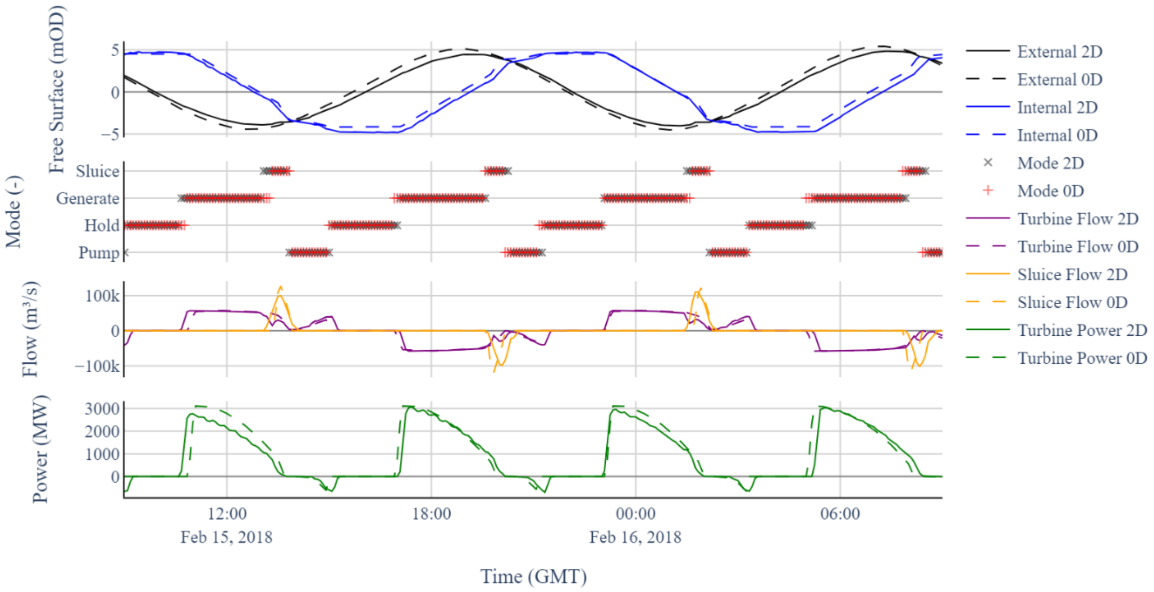

Figure E.3: Comparison of C3 behaviour between 0D and 2D in final 24 hours of 2D simulation (mean tide)